Novel Applications of Terahertz Quantum Cascade Lasers: Gas Spectroscopy, Active control & Nearfield Imaging

Binbin Wei

Darwin College

Department of Physics

University of Cambridge

October 2019

This dissertation is submitted for the degree of

Doctor of Philosophy

Declaration

This dissertation is the result of work carried out in the Semiconductor Physics Group at the Cavendish Laboratory from October 2015 to September 2019. I hereby declare that except where specific reference is made to the work of others, the contents of this dissertation are original and have not been submitted in whole or in part for consideration for any other degree or qualification in this, or any other universities. This dissertation is the result of my own work and includes nothing which is the outcome of work done in collaboration except as declared in the Acknowledgements and specified in the text. This dissertation contains fewer than 60,000 words.

Binbin Wei

October 2019

Abstract

Since the advent of Terahertz (THz) quantum cascade lasers (QCLs) in 2002, they have seen significant improvement in output power, operating temperature, and spectral coverage as well as having been widely applied to astronomical applications, imaging, and spectroscopy because of their high output power and narrow spectral linewidth. In this work, three techniques, self-mixing gas spectroscopy, THz amplitude modulation and THz nearfield imaging, will be experimentally studied and demonstrated. These techniques can either expand or increase the efficiency of their corresponding applications using other techniques.

The dissertation starts with a brief introduction of the basic knowledge of THz QCLs and some characterization methods for a THz system, as well as a summary of their main applications and their current capabilities.

When the lasing of a THz QCL is suppressed, it becomes a quantum cascade amplifier (QCA), which compared with a THz QCL can enhance the sensitivity in both spectroscopy and imaging applications. A THz QCA has been achieved by adhering an antireflection-coated Si lens to the QCL facet and is then used as the source for THz gas spectroscopy based on a self-mixing effect, in which the THz QCL functions as both the light source and the detector. This offers an approach to achieving a compact spectroscopy system with a fast response.

For spectroscopy, communication and astronomical applications, the ability to actively control the amplitude of the THz radiation is desired. This has been demonstrated with a graphene loaded metamaterial device, with which and a PID feedback loop, the output power fluctuation of a THz QCL is reduced from 1.52% to 0.043% of the total power.

An amplitude stabilised THz source is also essential for high resolution THz imaging, where amplitude fluctuations will distort the acquired THz images. A scattering type nearfield microscope (s-SNOM) with a better than $\lambda/1000$ resolution has been demonstrated with a tuning fork based atomic force microscope (AFM) and a partially suppressed THz QCL. The detection scheme is also harnessing the self-mixing effect. Compared with conventional detection methods, this can give a fast response and high sensitivity, which are essential for high-speed high-resolution imaging. The performance of this home-built THz s-SNOM has then been significantly improved by vibration isolation and electronic noise reduction and it has been used to examine a variety of samples. It is able to reveal the plasmonic resonance of resonant structures,

spatially map the electric field distribution on a metamaterial device and image subsurface plasmons. By using tips of different materials, it has also been found that a gold coating can improve the THz sensitivity of the system.

Afterwards, to optimise the design of metamaterials, a special metasurface has been designed to study the influence of the geometric parameters on the optical performance of it. This can be achieved by probing the electric field distribution of the metasurface with the THz s-SNOM. The dissertation is then concluded with all the results obtained and a brief overview of what can be done in the future in related research fields.

Binbin Wei
Cambridge
October 2019

Acknowledgements

There are many people and organisations I need to thank for helping me finish my PhD work in Cambridge. Firstly, I would like to thank my supervisors Prof. David Ritchie and Dr. Harvey Beere for offering me the opportunity to study in Cambridge and their help throughout my PhD study and the financial support from the Engineering and Physical Sciences Research Council for all my research projects.

I would like to give special thanks to Dr. Riccardo Degl'Innocenti for teaching me basic semiconductor processing techniques, sharing his expertise on optical experiments and all the discussion and advice on amplitude stabilization and THz s-SNOM projects. Even after he moved to Lancaster, he is still always there to offer help whenever it is needed. Thanks also goes to Dr. Yuan Ren for teaching me THz QCL processing and building up a basic QCL characterisation system, as well as all the advice and help on the self-mixing spectroscopy project, and to Dr Peter Spencer for all the help and meaningful discussions on all my work.

I would like to acknowledge the help I got from Nikita Almond, Wladislaw Michailow, and Dr. Robert Wallis on the THz s-SNOM project and our collaborator Thomas Siday and Dr. Oleg Mitrofanov on the indium resonant tips. I would also like to thank Stephen Kindness for all the help on the metamaterial devices as well as Philipp Braeuninger-Weimer, Jack Alexander-Webber and Oliver Burton for providing us graphene used in all the projects.

I am indebted to Yuqing Wu, Chong Chen, James Luis, Jinggao Sui, Teng Yi and Hangtian Hou for all the support and help, both in my research and daily life throughout my PhD.

Thanks goes to all my friends in and around Cambridge (Andrew, Barney, Chaochao, Chisom, David, DCBC family, Junzhan, Maomao, Philipp, Raphäel, Timothé, Xingran, Zernep, Zhenyuan, etc.) for making my life here colourful and meaningful and to all my other friends for your support.

Thanks goes to Darwin College, DCBC, DCSA, DarGar and CCRC for providing me platforms to meet nice people and enjoy my life in Cambridge.

And thank you to my parents and elder brother, for everything.

Publications

Journal articles

B. Wei, S.J. Kindness, N.W. Almond, R. Wallis, Y. Wu, Y. Ren, S.C. Shi, P. Braeuninger-Weimer, S. Hofmann, H.E. Beere, D.A. Ritchie, R. Degl'Innocenti, Amplitude stabilization and active control of a terahertz quantum cascade laser with a graphene loaded split-ring-resonator array, Appl. Phys. Lett. 112 (2018). doi:10.1063/1.5027687.

R. Degl'Innocenti, R. Wallis, **B. Wei**, L. Xiao, S.J. Kindness, O. Mitrofanov, P. Braeuninger-Weimer, S. Hofmann, H.E. Beere, D.A. Ritchie, Terahertz Nanoscopy of Plasmonic Resonances with a Quantum Cascade Laser, ACS Photonics. 4 (2017) 2150–2157. doi:10.1021/acsphotonics.7b00687.

S.J. Kindness, D.S. Jessop, **B. Wei**, R. Wallis, V.S. Kamboj, L. Xiao, Y. Ren, P. Braeuninger-Weimer, A.I. Aria, S. Hofmann, External amplitude and frequency modulation of a terahertz quantum cascade laser using metamaterial/graphene devices, Sci. Rep. 7 (2017) 7657.

S.J. Kindness, N.W. Almond, **B. Wei**, R. Wallis, W. Michailow, V.S. Kamboj, P. Braeuninger-Weimer, S. Hofmann, H.E. Beere, D.A. Ritchie, R. Degl'Innocenti, Active Control of Electromagnetically Induced Transparency in a Terahertz Metamaterial Array with Graphene for Continuous Resonance Frequency Tuning, Adv. Opt. Mater. (2018). doi:10.1002/adom.201800570.

S.J. Kindness, N.W. Almond, W. Michailow, **B. Wei**, L. Jakob, K. Delfanazari, P. Braeuninger-Weimer, S. Hofmann, H.E. Beere, and D.A. Ritchie, ACS Photonics (2019). doi:10.1021/acsphotonics.9b00411

R. Degl'Innocenti, L. Xiao, S.J. Kindness, V.S. Kamboj, **B. Wei**, P. Braeuninger-Weimer, K. Nakanishi, A.I. Aria, S. Hofmann, H.E. Beere, D.A. Ritchie, Bolometric detection of terahertz quantum cascade laser radiation with graphene-plasmonic antenna arrays, J. Phys. D. Appl. Phys. 50 (2017). doi:10.1088/1361-6463/aa64bf.

Conference papers

B. Wei, R. Wallis, S. Kindness, O. Mitrofanov, H.E. Beere, D.A. Ritchie, R. Degl'Innocenti, Terahertz s-SNOM with> λ/1000 resolution based on self-mixing in quantum cascade lasers, in: CLEO® / Europe-EQEC, Optical Society of America, 2017: p. CC_4_2.

B. Wei, S.J. Kindness, N.W. Almond, R. Wallis, Y. Wu, Y. Ren, P. Braeuninger-Weimer, S. Hofmann, H.E. Beere, D.A. Ritchie, R. Deglalnnocenti, Amplitude Stabilization of a Terahertz Quantum Cascade Laser with an External Metamaterial Amplitude Modulator, in: 2018 Conf. Lasers Electro-Optics, CLEO 2018 - Proc., 2018.

S.J. Kindness, D.S. Jessop, **B. Wei**, R. Wallis, V.S. Kamboj, L. Xiao, Y. Ren, P. Braeuninger-Weimer, S. Hofmann, H.E. Beere, Optoelectronic control of an external cavity quantum cascade laser using a graphene loaded metamaterial array, in: Lasers Electro-Optics (CLEO), 2017 Conf., IEEE, 2017: pp. 1–2.

S.J. Kindness, D.S. Jessop, **B. Wei**, R. Wallis, V.S. Kamboj, L. Xiao, Y. Ren, P. Braeuninger-Weimer, S. Hofmann, H.E. Beere, D.A. Ritchie, R. Degl'lnnocenti, 100 % amplitude modulation of an external cavity terahertz QCL using an optoelectronic chopper based on metamaterials and graphene, in: Opt. InfoBase Conf. Pap., 2017.

S.J. Kindness, N.W. Almond, R. Wallis, **B. Wei**, V.S. Kamboj, P. Braeuninger-Weimer, S. Hofmann, H.E. Beere, D.A. Ritchie, R. Degl'lnnocenti, Active frequency modulation of metamaterial/graphene optoelectronic device using coupled resonators, in: Opt. InfoBase Conf. Pap., 2018. doi:10.1364/CLEO_QELS.2018.FW3H.

R. Degl'Innocenti, S.J. Kindness, N.W. Almond, **B. Wei**, R. Wallis, V.S. Kamboj, P. Braeuninger-Weimer, S. Hofmann, H.E. Beere, D.A. Ritchie, Metamaterial/graphene amplitude and frequency modulators for the active control of terahertz quantum cascade lasers, in: Proc. SPIE - Int. Soc. Opt. Eng., 2018. doi:10.1117/12.2320506.

Contents

Chapter 2

Chapter 3

List of Figures

List of Tables

List of Abbreviations

2D	2-dimensional
ADFB	Aperiodic distributed feedback
AFM	Atomic force microscope
AIP	Active isolation platform
ALD	Atomic layer deposition
AOM	Acousto-optic Modulator
AR	Antireflection
a.u.	Arbitrary unit
CCD	Charge-coupled device
CVD	Chemical vapour deposition
LIV	Light-current-voltage
CW	Continuous wave
DFB	Distributed feedback laser
DFG	Difference-frequency generation
E-beam	Electron beam
EM	Electromagnetic
EOS	Electrooptic sampling
FET	Field effect transistor
FFT	Fast Fourier transform
FTIR	Fourier Transform Infrared Spectroscopy
FWHM	Full-width at half-maximum
GSD	Ground state depletion
HDPE	High-density polyethylene
IPA	Isopropyl alcohol
JPL	Jet Propulsion Laboratory
LD	Laser diode
LO	Longitudinal-optical
LRC	Inductor-resistor-capacitor
LT	Low temperature
LTEM	Laser terahertz emission microscopy
MEK	Methyl ethyl ketone
MIBK	Methyl isobutyl ketone
NIMs	Negative-index materials
OPO	Optical parametric oscillation
PALM	Photoactivatable localization microscopy

PID	Proportional-integral-derivative
PMMA	Polymethyl methacrylate
PSD	Position-sensitive detector
QAM	Quadrature amplitude modulation
QCA	Quantum cascade amplifier
QCL	Quantum cascade laser
QTF	Quartz tuning fork
RF	Radiofrequency
RTD	Resonant tunnelling diode
SAW	Surface acoustic wave
SEM	Scanning electron microscopy
SEPHC	Surface emitting photonic crystal
SIB	Sound isolation box
SiNW	Silicon Nanowires
SLM	Spatial light modulator
SNOM	Scanning nearfield optical microscopy
SNR	Signal to noise ratio
SPD	Single pixel detector
SPEM	Saturated pattern excitation microscopy
SPM	Scanning probe microscopy
SPP	Surface plasmon polaritons
SRR	Split-ring resonators
s-SNOM	Scattering-type scanning nearfield optical microscopy
STED	Stimulated emission depletion
STM	Scanning tunnelling microscopy
STORM	Stochastic optical reconstruction microscopy
TDS	Time domain spectroscopy
THz	Terahertz
UTC-PD	Uni-travelling-carrier photodiode

Chapter 1
Introduction

Terahertz (THz) radiation offers many intriguing research opportunities, ranging from fundamental science to practical applications. In this chapter, an overview of the application of THz radiation and THz sources will be given. At the same time, two of the most widely used THz sources, THz quantum cascade laser (QCL) and THz time-domain spectroscopy (TDS), will be discussed in detail as well as the production of THz functional materials with a metamaterial approach. A brief introduction is then given for three important applications of THz radiation investigated later in other chapters, which are spectroscopy, communication and imaging.

1.1 THz radiation

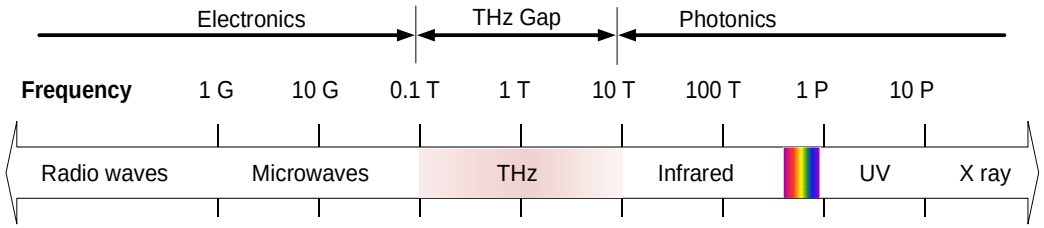

Wavelength	30 cm	3 cm	3 mm	300 μm	30 μm	3 μm	300 nm	30 nm
Wavenumber (cm^{-1})	0.033	0.33	3.3	33	330	3300	33000	330000
Photon energy (meV)	4×10^{-3}	4×10^{-2}	4×10^{-1}	4	40	400	4000	40000
Temperature (K)	0.05	0.5	5	50	500	5000	50000	500000

Figure 1.1 The electromagnetic spectrum

The THz region, which lies at the gap between visible light and microwave, as shown in Figure 1.1, is usually loosely defined by the frequency range from 0.1 THz to 10 THz [1], [2]. It is often referred to as the last frontier of the electromagnetic spectrum because of the relatively low maturity of components and systems for THz applications, compared to photonics and electronics. However, many breakthroughs have been made during the last two decades, ranging from the sources, detectors and modulators, etc.

[1], [3]–[11], which are the key components for a THz system. This has promoted the development of a variety of THz applications, including information and communication technology [12]–[15], non-destructive evaluation [16], biomedical research and technology [17], [18], environmental monitoring [19], sensing and imaging [20]–[22], etc.

1.2 THz sources

Figure 1.2 shows some of currently existing THz sources, which are mainly derived from three approaches. The first and oldest approach is optical THz generation. In this approach, THz radiation is produced either through nonlinear optical effects (such as optical rectification (OR) [23], [24], difference-frequency generation (DFG) or optical parametric oscillation (OPO) [25], [26]), or generating an ultrafast photocurrent in a photoconductive switch or semiconductor antenna using either electric-field carrier acceleration or the photo-Dember effect [27], [28].

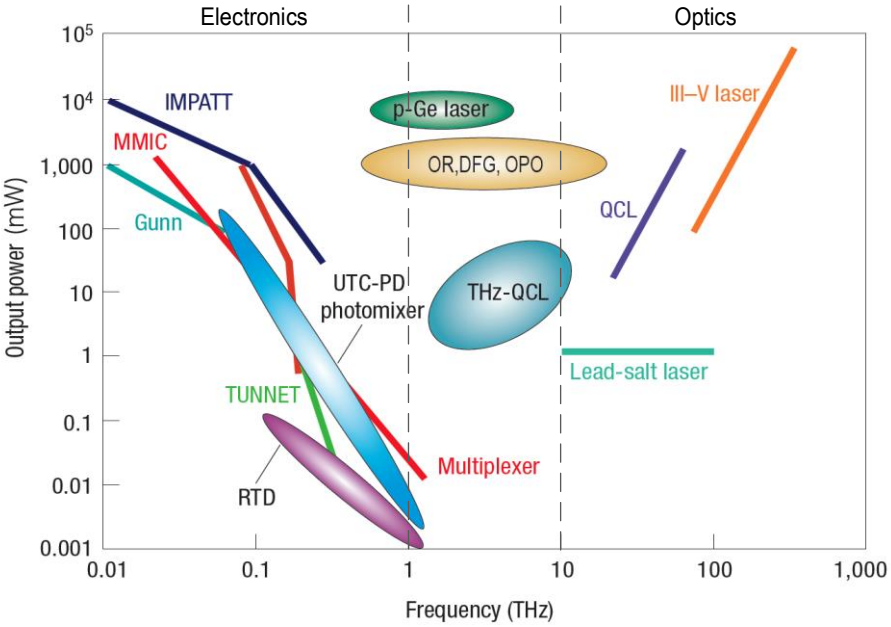

Figure 1.2 THz emission at different frequency ranges, reprinted by permission from [2] © 2007, Springer Nature.

The second approach is based on solid-state electronic devices, which have entered from the low frequency end of the THz range, among which sits the uni-travelling-carrier photodiode (UTC-PD) that exhibits promising characteristics [29]. It produces high-quality sub-THz waves by the means of photo mixing and the emission is typically tunable up to 1.5 THz. The THz waves in a UTC-PD are generated by the optical beating of the light from two different wavelength laser diodes (LDs) with the emission

frequency being defined by the difference between the two wavelengths. They can produce a typical power on the order of mW at 300 GHz [30] and μW at 1 THz [31].

The final approach is the semiconductor laser, namely THz QCL, which will be discussed in detail in the next section. Apart from that, other approaches have been explored as well, such as the resonant tunnelling diodes (RTDs) [32], free-electron laser [33], etc.

1.3 Terahertz quantum cascade lasers

Since being first demonstrated, THz QCLs have become one of the most promising, high power, compact source of THz radiation [34]. They utilise intersubband transitions inside a semiconductor's conduction band to achieve THz emission. The advantage of using intersubband transitions is that the emission frequency is no longer determined directly by the band gap of the materials. Instead, it is set by the design of the active region, which enables tuning of the emission frequency over a large bandwidth without changing the material system. This is achieved by changing the energy separation of the electronic states through changing the size of quantum wells. Though the idea of using intersubband transitions for radiation amplification was first proposed in 1971 by Kazarinov and Suris [35] in a superlattice structure, it took more than 20 years before the birth of the first QCL in 1994 operating in the mid-infrared [36] because of significant technical challenges. It took a further 8 years before demonstration of the first THz QCL in 2002 [37].

The first THz QCL worked at 4.4 THz with a maximum operating temperature of 50 K. Now, with all these years of development, the spectral coverage, output power and temperature performance of THz QCLs have seen dramatic improvement. The emission frequency covers a range from 1.2 THz to 7 THz [38][39]. As for the output power, THz QCLs working in continuous wave (CW) mode can already produce an output of 100 mW [40] while the output power of a pulsed one can already reach 2.4 W [41]. Meanwhile, the temperature performance has also improved greatly. With the application of metal-metal waveguides, the highest operating temperature has reached 210 K, allowing operation with a thermoelectric cooler [42].

1.3.1 Operating principle

The basic operating principle of a quantum cascade laser can be understood through Figure 1.3 by taking a longitudinal-optical (LO) phonon active region design as an example. In this five-state system, electrons in the state 1' are injected to the upper lasing state 5 of the next period through quantum tunnelling. The radiation transition

then takes place between state 5 and 4. The lower radiative state (state 4) is selectively delocalized by anticrossing it with the excited state in the wide quantum well (state 3), where a fast depopulation through resonant phonon scattering into state 2 happens. As a result, the lifetime of state 4 is quite short (usually several ps). The energies of a resonant phonon in GaAs and AlAs are around 36 meV and 50 meV, respectively. Therefore, the energy difference between state 3 and state 2 is designed to be a value between these two numbers depending on the material percentage of the quantum well barriers. Here, it is 39.3 meV. In addition, due to a relatively thick barrier, the scattering time of the upper lasing state to the injector doublet 2 and 1 is quite long (usually tens of ps), so that a population inversion is established. The electrons in state 1 will then be injected into the upper radiative state of the next period. This process goes on across the whole active region.

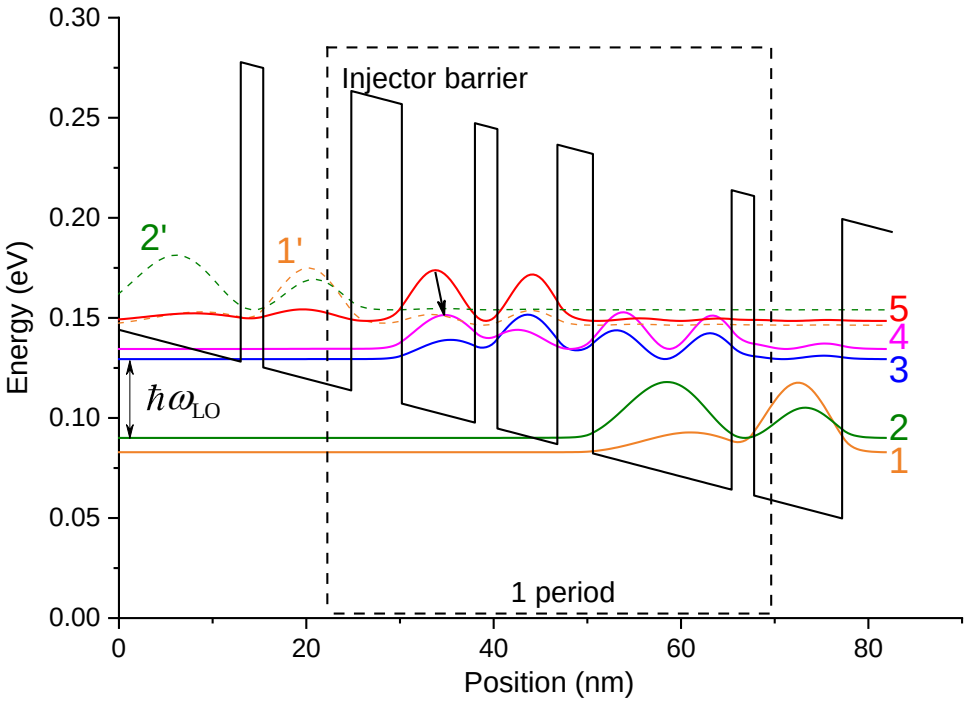

Figure 1.3 Conduction band diagram of a THz QCL with a resonant-phonon active region design [43].

1.3.2 Rate equation

As with other types of lasers, a rate equation model can be used to understand the requirements to achieve lasing within a QCL. The active region can be simplified as a three-level system, as shown in Figure 1.4 [44]. Population inversion, and thus laser action, occurs between level 3 and level 2. The injector is assumed to consist of only one level with a constant population n_g. Under the right applied bias, it will be aligned

with the upper level of the next period so that electrons will be injected via resonant tunnelling into the upper state (n=3 state) from the ground state of the injector in the previous period at a rate of J/e. Three processes are related to the electrons in the n=3 state: scattering from this state to n=2 and n=1 states with rates τ_{32}^{-1} and τ_{31}^{-1}, respectively and escaping into the continuum with a lifetime τ_{esc}. Thus, the following relationship exists

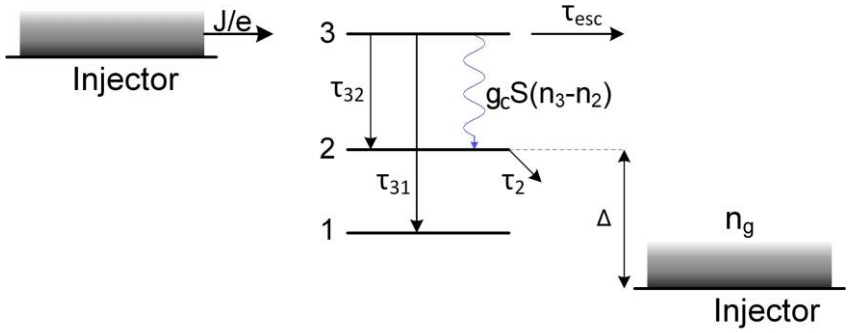

Figure 1.4 Rate equation model diagram of a three-level system, adapted from [44]

$$\tau_3^{-1} = \tau_{32}^{-1} + \tau_{31}^{-1} + \tau_{\mathrm{esc}}^{-1} \ , \tag{1.1}$$

where τ_3 is the life time of the n=3 state. At the same time, there is also a possibility that electrons are thermally activated to the state n=2 with an equilibrium population n_2^t. This process can be approximated by an activated behavior

$$n_2^t = n_{\mathrm{g}} e^{-\Delta/kT} \ , \tag{1.2}$$

where n_{g} is the sheet doping density of the injector and Δ is the energy difference between the Fermi level of the injector and the n=2 state of the laser transition. Therefore, assuming that the electron density within the three levels are n_1, n_2 and n_3 respectively, the population change of the three levels may be written as

$$\frac{\mathrm{d}n_3}{\mathrm{d}t} = \frac{J}{e} - \frac{n_3}{\tau_3} - S g_{\mathrm{c}}(n_3 - n_2) \ , \tag{1.3}$$

$$\frac{\mathrm{d}n_2}{\mathrm{d}t} = \frac{n_3}{\tau_{32}} + S g_{\mathrm{c}}(n_3 - n_2) - \frac{n_2 - n_2^t}{\tau_2} \ , \tag{1.4}$$

$$\frac{\mathrm{d}S}{\mathrm{d}t} = \frac{c}{n_{\mathrm{r}}}\left[S\left(g_{\mathrm{c}}(n_3 - n_2) - \alpha_{\mathrm{tot}} \right) + \beta \frac{n_3}{\tau_{\mathrm{sp}}} \right] \ . \tag{1.5}$$

Here, S is the photon density, which is defined as the photon flux per period and unit

active region width. It has a different unit from the electron density n_i, which is defined as sheet density per period. It should be noted that these equations only represent one period of the active region. n_r is the refractive index. α_{tot} is the total modal loss, which is a sum of the waveguide loss α_w and mirror loss α_m. β is the fraction of the spontaneous emission coupled in the laser mode while τ_{sp} is the lifetime of spontaneous emission. g_c is the gain cross-section, which is usually considered as one for all the periods in the active region together. It can be expressed as

$$g_c = \Gamma \frac{4\pi e^2}{\epsilon_0 n_r \lambda} \frac{z_{32}^2}{2\gamma_{32} L_p} , \tag{1.6}$$

where z_{32} is the dipole matrix element, $2\gamma_{32}$ is the full width at half maximum (FWHM) broadening of the transition, is the wavelength and L_p is the length of the period. Γ is the total overlap factor, which indicates the optical overlap of the mode with the gain medium [45].

When the laser operates below the threshold current, the time derivatives in the rate equation and the photo density S should all be zero. In addition, as $\tau_{esc} \gg \tau_3$, the amplified spontaneous emission can be neglected, as it only becomes significant when the current is extremely close to the threshold. From the first two equations, the population inversion can be obtained as

$$\Delta n = \frac{J\tau_3}{e}\left(1 - \frac{\tau_2}{\tau_{32}}\right) - n_2^t = \frac{J\tau_{eff}}{e} - n_2^t . \tag{1.7}$$

where $\tau_{eff} = \tau_3(1 - \tau_2/\tau_{32})$ is the effective lifetime and relates the population inversion to the electrical pumping. From the equation (1.7), it can be seen that population inversion can only happen when $\tau_{eff} > 0$, or in other words $\tau_2 < \tau_{32}$. The threshold current density is reached when the modal gain $g_c \Delta n$ can compensate for the total loss.

$$J_{th} = e\frac{\alpha_{tot}/g_c + n_2^t}{\tau_{eff}} \tag{1.8}$$

The photon density *S* can be obtained by solving the rate equation as

$$S = \frac{\Gamma}{eL_s \frac{c}{\tau_{eff}} \alpha_{tot}} (J - J_{th}) \frac{\tau_{eff}}{\tau_{eff} + \tau_2} . \tag{1.9}$$

The output power *P* is proportional to the photon density *S* and the mirror loss α_{m1} by:

$$P = \hbar \nu \left(\frac{N_{\mathrm{p}} A L_{\mathrm{s}}}{\Gamma} \right) \left(\frac{c}{\tau_{\mathrm{eff}}} \right) S \alpha_{\mathrm{m1}} \tag{1.10}$$

with N_{p}, A, and L_{s} denoting the number of QCL stages, the area of the current cross-section and the cavity length. When the current density becomes larger than the threshold, the gain is clamped and S climbs linearly. The slope efficiency η for the whole stack is then defined as

$$\eta = \frac{\mathrm{d}P}{\mathrm{d}I} = \frac{\mathrm{d}P}{\mathrm{d}S} \frac{\mathrm{d}S}{\mathrm{d}J} = \frac{N_{\mathrm{p}} h\nu}{e} \frac{\alpha_{\mathrm{m1}}}{\alpha_{\mathrm{tot}}} \frac{\tau_{\mathrm{eff}}}{\tau_{\mathrm{eff}} + \tau_2} \tag{1.11}$$

From equation (1.9) and equation (1.11), it can be seen that to achieve a low threshold and high efficiency laser, the following design optimisation should be pursued: a large ratio of upper-state to lower-state lifetime τ_{32}/τ_2, a low waveguide loss α_{w}, a narrow transition linewidth $\Delta\nu_{32}$ and a long upper-state lifetime τ_3. Following these criteria, several active region designs and two types of waveguides have been developed for THz QCLs, which will be discussed in the next two sections.

1.3.3 Active region design

The goal of the active region designs that will be discussed here is to provide the maximum gain while minimizing the accompanying loss. Traditionally, the peak gain of the intersubband transition is used to evaluate an active region design. It is defined as

$$g(\nu_0) \propto \frac{\Delta N f_{21}}{\Delta \nu} \ , \tag{1.12}$$

where ΔN is the three-dimensional intersubband population inversion, f_{21} is the oscillator strength between the upper and lower transition states and $\Delta\nu$ is the transition linewidth. Up to now, four types of active region designs have been developed.

1.3.3.1 Chirped superlattice

In a chirped superlattice design, several quantum wells are coupled together in a superlattice to create so-called minibands of states when an appropriate electric field is applied. A population inversion is established based on the idea that intra-miniband scattering (scattering of electrons between the tightly coupled states within the miniband) is favoured over inter-miniband scattering. The radiative transition takes place between the lowest states of the upper minibands and the highest state of the lower minibands, as shown in Figure 1.5 (a).

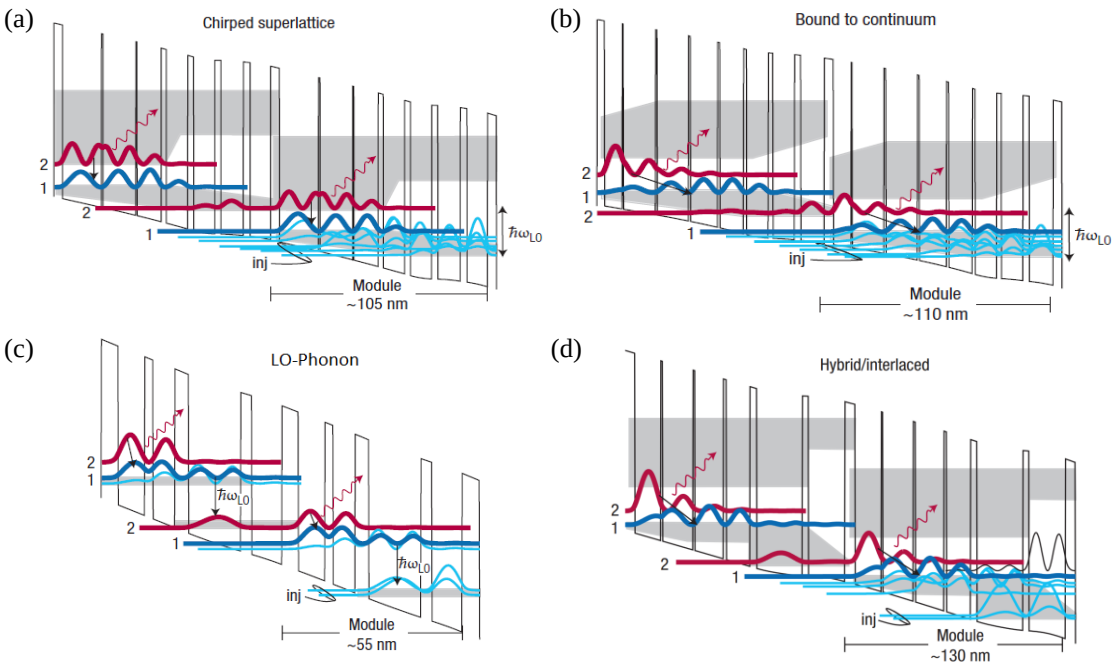

Figure 1.5 Conduction-band diagrams for (a) chirped superlattice, (b) bound-to-continuum, (c) LO-phonon and (d) hybrid active region designs, adapted with permission from reference [46] © 2007, Springer Nature.

1.3.3.2 Bound-to-continuum

To improve injection efficiency, the bound-to-continuum design shown in Figure 1.5 (b) was developed [47]–[50]. It is a modification of the chirped superlattice design in that the lower radiative state remains the same and the depopulation is still through intra-miniband scattering. What makes a difference is that the upper radiative state is essentially made to be a bound 'defect' state in the minigap [47] so that the injector states couple more strongly with the upper state than with the lower miniband, making the injection process more selective. Compared with a chirped superlattice design, the bound-to-continuum design possesses a more diagonal transition but a smaller oscillator strength as the overlap within the miniband states is reduced. As the injection efficiency is improved and a longer upper state lifetime is obtained, the bound-to-continuum design shows a better temperature and power performance [50]. However, the highest operating temperature is still limited because of the scaling of miniband width with the photon energy. For a bound-to-continuum design to work, the miniband width w needs to be much larger than the broadening of each individual level Δ and larger than the thermal energy kT [51]. The energy of THz photons is around 10 meV for THz QCLs, therefore, the miniband width is around this number as well. At a higher temperature, the broadening of each individual level will be larger and either the $w \gtrsim \Delta$ or $w > kT$ condition will be broken when the temperature increases to a certain number.

Meanwhile, the depopulation of the upper radiative states through thermally activated LO-phonon scattering will be increased at a higher temperature, making it more difficult to achieve a population inversion.

1.3.3.3 LO-phonon depopulation

As the name suggests, this design achieves depopulation, which has been discussed in Section 1.3.2, through a LO-phonon mediated transition. In this design, the lower radiative state is brought into a broad tunnelling resonance with the excited state in the adjacent quantum wells, so that its wave function is spread over several quantum wells, as shown in Figure 1.5 (c). Consequently, there is a strong spatial overlap between the lower radiative state and the injector states, achieving a fast depopulation through LO-phonon scattering. Since it was first demonstrated at MIT [52], many variations have been developed. Also, most of QCLs with high temperature performance are achieved through the combination of this design with a metal-metal waveguide [53].

1.3.3.4 Hybrid design

To achieve very long wavelength operation, hybrid structures have been developed. In a hybrid design, phonon-assisted depopulation has been incorporated with a bound-to-continuum optical transition [51][54], shown in Figure 1.5 (d). The direct coupling between the upper state and the extractor well is reduced since they are physically separated by the length of the miniband region. The alignment condition on the extraction stage is also relaxed by the fact that it has to be satisfied over the width of the miniband and no longer over the one of a single state [51].

1.3.4 The waveguide

The waveguide is another critical component of a QCL, which is used to confine the radiation. There are two things to consider when designing a QCL waveguide: maximising the overlap of the waveguide mode with the active region Γ and maintaining a low waveguide loss α_{w}. To achieve lasing, at least the following threshold condition should be satisfied

$$\Gamma g_{\mathrm{th}} = \alpha_{\mathrm{w}} + \alpha_{\mathrm{m}} \ . \tag{1.13}$$

The mirror loss α_{m} can be calculated from the following formula

$$\alpha_{\mathrm{m}} = \frac{-\ln\left(R_1 R_2\right)}{2L} \ . \tag{1.14}$$

For a GaAs interface, $R_1=R_2=0.32$, and thus the mirror loss of a 2.5 mm laser will be 4.56 cm^{-1}. To reduce the mirror loss, a high reflection coating can be applied to the facets of the laser. As for the waveguide, unlike the situation in mid-infrared QCLs, it is unrealistic to use dielectric mode confinement to confine radiation in a THz QCL for two reasons [40]. At first, the guiding layer thickness in such a waveguide scales approximately with the wavelength λ, so that >10 μm of material would be required to obtain effective confinement, which is beyond the achievable thickness of conventional epitaxy process. Furthermore, loss due to free carrier absorption increases as λ^2 for frequencies above the plasma frequency. To overcome these obstacles, two waveguides using surface plasmons to confine the radiation have been developed.

1.3.4.1 Surface plasmons

When two adjacent media have dielectric constants with opposite signs, there will be a surface plasmon at the boundary [55]. In a THz QCL waveguide, it usually exists at the metal-semiconductor interface. The electric field vector of the surface plasmon is perpendicular to the plane of the interface and the direction of propagation. It has a maximum intensity at the interface and decays exponentially when travelling through both materials. As the skin depth of surface plasmon in metal is usually very small, its intensity decays very quickly into the metal layer.

1.3.4.2 Single-plasmon (SP) waveguide

In a single-plasmon waveguide, a thin heavily n+ doped layer is grown between the active region and the semi-insulating GaAs substrate [37], as shown in Figure 1.6. Since the n+ layer is thinner than the THz skin depth, the mode has a large overlap with the substrate. As a result, the optical mode is not only confined between the top metallic contact layer and the n+ doped layer, but also extends substantially into the substrate, as shown in Figure 1.7. Nonetheless, the overlap with any doped semiconductor is small, which contributes to a minimized free-carrier loss. It is a compromise between a large overlap of the mode with the active region (Γ) and a small waveguide loss (a_w) to choose the thickness of the n+ doped layer because both Γ and a_w will increase when the thickness is increased. Typical values of Γ lie in the range 0.2-0.5 [56] in a single-plasmon waveguide.

However, this waveguide has two disadvantages. The first is that a ridge narrower than about 100 μm tends to squeeze the mode into the substrate, which sets a limitation of the minimum device area [43]. Secondly, at lower operation frequencies (<2 THz), the mode extends further into the substrate, which results in a reduction in Γ and makes it harder for the QCL to lase. Its main advantages are the ability to achieve high output

power (up to 2.4 W [41]) thanks to the reduced mode confinement and a high quality, quasi-Gaussian beam profile.

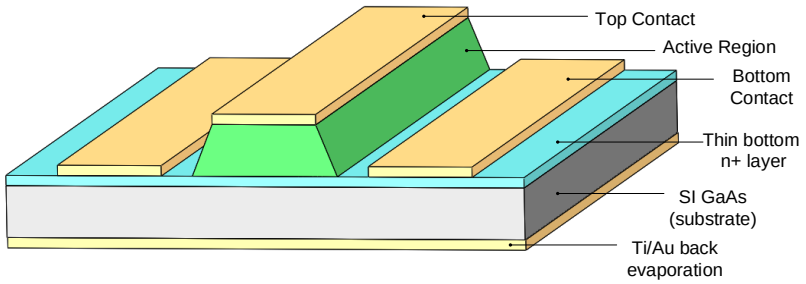

Figure 1.6 Schematic diagram for a single-plasmon waveguide

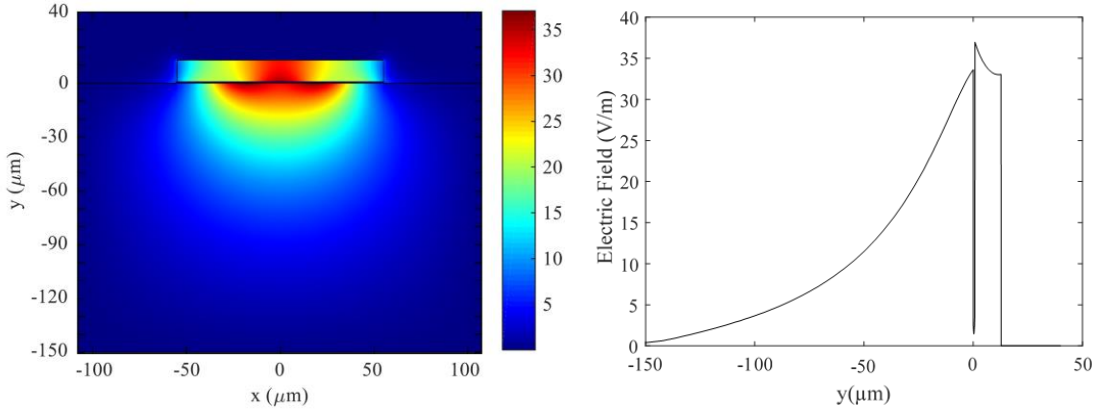

Figure 1.7 Two-dimensional mode intensity pattern (a) and its cross-section (b) for a single-plasmon waveguide from COMSOL simulations

1.3.4.3 Metal-metal (MM) waveguide

In a metal-metal waveguide, metal layers are placed above and below the active region (Figure 1.8), so that the optical mode can be nearly totally confined inside the active region ($\Gamma \approx 1$), as shown in Figure 1.9.

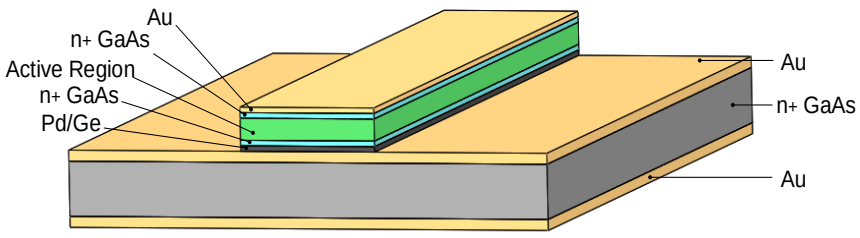

Figure 1.8 Schematic diagram for a metal-metal waveguide

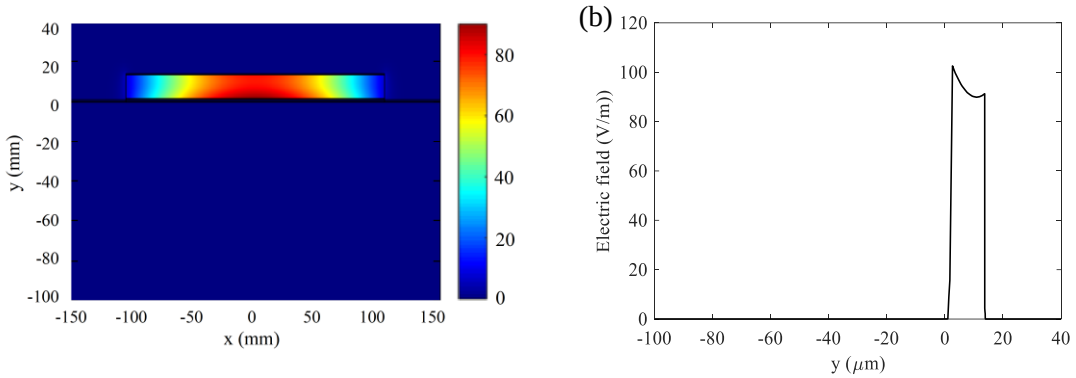

Figure 1.9 Two-dimensional mode intensity pattern (a) and its cross-section (b) for a metal-metal waveguide, from COMSOL simulations

Here, waveguide losses are dominated by absorption in the metal, and any re-absorption from the active region itself [46]. One advantage of this waveguide is that it has a good temperature performance due to a large overlap factor, which allows the use of a thinner and narrower ridge, giving better thermal management. Its drawbacks are the complexity to process, a lower output power and a poor beam profile. At present, the most widely used metal in MM waveguides is gold, but copper has demonstrated similar performance [57].

1.3.5 Characterization of a THz QCL

Standard characterization is conducted to test the performance of the laser to see whether it works as designed. The most important properties of a THz QCL are the electrical performance, current-voltage (IV) and current-light (IL) responses, and the spectrum. For applications which need the information of beam size and modal quality, a far-field beam profile scan is necessary as well.

1.3.5.1 Light-current-voltage (LIV) curve

Light-current-voltage (LIV) measurements are standard techniques in QCL characterisation. Figure 1.10 gives a schematic of the electronic configuration of the setup used for LIV measurements. To avoid heat build-up, the THz QCL is usually operated in a pulsed mode with high repetition rate (usually 10kHz for a single-plasmon THz QCL). The current through the device is measured using a pick-up coil and fed into an oscilloscope, which also measures the voltage applied to the device. The output power of the laser is detected by a THz detector (such as a Golay cell or bolometer) and the signal is then sent to a lock-in amplifier, which requires a reference pulse, supplied by a separate function generator at a frequency where the detector has the best signal to

noise ratio (SNR). The reference pulse gates the pulse generator as well as triggering the oscilloscope. All the data are finally fed into a NI data collector and displayed through a programme written with LabVIEW.

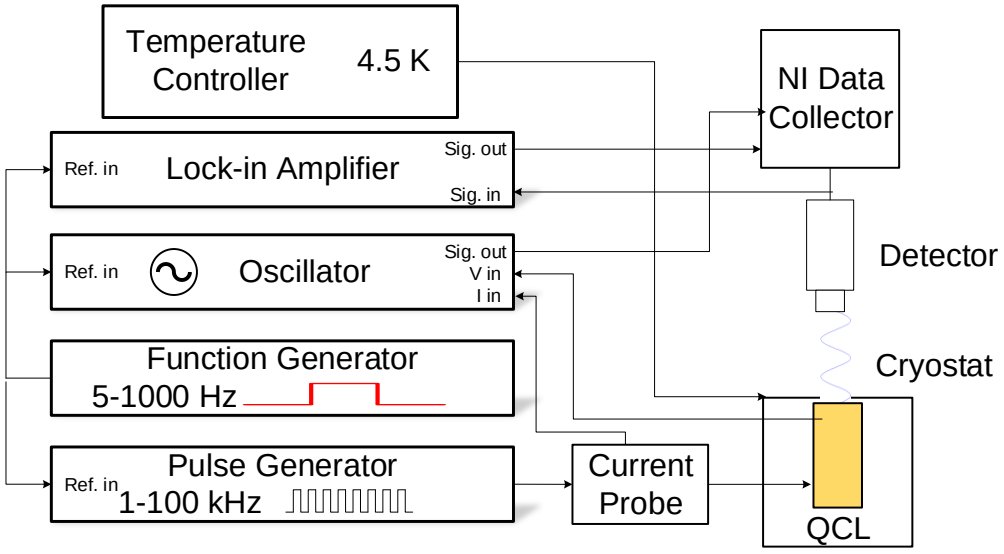

Figure 1.10 Schematic of the electronic configuration for the LIV measurements setup

LIV responses of a 2.67 THz single-plasmon waveguide THz QCL with a bound-to-continuum active region design measured using the method mentioned above are plotted in Figure 1.11 (a). At 4.5 K, the threshold current density is 104 Acm^{-2} and the maximum output power is 77 mW. When the operating temperature is increased, the threshold current increases and the dynamic range (the current density range within which the THz QCL lase) becomes smaller. The highest operating temperature of this QCL is 85 K, at which the threshold current is 225 Acm^{-2}. Figure 1.11 (b) shows the IV response of the QCL at 4.5 K. As can be seen, the THz QCL goes through 4 stages when the bias current/voltage is increased. To explain the difference between the 4 stages with respect to the alignment of the active region band diagram, the three-level system simplification in the rate equation model is utilised, as shown in Figure 1.12. The upper radiative state, the lower radiative state and the ground injector state are labelled as $|1\rangle$, $|2\rangle$ and $|g\rangle$, respectively. At zero bias (stage a in Figure 1.11 (b)), the states in all the periods are at the same level, shown in Figure 1.12 (a). During stage b, the bias voltage is increased, the states start to shift but are yet to become aligned, shown in Figure 1.12 (b). In this stage, the QCL still cannot lase but there is a small leakage path from the injector to the injector in the next period. When the laser gain overcomes device loss at the threshold current, the QCL reaches stage c, where the active region is

aligned, shown in Figure 1.12 (c). The QCL starts to lase from this point until the start of stage d, where the upper state $|2\rangle$ and ground state $|g\rangle$ starts to anti-cross, shown in Figure 1.12 (d). The discontinuous drop in the QCL differential resistance reveals the existence of photo-assisted current [58].

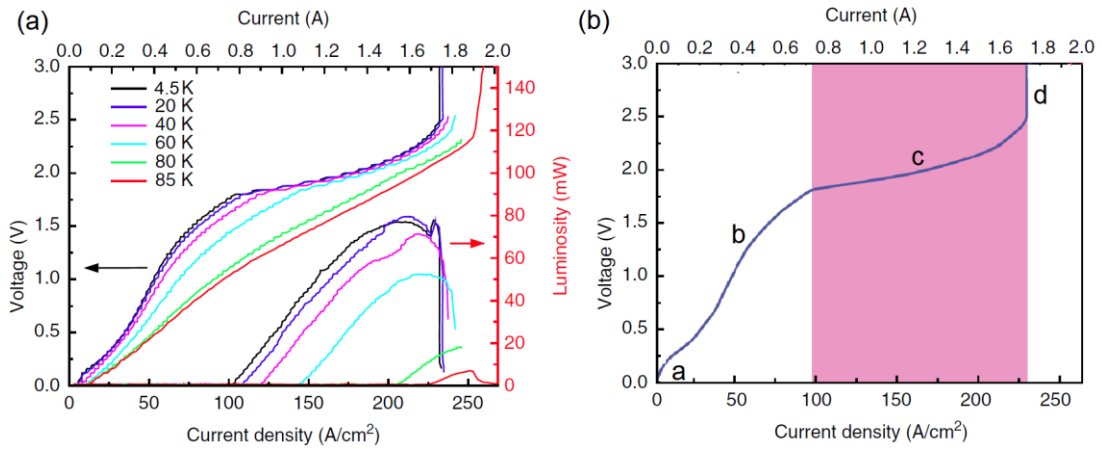

Figure 1.11 (a) LIV curve of a bound-to-continuum THz QCL with single-plasmon waveguide and (b) its IV response at 4.5 K. Adapted with permission from [58].

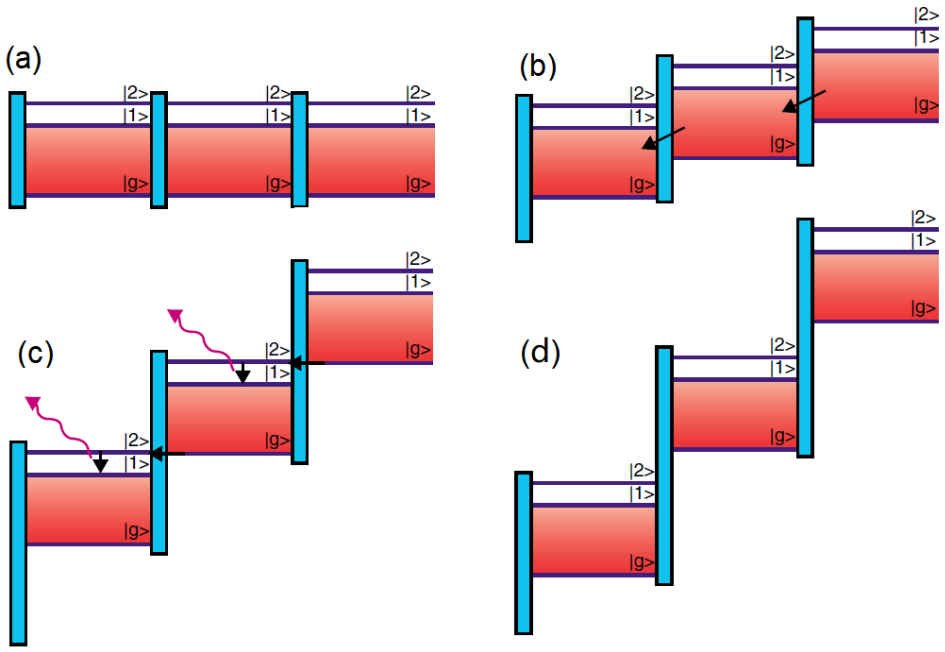

Figure 1.12 Four stages of a bound-to-continuum THz QCL operation when the bias is increased: (a) zero bias, (b) low bias, (c) alignment bias and (d) above alignment bias. Adapted from [59].

1.3.5.2 Spectrum

Another important characteristic of a QCL is its spectrum, which is measured through Fourier Transform Infrared Spectroscopy (FTIR). A FTIR spectrometer is essentially a Michelson Interferometer, where the radiation from the source (THz QCL) is directed to a beam splitter. Half of the radiation is reflected from a fixed mirror while the other half is reflected from a mirror moving continuously over a specific distance. An interference pattern is produced finally when two beams are recombined at the detector.

In this work, a Bruker IFS66v/S FTIR spectrometer is used to take all the spectra data and its maximum spectral resolution is 7.5 GHz. The spectra of a 2.7 THz QCL with a single-plasmon waveguide and bound-to-continuum active region design at different biases are measured. It is operated in pulsed mode at a frequency of 333 Hz to minimize heating and to obtain an optimal response from the bolometer. The results are displayed in Figure 1.13, which show that there are four modes in this laser. At low bias current (1300 mA), it operates in a single mode at 2.676 THz. When the bias current is increased to 1500 mA, it becomes multi-mode with a dominant mode at 2.703 THz.

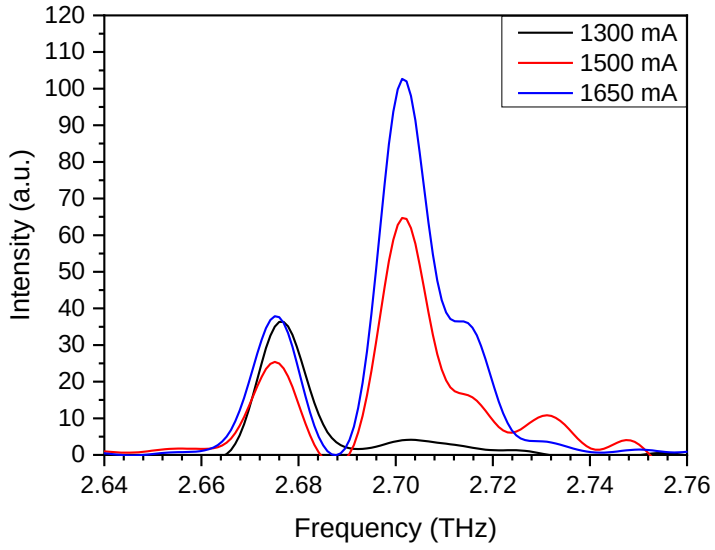

Figure 1.13 Spectra of a THz QCL with a single-plasmon waveguide and bound-to-continuum active region design at different biases

1.3.5.3 Beam Profile

To measure the beam profile of a THz QCL, the detector is placed on an xyz-stage which is driven by a stepping motor. By moving the stage, the detector can scan across the x-y plane and, therefore a plot of intensity as a function of position can be recorded. Typical beam profiles of a single-plasmon and a metal-metal waveguide THz QCLs are shown in Figure 1.14. The distance between the QCL facet and the detector is 14.5 mm.

It can be seen that for a single-plasmon THz QCL, the light beam is asymmetric in two directions because of the shape of the laser facet and mode profile in the waveguide. For a metal-metal THz QCL, the light beam is more divergent compared with the one for a single-plasmon THz QCL and with multiple lobes. Therefore, for all the self-mixing setups in this thesis, single-plasmon THz QCLs have been used because of the better beam quality, which makes it easier to couple the light from an external cavity back into the internal cavity of the QCL.

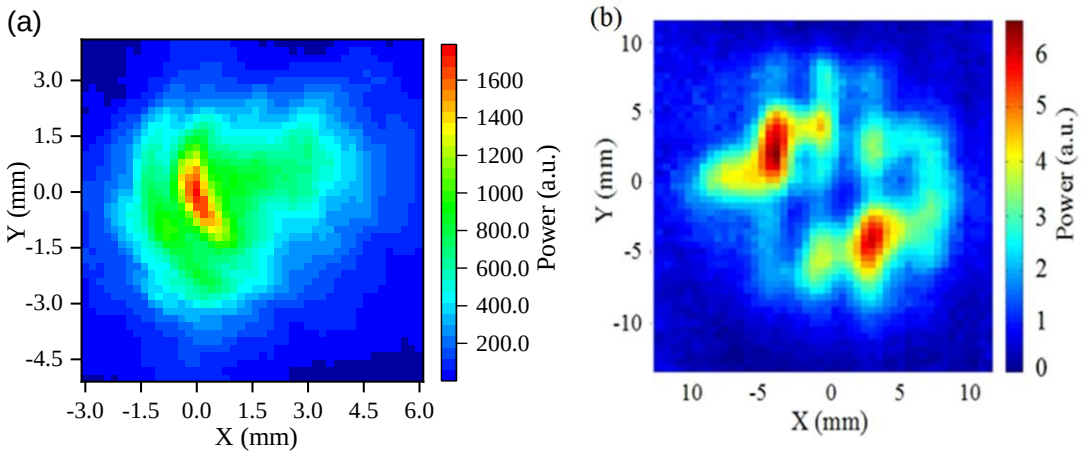

Figure 1.14 Beam profiles of (a) a 2 THz single-plasmon QCL and (b) a 2.85 THz metal-metal QCL, data from my colleagues Yuqing Wu (a) and Dr. Degl'Innocenti (b).

1.4 THz time domain spectroscopy

THz TDS is a powerful and unique spectroscopic technique with the capability of broadband THz generation and detection at room temperature. It has been used for contact-free optical property measurements of metal thin films [60], [61], 2D materials [62], [63], semiconductors [64], [65], metamaterials [66]–[68] and superconductors [69]. It has also been used to identify chemical components because of the THz fingerprint of many chemicals [70], [71] and to image buried features due to the strong penetration ability of THz radiation [70], [71]. These features make it particularly valuable for fundamental science, security, and medical applications.

1.4.1 Principle

In a THz TDS system, the time-domain signal directly measures the transient electric field rather than its intensity. This is achieved by sampling the unknown THz field with a known femtosecond laser pulse, which is referred to as the read-out pulse. As the detector is only sensitive if both pulses arrive simultaneously, it records the

convolution of the short read-out pulse with the longer THz pulse. The optical pulse is so short that it can be described as a delta-function, which allows us to measure the THz field as a function of time. Furthermore, as the detector is sensitive to the sign of the electric field, it gives phase information as well.

At this moment, the measured signal corresponds to the THz field amplitude at a single point in time. To measure the signal at all time-points, the read-out pulse is delayed relative to the THz pulse using a mechanical delay line. As shown in Figure 1.15, the output of the laser is split into two beams. One of the beams generates THz radiation, while the other one is used for the read-out of the THz signal. By moving the whole delay line box, the optical path is changed, thus changing the delay time.

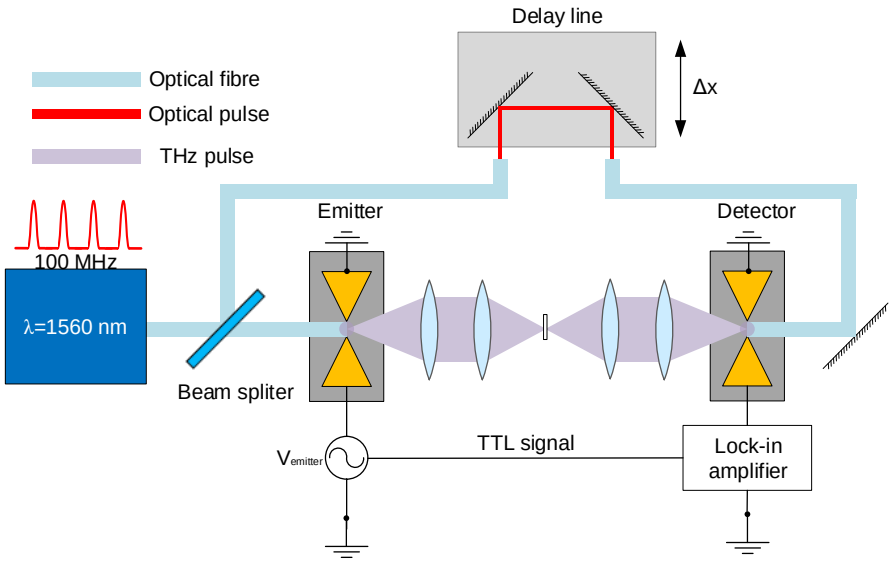

Figure 1.15 Schematic of the Menlo Systems Tera K15 THz-TDS system

The THz TDS system used in this work is the Tera K15 from Menlo Systems. The laser source is a mode-locked laser with a wavelength of 1560 nm and a repetition rate of 100 MHz. Both the THz emitter and detector are photoconductive antennas, which will be discussed in the next section. The configuration in Figure 1.15 shows the transmission scheme, however, the optical path can be rearranged for reflection measurements as well.

1.4.2 THz generation

The THz emitter is the key component of any THz TDS system. It transforms the femtosecond optical pulses emitted by a titanium-sapphire laser or a mode-locked fiber laser into picosecond THz pulses. There are three widely used techniques to generate THz pulses. The first one is the surface emitter based on the Photo–Dember effect [72].

When the surface of bulk or film semiconductors is photo-excited by an ultrashort optical pulse with photon energy above the bandgap of the material, a charge dipole will form in the vicinity of the semiconductor surface. This is because of the combined effect of a difference in mobilities for electrons and holes and the break of symmetry provided by the surface, which leads to an effective charge separation in the direction perpendicular to the surface [73].

The second technique is the photoconductive switch, or Auston switch, which consists of two transmission line antennas patterned on a semiconductor substrate. It uses an above-band-gap laser pulse to generate carriers in the conduction band of a semiconductor under an applied bias voltage [74]. The bias accelerates the newly formed carriers, which generate an electromagnetic pulse as an electron will emit electromagnetic radiation when its velocity changes [75].

The last technique is generating THz pulses through a nonlinear optical effect, namely optical rectification [76]. Optical rectification is the difference frequency analogue of second harmonic generation. When a light pulse interacts with a nonlinear medium, wave mixing between two frequency components, ω_1 and ω_2, occurs, which will generate a sum-frequency component $\omega_1 + \omega_2$, as well as a difference-frequency component $\omega_1 - \omega_2$. As the optical pulses have significant bandwidths, the high-frequency components can mix with the low-frequency components within a given pulse to produce a pulse at the difference frequency. Since the optical pulses have a bandwidth of a few THz, the difference frequencies fall in the THz range. The advantage of this approach is that as a non-resonant method, the THz pulse width is not limited by the response time of the material but only limited by the optical laser pulse width [74]. Some of the shortest THz pulses to date have been generated in this or a similar fashion [77], [78].

1.4.3 THz Detection

Like THz pulse generation, there are also several different approaches for detecting THz radiation. For a THz TDS system, as both the amplitude and phase information of the signal need to be acquired, coherent detection methods are needed. Thermal detectors like bolometers and Golay cells are not suitable here as they can only measure the total energy of the THz pulse instead of the evolution of the electric field over time. There are mainly two techniques used for THz detection in a TDS system: photoconductive detection and electro-optical sampling [79].

Photoconductive detection uses a similar or even identical device with the one used for photoconductive generation. Unlike in THz generation, the gap between the metal

antennas on the semiconductor substrate is not externally biased. Instead, the electrical bias is created by the electrical field of the THz electromagnetic pulse. When the laser beam is focused on the semiconductor gap, it generates free carriers, which increases the conductivity of the device. As a result, a current directly proportional to THz electric field is generated. Because the carriers in the semiconductor substrate have an extremely short lifetime (the carrier lifetime in LT-GaAs is typically about 100 to 300 fs [80]), the THz electric field strength is only sampled for an extremely narrow slice (femtoseconds) of the entire electric field waveform. Therefore, it gives a sharp temporal response, which in turn leads to a large THz bandwidth. The THz-driven current is on the order of picoamperes to nanoamperes [80], which means an amplifier is needed to acquire the signal.

When an amplified laser system is used, it is better to detect the pulses via electrooptic sampling (EOS) rather than with photoconductive antennas [81], [82]. It uses the same materials as for the generation of terahertz radiation by optical rectification. It is based on the Pockels effect in which the detector crystal becomes birefringent under the influence of an applied voltage. When the optical sampling pulse travels through the crystal at the same time as one point in the THz pulse, its polarization is slightly rotated. The magnitude of rotation is proportional to the magnitude of the THz field while the direction of rotation is determined by the sign of the field. A delay line is added to control when the readout pulse arrives at the detector crystal relative to the THz pulse. Therefore, the entire pulse amplitude as a function of time can be mapped out by scanning the delay line [74]. The signal is acquired through a lock-in amplifier, which is phase-locked to an optical chopper that modulates the THz generation. Within a pump-probe experimental setup, the chopper is used to modulate the pump beam.

1.4.4 THz TDS waveform and postprocessing

All the TDS measurements in this work are conducted with the Tera K15 from Menlo Systems. Therefore, it is necessary to know how to gather useful information from the raw waveforms acquired with this TDS system. The waveform for the THz pulse after it has passed through four lenses and air (no sample present) is shown in Figure 1.16 (a) and its Fourier transform is shown in Figure 1.16 (b). On the waveform, there is no current before -83 ps due to a lack of input electric field. From there on, the detector receives radiation from the emitter and generates some photocurrent, which first increases slightly and then begins to decrease. After this, the charges accelerate in opposite directions on the emitter; the induced dipole caused by the separation of charges produces a higher current density, resulting in a large radiation and thus a large

photocurrent. After ~77 ps, the photocurrent starts to oscillate and eventually attenuates below the noise floor. In the frequency domain, the signal has the highest amplitude at about 300 GHz and the signal level is above the noise floor below 3 THz. Many sharp dips can be seen in Figure 1.16 (b), which is due to water absorption.

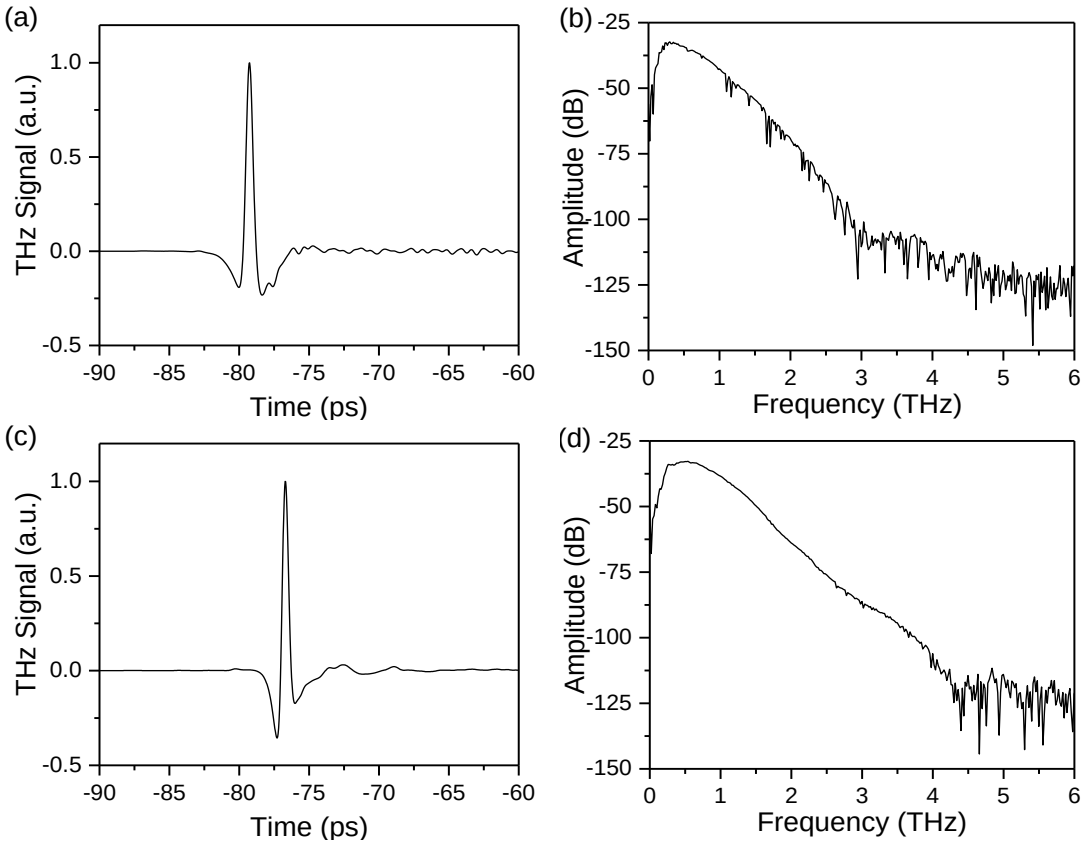

Figure 1.16 An exemplar data set for a TDS measurement. The waveforms have been normalized. (a) Wave form of the THz pulse in the time domain without nitrogen purging and 120 s integration time and (b) its Fourier transform; (c) Wave form of the THz pulse in the time domain with nitrogen purging and 300 s integration time and (d) its Fourier transform.

For most of our target applications, the THz QCL will be used as the light source and the QCLs fabricated in our group usually operate between 1.5 THz to 3.5 THz. To measure devices that work in this frequency range, the TDS system needs to have a good SNR. To push the TDS system to have a reasonable SNR between 3 THz and 3.5 THz, two measures need to be undertaken: using a long integration time and nitrogen purging. Figure 1.16 (c) shows the waveform of the pulse in a nitrogen-purged environment with 300 s integration time. Figure 1.16 (d) shows its Fourier transform. As can be seen, most of the water absorption lines have disappeared and the noise floor

has been pushed up to about 4 THz.

A metamaterial sample (which will be discussed in the next section) with gold features on a SiO_2/Si substrate is then measured in the system. To obtain the transmission spectrum of just the gold features, the substrate is taken as a background reference. At first, the waveforms of the pulse after passing through both the substrate-only area and the area with gold features are taken in a nitrogen-purged environment with 300 s integration time, as shown in Figure 1.17 (a). Because of the multiple reflections on the sample surface, more than one peak appears on the waveforms. The time separation between the two peaks is twice the time that it takes for the pulse to travel through the sample, which gives the thickness or refractive index when either of these two is known. The multiple reflections in the frequency domain introduce a Fabry-Pérot effect on the transmission spectrum, which will increase the difficulty for data

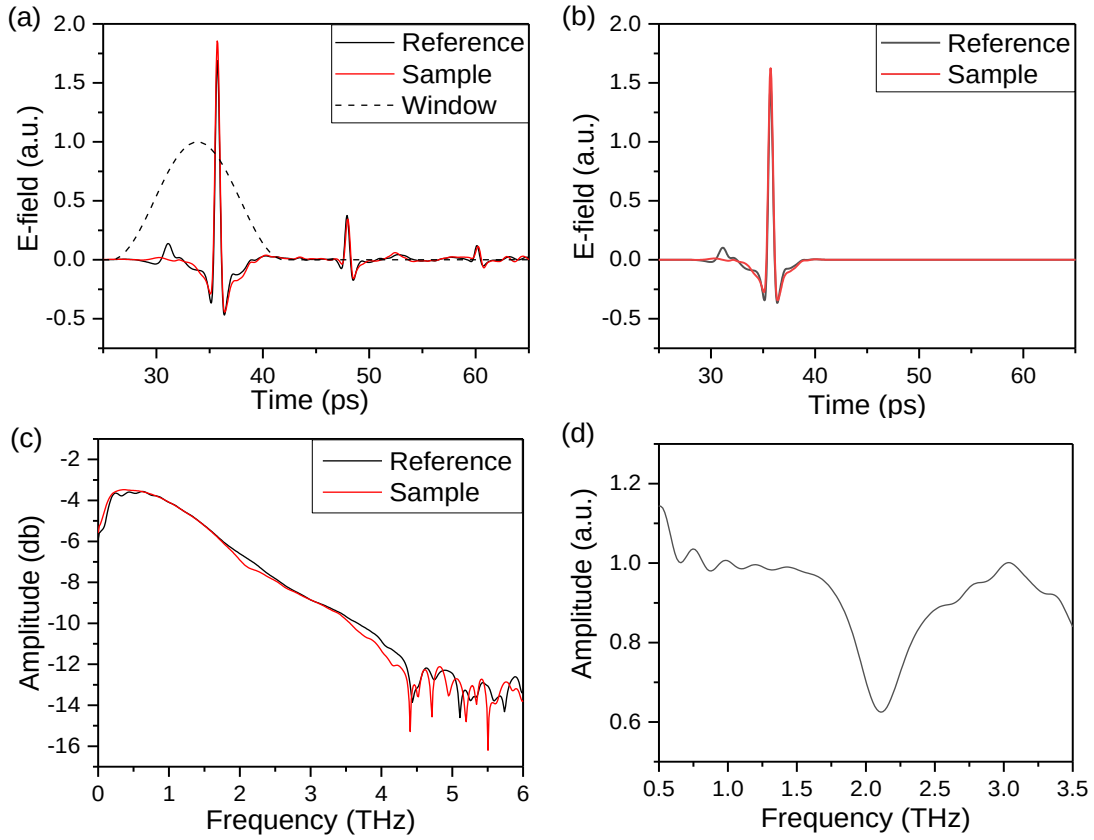

Figure 1.17 The postprocessing of THz TDS waveforms. (a) The original waveforms of THz pulses passing through the substrate (black solid line) and the substrate plus the sample (red solid line) and the window function (black dash line); (b) waveforms with the window function applied; (c) The Fourier transforms of the waveforms for the substrate (black) and the substrate plus the sample (red); (d) the transmission spectrum of the sample.

analyzing. As one peak contains all the information needed for deducing the transmission spectrum, the waveform is truncated to contain a single peak using an

appropriate window. Here, a 15 ps Hanning window is applied and the resulting waveform is shown in Figure 1.17 (b). Both truncated waveforms are then Fourier transformed into the frequency domain, shown in Figure 1.17 (c), which shows the transmission spectrum of the substrate and substrate plus gold features. Therefore, the difference of the two gives the transmission spectrum of the gold features, as shown in Figure 1.17 (d). The spectrum shows a reduced transmission at about 2.25 THz as the gold features are resonators at 2.25 THz. All the TDS data will be analysed in the same way for the following chapters.

1.5 Artificial THz functional materials：metamaterials

The lack of materials that have a strong response in the THz was one of the factors that hindered the progress of THz research. The electric response of natural conductive materials typically takes place at high frequencies (optics range) [83]. For magnetic response, inherently magnetic materials can be found that exhibit resonances at lower frequencies (microwave range). As a result, there is a natural breakpoint between magnetic and electric response in conventional materials between 1-3 THz, where electric response is dying out from the high-frequency end and magnetic response is dying out from the low-frequency end [84]. Unfortunately, this is the frequency range where most THz QCLs operate but nature does not provide any strongly dielectric or magnetic materials. However, the advent of metamaterials provides a solution for functional materials in this spectrum region.

Metamaterials are artificial electromagnetic (EM) media that are structured with resonating features, whose size and spacing are much smaller than the wavelength of EM waves. As a result, the microscopic detail of each individual feature cannot be sensed by EM waves. Instead, EM waves sample the average result of the collective response of the whole inhomogeneous objects assembly, which can be characterized by an equivalent homogenous material with effective relative permittivity ($\varepsilon_{r,eff}$) and permeability ($\mu_{r,eff}$) at the macroscopic level [85]. The EM properties of the material are then derived mainly from the structures and sizes of these resonating elements rather than from atoms or molecules as for conventional materials [86]. Therefore, metamaterials can be engineered to work at a designed frequency with a wide range of optoelectronic characteristics, which sometimes cannot be found on natural materials. Because of this, the name meta (beyond nature) is given. Examples for this include the negative-index materials (NIMs), in which both the permittivity and permeability are negative at the same frequencies [87]. NIMs have not been found in nature.

Various resonator structures have been developed to date, such as wire antenna [88], [89], Swiss rolls [90], split-ring-resonator [91]–[94], pair of crosses [95], metallic wire grids [95], etc. They have been designed for different applications: mainly electric or magnetic response and negative refractive index [66]. Resonant structures with a variety of electromagnetic properties have been demonstrated for modulating amplitude [92], [96], frequency [97], phase [98] and polarization [66] of EM waves. For negative refractive index metamaterials, they can be utilised for exciting applications like cloaking of objects from EM fields [99]–[103] and a superlens for nanoscale imaging [104], [105]. In this thesis, split-ring-resonator based metamaterial devices are used for THz modulation purposes, the detail of which will be discussed in Chapter 3.

1.6 THz applications

Thanks to the advancement in THz sources, detectors, modulators and other THz devices, the THz gap is shrinking fast. THz technologies have seen application in a wide range of areas. This thesis will explore some of the applications of THz technology in spectroscopy, communication and imaging. Therefore, it is necessary to have an overview of what THz technologies can offer to these applications.

1.6.1 THz Spectroscopy

Spectroscopy studies the absorption and emission of light and other radiation by matter as a function of the wavelength of the radiation. Historically, experiments in the terahertz region have been performed by Fourier-transform interferometry using radiation from a black-body source and a low-temperature bolometer as a detector. It is based on Fourier analysis of the time dependence of the reflected/ transmitted pulse, which gives the absorption/transmission as a function of frequency. This method is still useful today, but its application is limited. Thanks to breakthroughs in THz sources, it is now possible to generate broad band THz pulses or continuous-wave THz radiation, as discussed in Section 1.2. Room temperature THz detectors have been developed as well. The development of THz TDS is one of the main milestones that open a door to a whole branch of applications.

Compared with conventional infrared spectroscopy, THz spectroscopy has some important differences. First of all, unlike the absorption of infrared radiation in a solid, gas or liquid, which is typically due to the excitation of vibrational modes of the intramolecular bonds, the absorption of THz waves is due to low energy vibrations, such as the phonons in a semiconductor crystal or molecular vibrations in an organic material. These vibrations are a unique and distinct signature of a material, which makes

THz spectroscopy an important tool in identifying different substances, especially when they are hidden behind other layers because many materials are transparent to THz radiation [106]. In addition, as a low energy and non-ionizing radiation, it is suitable for spectroscopy of biomedical samples [107].

For security checks, THz spectroscopy makes it possible to differentiate explosives from safe materials [108]. Most common explosives have characteristic absorption lines in the range 0.2–3.0 THz, and these can be investigated even when covered by clothes or paper, which have no spectral lines in this region. As a particular spectroscopic signature is unique to an individual compound, it is also possible to determine if a 'white powder' is an explosive or a harmless entity, even in the presence of 'confusion materials' that have a similar visual appearance.

In the cultural heritage field, because of the unique spectral signatures of different materials, THz spectroscopy can be used to analyse artists' materials [109]. This provides a non-invasive approach to obtain material information of ancient artworks, which is very useful for art conservation and restoration [110].

In the pharmaceutical industry, it is essential to know the polymorphic form of a compound as different polymorphic forms of the same compound may have different effects on the human body. THz spectroscopy can be used to investigate the differences between the two polymorphic forms of a compound as it can reveal information about the crystallinity of a material [111].

At the same time, in astronomy, THz radiation is also one of the most-used diagnostics, harboring spectral signatures of ions, atoms, and molecules that are important for astrometric studies. As a result, THz spectroscopy will facilitate our understanding of the composition and origin of the Solar System, the evolution of matter in our Galaxy, and the star formation history of galaxies over cosmic timescales [112].

For fundamental research, THz spectroscopy, especially THz TDS, offers an approach to probe the optical properties of materials and to characterise THz devices [60], [62]–[64], [69], like THz modulators, which in another way, promotes the development of THz technologies.

1.6.2 THz communication

Compared to traditional microwave wireless communication, THz communication has the potential to achieve a much higher data transmission rate. According to the Shannon formula [113], the information capacity C is associated with the bandwidth, W, and the SNR:

$$C = W \log_2(1 + SNR) \ . \tag{1.15}$$

Therefore, a wider bandwidth can in principle offer a higher information capacity. It is obvious that the use of a higher carrier frequency in the THz range (0.1–10 THz) is mandatory when the minimum bandwidth reaches several tens of GHz. At the same time, THz signals also allow higher link directionality and offer a lower chance of eavesdropping when compared to their millimeter counterparts [114].

The biggest obstacle for THz communication is atmospheric attenuation [115], which limits the transmission distance. Because of this, the carrier frequency should be chosen depending on the application as the attenuation becomes stronger towards higher frequencies, as shown in Figure 1.18. For long distance (1-10 km), medium distance (100 m-1 km), and indoor (10 m-100 m) communications, < 150 GHz, <350 GHz and <500 GHz carrier frequencies need to be chosen, respectively [30]. There are two transmission windows above 600 GHz, which can also be used for indoor communications. Above 1 THz, the atmospheric attenuation is so strong that it is only suitable for nearfield communication.

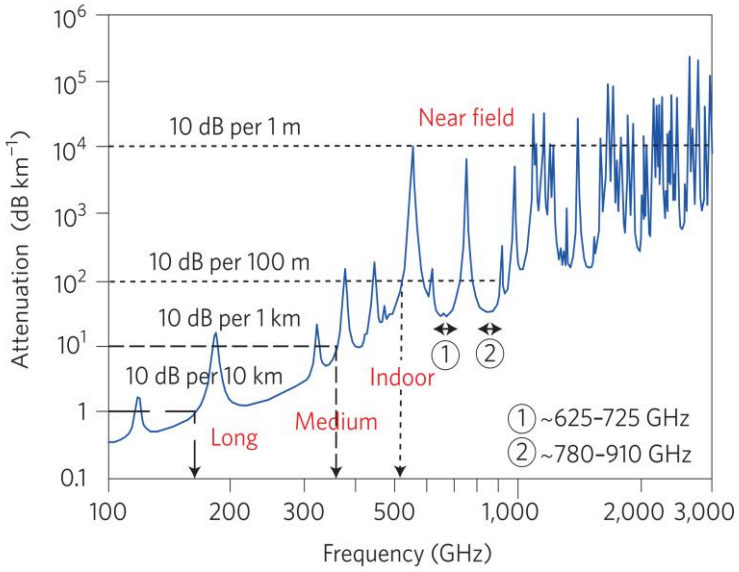

Figure 1.18 The attenuation of THz waves in atmosphere, reprinted with permission from [30] © 2016, Springer Nature

THz waves are also appealing for space communications. On one hand, compared to microwave communication, THz communication can offer higher information capacity and does not suffer from the atmospheric attenuation for communications beyond the low earth orbit. On the other hand, compared to free space optical communication, which is highly appealing for future interplanetary missions, the much

longer THz wavelengths give much larger beam widths, which increases the tolerance of beam alignment between the transmitter and the receiver.

There are two approaches to building up a THz communication system: photonics-based approaches and all electronics-based approaches. For photonics-based techniques, a high modulation index is obtained with optical-to-THz conversion using photon-mixing. A high-speed amplitude and/or phase coding is also introduced from optical coherent network technologies, which have been widely developed since the 2000s and are now a mature platform for fibre-optic core networks [116]. Coming to THz communication, photonics has played a key role in the THz transmitter field. The UTC based communication systems have been developed in several laboratories [117]–[121] and up to 100 Gbit/s data transmission rate has been achieved [121]. Regarding THz receivers, electronics-based approaches remain more efficient. The most widely used receiver is a waveguide-integrated detector using GaAs Schottky barrier diodes initially developed for radio astronomy applications [122]. Many THz communication systems use photonic transmitters combined with an electronic receiver. Some all electronics-based systems have been developed by borrowing techniques from radio astronomy [123], [124].

In many photonics-based THz communication systems, especially in networks using a modulation scheme known as quadrature amplitude modulation (QAM) [125], [126], a THz amplitude modulator is needed. Many THz modulation techniques have been developed, based on semiconductor electron-hole modulation [127], [128], metamaterial modulation [129]–[132] and some other modulation schemes. Active control of the output power of a THz QCL with a metamaterial modulator will be discussed and demonstrated in Chapter 3, which will be very useful for future THz communication.

1.6.3 THz imaging

Imaging with THz radiation has several advantages because it is a different region of the electromagnetic spectrum and can provide complementary information to that obtained with radiation at other frequency ranges. Compared to lower frequency imaging, it can achieve a higher spatial resolution because of the shorter wavelength; compared to the higher frequency imaging (infrared and visible light) it can image hidden objects as many commonly used materials, such as bags, clothes, many plastics, etc., are relatively transparent to THz radiation. Its high sensitivity to water content along with the fact that it is non-ionizing finds it applications in biomedical sciences, agriculture, etc. In addition, because many materials carry a unique THz spectroscopic

signature, THz radiation can be used for material recognition combined with spectroscopy methods.

Despite the fact that the potential value of THz imaging has been recognized for quite some time, the first THz imaging system was demonstrated just two decades ago in 1995 after the THz TDS system was developed [133]. Before that, it was hindered by the lack of suitable THz sources and detectors. Since then, a variety of THz sources and detectors have emerged, and many THz imaging systems have been developed to meet different application needs. Depending on the sample and the information of interest, either transmission or reflection imaging can be adopted. In addition, on top of active illumination imaging, passive THz imaging, which captures THz radiation either emitted or scattered by the imaging objects instead of illuminating the object with a light source, has also become an important topic of research [134], [135].

There are two limitations for conventional THz imaging. The first one is the long imaging acquisition time. Because of the lack of THz cameras, in most THz imaging systems, image acquisition is done through raster scanning the sample pixel by pixel. The development of a fast and sensitive THz focal plane array detector has been a research goal in this field for many years. One of the earliest attempts is to use a large-area electro-optic crystal, which converts the THz signal to optical signal, therefore a conventional CCD can be used to acquire the image [136]. However, the large area of the optical read-out beam means that a high power or amplified laser pulse is needed, which makes the system large and complex. Therefore, this approach is impractical for many applications. The combination of the invention of the THz QCL and the microbolometer focal plane array makes it possible to do video-rate imaging with a compact system as the output power of a THz QCL is large enough to be detected by the microbolometer array [137].

Table 1.1 Summary of the specifications for four types of commercially available focal plane arrays, from reference [138] © 2018 Optical Society of America

Camera	Pixel number	Pixel size (μm)	Frequency range (THz)	NEP ($nW \cdot Hz^{-1/2}$)	Responsivity ($kV \cdot W^{-1}$)	Frame rate (fps)
CMOS	32×32	80	0.3 – 1.3	0.4	140	30
GaAs heterostructure	64×64	1500	0.05 – 0.7	1	50	24
Microbolometer	320×240	50	0.6 – 4.0	0.03	18 (at peak)	25
Pyroelectric	320×320	75	0.1 and up	13	N/A	50

Up to now, four types of focal plane arrays have been developed, with their typical specifications displayed in Table 1.1 [139], [140]. All of them operate at room temperature with video-rate readout. The availability of these array cameras will significantly facilitate THz research with high power sources. For instance, one such camera can be used to optimizing the alignment of a delicate THz optical path, which is usually challenging.

Another approach to improving the image acquisition speed is single-pixel imaging, which produces images by interrogating a scene with a series of spatially resolved illumination patterns while measuring the correlated intensity on a detector without spatial resolution [141]–[146]. It is a compressing imaging method, in which images can be acquired with fewer measurements than image pixels [146]. In single-pixel imaging, a single-pixel camera is usually used. It consists of a spatial light modulator (SLM) and a single-pixel detector (SPD). The SLM generates random masks for the illuminating light or the receiving light. When one measurement is done, the signal from the SPD is a random combination of information from all the pixels. An image of the scene is reconstructed from $M \leqslant N$ (N is the pixel number, which is determined by the SLM) light measurements taken by a single sensor sequentially from different combinations of the N pixels as determined by random 0/1 test functions, where '0' means light cannot transmit the SLM at this pixel while '1' means light can transmit at this pixel. When considering THz imaging, the difficulty will be the THz SLM. Up to now, mainly two types of SLMs have been achieved for THz applications.

A metamaterial SLM has been developed for a THz single-pixel imaging system [144], shown in Figure 1.19 (a). In another way, the optical pulse used to generate the THz pulse can be modulated with a conventional SLM, which will produce a spatially modulated THz pulse [141], shown in Figure 1.19 (b). Many image reconstruction methods have been developed as well thanks to the advances in signal processing [147], [148][149], [150]. However, research is still ongoing, trying to understand precisely how the image properties are compressively sensed, and to develop new algorithms to reconstruct an image.

Another limitation of conventional THz imaging is the resolution. Due to the much longer wavelength, it cannot achieve a resolution as high as its visible or infrared counterparts with conventional imaging techniques due to diffraction. Many new techniques have been developed to push the resolution beyond the diffraction limit, among which nearfield imaging techniques have seen many applications in THz frequency range. A detailed introduction of THz nearfield imaging will be given in Chapter 4. Most of these techniques were adapted from more conventional photonics or

electronic approaches.

There are also some sub-wavelength imaging techniques which are unique to the THz range. One such example is Laser Terahertz Emission Microscopy (LTEM) [151]–[153]. Many materials emit a burst of THz radiation when illuminated with short optical pulses because of ultrafast photogeneration of charges followed by carrier acceleration in a local potential. This generated THz signal can be detected in the far field, using common optoelectronic techniques. In a LTEM, the sample is illuminated with a femtosecond laser pulse, focused using conventional optics to the diffraction limit. The optical illuminating beam is raster scanned across the sample and the corresponding THz signal is taken at each scanning position to form the THz image. In this way, the image not only contains information about the THz response of the sample, but also has a spatial resolution determined by the optical spot size rather than by the THz wavelength. Micrometer resolution can be achieved with this method.

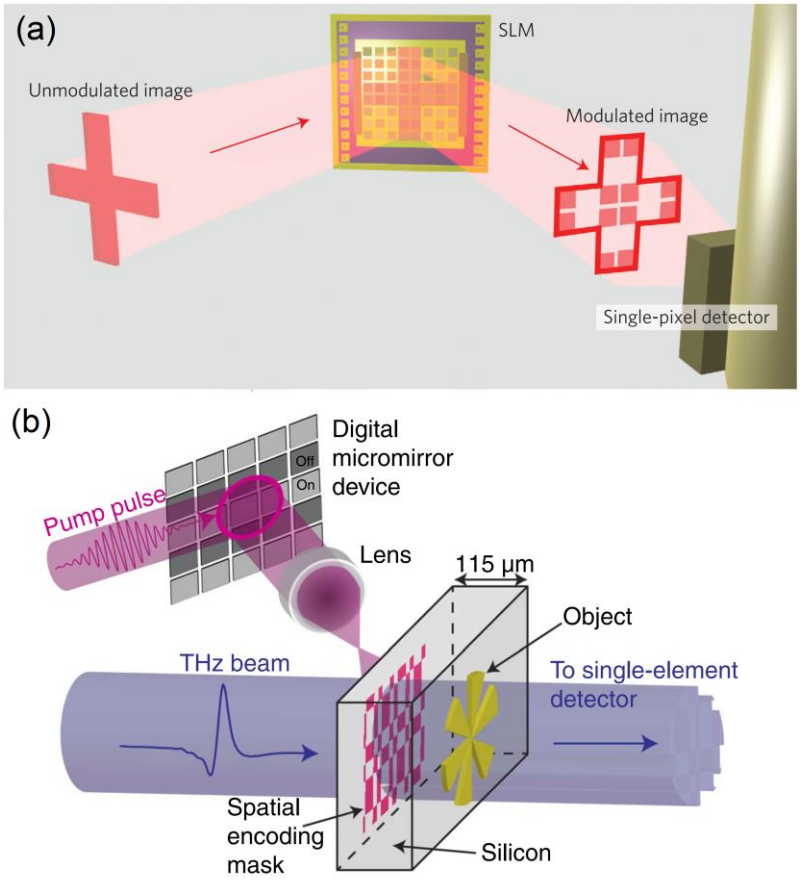

Figure 1.19 Examples of spatially modulated THz radiation, (a) Using a THz metamaterial SLM adapted with permission from [144] © 2014, Springer Nature; (b) Modulating the pump pulse used to generate the THz pulse, modified from [154]. © The Authors, some rights reserved; exclusive licensee American Association for the Advancement of Science. Distributed under a Creative Commons Attribution License 4.0 (CC BY) https://creativecommons.org/licenses/by/4.0/.

1.7 Thesis overview

This thesis focuses on the application of THz technology with a THz QCL in two different areas: spectroscopy and nearfield imaging, as well as providing power-stable and controllable THz sources for various THz applications.

Chapter 2 demonstrates THz spectroscopy based on the self-mixing effect of a quantum cascade amplifier (QCA). The concept of a QCA and the principle of self-mixing spectroscopy are discussed. Based on these concepts, an exemplar gas spectroscopy setup is designed and demonstrated.

In Chapter 3, the output power of a THz QCL is stabilised and actively controlled with a graphene loaded metamaterial modulator. This involves the design, simulation, fabrication and test of the modulator, which is then incorporated into a feedback system to control the output power of a THz QCL. The effectiveness of the stabilization is evaluated with the Fourier transform and Allan Variance.

In Chapter 4, a THz scanning-type nearfield microscope is homebuilt based on a THz QCL and a quartz tuning fork atomic force microscope. The principles of nearfield imaging and atomic force microscopy are discussed. The system is built and demonstrates a resolution better than $\lambda/1000$ on THz image. The performance of the system is further improved by reducing tip oscillation and electronic noises.

In Chapter 5, the application of the THz nearfield imaging system is explored with different samples. Imaging of plasmonic resonance, electric field mapping and subsurface imaging are demonstrated. The influence of the tip material on the performance of the system is studied as well. Furthermore, THz metamaterials with varied geometric parameters have been designed based on COMSOL simulations and THz TDS measurements and have been fabricated to study the influence of different geometric parameters on the optical properties of the metamaterial devices. These samples can also be measured in a THz s-SNOM system, which will help people to understand the working mechanism of this type of devices and find directions to optimise the device design.

Chapter 6 summarises all the work having been done in this thesis and gives suggestions of potential improvement or applications for current techniques. Several new research ideas closely related to the work presented in this thesis are proposed as well.

Chapter 2
Self-mixing spectroscopy with a THz quantum cascade amplifier

THz spectroscopy can provide information which cannot be obtained with spectroscopy at other frequency ranges. In this chapter, a THz gas spectroscopy system based on a THz quantum cascade amplifier is proposed and demonstrated. A THz QCL is first made into an amplifier, which can be achieved in several different approaches, as to be discussed. This is then put into an external cavity as the light source for the spectroscopy system, which utilises a self-mixing detection method by monitoring the laser voltage. Measurement of methanol absorption is demonstrated with this system. Furthermore, two critical elements for achieving a broadband spectroscopy system with an external cavity THz QCL, broadband antireflection coating and frequency tuning are discussed.

2.1 THz quantum cascade amplifier

As at other frequency ranges, a THz amplifier is useful to produce coherent radiation with high SNR at the THz frequency range. This work builds on the modification of a THz QCL gain medium to achieve an amplifier [155]. Two requirements need to be satisfied to achieve a THz amplifier in this case, namely, gain of THz radiation and suppression of the lasing. The first condition is automatically met when using the ridge of a QCL as the gain medium of the amplifier. To suppress lasing, an angled front facet could be utilised to minimise facet reflections [156]. However, it deforms the wavefront as well as the beam quality, resulting in a severely astigmatic beam. Another method is applying an anti-reflection coating on one of the QCL facets, which is the most commonly used method [155] and will be discussed in the next section.

2.1.1 Anti-reflection coating

According to the Fresnel equations, two conditions need to be met to achieve zero reflection:

$$\begin{cases} n_{\mathrm{AR}} = \sqrt{n_{\mathrm{air}} n_{\mathrm{cavity}}}, & \text{refractive index matching} \\ d = \dfrac{(2m+1)\lambda}{4n_{\mathrm{AR}}}, & \text{thickness condition: quarter-wave layer} \end{cases} . \qquad (2.1)$$

where n_{AR} is the refractive index of the coating, n_{air} and n_{cavity} are the refractive index of the air and the cavity medium, m is an odd integer and λ is the wavelength of radiation. A schematic diagram of the coating is shown in Figure 2.1. As the refractive index of a THz QCL ridge is about 3.6 [157] and the refractive index of air is nearly 1.0 in the THz frequency range, this gives a refractive index of 1.9 for the anti-reflection (AR) coating. Therefore, SiO_2 becomes an ideal material for AR coating because its refractive index can be tuned between 1.9 and 2.1 depending on the deposition method and parameters used during the coating process [158]. However, according to equation (2.1), the thickness of the coating increases as the frequency of the laser goes down. Generally, a coating thickness of 10-20 μm (13.16 μm for 3 THz and 19.74 μm for 2 THz if the refractive index of the SiO_2 is 1.9) is necessary at THz frequency range, which poses a great difficulty on the coating process as it is challenging to get SiO_2 coating thicker than 10 μm.

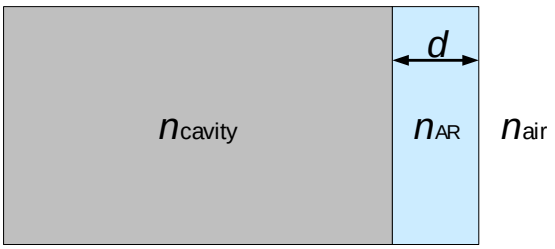

Figure 2.1 Schematic of antireflection coating on a laser facet

Another material having been exploited is parylene C, which has a refractive index of 1.62 [159]. It is often used in industrial applications as a coating layer for corrosion resistance and electrical insulation. It possesses many properties, such as deposition of films >10 μm, good thermal and mechanical stability, low absorption across the THz range (11.0 ± 2.2 cm^{-1} at 2.0 THz [160]), which lend it to an effective THz AR coating. Taking the QCL active region refractive index of ~3.6 and a surrounding refractive index of 1, the reflectivity as a function of film thickness when parylene C is used as the AR coating can be calculated, as shown in Figure 2.2 and gives a minimum reflectivity of ~3% for an optimum coating thickness of 16 μm at 2.9 THz.

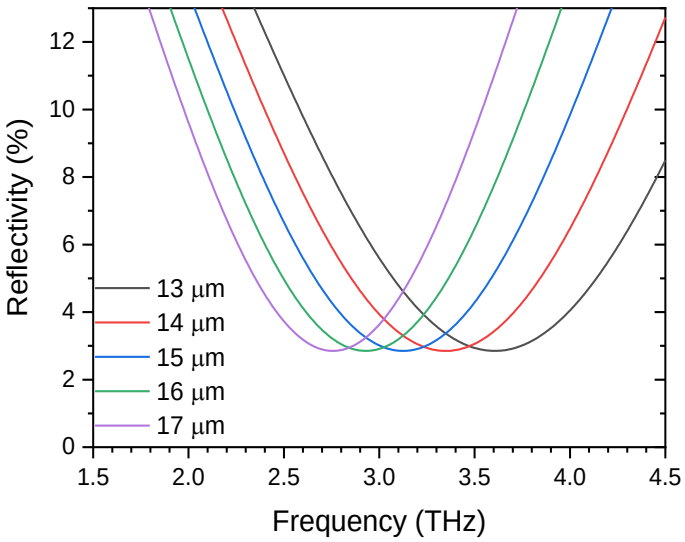

Figure 2.2 The calculated reflectivity of parylene C coatings with thickness from 13 μm to 17 μm on a THz QCL facet (with refractive index of 3.6). The reflectivity is calculated using the Transfer Matrix Method reported in reference [161].

Full suppression of THz radiation from a 2.9 THz QCL with parylene C coating has been demonstrated [155]. The parylene C coating is deposited onto both facets of the laser by vapour deposition under vacuum conditions at room temperature with a rate of 0.2-0.3 μm per minute. Actual coating thicknesses are measured from planar GaAs control chips coated during the same process runs. The optimal thickness measured in the experiments is 17.7 μm instead of the calculated 16 μm. The discrepancy between the observed experimental and theoretical AR coating thickness on the laser facet to fully suppress lasing is attributed to (a) the differences in coating a planar to a facet surface and (b) potential variations in the refractive index of parylene, since a reduction of 0.1 equates to increasing the optimum thickness by ~1 μm.

2.1.2 From a THz QCA to an external cavity THz QCL

For many applications, such as spectroscopy and imaging [162], the THz QCA is utilised in an external cavity. In this case, only one fact of the laser is coated, and an external reflector is put next to it, acting as the second cavity mirror, as shown in Figure 2.3 (a). The lasing will be restored with the external cavity when the cavity loss is reduced to below the gain of the active region.

To make it easier to couple the radiation from an amplifier to the external cavity and then couple it back, a silicon lens is usually attached onto one facet of the laser. Instead of applying an antireflection coating directly on the laser facet, the silicon lens is coated first and then attached to the laser facet, as shown in Figure 2.3 (b). As the antireflection

coating is now on Si, which has a refractive index of around 3.43 [163], it is still effective to use parylene C as the antireflection coating. Furthermore, as the square root of the refractive index of Si (1.85) is closer to 1.62 than that of QCL cavity (1.9), a lower minimum reflection can be achieved (2% instead of 3% compared to coating directly on the QCL facet).

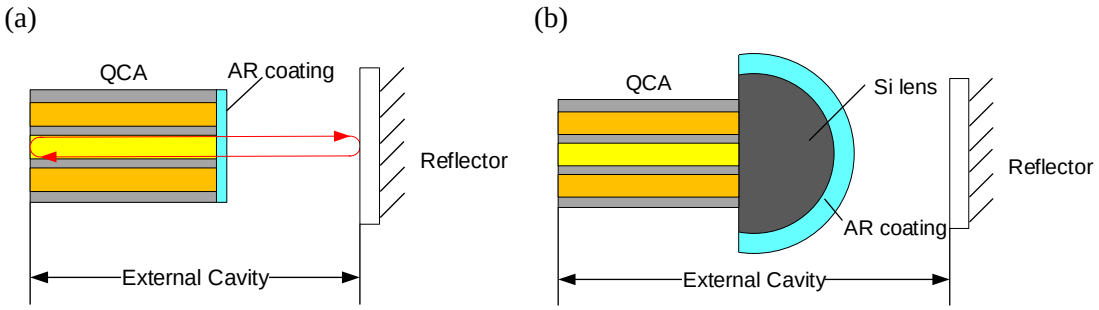

Figure 2.3 Schematic of (a) an external cavity QCL based on a QCA and an external reflector and (b) an external cavity QCL with Si lens coupling

A QCL (QCL-A in Appendix A) with a 2.9 THz bound-to-continuum active region design is modified into a QCA with an AR coated Si lens. The thickness of coating is 18 μm. A gold coated flat mirror is then put next to the Si lens to form an external cavity QCL. The LIV responses of the original laser, the QCA and the external cavity QCL are displayed in Figure 2.4.

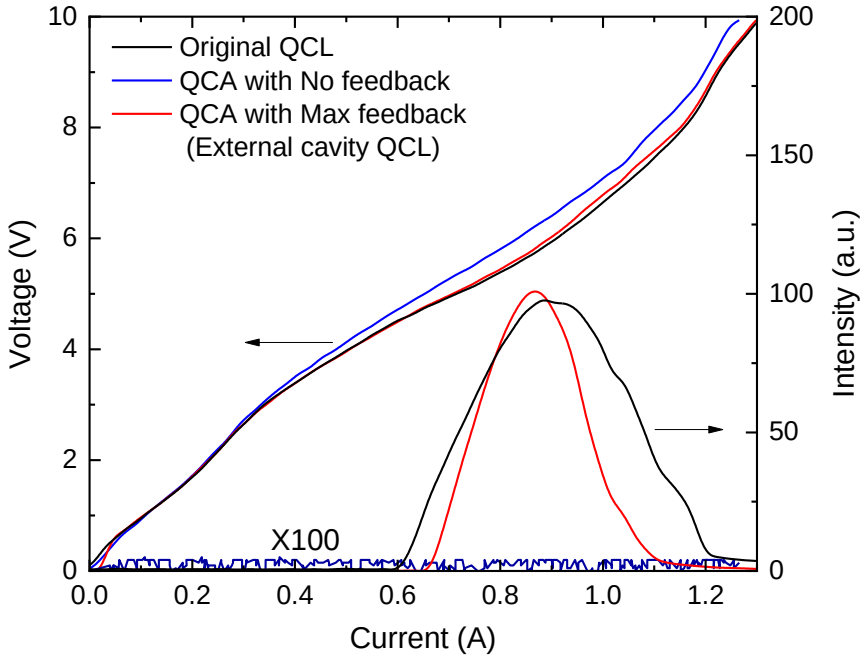

Figure 2.4 LIV responses of a 2.9 THz QCL (black), a QCA (blue) and an external cavity QCL (red) modified from it.

When the AR coated lens is applied on the QCL, the lasing is totally suppressed and the QCL becomes a QCA. When the mirror is added, the lasing is restored and the maximum power reaches the similar level as the original QCL. However, the threshold current of the external cavity QCL is still higher than the original QCL, which means the loss of the external cavity (mainly comes from the coupling loss) is larger than the internal laser cavity.

2.2 Self-mixing for a THz quantum cascade amplifier

When the emitted laser radiation is coupled back from an external reflector into the internal laser cavity through an emission facet of the laser, the reflected radiation will interfere with the internal laser field, which will cause a perturbation to many characteristics of the laser, such as emission frequency, threshold gain, output power and terminal voltage [164]. This effect is called self-mixing. In the case of a QCL, self-mixing will induce a perturbation on the differential resistance of the QCL as it will influence the photon density and thus photon-assisted transport. The result is a voltage perturbation due to the external feedback.

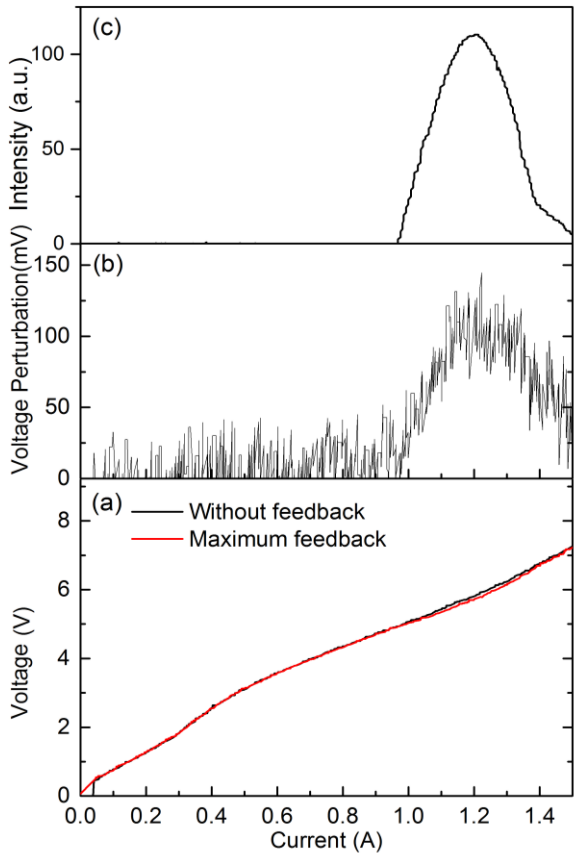

Figure 2.5 Self-mixing effect of a THz QCL. (a) the current-voltage curve of the amplifier with and without feedback from a flat gold coated mirror; (b) voltage perturbation induced by self-mixing; (c) the intensity of the amplifier with maximum feedback.

In a QCL, it is hard to couple a large number of photons back to the cavity because of the facet reflection. However, in a QCA, as the facet is covered with AR coating, this can be easily achieved. When a gold coated flat mirror is put next to the QCA, an external cavity QCL will be formed, as shown in Figure 2.3 (b), and the lasing can be restored. Figure 2.5 gives the current-voltage curve (measured with the same setup shown in Figure 1.10) of a 2.9 THz QCA (modified from QCL-B in Appendix A) with and without external feedback from the gold coated flat mirror. The QCL is operated in pulsed mode (10 kHz, 5 duty cycle). The voltage perturbation is the difference between the two current-voltage curves. As can be seen, the highest voltage perturbation for the external cavity QCL can reach 125 mV. In addition, the voltage perturbation is correlated with the intensity of the external cavity QCL, which is measured at the rear facet of the QCL. This proves an enhanced photon-assisted transport. Therefore, the external feedback strength can be measured by monitoring the voltage of the QCL.

It needs to be mentioned here that the QCA self-mixing setup here is different from a normal QCL self-mixing setup, where there is no AR coating on the QCL facet. For the latter situation, the system operates at a weak feedback scheme and the voltage perturbation signal V_{SM} is not only dependent on the feedback strength but also sensitive to the phase difference between the internal laser field and the external feedback because of the interference between them [165].

Therefore, any change on the optical path length and the wavelength will affect the self-mixing signal as well. For the QCA approach, as there is no internal laser field, no interference exists in the system. Therefore, the self-mixing signal is solely determined by the feedback strength.

2.3 Self-mixing spectroscopy: principle

THz molecular spectroscopy has significant scientific potential since many absorption and emission molecular lines of interest in astrophysics [2] and atmospheric sciences fall in this spectral region [166], where many chemical species have very strong characteristic rotational and ro-vibrational transitions. Moreover, for gases, the typical absorption strengths are ~100 times stronger than in the microwave region. The QCL is a particularly attractive source for this application as it offers a quantum-limited spectral purity below any other semiconductor sources [167]. To date, most THz QCL spectroscopy approaches have required external instrumentation (detectors, mixers or spectrometers). Clearly the self-mixing detection approach afforded by the THz QCL offers several operational advantages.

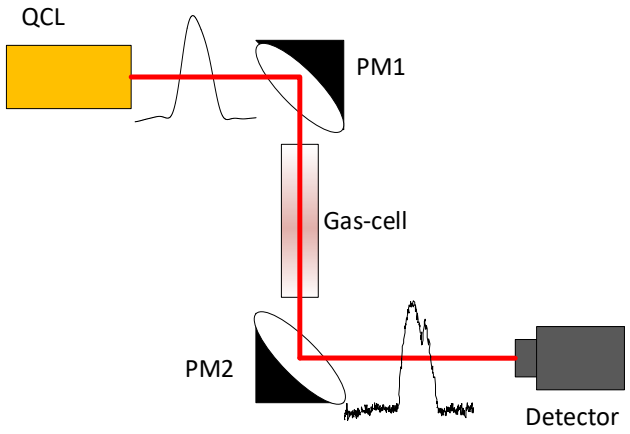

Figure 2.6 A diagram of stark-shift induced absorption line on the current-intensity curve

If a QCL reveals a significant stark shift, the spectrum of it will be shifted within a frequency range when the applied bias on it is tuned. In such a situation, when the laser goes through a gas-cell containing gas with absorption lines at this frequency range, there will be some absorption lines on the current-intensity curve of the QCL, as shown in Figure 2.6.

In addition, when the gas-cell is put inside an external cavity (as shown in Figure 2.7), the external cavity will provide a frequency, thus voltage dependent feedback to the internal cavity. Considering the effect of self-mixing, there should also be a dip on the current-voltage curve where the voltage is equal to the corresponding voltage of the frequency at which there exists the absorption line. Therefore, this effect can be utilised for spectroscopy. Compared with the traditional approach for spectroscopy by measuring the frequency-intensity curve with a frequency tuneable QCL, this approach needs fewer instruments and less calculation, which means a faster response.

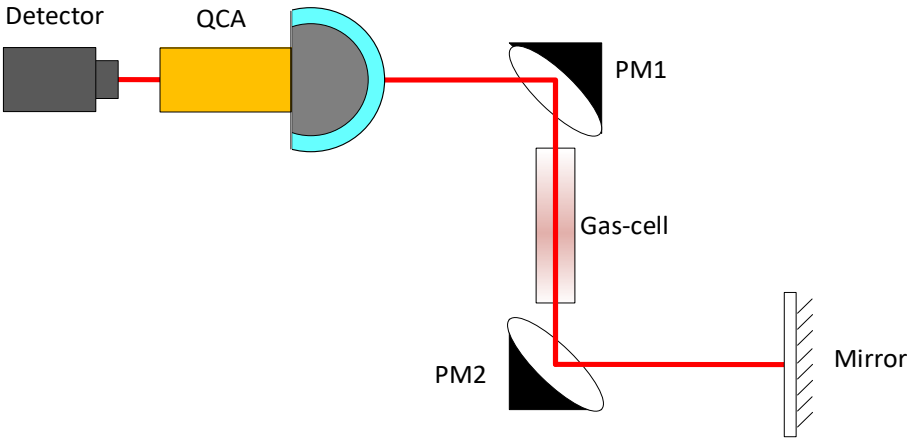

Figure 2.7 A schematic diagram of the setup for the self-mixing spectroscopy experiment

2.4 Self-mixing gas spectroscopy: light source

For self-mixing spectroscopy, three critical elements need to be determined before carrying out the experiment, which are the active region design, waveguide type of the THz QCL as well as gas species. First of all, bound-to-continuum active region design is chosen as the radiation transition in it is usually quite diagonal, which can contribute to a large stark-shift [38]. As to the waveguide, single-plasmon waveguide is chosen for the reason that it gives a good beam quality, therefore, the laser radiation can be easily coupled back into the internal cavity. Most of the devices to be used in this experiment work at frequencies around 2-3 THz, where methanol has many strong absorption lines. As a result, methanol is utilised in this work.

2.4.1 Absorption spectrum simulation

The absorption spectrum of methanol is simulated to find a suitable frequency range, where there are strong methanol absorption lines but no strong water absorption lines. Water lines will introduce background noise when the experiment is performed in an ambient environment and should be avoided. In the ambient environment, it is difficult to accurately control the pressure of the water vapor. If water absorption lines overlap with some methanol lines, these lines cannot be used for gas spectroscopy as the humidity of the environment might change over time and it will be difficult to isolate the absorption of methanol from water vapor absorption. As a result, it is essential to find a spectral range where methanol does not have overlapping absorption lines with water vapor. When the spectral range is decided, the light source can be chosen from the THz QCLs which can lase in this spectral range.

For gas spectroscopy, the most significant parameter is the absorption strength/ coefficient α_{gas}. It determines the single pass Beer–Lambert power transmission factor *T*, which can be obtained from the Beer–Lambert law as

$$T = \exp(-\alpha_{\text{gas}} L_{\text{gas}}) \tag{2.2}$$

where L_{gas} is the length of the gas-cell. The absorption coefficients of water and methanol can be calculated using cataloged data from Jet Propulsion Laboratory (JPL) database [168]. The cataloged absorption coefficient values are calculated at 300 K, which can be converted into HITRAN [169] intensities with a temperature adjustment to values at 296 K (the temperature at which all the parameters in HITRAN database are taken and of the lab where the experiments will be conducted) with the following equation [170]

$$S_{\mathrm{H}}(296\ \mathrm{K}) \approx I_{\mathrm{a}} \frac{I_{\mathrm{JPL}}}{2.99792458\times10^{18}} \exp\left[-\frac{hcE''}{k_{\mathrm{B}}}\left(\frac{1}{300}-\frac{1}{296}\right)\right]\left(\frac{300}{296}\right)^{n+1}. \qquad (2.3)$$

Here, S_{H} is the line intensity, I_{a} is the isotopic abundance of the gas, I_{JPL} is the line intensity from the JPL database, h is the plank constant, c is the speed of light, E'' is the lower-state energy of the transition (can also be obtained from the JPL catalog) and k_{B} is the Boltzmann constant. For linear molecules, n=1 and n =3/2 for nonlinear molecules. The number 2.99792458×10^{18} is used to convert the units from nm^{2}MHz of JPL to HITRAN units cm^{-1}/(molecule/cm^2). The line intensities are incorporated with a Voigt profile to account for self-broadening at 1 Torr, giving a FWHM of 30 MHz (from the HITRAN database [169]). It also accounts for the Doppler broadening, the FWHM of which can be calculated through the following equation [171]

$$f_{\mathrm{FWHM}}(T) = \frac{2\nu_{\mathrm{ij}}}{c}\sqrt{\frac{2N_{\mathrm{A}}k_{\mathrm{B}}T\ln 2}{M}} \qquad (2.4)$$

where ν_{ij} is the wavenumber of the spectral line transition (cm^{-1}) in vacuum, M is the molar mass of the isotopologue in grams and N_{A} is the Avogadro constant.

The absorption spectra of methanol and water have been simulated with this method within the spectral range between 2.245 THz to 2.255 THz at 1 Torr and 296 K, shown in Figure 2.8. The absorption intensity of water is magnified by 10 times for clarity. As can be seen, there are many methanol lines between 2.2458 THz and 2.2472 THz and there is no water absorption line in this region, which makes this spectral range suitable for methanol gas spectroscopy.

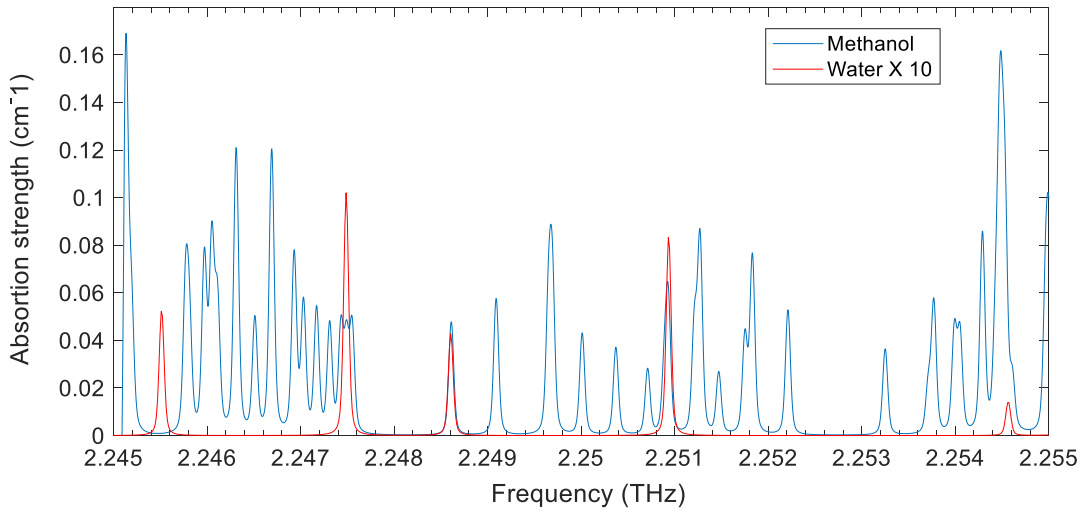

Figure 2.8 Simulated absorption spectrum of methanol and water around 2.25 THz with open data from Jet Propulsion Laboratory [168].

2.4.2 Active region design

A 2.25 THz single-plasmon QCL (QCL-C in Appendix A) is utilised as the light source firstly because it hits the right spectral range, can operate with a single mode within a large current density range and has a bound-to-continuum active region [172]. The layer structure of the active region as well as the conduction band diagram of it calculated with Nextnano under an electric field of 1.6 kV/cm is shown in Figure 2.9. The calculated transition energy is 9.087 meV, which corresponds to 2.2 THz.

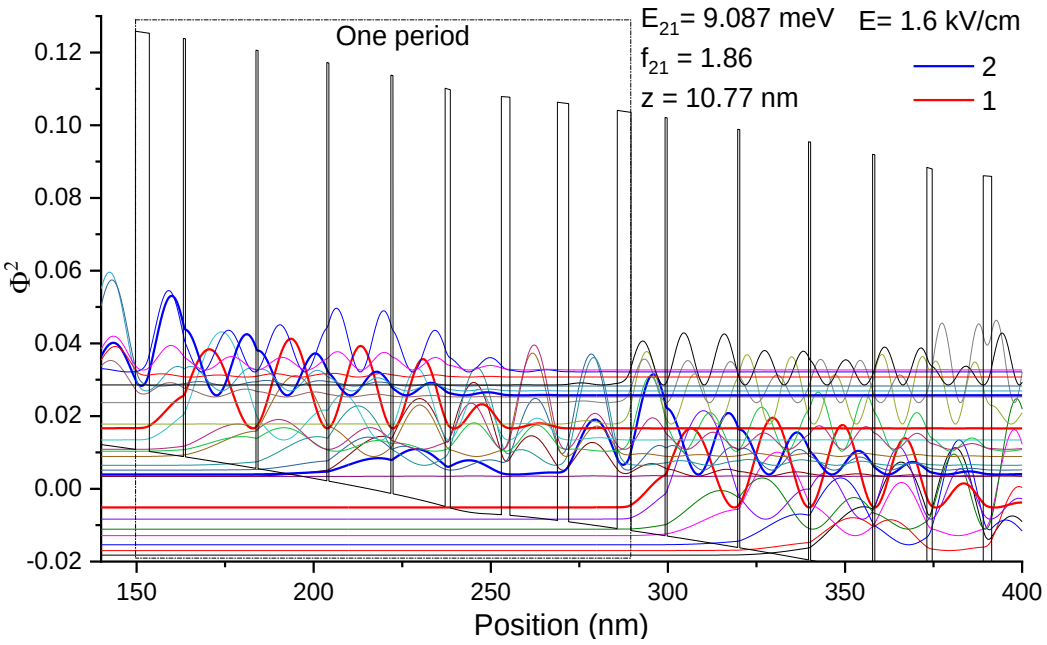

Figure 2.9 Conduction band diagram of QCL-C calculated with Nextnano. The GaAs/$Al_{0.15}Ga_{0.85}As$ layer sequence of one period of the active region starting from the injection barrier is as follows: **3.9**/9.6/**0.6**/19.9/**0.6**/19.4/**0.6**/17.5/**0.6**/14.7/**1.5**/14.4/**2.4**/13.4/ **3.2**/13.7, where thicknesses are in nanometers and $Al_{0.15}Ga_{0.85}As$ barriers are in bold, the last 10 nm of the 14.4 nm GaAs well is doped to n= 2.5×10^{16} cm^{-3}.

The transition frequencies at different bias voltages are calculated as well, as shown in Figure 2.10. When the bias voltage is increased from 1.5 kV/cm to 1.8 kV/cm, the transition frequency changes from around 2.1 THz to 2.29 THz, which is a very large shift. This shows that this active region design has a potential of achieving a large Stark-shift. However, in practice the bias voltage of a QCL cannot be changed by such a large value because of the limited dynamic range, which will limit the frequency tuning range. Also, as the longitudinal modes are constrained by the cavity length, stark-shift can only cause mode hopping in a QCL. However, according to the Kramers Kronig relationship, because of stark-shift, the refractive index of the active region will be tuned when the bias voltage is changed. Therefore, fine frequency tuning of a THz QCL can still be

achieved by changing the bias voltage, but the tuning range will be small as the current change induced refractive index change is usually small.

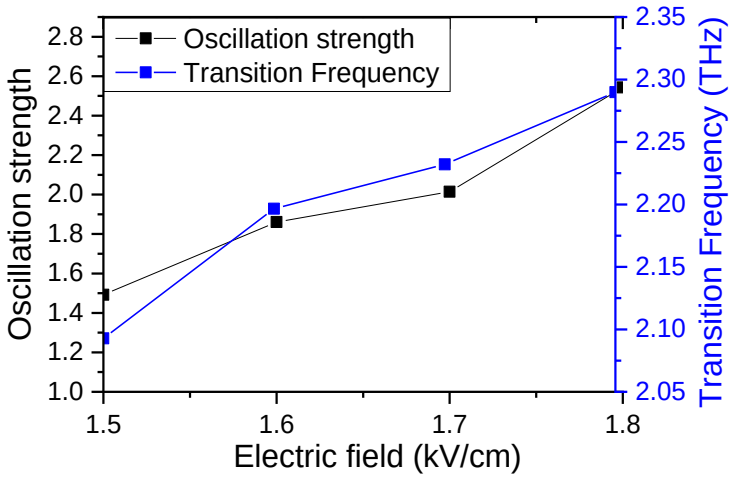

Figure 2.10 Oscillation strength and transition frequency of the active region at different bias voltages. The transition frequency shows a clear Stark-shift.

Spectra of QCL-C at different currents are then measured with the FTIR, shown in Figure 2.11. The spectra are plotted with the intensity normalised and show a central frequency at about 2.2473 THz, which is 47.8 GHz higher than the transition frequency calculated with the Nextnano. The difference mainly arises from two places, the difference between the nominal layer thickness and the real layer thickness and the simplifications made in the Nextnano calculations. Despite the difference, the Nextnano calculation gives a close prediction of the emission frequency of a THz QCL. It can be also seen from Figure 2.11 that the lasing frequency is shifted by 1 GHz (from 2.2468 THz to 2.2478 THz) when the bias current is increased from 725 mA to 850 mA.

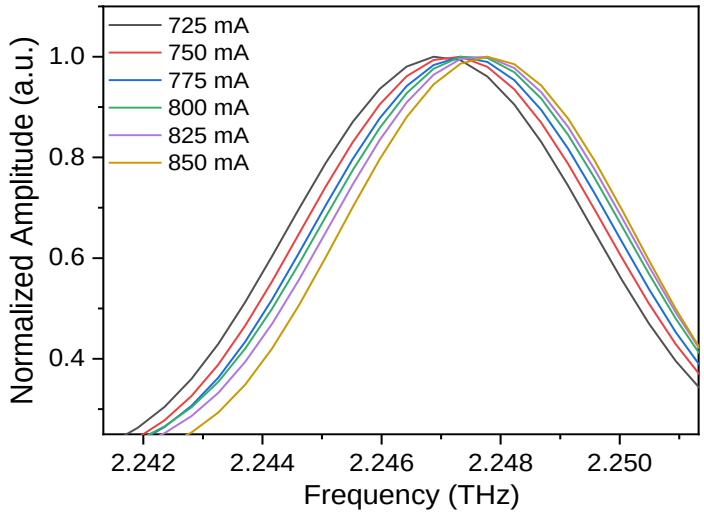

Figure 2.11 Spectrum of QCL-C measured with FTIR with the intensity normalized

2.4.3 Absorption line measurement

QCL-C (2.5 mm ridge) and another QCL (QCL-D in Appendix A, 2 mm ridge) made from the same wafer (V208), are measured in the setup in Figure 2.6. It is found that an absorption dip on the current-intensity curve can be seen even without a gas-cell, as shown in Figure 2.12. The current-intensity curves of the devices are then measured when the Golay cell is placed at different locations: just next to the high-density polyethylene (HDPE) window of the cryostat or behind two parabolic mirrors. For both QCLs, when the Golay cell is put next to the window, there is no absorption line on the current-power curve. However, when the Golay cell is 15 cm away after two parabolic mirrors from the window, a strong absorption dip can be seen on both of the current-power plots. As there is no gas-cell in the optical path, the absorption is not from methanol. One possibility for this is the absorption of water vapor in the air.

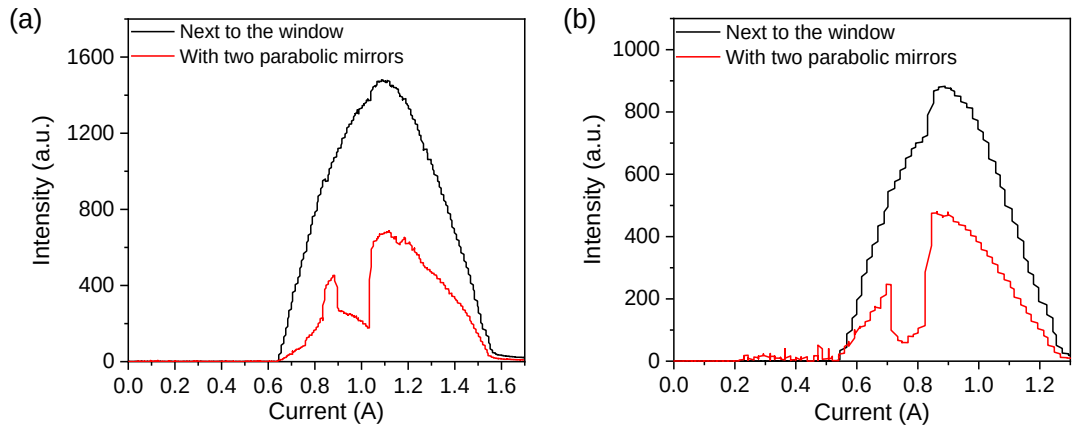

Figure 2.12 Current-intensity curves of QCL-C and QCL-D when the detector is placed at different places. (a) QCL-C; (b) QCL-D.

To confirm this assumption, two other experiments are conducted. In the first experiment, the current-intensity curves of QCL-D are measured when the Golay cell is put at different distances from the THz window. The intensity values are normalised so that the strength of absorption can be compared at different distances. If it is absorption of water vapor, the absorption strength should increase when the distance gets larger. The results are plotted in Figure 2.14 (a), which confirms that the dip on the curve is due to absorption of something in the air.

The second experiment is designed to further confirm that the absorption is from water. In this experiment, the whole THz system is put inside a large sealed plastic box with a small hole on the top surface of it (a schematic diagram of the setup is displayed in Figure 2.13). Before the measurement, nitrogen gas is injected into the box from the top surface. Consequently, nearly all the water vapor inside the box will be forced out.

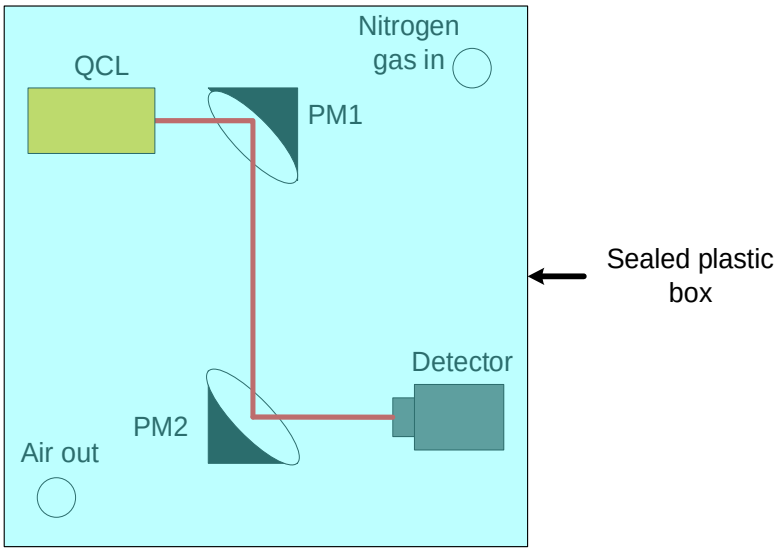

Figure 2.13 Schematic diagram of the setup for the sealed plastic box experiment

The current-power curves of the laser (shown in Figure 2.14 (b)) are then measured when there is a continuous nitrogen gas flow and every five minutes after the nitrogen gas flow is turned off. It is evident that, when the air in the sealed plastic box is replaced by nitrogen gas, the absorption line disappeared. Also, it can be seen that, after the gas flow is stopped, the absorption line becomes stronger as the air goes back into the box gradually. These two experiments demonstrate that the dip is due to absorption of water. Therefore, the two lasers are not suitable for methanol gas spectroscopy.

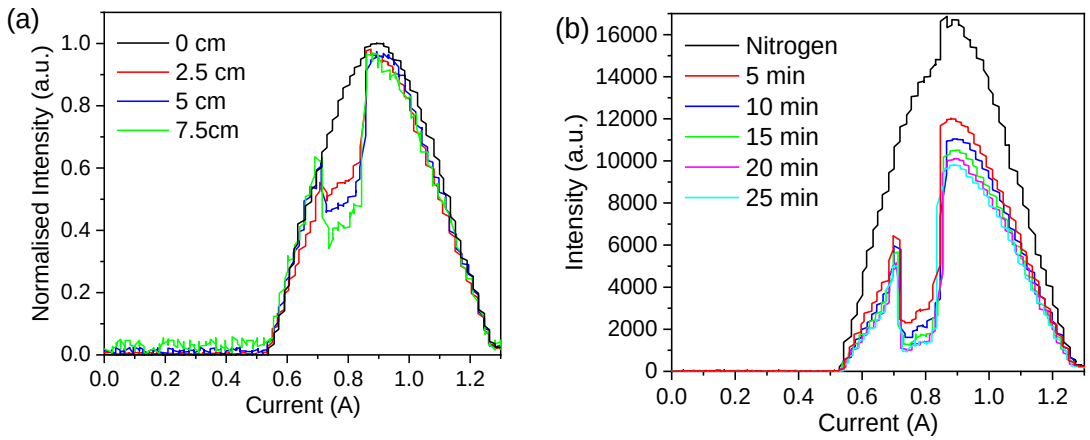

Figure 2.14 Current-intensity curves of QCL-D measured (a) at different distances and (b) in a sealed box with continuous nitrogen gas and 5, 10, 15, 20 and 25 minutes after the nitrogen gas was turned off.

When checking Figure 2.8 again, a strong water absorption line can be found at 2.2475 THz, which is very close to frequency of QCL-D (2.2473 THz) when the current is 0.8 A. Even though it is 5 times weaker compared to the methanol absorption lines around the same frequency, it absorbs a large amount of the THz QCL power. This

proves the assumption of water absorption and demonstrates that the absorption spectrum simulation method used here is valid.

2.4.4 Light source

As the QCLs from the V208 wafer (QCL-C and QCL-D) have been identified as unsuitable for gas spectroscopy because of the strong water absorption line, another THz QCL needs to be found as a suitable light source. To find a suitable frequency range, the absorption spectra of water and methanol are simulated with the method described in the previous section. It is found that there is no water absorption line between 2.352 THz and 2.354 THz. Meanwhile, there are several strong methanol absorption lines within this frequency range, as shown in Figure 2.15.

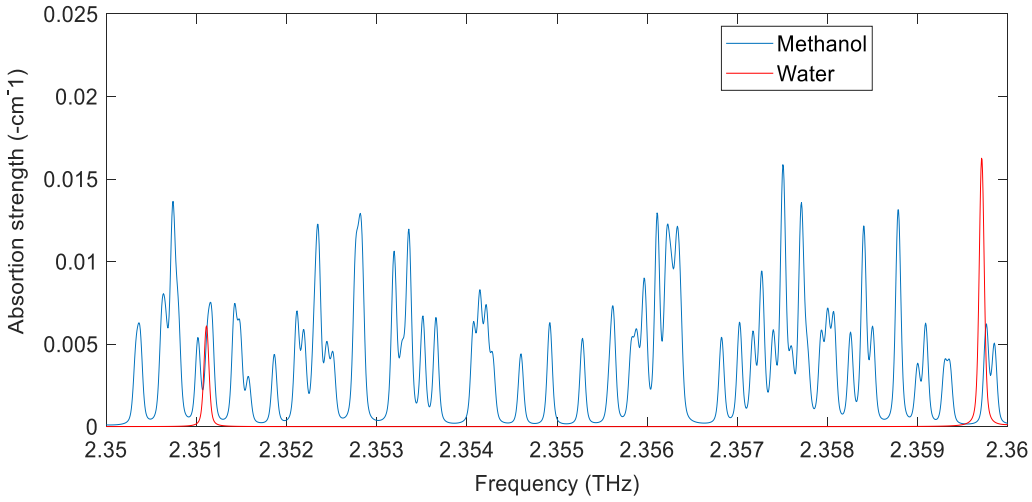

Figure 2.15 Simulated absorption spectrum of methanol and water around 2.35 THz with open data from Jet Propulsion Laboratory [168].

Therefore, a 2.352 THz QCL (QCL-E in Appendix A) which has the same active region design but not from the same wafer with the V208 lasers is chosen and tested. Figure 2.16 shows its spectra at different currents, which give a centre frequency of about 2.352 THz.

When the current is increased from 0.67 A to 0.94 A, the emission frequency is blue shifted by about 2 GHz. Compared to a V208 QCL, the frequency of the QCL-E is slightly higher. There might be two reasons for this. Firstly, the thickness of the layers in different MBE growth processes can differ by about ±1%. In addition, even if two QCLs are processed from different parts of the same wafer, because of the growth rate difference from the center to the edge, there will be a thickness change on each layer, thus shifting the frequency. Therefore, QCL-E already meets two conditions of a suitable light source for self-mixing spectroscopy.

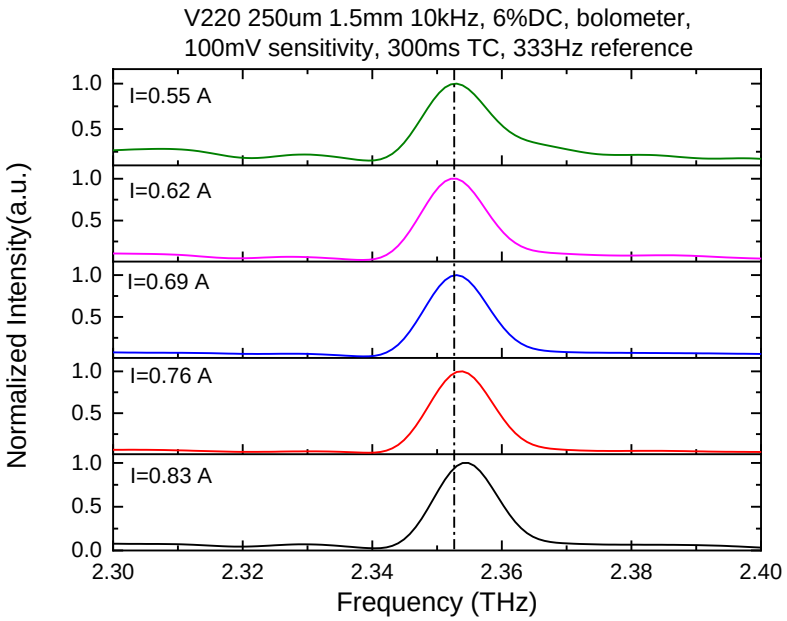

Figure 2.16 Spectra of QCL-E at different currents

The last but most important condition of the light source is a measurable self-mixing signal. To increase the sensitivity, a QCA instead of a QCL is used here. The QCA is achieved in the same way as discussed in Section 2.1.2 from QCL-E, namely by attaching an anti-reflection coated Si lens onto one QCL facet. The thickness of the antireflection parylene C coating is 22 µm. It is then made into an external cavity QCL with a flat gold coated mirror. Figure 2.17 shows the LIV response of the QCA with and without external feedback. A voltage perturbation of 90 mV is achieved when using a flat gold mirror as an external feedback element. Up to now, QCL-E has met all the requirements of the light source and therefore will be used in the final experiment.

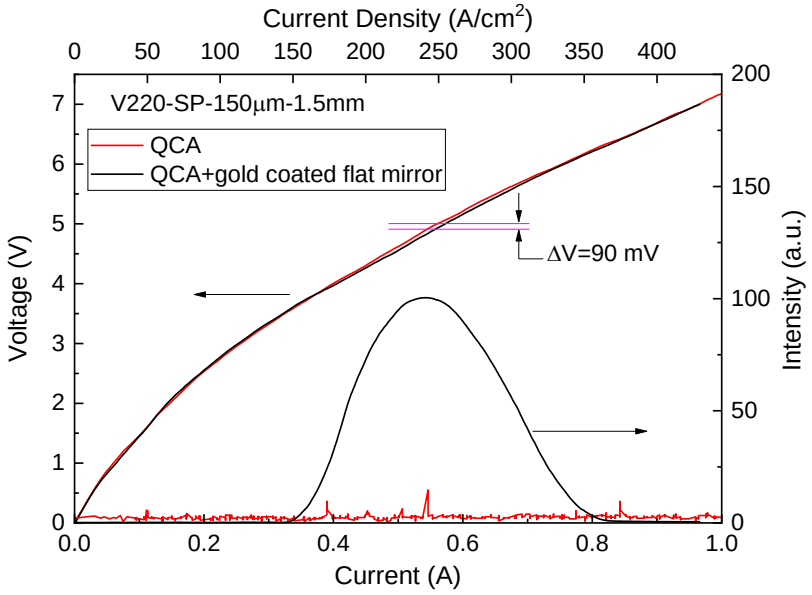

Figure 2.17 LIV response of the laser used for self-mixing spectroscopy

2.5 Self-mixing gas spectroscopy: experiment

Figure 2.18 shows a schematic of the final setup for the self-mixing gas spectroscopy experiment. The QCA (modified from QCL-E) is operated at 10 kHz with 6% duty cycle. A traditional double pass gas cell (with 210 mm path length) has been constructed: a vacuum arrangement with polyethylene windows, a methanol gas reservoir, dual gas bleed valves, a vacuum gauge and high vacuum pumping to control the gas concentration in the cell. The full spectroscopy arrangement collimates the THz beam from the QCA using a pair of off-axis parabolic mirrors which passes through the gas cell, as shown in Figure 2.18. Also incorporated into the set-up is a traditional Golay cell detector; as lasing is only rebuilt with optical feedback, the measured THz output signal will be dependent on the level of feedback which is determined by the THz absorption in the beam path (i.e. the concentration of methanol in the gas cell).

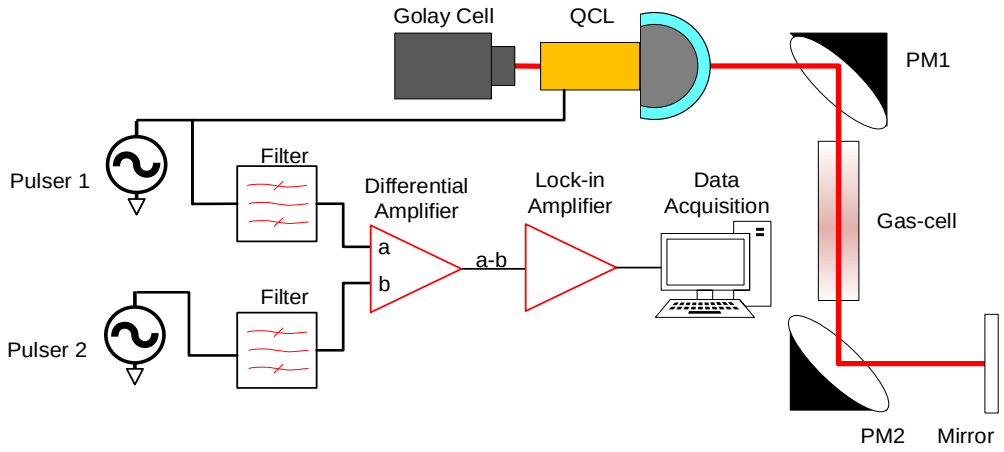

Figure 2.18 Schematic of a setup for external cavity THz QCL based self-mixing spectroscopy. The absorption of THz radiation is measured in two ways: direct output power measured with a Golay cell and the terminal voltage perturbation of the external cavity QCL.

For signal acquisition, to be able to detect and record the small voltage perturbation signal, a differential detection method is utilised in this work. As shown in Figure 2.18, pulser 1 generates a 10 kHz pulse to bias the QCL. A second pulser (pulser 2) is used to generate a reference signal, which has the same repetition rate (10 kHz) and pulse duration as the bias pulse. The two signals are then fed into a differential amplifier after passing through a band pass filter, which will filter the background noise. The amplified differential signal is then measured with a lock-in amplifier. Before the measurement, the amplitudes of the two pulses are adjusted to get a minimum differential signal. During the measurement, when the terminal voltage of the external cavity QCL changes because of the gas absorption induced optical feedback change, it will generate a larger differential signal, which is determined by the gas concentration.

To demonstrate the effectiveness of this approach, both the optical power and the voltage perturbation signal of the external cavity QCL with a gas cell are recorded at the same time with different methanol concentrations. Figure 2.19 shows the measurement results. When the methanol pressure is increased from 0 mbar to 24 mbar, the output power reduces, and this is replicated in the voltage perturbation. An absorption feature can be seen on both graphs at different gas pressures. The position of the absorption feature is different at different pressures, which might due to the refractive index difference of the gas at different pressures.

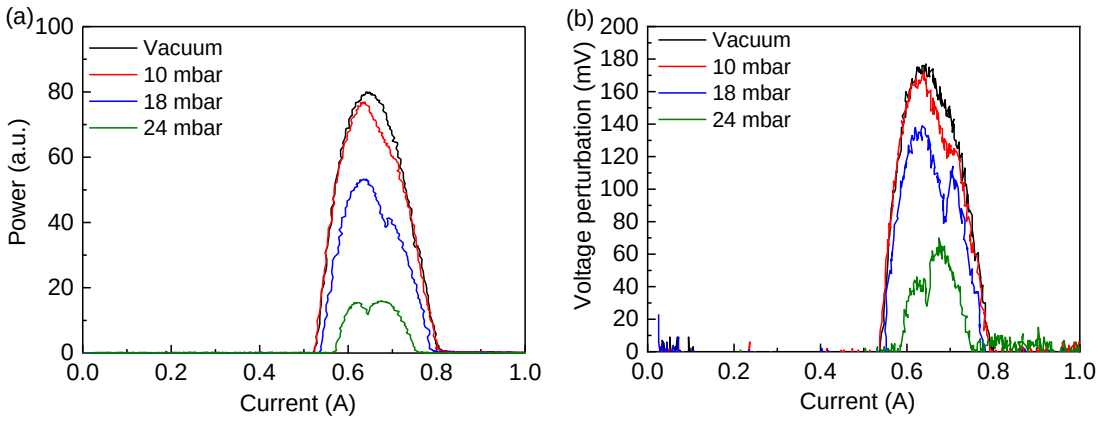

Figure 2.19 Transmission power of the THz QCL through a gas cell at different methanol pressures measured with (a) a Golay cell and (b) the voltage perturbation.

Furthermore, the position (QCL bias current) of the maximum absorption at different gas pressure on the two graphs matches with each other, as shown in Figure 2.20. Therefore, instead of measuring the output power, the voltage perturbation can be measured for gas spectroscopy.

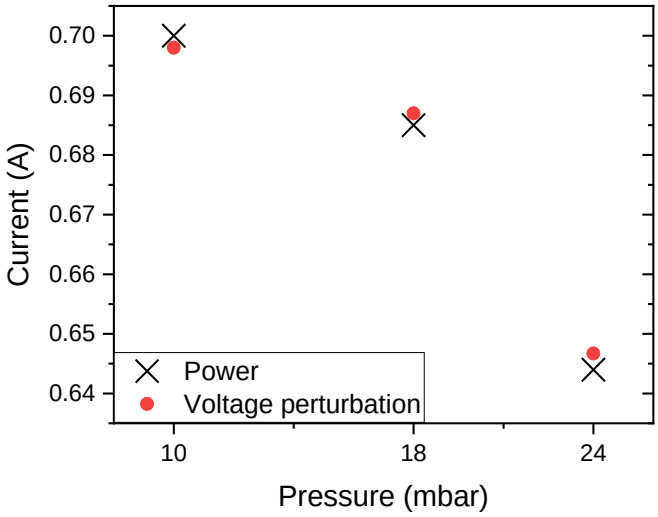

Figure 2.20 Position (current) of the absorption line at different methanol pressures detected from the power and the voltage perturbation.

For this setup, even though the lasing of the QCL is suppressed, the reflectivity of the laser facet is still above 3% (3% is the lowest reflectivity that can be achieved with parylene C, as shown in Figure 2.2). Therefore, the QCL cavity mode will still influence the lasing mode. When the current, thus the frequency is changed, the phase difference between the internal cavity and the external cavity will change, which will generate a self-mixing fringe when the external cavity feedback is a weak feedback. However, in this case, the system operates at a strong feedback regime, therefore, the influence of the internal cavity is negligible and there is no self-mixing fringe.

Compared to measuring the power, there are three advantages measuring the terminal voltage. First of all, the response of terminal voltage change is very fast, which is determined by QCL dynamics and is usually at picosecond level [173]. In addition, it is more sensitive to measure the voltage than to measure the power. Also, an additional power detector is not needed for the self-mixing setup, making it possible to achieve a compact system.

2.6 Broadband THz quantum cascade amplifier

For gas spectroscopy, it is desirable to have a broadband system. A broadband self-mixing spectroscopy system can be achieved if the normal external cavity QCL can be replaced with a broadband external cavity QCL. There are two requirements to achieve this. The first one is to have a broadband THz QCA, which requires an active region with a broadband gain and a broadband lasing suppression. Several THz QCL active regions with broadband gain have been developed up to now [38], [49], [174]–[177], which is not the focus of the work in this thesis and will not be discussed in detail. The broadband lasing suppression can be achieved either through a broadband AR coating (Section 2.6.1) or applying AR coating centred at different frequencies on the two facets of the QCL (Section 2.6.2). The second one is an external element to tune the frequency of the external cavity QCL, which will be discussed in Section 2.7.

2.6.1 Broadband AR coating

A broadband AR coating at THz frequency range is essential for achieving a broadband THz quantum cascade amplifier, which could be used for a wide range of applications, such as frequency tunable external-cavity THz QCLs, spectroscopy, etc.

Due to the small bandwidth, standard dielectric quarter-wave AR coatings discussed in the previous section are not suitable for applications with multiple wavelengths or broadband terahertz emission. As a result, new structures need to be exploited to promote research in these areas. To date, several structures have been developed to

achieve broad band AR at THz frequency range. To begin with, ultrathin (nm thickness) metallic layers were demonstrated to work as efficient impedance-matching layers in the terahertz frequency ranges and show broadband performance [178]. This method was then improved further by using randomly nanostructured gold films, which reveals a significantly better broadband AR performance than homogeneous metal films at least in the terahertz frequency range [179]. It has been experimentally demonstrated that reflected electric field amplitude of a broadband terahertz pulse in a silicon substrate can be suppressed to below 1% of that without coating. However, when a THz wave passes through such a coating, there is a severe absorption, which will significantly reduce the input power.

Another possible approach to achieving broadband AR coating is using the thin film structure, which has been widely used to achieve a designed reflectivity for a variety of optical components and can achieve better AR properties. Figure 2.21 gives an example of the thin film structure.

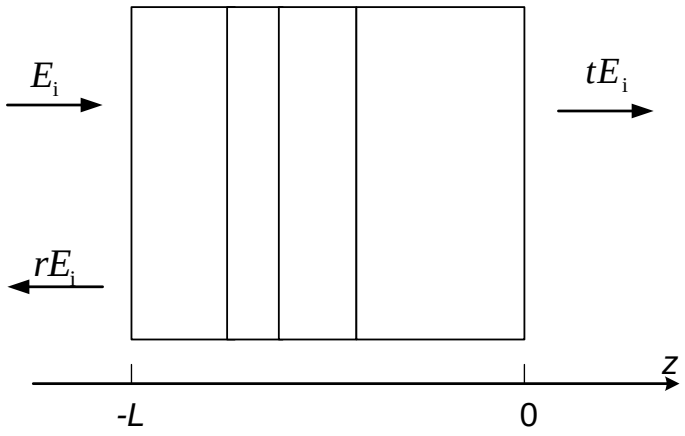

Figure 2.21 A schematic diagram of a thin film structure

At Z=-L, the x component of the electric field E_x and the y component of the magnetic field H_y of the optical wave satisfy the following relation [180]

$$\begin{aligned} E_x(-L) &= (1+r)E_i \\ H_y(-L) &= (1-r)E_i / Z_1 \end{aligned}, \tag{2.5}$$

where Z_1 is the impedance of the first layer and r is the field reflectivity. As a result,

$$Z_1(1+r)/(1-r) = E_x(-L)/H_y(-L) = Z_{in}, \tag{2.6}$$

where Z_{in} can be seen as the input impedance the stack presents to light travelling from

the left. Thus, the intensity reflectivity can be obtained as follows

$$R = r^2 = \left(\frac{Z_{\text{in}} - Z_1}{Z_{\text{in}} + Z_1} \right)^2 . \tag{2.7}$$

Furthermore, the input impedance of one specific layer can be calculated through the following formula

$$Z_{\text{in}} = \frac{E_{\text{x}}(-L)}{H_{\text{y}}(-L)} = \frac{Z_{\text{load}} - iZ_{\text{layer}} \tan(kL)}{1 - i(Z_{\text{load}} / Z_{\text{layor}}) \tan(kL)} . \tag{2.8}$$

Here, Z_{load} is the value of the ratio $E_{\text{x}}(0)/H_{\text{y}}(0)$ existing on the plane $z = 0$. It is the input impedance of whatever lies to the right of $z = 0$. Z_{layer} is the impedance of the layer being considered. According to equation (2.8), there are two special situations

$$\text{quarter-wave layer:} \quad \tan(kL)=\infty, \qquad Z_{\text{in}} = Z_{\text{layer}}^2 / Z_{\text{load}} . \tag{2.9}$$

$$\text{half-wave layer:} \quad \tan(kL)=0, \qquad Z_{\text{in}} = Z_{\text{load}} . \tag{2.10}$$

Considering the case of using a series of quarter-wave layers and according to equation (2.7), to achieve totally anti-reflection, the following condition needs to be satisfied:

$$Z_{\text{in}} = Z_1 . \tag{2.11}$$

Assuming that the multilayer is composed of one layer with refractive index n_1 and a p times' repetition of two different layers with refractive index being n_2 and n_3 respectively, then the input impedance for the first layer will be

$$Z_{\text{in}} = \left(\frac{n_2}{n_3} \right)^{2\text{p}} n_{\text{air}} . \tag{2.12}$$

As a result, the condition of anti-reflection is

$$Z_1 = n_1 = Z_{\text{in}} = \left(\frac{n_2}{n_3} \right)^{2\text{p}} n_{\text{air}} . \tag{2.13}$$

If one more layer of refractive index n_2 is added to the multilayer film, then the anti-reflection condition becomes

$$n_1 = n_2^2 \left(\frac{n_2}{n_3} \right)^{2\text{p}} n_{\text{air}} . \tag{2.14}$$

If there is just one layer, then the condition becomes

$$n_1 = n_2^2 n_{\text{air}} . \tag{2.15}$$

which is just the condition described in equation (2.1). Therefore, instead of just coating a single layer, it seems to be a promising approach coating a multilayer on the facet to achieve a better anti-reflection condition. When it comes to the THz QCL coating, in a two layer situation, if the refractive indexes of the two layers are 2.85 and 1.517 and they are coated with quarter-wave thicknesses at 3 THz, the reflection spectrum of the coating will be the one shown in Figure 2.22. It gives a reflectivity of below 0.1% from 2.8 THz to 3.2 THz. Therefore, if suitable coating materials can be found, this approach can provide a very low reflectivity within a broadband.

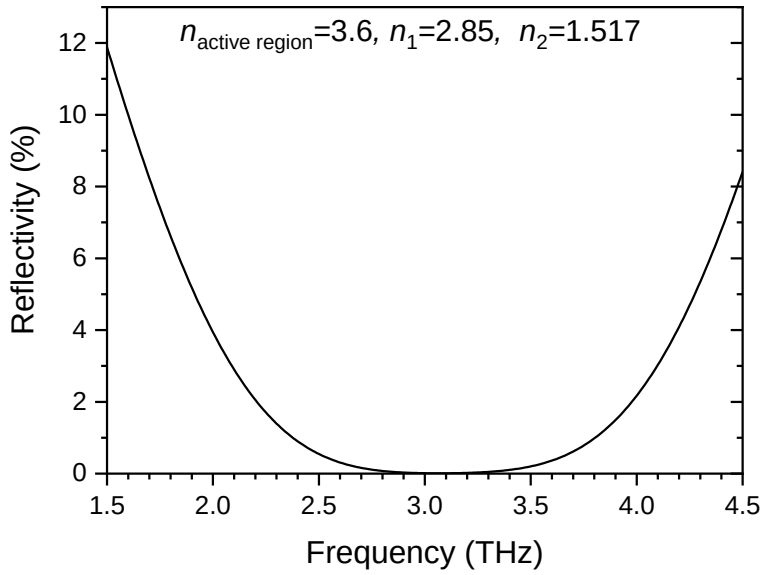

Figure 2.22 The reflectivity of a two-layer coating at different frequencies. The coating consists of quarter-wave layers for 3 THz with coating material refractive index of 2.85 and 1.517 respectively. The reflectivity is calculated using the Transfer Matrix Method reported in reference [161].

Meanwhile, a so-called multilayer inverted photonic structure was developed based on the gradient index anti-reflection theory [181]. This structure seems to be promising to provide broadband AR for a THz QCL cavity as it could be fabricated on GaAs substrate and have a good AR performance at the THz frequency range. For a three-layer design, its structure is shown in Figure 2.23, which can be fabricated using iron etching. According to the simulation, these structures can achieve a reflectance smaller than 0.1 at frequency from 2 THz to 10 THz. In addition, by changing the structure period and depth, the AR frequency range can be tuned.

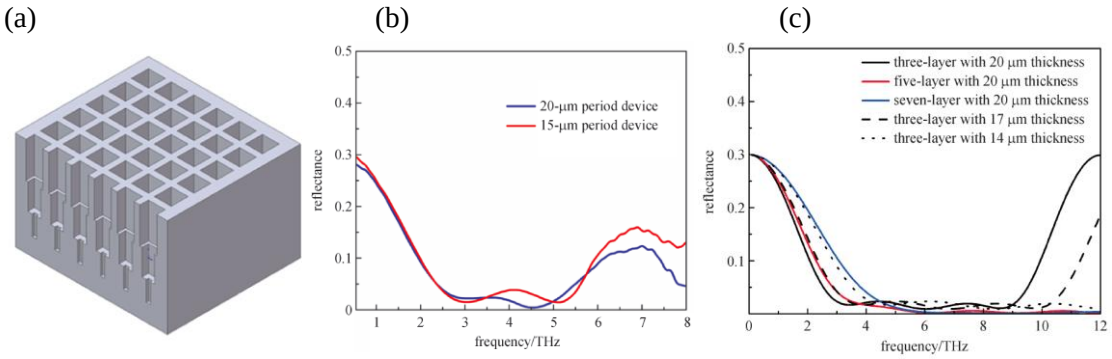

Figure 2.23 Data for an inverted photonic structure, adapted with permission from [181] © 2013, Springer Nature. (a) Structure of a three-layer design; (b) Fourier transform reflectance spectra of a 20-μm period and a 15-μm period inverted photonic structure; (c) Simulated reflectance of different inverted photonic designs.

2.6.2 Amplifier with two AR coated lenses

Another approach to achieving broadband QCA is applying AR coatings centred at different frequencies on the two facets of a broadband THz QCL. Here, silicon lenses with AR coatings at 2.8 THz and 3.0 THz are attached on the facets of a single-plasmon THz QCL with a bound-to-continuum active region design (QCL-F in Appendix A) [182] and 1.1 mm cavity length. The transmission spectra of the two lenses are shown in Figure 2.24. For both AR coated lenses, the transmission is higher than 67% from 2.75 THz to 3.0 THz, which is the spectral range of QCL-F.

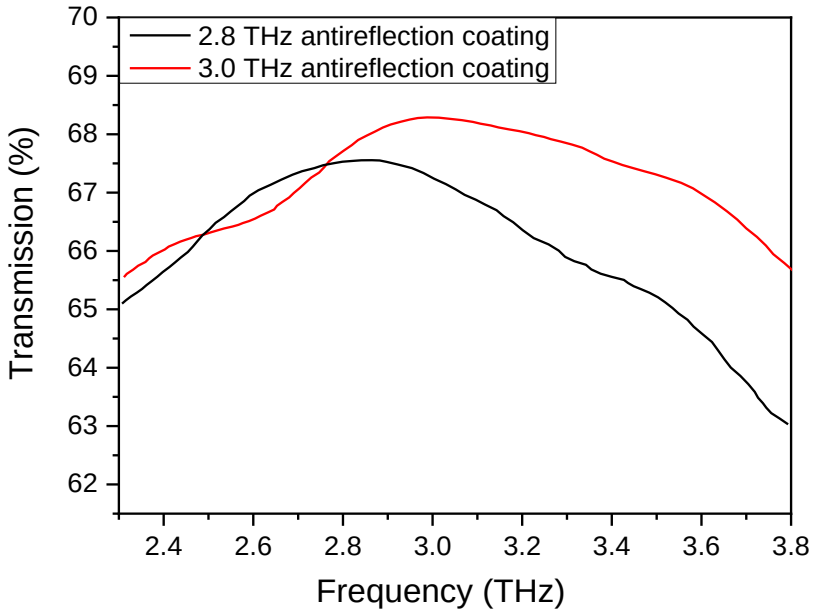

Figure 2.24 Transmission spectra for Si lenses with AR coating centred at 2.8 THz and 3.0 THz respectively, data from Tydex.

Figure 2.25 gives the current-voltage-intensity response of QCL-F with different configurations. When only one lens (with AR coating at 3.0 THz) is attached onto one facet of the QCL, the QCL is partially suppressed and the output power is about 10 times lower compared to the original laser. After the second lens (with AR coating at 2.8 THz) is attached, the QCL is totally supressed from lasing. The figure also shows that current-voltage responses of the QCL are different in the three configurations. The terminal voltage of the QCL is higher when lasing is suppressed. The reason is that when the lasing is suppressed, the photo-assisted transport in the semiconductor active region of the QCL is lower, therefore the resistance is higher.

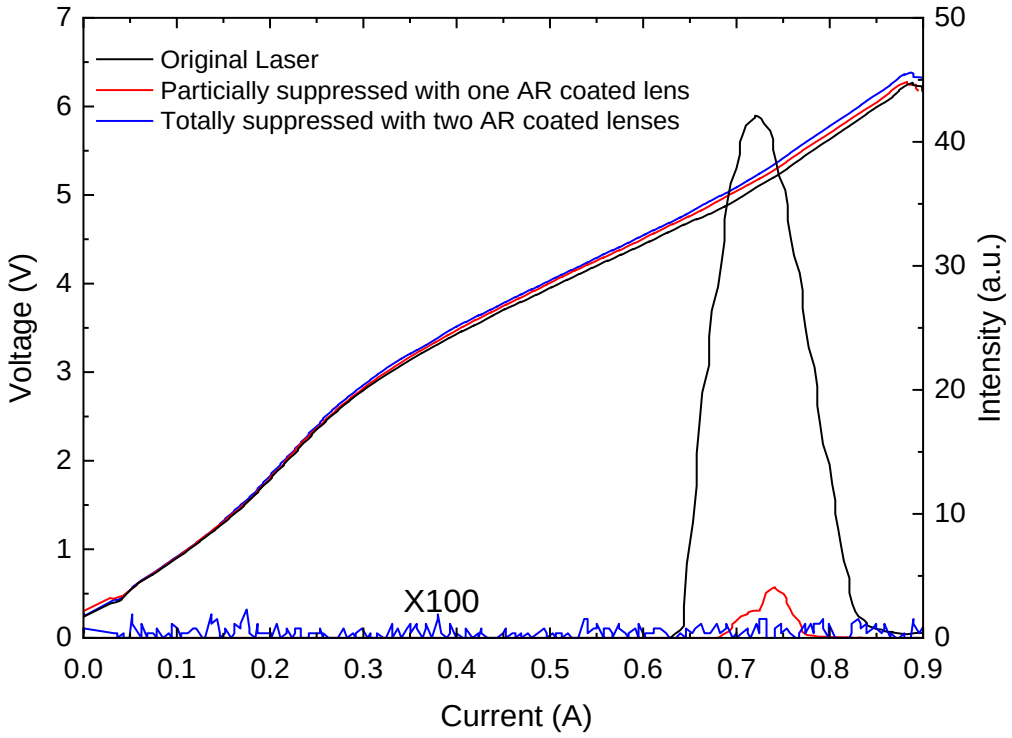

Figure 2.25 Current-voltage-intensity plots of QCL-F in three different operational conditions: original laser (black), partially suppressed with one AR coated lens (red) and totally suppressed with two AR coated lenses (blue). The intensity of the totally suppressed QCL is magnified by 100 times for comparison.

Furthermore, to evaluate the performance of the QCA as an amplifier, as shown in Figure 2.26 (a), it is put next to a seeding laser (QCL-G in Appendix A), which has the same active region design as the QCA (V557), on the same cold finger. The distance between the seeding laser and the QCA is about 0.5 mm. The seeding laser is also processed into a single-plasmon waveguide and has a cavity length of 2.5 mm. During the experiment, the bias current of the seeding laser is kept at a fix value while the bias

current of the QCA is increased from 0 A to 1.1 A. Figure 2.26 (b) displays the output power of the whole system at different seeding laser bias currents. When the QCA bias current is larger than 0.2 A, there is a power enhancement on the system, which is dependent on the QCA bias current. The enhancement reaches the maximum when the QCA bias current is at J_{max} (the current at which the original laser for the QCA has the highest power). The corresponding gain curves of the QCA at different seeding laser bias currents have been calculated as well (gain=$10\log(P_{out}/P_{in})$), as shown in Figure 2.26 (c). Here P_{in} is the power without the amplifier while P_{out} is the power with the amplifier. The gain curves all follow the same trend and the highest gain is achieved at J_{max} (0.6 A), with the average maximum gain being about 1 dB.

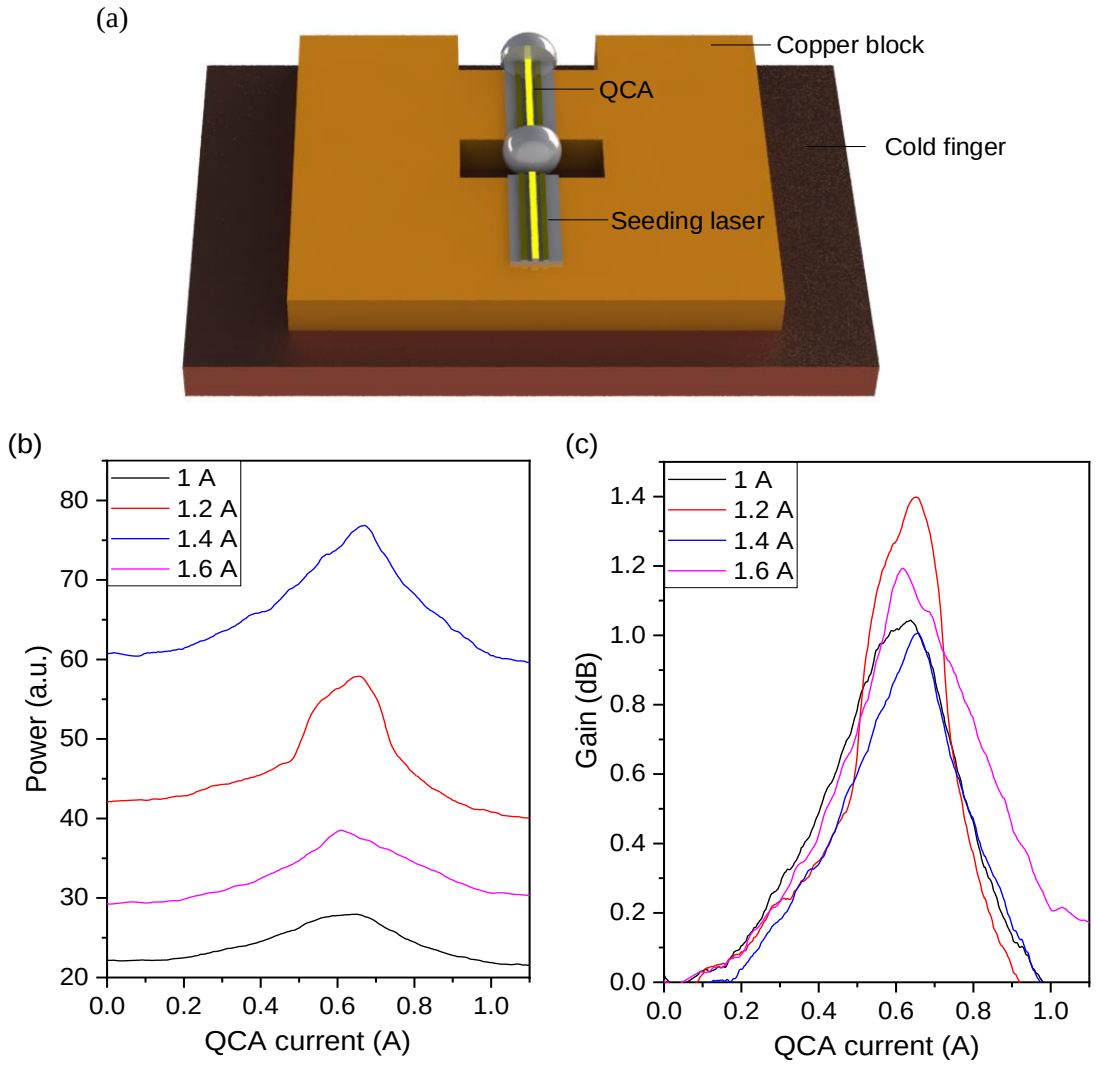

Figure 2.26 (a) The layout of QCA and the seeding laser, (b) output power and (c) gain of the QCA when the seeding laser is biased at different currents.

The spectra of this system in different operating conditions, shown in Figure 2.27, have been measured with an FTIR as well to study the influence of the QCA on the emission frequency of the seeding laser. The bottom graph (with no QCA bias current) in Figure 2.27 gives the spectra of the seeding laser after the radiation goes through a QCL ridge. As can be seen, five modes exist at different bias currents and there is a red shift on the frequency of the main lower frequency (2.83 THz) mode when the bias current is increased. When the QCA is biased above the threshold current, the red shift is not present anymore and the emission frequency is dominant by the seeding laser despite the fact that there is still difference between the spectra of the same seeding laser current when the QCA bias is different.

From Figure 2.26 (b), it can be seen that the gain of the QCA is almost consistent when the seeding laser bias current is changed from 1 A to 1.6 A, which means the gain of the QCA covers at least a spectral range from 2.83 THz to 2.91 THz (the frequency of the two main modes of the seeding QCL). A wider spectral coverage of the gain curve can be achieved if an active region with a broader gain curve is utilised.

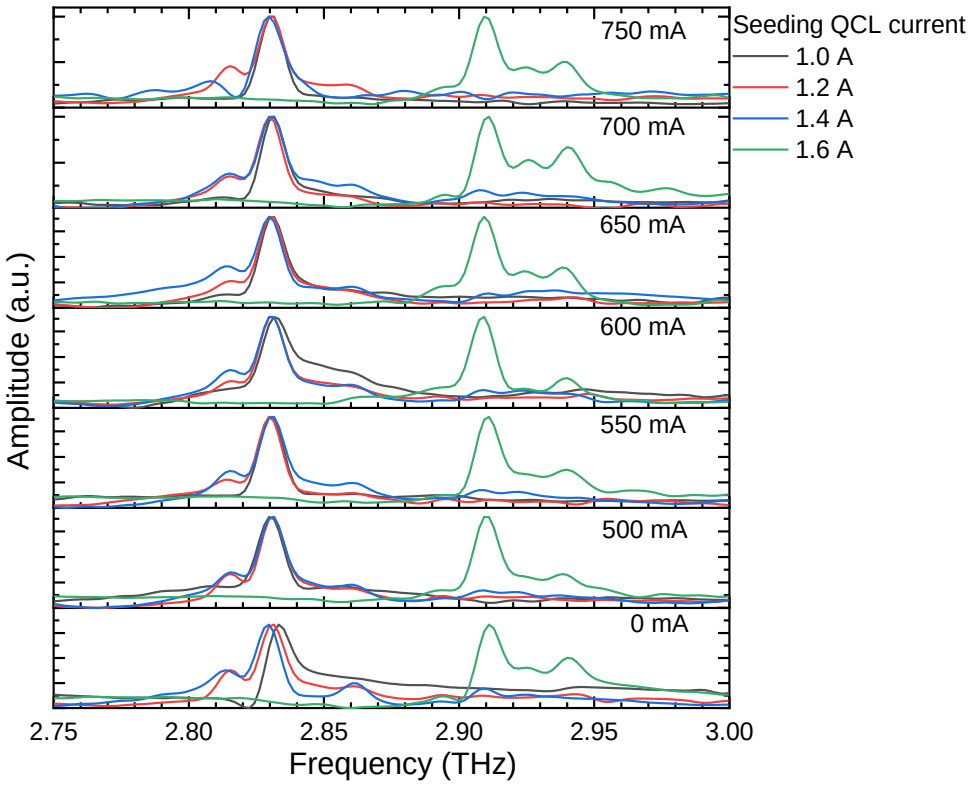

Figure 2.27 The spectra of the system when the seeding laser and QCA are biased at different currents. From the bottom graph to the top graph, the QCA current is increased from 0 mA to 750 mA. The spectra of the system at a constant QCA current but different seeding laser current are displayed in different colors, as specified in the top right corner of the graph.

2.7 External frequency tuning element

When a broadband THz QCA is ready, a frequency tuning element is then needed for the external cavity laser. A variety of approaches have been developed to tune the frequency of a THz QCL.

2.7.1 Current existing frequency tuning methods for THz QCLs

One of the original method to tune the frequency of a QCL is by changing the operation temperature of it as the temperature dependence of the refractive index causes a decrease in frequency towards higher temperatures. Nonetheless, this is a rather inconvenient and inherently slow approach and the frequency tuning range is small with a maximum fractional frequency change of at most 3×10^{-3} [183].

Electric field tuning offers another approach. Stacking together two active region designs with different frequencies in a single QCL makes it possible to switch the lasing between two frequencies by changing the bias voltage applied on the device [184]. Also, using some special active region design, the QCL can lase at another frequency by reversing the applied bias [185]. In addition, a THz QCL which could be tuned in a step-wise manner from 3.07 to 3.40 THz by changing the applied electric field across the device has been demonstrated by reducing the gallium growth rate successively during growth of the active region [186]. Furthermore, Stark shift of the intersubband transition could be exploited to achieve step-wise frequency tuning [38]. A 240 GHz shift has been achieved through this approach. A broadband multimode laser with emission spanning over 1.2 THz of bandwidth has also been demonstrated by employing a single active region design based on a resonant phonon two-quantum well scheme [187].

A common method used to achieve single mode operation of a laser is distributed feedback, which could also be adopted to a THz QCL. Since the grating is written into the crystal of the laser, there is small flexibility to mechanically change the periodicity of it. Consequently, this method usually needs to be used with the combination of the previous two methods. One feasible approach to achieve a broad tuning range is to fabricate a DFB-QCL arrays [188]. Another potential approach is to produce a periodicity switchable grating inside the waveguide of a QCL using surface acoustic waves (SAW). Simulations have been conducted to theoretically examine the feasibility of it [189].

A novel tuning mechanism based on a unique ‘wire laser’ device for which the transverse dimension is much smaller than the central wavelength was demonstrated by

Hu *et al.* from MIT [190]. Sinusoidal corrugations are etched on one side of a metal–metal ridge waveguide to provide first-order distributed feedback to achieve single-mode operation and the transverse mode outside the solid core was manipulated by a movable object to change the resonant frequency of the cavity, thus tuning the laser, as shown in Figure 2.28. A 137 GHz (3.6%) tuning from a single laser device at 3.8 THz was achieved with continuous single-mode redshift and blueshift tuning for the same device by using either a dielectric or metallic movable object.

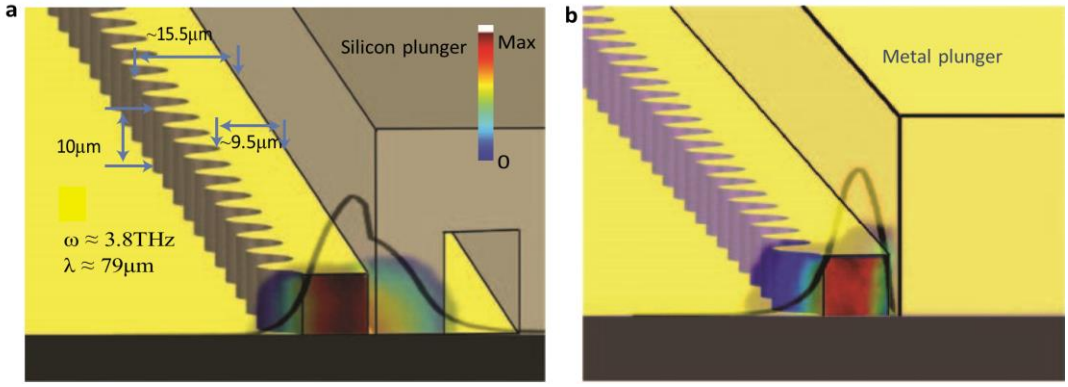

Figure 2.28 Schematics illustrating the tuning mechanism of the wire laser with (a) a silicon plunger and (b) a metallic plunger, adapted with permission from [190] © 2009, Springer Nature.

More recently, a method of tuning terahertz lasers via graphene plasmons was reported [191]. In this work, a hologram designed to define multi-colour THz QCL emission was firstly introduced to the metalized laser ridge surface as a series of subwavelength slits to achieve an aperiodic distributed feedback (ADFB) QCL, as shown in Figure 2.29. Then, a layer of graphene was transferred onto the ADFB QCL and a polymer electrolyte (LiClO4, PEO) layer was manually deposited over the graphene. By varying the gate voltage of the graphene, the spectrum of the laser could be tuned.

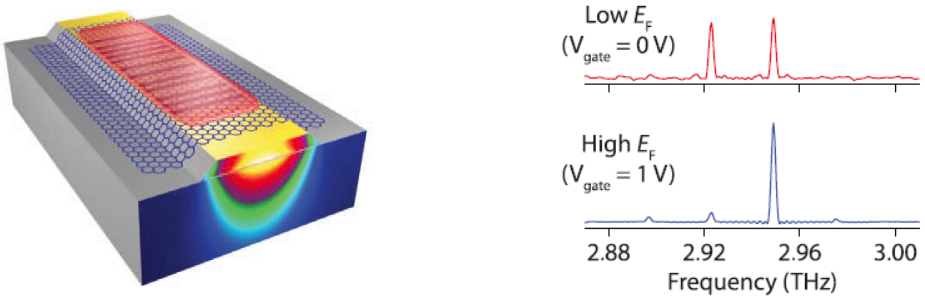

(a) (b)

Figure 2.29 Tuning terahertz lasers via graphene plasmons: (a) Schematic of the device reported in [191]; (b) Laser emission spectra measured after electrolyte deposition for ungated (low E_F) and gated (high ns, high E_F) graphene, collected just above laser threshold. From [191], reprinted with permission from AAAS.

On top of the above methods, tunable THz emission has also been achieved through difference frequency generation in mid-infrared quantum cascade lasers. Room temperature single mode THz emission from 1.0 to 4.6 THz with output power up to 32 μW was obtained respectively within two mid-infrared active regions based on the single-phonon resonance scheme and a Cerenkov phase-matching [192]. Furthermore, an external-cavity terahertz quantum cascade laser source tunable between 1.70 and 5.25 THz was demonstrated with a Littrow configuration, as shown in Figure 2.30 [193]. Despite the advantage of the ability to work at room temperature, there are two difficulties to overcome within this approach. Firstly, due to the low efficiency of the difference frequency generation, at present the output power of such devices is relatively low compared with a THz QCL. Besides, apart from the THz radiation, there is always a large signal at infrared present.

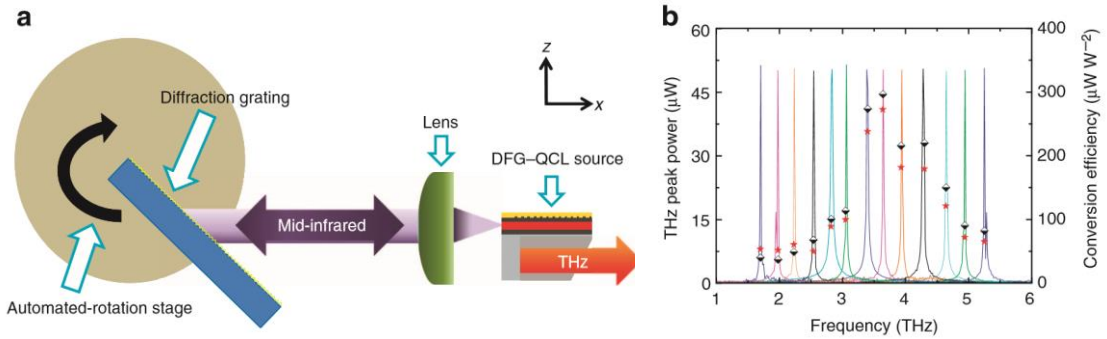

Figure 2.30 Broadband tuning with an external cavity setup. (a) Schematic of the external cavity system operated in the Littrow configuration. (b) THz spectrum displaying a tuning bandwidth of 3.55 THz for this external cavity system. The THz power (red star, bottom and left axes) and conversion efficiency (black–white diamond, bottom and right axes) is shown for each mode. Adapted with permission from [193] © 2013, Springer Nature.

External cavity QCL is a research field that attracts intensive attention regarding to frequency tuning. In external cavity lasers, tunable feedback is provided by the insertion of a controllable optical element like a grating or a movable mirror [194]. In practice, there are two things to consider for achieving an effective external cavity. The first one is to efficiently suppress the unwanted reflections at the device facet. At present, this is commonly achieved by depositing an AR coating on the device facet coupled to the external optics [158][159]. Another thing is to improve the coupling efficiency of the radiation to an external element. In this case, a silicon hyper-hemispherical lens can be attached to the facet to focus the light, thus enhancing the coupling efficiency [195]. A grating is the most commonly used feedback element and by tuning the angle of a grating a 165 GHz tuning can already be achieved, as shown in Figure 2.31 [195].

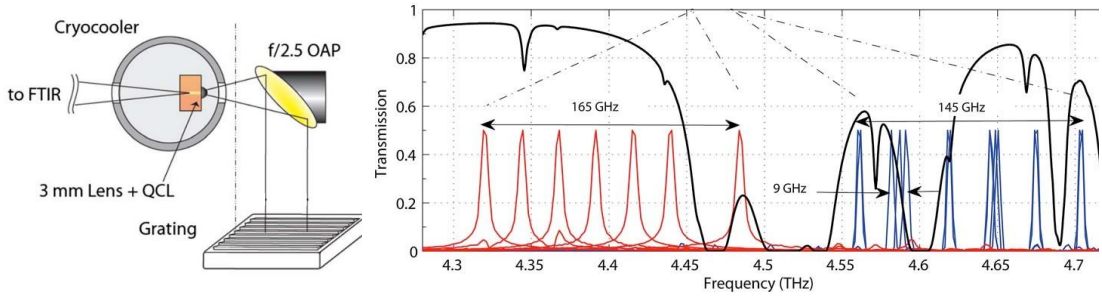

Figure 2.31 (a) An External-Cavity QCL configuration with an off-axis parabolic mirror; (b) Emission spectra of a 100 μm wide by 1.5 mm long (red) QCL and a 150 μm wide by 1.25 mm long QCL, frequency tuned by changing the grating angle. The calculated atmospheric transmission through the external cavity is shown on the topmost part of the same graph. Adapted from [195] © 2010 Optical Society of America.

2.7.2 Self-mixing spectroscopy with a broadband external cavity THz QCL

Among all the previous discussed approaches, the external cavity method is promising for self-mixing spectroscopy as an external cavity always exists in a self-mixing setup. There are two differences between the setup discussed in Section 2.5 (Figure 2.18) and a broadband setup: the normal QCA needs to be replaced with a broadband QCA; a frequency selective element (be it a grating or metamaterial frequency modulator) instead of a flat mirror is needed as the external reflector, as shown in Figure 2.32. The broadband amplifier has been discussed in Section 2.6. For external cavity frequency tuning, two methods have been developed in our group: grating and graphene loaded metamaterial arrays. Here, the first approach will be discussed in detail.

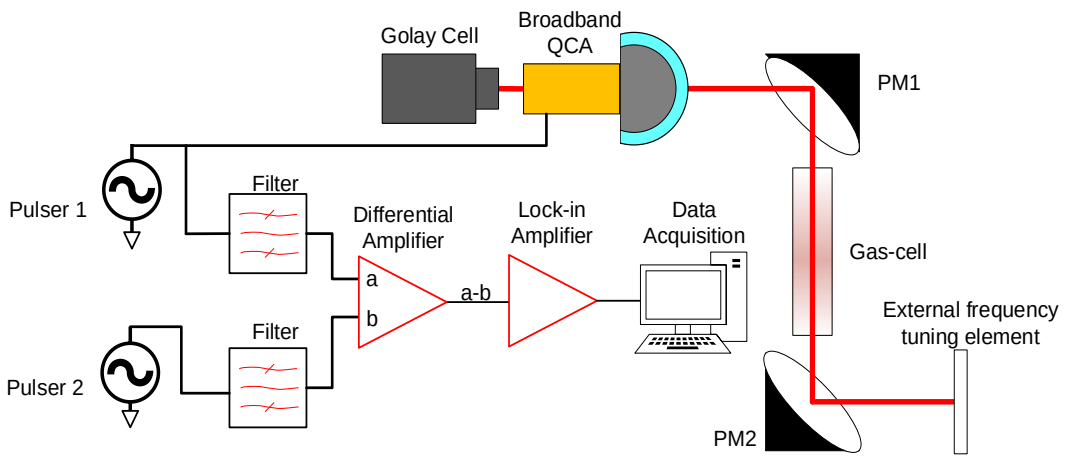

Figure 2.32 Schematic of a broadband self-mixing spectroscopy setup

2.7.3 Broadband frequency tuning of a THz QCL with a grating

The external cavity tuning configuration is also based on a fully suppressed THz QCL (or QCA) as the gain medium, which is optically coupled to a Littrow grating to provide the optical feedback. The ruled reflection (Littrow) grating was made using low expansion glass as the substrate with aluminum on top, for a blaze wavelength of 112.5 μm (2.67 THz), a groove density of 7.9 g/mm and nominal blaze angle of 26.75 deg. The grating behaves as a band-pass filter where the bandwidth is determined by the beam spot size on the grating: the larger the illuminated area on the grating, the narrower the reflection bandwidth is. Figure 2.33 (a) shows a schematic of this Littrow grating configuration while Figure 2.33 (b) gives the reflection spectra of the grating at different light incident angles.

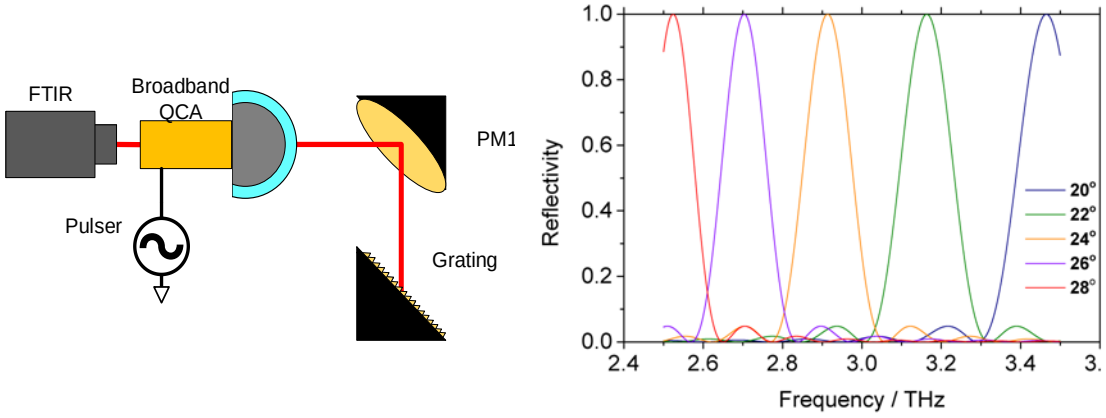

(a) (b)

Figure 2.33 (a) Schematic of the Littrow grating configuration; (b) Reflection spectra of the grating with different light incident angles

The THz QCA (modified from QCL-A in Appendix A) source is a 2.2 mm long, 250 μm wide 2.9 THz bound-to-continuum active region single plasmon QCL coupled to an AR coated silicon lens. Directly mounting the AR coated silicon lens on the front facet of the laser reduces the reflection from the laser/air facet of the laser. The hyper-hemispherical lens also provides a more collimated beam. The dominant feedback frequency is determined by the angle of the grating, such that an 8 degrees shift of the angle would theoretically cover ~1THz, as shown in Figure 2.33 (b), which covers the widest QCL lasing bandwidths [176].

Adjusting the grating angle, single mode frequency tuning is achieved. As shown in Figure 2.34 (data taken by my colleague Dr. Yuan Ren), 103 GHz tuning is achieved around the central frequency of ~2.9 THz with a grating angle change of 1.1 degree.

Frequency hopping is observed between the longitudinal modes of the device spaced at 17 GHz, which is due to longitudinal cavity modes associated with the Fabry-Pérot waveguide. To achieve continuous frequency tuning, this needs to be avoided and the reflectivity of the QCL facet needs to be further reduced, which requires an AR coating with a broadband response and better performance.

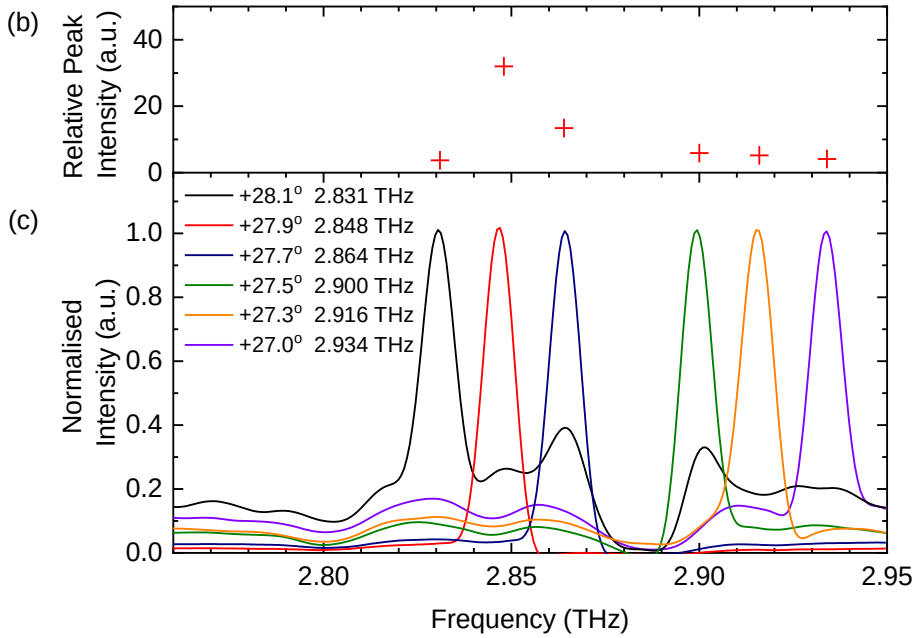

Figure 2.34 Normalised spectra from QCL-A coupled to an AR coated silicon lens. All the spectra are recorded under the same working condition with a 10 kHz repetition rate and 6% duty cycle, driving current 1.33 A and are normalised to the same scale. The frequency resolution is limited by the FTIR resolution of 0.25 cm^{-1}. Upper panel represents the emission intensity at the different frequencies.

Figure 2.35 shows the laser emission wavelength as a function of the grating angle. The solid line represents the theoretical calculation of the wavelength, as $\lambda = 2d\sin\alpha$ (α is the light incident angle and d is the line spacing of the grating). The deviations of the measured wavelength values from the calculated ones are within the 17 GHz free spectral range of the Fabry-Pérot cavity of the laser itself. The tuning range of this external cavity as a percentage of centre frequency is 3.6%. The performance of this set-up is consistent with previously published external cavity results, 90 GHz centred at 4.8 THz (1.9% range) using SiO_2 as the AR facet coating and a mechanical mirror [158] and 165 GHz centred at 4.4 THz (3.8% range) using a silicon lens coated with low density polyethylene with a Littrow grating [195]. However, the use of Parylene C extends this approach across a wider frequency range and in particular lower THz frequency range that is interesting to spectroscopic applications.

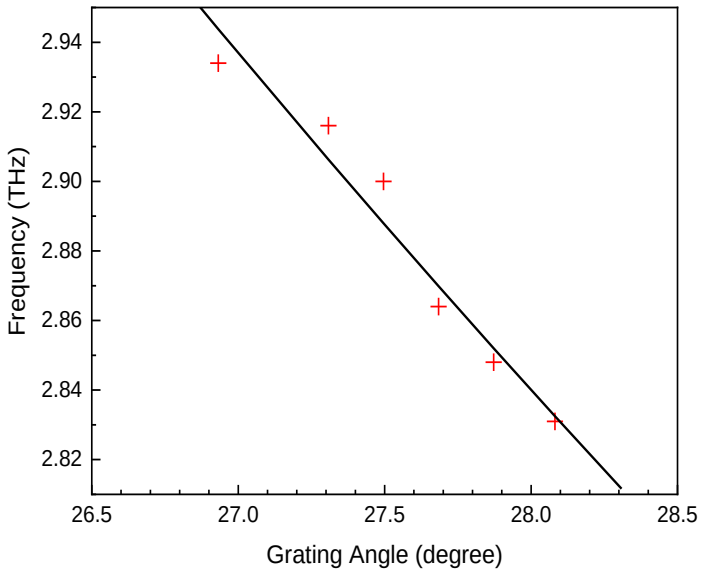

Figure 2.35 External cavity laser emission frequency as a function of the grating angle. Red crosses represent the recorded measurement results and the black line the theoretical calculation.

2.8 Conclusion

In this chapter, a self-mixing spectroscopy setup has been demonstrated using a THz QCA. Several key elements (light source, gas and data acquisition method) of the setup are discussed and an exemplar experiment is performed to demonstrate the effectiveness of this approach. A potential approach for broadband spectroscopy has been proposed as well.

The self-mixing spectroscopy system is based on an external cavity THz QCL, which consists of a THz QCA and an external feedback element. In this work, an AR coated Si lens is attached to one facet of a THz QCL to make it an amplifier.

The active region design for the amplifier to be used for the setup is then decided by considering whether it has a clear Stark-shift for tuning the frequency through changing the bias. The final choice of the active region design is a bound-to-continuum design with a central transition frequency around 2.3 THz. The simulated transition frequency of it shows a clear Stark-shift. Two THz QCLs are fabricated from two different wafers with this active region design. Their emission frequencies are 2.247 THz and 2.352 THz, respectively.

The 2.247 THz laser is first tested and features a strong water absorption line when the bias current is around 0.8 A, which is confirmed by the absorption line simulation with data from JPL database. Therefore, this QCL is not suitable for gas spectroscopy

experiments. Around 2.352 THz, the simulated absorption spectra present no strong water absorption lines but many methanol absorption lines. As a result, this THz QCL has been chosen as the final light source.

The 2.352 THz QCL is made into a QCA, which forms an external cavity THz QCL with a gas cell in the optical path of the external cavity. The self-mixing signal (voltage perturbation) is recorded with a differential signal method, which is comparable to the power signal taken at the same time with a Golay cell. It shows that the voltage perturbation is proportional to the methanol pressure.

Finally, a proposal for broadband gas spectroscopy with a THz QCA is suggested. Two approaches to achieving a broadband QCA, broadband AR coating/structure (the thin film structure and the inverted photonic structure) and two AR coated lenses, have been discussed as well. The two-lenses approach has demonstrated about 80 GHz bandwidth, which is promising for broadband spectroscopy applications. An external cavity THz QCL with a broadband QCA and a grating as frequency tuning element is then demonstrated, which gives about 103 GHz frequency shift with a 1.1-degree grating angle change.

The work in this chapter has demonstrated the potential of using a THz QCA for gas spectroscopy with the self-mixing detection method. Compared with using a THz QCL, this approach can give higher sensitivity as the QCA is more sensitive to the external feedback change. The self-mixing detection offers a fast response and the possibility of a more compact spectroscopy system. It also removes the need of a THz detector and has a potential for broadband gas spectroscopy applications.

Chapter 3
Amplitude stabilization of a THz QCL with graphene loaded metamaterial

In this chapter, an all-electronic approach to actively stabilising the output power of a THz QCL is demonstrated, using a graphene loaded metamaterial device. This configuration can be used to generate a stable THz signal or one with a designed waveform. To demonstrate the effectiveness of this approach, a THz modulator based on graphene and metamaterials is designed and fabricated. The theory of modulation, design procedures, including finite element software simulation, and fabrication process of the metamaterial device are also discussed. A series of experiments are then designed and implemented to confirm the results of both theory and simulation.

3.1 Motivation and state of art

THz QCLs are widely used solid-state sources for astronomical applications [196], imaging [162], and spectroscopy [197] because of their high output power [46] and narrow spectral linewidth [167]. A THz source with a stable output power is needed for many applications. During astronomical observations, long integration times are required to achieve a suitable SNR, which requires the amplitude of the light source to be kept stable within the integration time [198]. For imaging, it is also important to have a stabilised THz source for conducting accurate quantitative measurements of a sample. In QCL-assisted spectroscopic applications [199], active amplitude stabilization is also required, e.g., when monitoring the presence/concentration of noxious or greenhouse gases with high precision. Additionally, THz wireless communication is a promising application of THz sources; there have already been successful demonstrations of high bit rate sub-THz communications [125], [200]. In many protocols for communication applications, precise control of the laser intensity is required, thus aiding the reduction in bit error rate.

However, there are many factors that introduce fluctuations into the THz QCL output power. Firstly, it is sensitive to bias voltage instability and temperature fluctuations [201], which are intrinsically present in the measurement setups used to

operate the laser [202]. In addition, light propagating through an external unpurged atmosphere suffers from extra power fluctuations due to strong THz absorption [203]. Furthermore, frequency instabilities will lead to power fluctuations as well: both quantum limited frequency fluctuations [167] because of intrinsic line broadening and mode-hopping due to changing operating conditions. Therefore, it is of great importance to realise an active stabilization of the output laser power.

Significant work has been done to stabilise the QCL frequency. With mode-locking, the frequency fluctuations can be reduced below 1 kHz [167] and with active bias current control the frequency stability has been improved from 15 MHz to 300 kHz [204].

To date, amplitude stabilisation of the THz QCL has concentrated on passive control of the operating conditions of the QCL through precise control of the cryostat's temperature and using a stable power source. An alternative active approach is compensating the fluctuation through active amplitude modulation, which can be done by active control of the transmission through an external element. In reference [202], a swing arm attenuator (voice coil), the transmission of which can be tuned by changing the bias voltage, is used to modulate the output power of a THz QCL, as shown in Figure 3.1 (a). A proportional-integral-derivative (PID) control loop is then used to keep the laser output power stable: when the power measured on the hot electron bolometer mixer (the DC current of the mixer) increases, the attenuation of the voice coil will be increased and vice versa. The power transmitted through the attenuator in two laser working modes (free running and amplitude stabilised) are shown in Figure 3.1 (b). With amplitude stabilisation, the power oscillation reduces by about 60%.

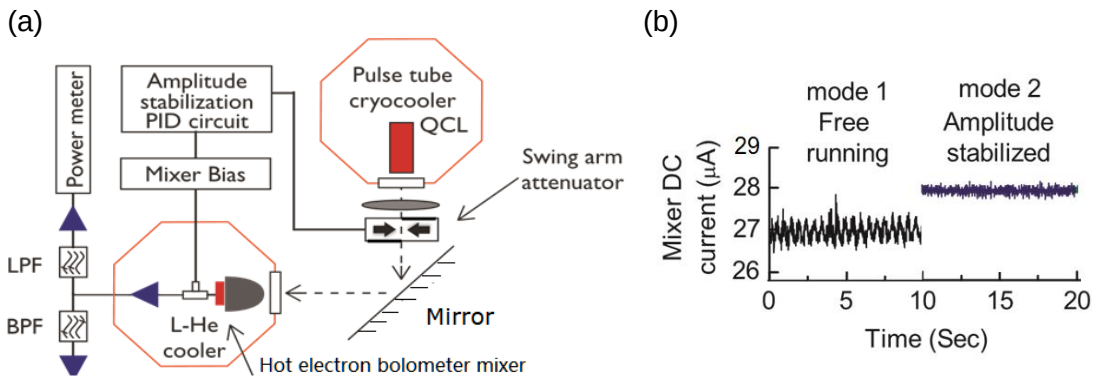

Figure 3.1 (a) Schematic of a set-up for amplitude stabilization; (b) The signal of the detector when the laser is free running and with PID control. adapted from [202], with the permission of AIP Publishing.

The approach used in this work, in order to make the system more compact, is to replace the voice coil with a graphene loaded metamaterial modulator. The transmission of the modulator can be tuned by changing the bias voltage applied on the graphene. A PID control loop is used to adjust the bias in response to the transmitted laser power.

3.2 Graphene loaded metamaterial as a THz amplitude modulator

To achieve amplitude stabilization, an active amplitude modulator is typically employed, and graphene loaded metamaterial arrays provide an extremely promising solution, particularly in terms of modulation depth, speed [205] and ease of implementation [91]. Metamaterials provide strong confinement of the EM radiation at a designed frequency [92], primarily determined by the shape and size of the resonant unit, rather than its material composition, and are normally engineered as metallic features on a dielectric substrate. The electrical conductivity of graphene can be significantly tuned by modifying the carrier concentration [206]. The combination of these concepts is the key to achieving efficient tunable reflectivity/transmittivity within a certain frequency range. To date, many THz modulators have been developed based on graphene loaded metamaterials [207] with different resonator structures, among which the split-ring resonator (SRR), with a schematic geometry shown in Figure 3.2 (a), has proved to be suitable for amplitude modulation purposes. Compared to the conventional dipole antenna structure, the SRR has a sharper resonance, which is essential for achieving a high modulation depth.

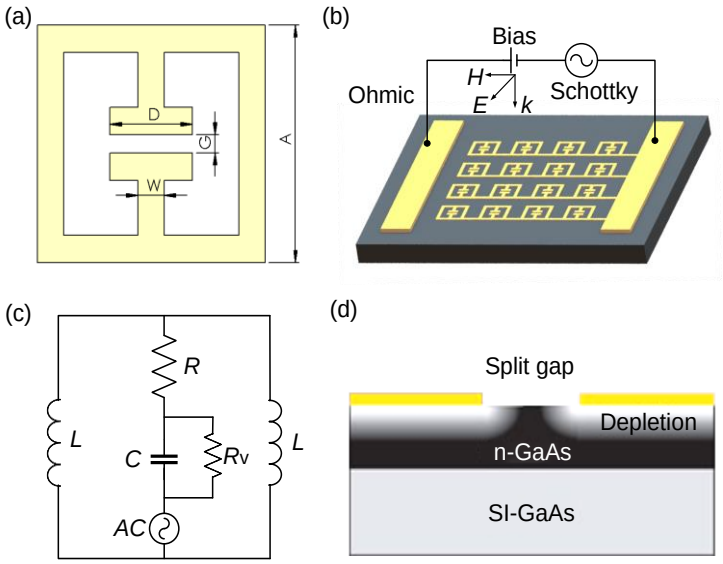

Figure 3.2 SRR based THz modulator by Chen et al.: (a) single SRR element; (b) bias configuration; (c) an equivalent circuit model; (d) cross sectional diagram showing the current density in depletion region and substrate near the split gap. Adapted with permission from [92] © 2006, Springer Nature.

The SRR elements were first proposed for negative permittivity metamaterials [208]. The same year saw the fabrication of an SRR array on a semiconductor substrate for modulating THz radiation [92]. In this device, the SRR array and the substrate form a Schottky diode, as shown in Figure 3.2 (b). The current density and thus conductivity of the substrate at the gap can be tuned by varying the bias between the Schottky and Ohmic contacts. An equivalent circuit model (shown in Figure 3.2 (c)) is built to study the electric properties of the device, with *L* being the inductance of one sub ring, *R* being the Ohmic loss of the SRR, *C* being the capacitance and R_V being the dissipation loss due to the substrate free carrier absorption within the split gap. The total impedance of this inductor-resistor-capacitor (LRC) circuit is

$$Z(f) = R + i\pi fL + \frac{1}{i2\pi fC + \frac{1}{R_V}} \quad . \tag{3.1}$$

At resonance, the reactance of the circuit is zero, which means the imaginary part of *Z* is zero ($Im(Z(f_R)) = 0$). From this condition, the resonance frequency can be calculated as

$$f_R = \frac{1}{2\pi}\sqrt{\frac{2}{LC} - \frac{1}{(CR_V)^2}} \quad . \tag{3.2}$$

As can be seen from equation (3.2), when varying the bias, the value of R_V and *C*, which are determined by the current density of the substrate within the split gap, will change, thus altering the resonant frequency. The Q factor of the circuit, which determines the resonance strength, can be solved as

$$Q = \pi f_R \left(\frac{L}{R + \left(\frac{R_V}{1 + 2CR_V^2 / L} \right)} \right). \tag{3.3}$$

Increasing the bias will increase the depletion in the substrate, giving a larger *R* and *C*, which will increase the Q factor and vice versa. Therefore, active modulation of the amplitude can be achieved through this approach. An alternative of using a Schottky diode is to use a layer of graphene to tune the capacitance and resistance within the split gap area. Graphene loaded SRRs operating with ultra-low bias have been demonstrated [209], [210], and 100% modulation depths have been achieved by combining an active metamaterial with a THz QCL [97]. In this thesis, an SRR device based on this approach is designed to operate at 2.85 THz (the frequency of the laser that will be used) and fabricated.

3.2.1 Structure and geometry

The device used in this work is based on the SRR modulator reported in reference [97]. Figure 3.3 (a) and (d) give the geometry and corresponding geometrical parameters of an SRR element, respectively. It follows the same design from Chen's work [92] but with different geometrical ratios, making sure that there are no too small features on the device so that it is easy to be fabricated. The device adopts a back-gate scheme, as shown in Figure 3.3 (b). The substrate is p-doped silicon with a layer (300 nm) of thermal oxide (SiO_2) on top. A monolayer of graphene is transferred onto the oxide [211] and then a 100 nm layer of dielectric (Al_2O_3) is applied on it to protect the graphene. The SRR features are then thermally evaporated onto this dielectric layer. Two big electrodes are evaporated on the sides of the device so that the graphene can be back-gated by applying a bias between the p-doped silicon substrate and these electrodes. Figure 3.3 (c) shows the scanning electron microscopy (SEM) micrograph of one finished device.

(a)

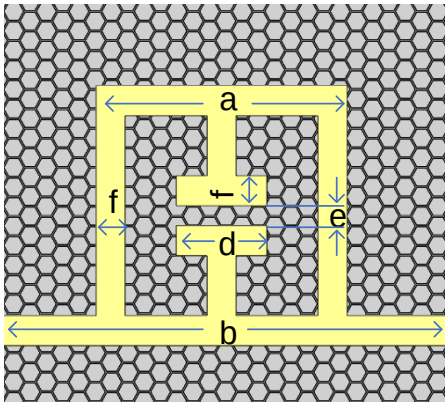

(b)

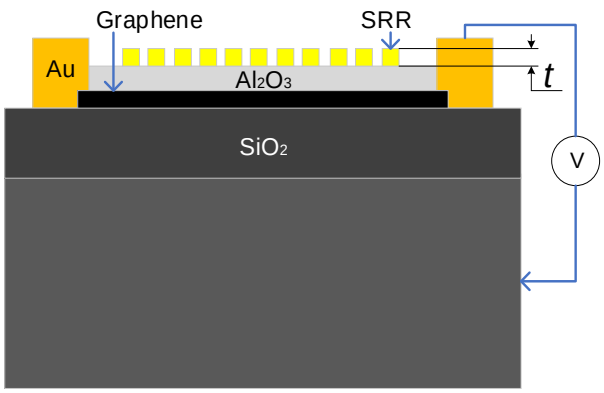

(c)

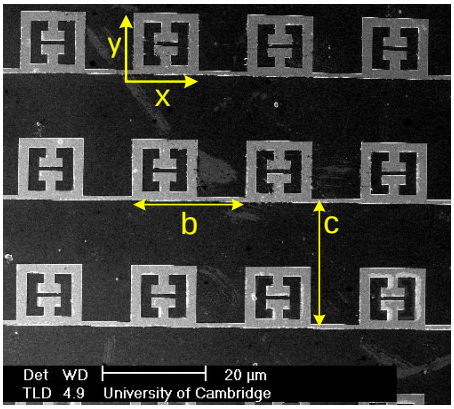

(d)

Name	Expression	Description
a	Variable	SRR length
b	$1.75 \cdot a$	SRR pitch in x direction
c	$2 \cdot a$	SRR pitch in y direction
d	$0.36 \cdot a$	SRR plate width
e	0.8 µm	SRR capacitive gap
f	2 µm	SRR metal width
t	100 nm	SRR thickness
X	3 mm	Active area device width $\vec{x}$
Y	3 mm	Active area device length $\vec{y}$

Figure 3.3 (a) Schematic of the geometric parameters of a single SRR; (b) cross sectional representation of the fabricated device illustrating the back-gating biasing scheme; (c) SEM picture of the SRR device; (d) list of the SRR parameters.

3.2.2 COMSOL Simulation

To get the right dimensions for the SRR unit cell, a finite-element simulation is completed using COMSOL Multiphysics. Figure 3.4 shows the unit cell of the SRR used in the simulation and the radiofrequency (RF) module is used to study the frequency response. The model in the simulation is built to analyse the response of the device to an incoming plane wave with wavevector $\vec{k}$ and electric field $\vec{E}$. The governing equation is the electric wave equation in frequency domain

$$\nabla \times \mu_r^{-1}\left(\nabla \times \mathbf{E}(\mathbf{r})\right) - k_0^2\left(\varepsilon_{\mathrm{r}} - \frac{i\sigma}{2\pi f \varepsilon_0}\right)\mathbf{E}(\mathbf{r}) = \mathbf{0} \ . \tag{3.4}$$

Here ε_0 is the vacuum permittivity; μ_{r}, ε_{r} and σ are the relative permeability, the relative permittivity, and the conductivity of the material; f is the frequency. The detailed material parameters used in the simulation are listed in Table 3.1. The permittivity for the p-doped Si is determined by the Drude free-carrier expression for semiconductor materials as given by the following equation [212]

$$\varepsilon_{\mathrm{r,Si}}(f) = \varepsilon_{\infty,\mathrm{Si}} - \frac{ne^2}{\varepsilon_0 m\pi(f^2 + if\tau^{-1})} \tag{3.5}$$

$\varepsilon_{\infty,\mathrm{Si}}$ is the high frequency relative permittivity. n is the free charge carrier density. e is the elementary charge. ε_0 is the free space permittivity. f is the frequency of the electromagnetic radiation, and m is the effective charge carrier mass and τ the average lifetime of the carrier. Its conductivity can also be described with the Drude model as

$$\sigma_{\mathrm{Si}}(f) = \frac{\sigma_{\mathrm{Si,DC}}}{1 - i2\pi f \tau_{\mathrm{Si}}} \ ; \tag{3.6}$$

$\sigma_{\mathrm{Si,DC}}$ is taken from the resistivity of the Si substrate ($100\,\Omega{\cdot}cm$). Correspondingly, $n = 1.3\times10^{14}\ cm^{-3}$ and $\tau = 10\,ps$ .The conductivity $\sigma(f)$ and permittivity $\varepsilon_{\mathrm{r}}(f)$ of Au/graphene can also be calculated with the Drude model. For Au, they can be calculated through the following equations:

$$\sigma_{\mathrm{Au}}(f) = \frac{\sigma_{\mathrm{Au,DC}}}{1 - i2\pi f \tau_{\mathrm{Au}}} \ ; \tag{3.7}$$

$$\varepsilon_{\mathrm{r,Au}}(f) = 1 + \frac{i\sigma_{\mathrm{Au}}(f)}{2\pi\varepsilon_0 f} \ . \tag{3.8}$$

The DC conductivity of Au $\sigma_{\mathrm{Au,DC}}$ is taken as 4.4×10^7 S/m and the scattering time τ_{Au} is taken to be 2.3×10^{-13} s [213], [214]. The Drude model permittivity for the graphene is taken as

$$\varepsilon_{r,G}(V_G, f) = 1 - \frac{i\sigma^S_{G,AC}(V_G, f)}{2\pi f \varepsilon_0 \Delta_G}, \tag{3.9}$$

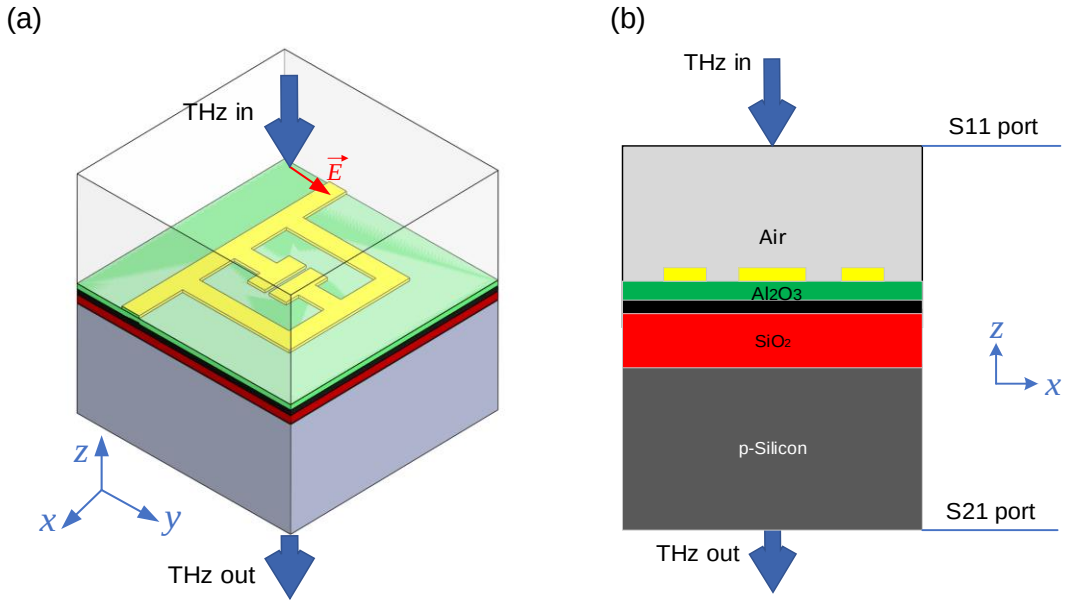

Figure 3.4 A unit cell of the SRR device in COMSOL simulation: (a) orthonormal view; (b) view of the cross-section in the middle of the capacitive gap. The THz light enters the cell perpendicularly through a port, with a polarization perpendicular to the gap. The reflection (S11) and transmission (S21) coefficients can be obtained through the boundary conditions of S11 and S21 port, respectively.

where Δ_G is the simulated thickness of the graphene layer. It is the factor that allows a bulk property like permittivity to be defined for a two dimensional system such as graphene by scaling the sheet conductivity [89]. $\sigma^S_{G,AC}(V_G, f)$ is the complex sheet conductivity given by

$$\sigma^S_{G,AC}(V_G, f) = \frac{\sigma^S_{G,DC}(V_G)}{1 + i2\pi f \tau_G} \tag{3.10}$$

where $\sigma^S_{G,DC}$ is the DC sheet conductivity of the graphene, V_G is the applied bias, τ_G is the average scattering time.

Table 3.1 Material parameters used in the COMSOL simulation

Material	**Air**	**Au**		**Si**	**Graphene**	Al_2O_3
μ_r	1	1	1	1	1	1
ε_r	1	$\varepsilon_{r,Au}(f)$	3.9 [215]	$\varepsilon_{r,Si}(f)$	$\varepsilon_{r,G}(V_G, f)$	9.1 [97]
σ	0	$\sigma_{Au}(f)$	0	$\sigma_{Si}(f)$	$\sigma^S_{G,AC}(V_G, f)/\Delta_G$	0

In the simulation, the THz wave enters the unit cell via an electromagnetic port boundary on the upper z surface (S11 port) with a linearly polarized electric field either in the x or y direction. The wave vector of this port is perpendicular to the SRR surface (in the z direction). The wave vector should remain in the same direction when passing through the device and arriving at port S21. Because of the periodic nature of the device, it is sufficient to just simulate one unit-cell and apply appropriate periodic boundary conditions: the Floquet boundary condition. For the Si substrate and air area, because the device structure is symmetric in both directions, periodical boundary conditions can be applied in both directions (x and y). For the SiO_2, Au, Graphene and Al_2O_3 layers, as they are very thin, the loss due to wave vector mismatch is negligible, the same periodic boundary conditions can be applied on them as well. Finally, perfectly matched layers are added next to both ports (S11 and S12) to avoid back-reflection.

The transmission spectrum of the device is obtained through the S_{21} parameter, which is the scattering parameter at port 2 from port 1. The transmitted power is

$$P_t = |S_{21}|^2 \tag{3.11}$$

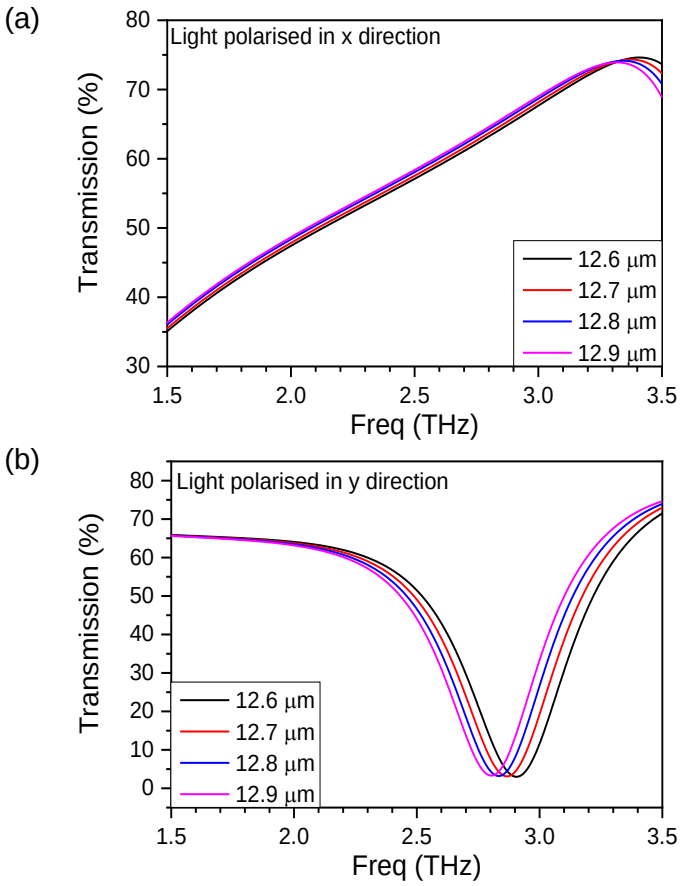

Figure 3.5 Transmission spectrum of the SRR device of different sizes from COMSOL simulation with no graphene on the sample and the polarisation of light in: (a) x direction; (b) y direction.

A parametric sweep of the nominal size *a* (12.6 µm, 12.7 µm, 12.8 µm and 12.9 µm) of the SRR is first done to get the resonance frequencies of four different sized devices. In this simulation, the graphene is not added into the model to get the response of a static device. Figure 3.5 shows the transmission spectrum when the polarization of light is in: (a) x direction; (b) y direction. There is no resonance within the frequency range simulated when the light polarization is in the x direction while a strong resonance can be seen around 2.8 THz for all the devices when the light polarization is in the y direction. This also confirms that the chosen nominal sizes are approximately correct for devices designed to work around 2.85 THz.

Final device chips use all 4 different sizes to increase the usability of the fabrication as there is usually a small mismatch on the resonance frequencies between simulated and fabricated devices. From equation (3.2), it can be seen that, when increasing *a*, the inductance *L* will increase, which results in a lower resonance frequency, as confirmed by the simulation. When the nominal size is increased from 12.6 µm to 12.9 µm, the resonant frequency decreases from 2.91 THz to 2.8 THz.

To study the modulation of transmission with changing the graphene conductivity, a parametric sweep of the graphene conductivity varying from 0.3 mS to 0.6 mS is done. These numbers are taken from sheet conductivity measurements of the graphene layer which undergoes the same fabrication steps with the graphene used on the sample and gate voltage from 10V to 40 V. Figure 3.6 gives the simulated transmission spectra of the 12.8 µm device at different graphene conductivities. When increasing the sheet conductivity from 0.3 mS to 0.6 mS, the transmission increases by 7% (from 21.5 % to 28.5%) and a modulation depth of 32.56% can be obtained. Meanwhile, the resonant frequency shifts by 30 GHz.

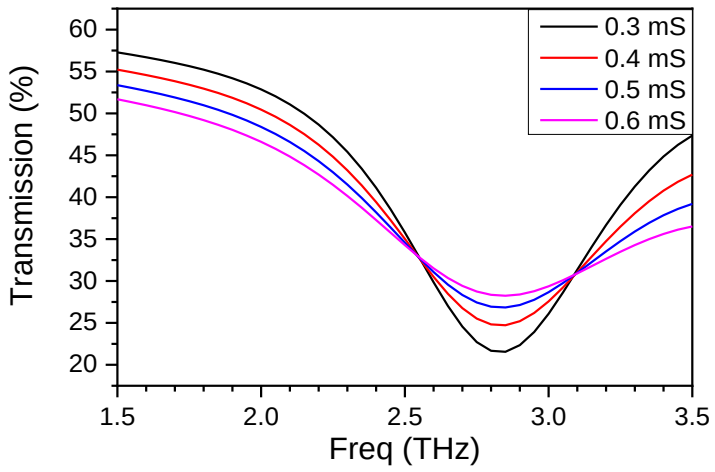

Figure 3.6 Transmission spectra of the SRR device from COMSOL simulation with graphene conductivity varying from 0.3 mS to 0.6 mS and the light polarization in *y* direction.

3.2.3 Fabrication of the modulator

The fabrication of the device takes 16 steps, as shown in Figure 3.7. A 525 ± 25 μm thick, Boron doped p-Si substrate with a 300 nm thermal oxide (SiO_2) is first cleaved into small chips measuring 10 mm×10 mm and large area monolayer chemical vapour deposition (CVD) graphene [211] is transferred onto the SiO_2 layer.

The first step is to fabricate a reliable back contact for back-gating. The chip is put into a thermal evaporator upside down with graphene being covered by a layer of photo resist for protection. A layer of 10/90 nm Ti/Au is then evaporated onto the back surface of the chip.

The next stage is to define the graphene pattern. The graphene layer is spin coated with a layer of Shipley 1805 positive photoresist at 5000 rpm for 60 s followed by a soft bake at 90 °C for 60 s. This is followed by define an array of four 3 mm×3 mm squares, by photolithography using a dosage of around 150 mJ/cm^2 with a 436 nm wavelength. For this sample, large area graphene is used and no alignment mask for graphene is needed. However, a rough alignment of the graphene pattern relative to the chip edges is performed to make sure that the pattern is in the centre of the chip surface. The sample is developed in MF319 for 90 s afterwards to remove the photoresist at the area exposed and then exposed to two 45 s rounds of low power (<100 W) microwave induced oxygen plasma to remove the graphene that is not covered by photoresist. To remove the residual of photoresist, the sample is cleaned in acetone, then isopropyl alcohol (IPA) and dried with N_2 gas.

After the graphene pattern is defined, the source and drain electrodes for biasing the graphene need to be evaporated on top of the graphene. This follows the similar procedure with defining the graphene pattern: spinning coating the sample with a layer of Shipley 1813 positive photoresist at 5000 rpm for 60 s followed by a soft bake at 90 °C for 60 s; over-exposing the sample with the photolithographic pattern for the source/drain electrodes at a dosage of around 300 mJ/cm^2 with a 436 nm wavelength; a 120 s immersion of the sample in chlorobenzene for an undercut profile to ease the lift-off; developing the sample in MF319 for 120 s; thermally evaporating a layer of 10/80 nm (nominal values) Ti/Au; leaving the sample in acetone for 24 hours; lift off, cleaning and drying. In this stage, a set of alignment marks for aligning subsequent steps are evaporated on the sample as well.

The graphene layer is then encapsulated by a 100 nm layer of Al_2O_3 deposited via atomic layer deposition (ALD). The stop-flow mode ALD technique is used to uniformly deposit an encapsulation layer on the graphene which is continuous and pin-hole free, resulting in a high graphene mobility. This layer also passivates the graphene,

inhibiting any Dirac point drift to higher voltages when exposed to the ambient environment.

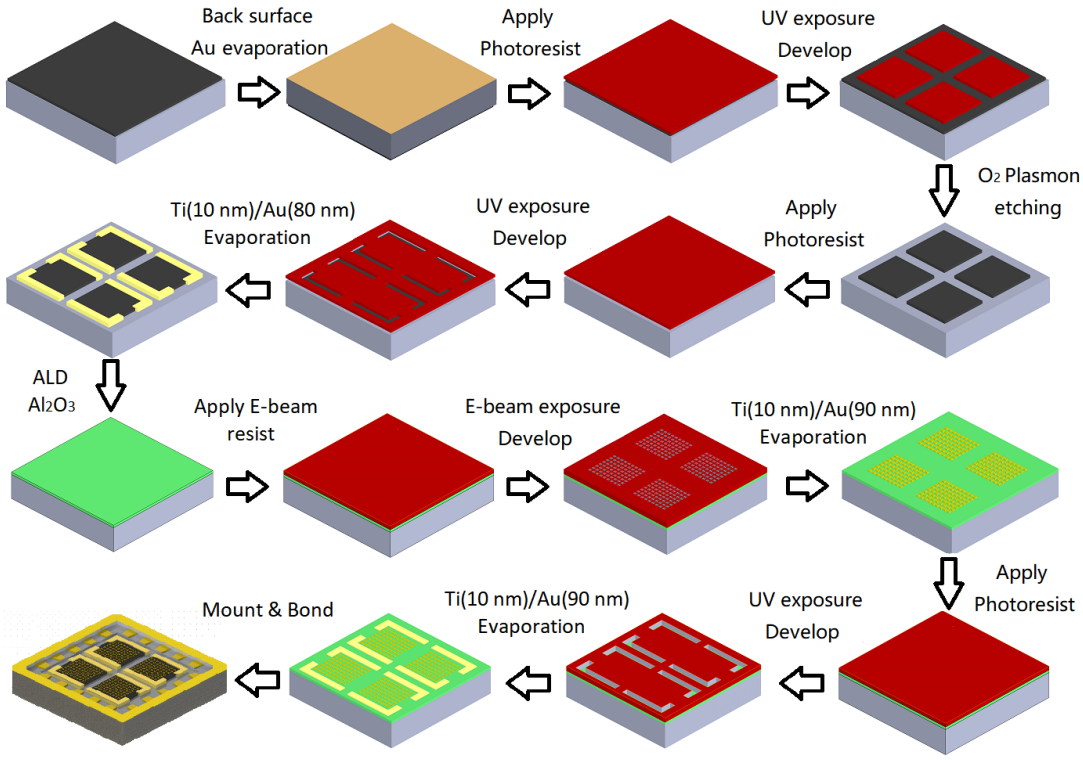

Figure 3.7 Fabrication procedures of a graphene loaded SRR device

The SRR pattern is then evaporated on top of the ALD layer. As the features are very small, electron beam (E-beam) lithography is used here. Two layers of positive polymethyl methacrylate (PMMA) E-beam resist are spin coated on the sample. The resist used and corresponding spin coating parameters are listed in Table 3.2. The sample is then aligned with the alignment masks defined before and exposed with an electron beam. Afterwards, it is developed in IPA: MIBK: MEK at a ratio of 15:5:1 for 6 seconds and then cleaned with IPA. A layer of 10/80 nm Ti/Au is then thermally evaporated onto the sample, which is followed by 24 hours' immersion in acetone for lift-off.

At this stage, the source and drain electrodes are covered by the ALD layer. To get access to the electrodes, a further lithographic step is required in order to open apertures in the dielectric film and wire-bond the source and drain electrodes. After the exposure, the sample is put into MF319 for a long time to remove the oxide layer on top of the electrode as the developer can also etch oxide. Another thermal evaporation of 10/90 nm Ti/Au is done to provide more metal for Au wire bonding.

Table 3.2 Spin coating parameters for E-beam resists

E-beam resist	Spin speed (rpm)	Spin time (s)	Baking temperature (°C)	Baking time (min)
495k PMMA (A7 neat)	4000	60	180	10
950k PMMA (A11 1:5 MIBK)	4000	60	180	10

Finally, the chip is cleaved into four parts and each part is mounted onto a chip carrier, which has a hole in the centre for transmission measurement of the sample. Au wires are then used to bond the electrodes to the carrier for electrical connection.

3.2.4 Characterization of the modulator

The device used in the final setup is the SRR with the nominal size *a* being 12.8 μm and is fabricated by my colleague Stephen Kindness. The 12.8 μm device is chosen as its measured resonant frequency is closest to the QCL frequency. All the results below are measured on this device. The sheet resistance of the graphene layer is first measured by applying a voltage between the source and drain electrodes to check whether the metal contact and the electric connection work. Two Model 2400 Keithley source/measure units (SMUs) are used with the first one sourcing a constant current between source and drain and the second one sweeping a DC voltage applied between the p-doped Si substrate and graphene contacts. The voltage required to provide this constant current between source and drain is then measured, thus the resistance can be determined.

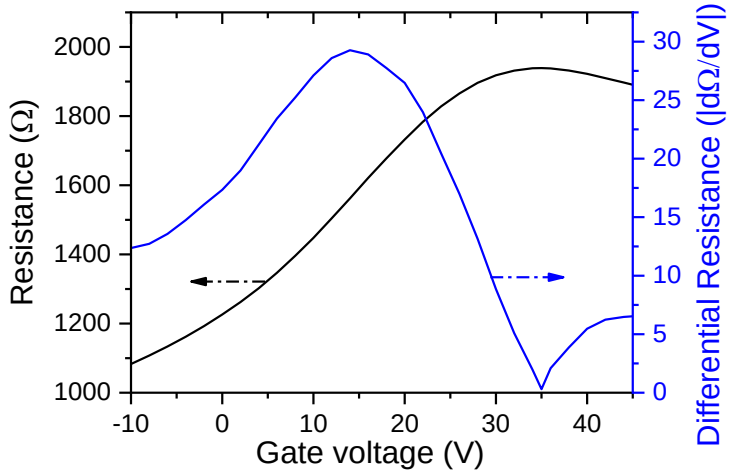

Figure 3.8 Electrical characterization of the graphene used for the SRR device: the sheet resistance (black line) and the absolute value of the differential resistance (blue line).

Figure 3.8 shows the resistance and calculated differential resistance at different back-gate voltages. The graphene sheet conductivity range is then determined to be $0.3-1.1\,\mathrm{mS}$, giving a reference for the conductivity values used for COMSOL simulations. The Dirac point, the back-gate voltage of minimum graphene carrier concentration and thus zero differential resistance, of the device is 35 V.

Once confirmed that the electric connection is working and the sheet conductivity of graphene can be tuned within a usable range, a THz time-domain spectroscopic (THz-TDS) system (Menlosystems, model K-15) is used to get the transmission spectra of the device when the back-gate voltage is changed from 0 V to 30 V. The spectra are displayed in Figure 3.9 and show a resonance around 2.8 THz, which is 50 GHz lower than the COMSOL simulation results. Considering some parameters in the simulation have been simplified, it is expected to see a slight mismatch between the simulation and measurement results. The transmission is reduced by 6.25% (from 31.65% to 25.4%) when the back-gate voltage is increased from 0 V to 30 V at 2.85 THz, which gives a modulation depth of 24.6%.

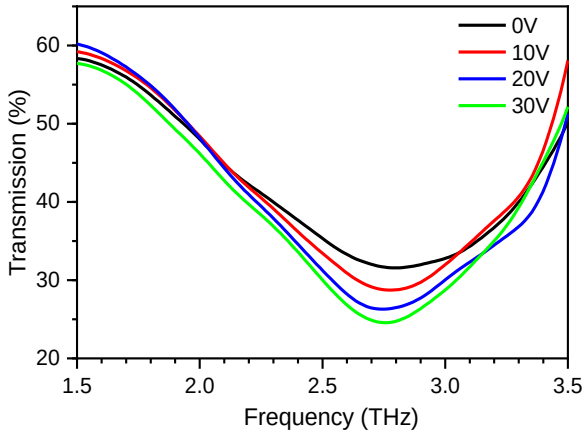

Figure 3.9 Transmission spectra of the SRR device at four different voltages measured with a THz-TDS system.

3.3 Experimental configuration: transmission

To actively control or stabilise the output power of a THz QCL, a PID control loop can be used with two possible optical path configurations: transmission or external cavity. The transmission configuration is not sensitive to alignment, thus very stable, which is a desirable feature for stabilization purposes. As a result, the transmission configuration is first utilised in this work. The disadvantage of using this configuration is that the modulation depth will not be as high as in an external cavity setup, where the

modulation effect will be amplified by the Fabry–Pérot cavity and can be as high as 100% [228]. The external cavity configuration will be discussed in Section 3.6.

3.3.1 Configuration

In the transmission configuration, as shown in Figure 3.10, the output power of the QCL passing through the SRR device is modulated. To avoid the formation of an external cavity, the parabolic mirror is aligned so that the reflection from the SRR device will not go back to the laser cavity. Therefore, the operation of the SRR device will not intervene in the operation of the QCL.

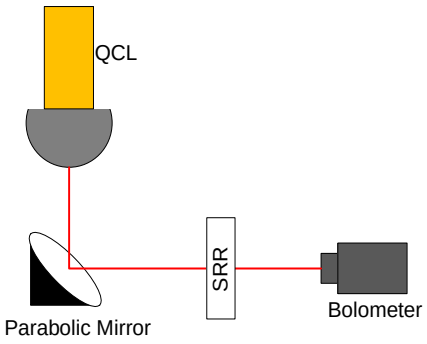

Figure 3.10 Transmission configuration for amplitude stabilization

3.3.2 Laser source

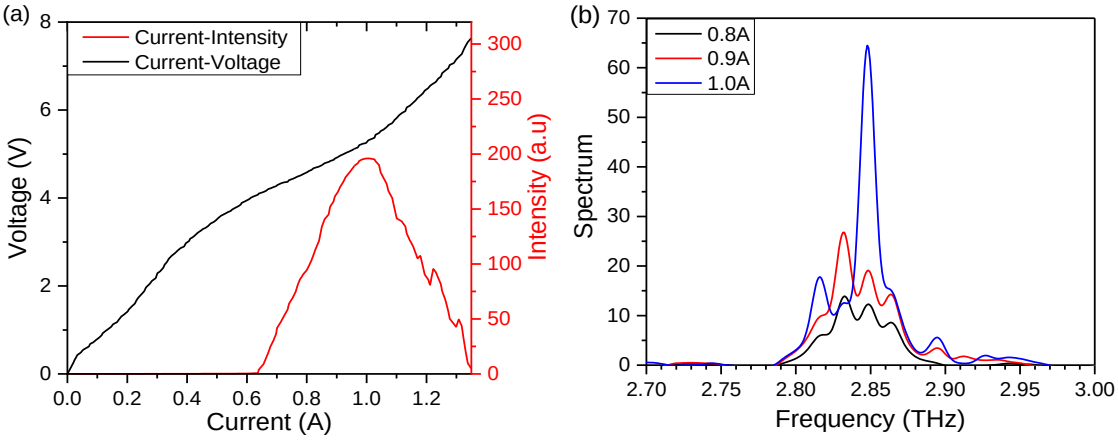

Figure 3.11 (a) LIV response and (b) spectra of the THz QCL at different bias currents

The light source is a 2.85 THz single-plasmon QCL (QCL-G in Appendix A) with a bound-to-continuum active region design [182]. It is mounted onto a cold finger in a continuous flow He cryostat, the temperature of which is held at 5 K with an average observed fluctuation of +/-0.2 K. The laser is operated in pulsed mode with a repetition

rate of 10 kHz and a 5% duty cycle. The LIV of the laser is shown in Figure 3.11 (a). The output power of the laser reaches its maximum at 1.0 A, which is also the current at which the laser is operated during all the following measurements. The spectra of the laser output at different bias currents are shown in Figure 3.11 (b). It has a main emission peak at 2.85 THz when operating at 1.0 A. CW emission is compatible with this approach by modifying the experimental setup with an additional optical chopper.

3.3.3 Modulation depth

To test the effectiveness of the SRR device as an amplitude modulator, two sets of experiments are conducted: output power and output power modulation at different gate voltages. The same setup is used in both experiments and the schematics of it is displayed in Figure 3.12. The optical setup is the one shown in Figure 3.10. For the electronics part, a constant DC voltage $V_{G,DC}$ and a 1 kHz square wave pulse $V_{G,AC}$ are fed into a mixer (a sum amplifier). The output of the mixer is a square wave pulse with a DC offset and is applied onto the back-gate of the SRR device while the graphene on the device is grounded.

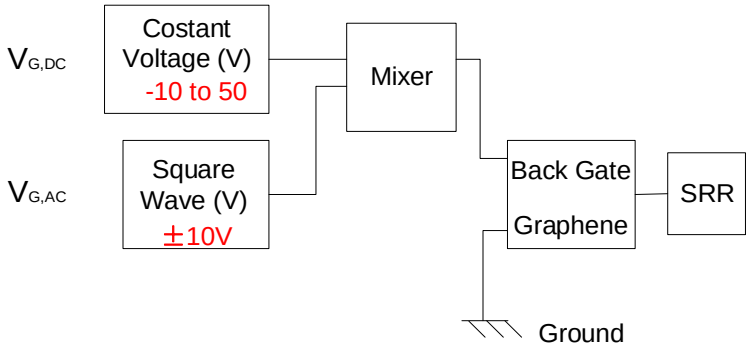

Figure 3.12 Electrical configurations of the experiments for measurement of absolute output power at different gate voltages and power modulation with a ± 10 V gate voltage change.

In the first experiment, the pulse generator is off ($V_{G,AC} = 0$), meaning that the back-gate voltage of the device is kept at a DC voltage, which is swept from -10 V to 50 V and the corresponding output power of the laser transmitted through the SRR device is recorded with a lock-in amplifier at 300 Hz (the gating frequency for the QCL bias). The black line in Figure 3.13 gives the power transmitted through the device at different gate voltages, which shows the opposite trend compared with the resistance curve in Figure 3.8 as lower resistance gives a high transmittance.

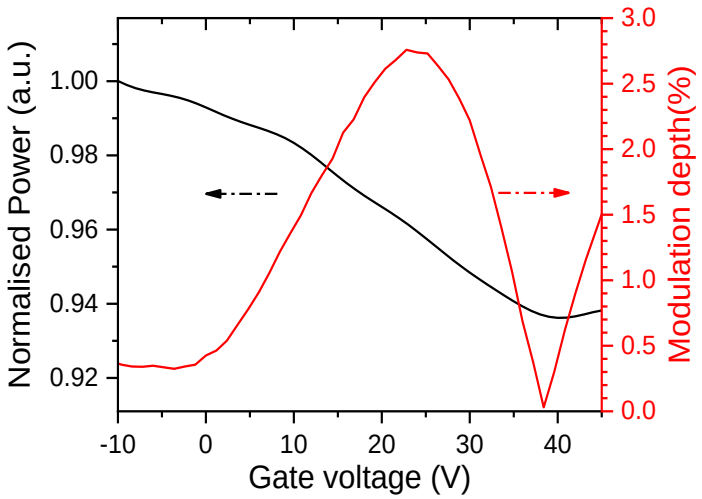

Figure 3.13 The output power (black line) transmitted through the SRR device and the modulation depth (red line) at different back-gate voltages.

The purpose of the second experiment is to find out at which offset $V_{G,DC}$ the highest power modulation can be achieved when the gate voltage is changed by ± 10 V. In this experiment, the amplitude of the square wave is set to be 10V ($V_{G,AC} = \pm 10V$). As a result, the output of the mixer is a 10 V square wave with a constant offset swept from -10 V to 50 V. The transmitted power through the SRR device is measured at the frequency of the square wave using a lock-in amplifier, which will only show the power change when the gate voltage is changed from $V_{G,AC}$+10 V to $V_{G,AC}$-10 V. The modulation depth is then calculated by dividing this power change with the absolute power at this gate voltage. As can be seen from the red line in Figure 3.13, when $V_{G,AC}$=23 V, the highest modulation (2.7%) can be reached. At the Dirac point, a 0% modulation is expected. This is seen at about 38.5 V, which is slightly higher compared with the number from the resistance measurement (35 V). This is suspected to be due to the hysteresis of the graphene charges, as observed for this type of device [216], and in agreement with previous measurements.

3.3.4 Experimental setup

Figure 3.14 (a) gives a 3D illustration of the setup while Figure 3.14 (b) shows a schematic of the electronic components implemented for the amplitude stabilization and control of the QCL. A 4 mm diameter uncoated high-resistivity hyper-hemispherical Si lens is attached onto the facet of the laser to collimate the beam and an off-axis parabolic mirror is then used to focus the collimated beam onto the hybrid graphene-SRR array. The output power of the laser after passing through the SRR device is collected with a liquid-He cooled Si-bolometer. The signal recorded by the bolometer is first extracted

by a lock-in amplifier at a reference frequency of 1 kHz, which is also the modulation frequency given to the QCL, and then sent to the PID controller. This generates a DC output when the signal from the bolometer deviates from a designated setpoint, which can be adjusted to determine the target power of the laser after transmission through the SRR device. The output voltage range of the PID controller is -10 V to 10 V. This DC output is applied on the back gate of the SRR device to control its transmission properties, thus compensating any changes in laser power.

(a)

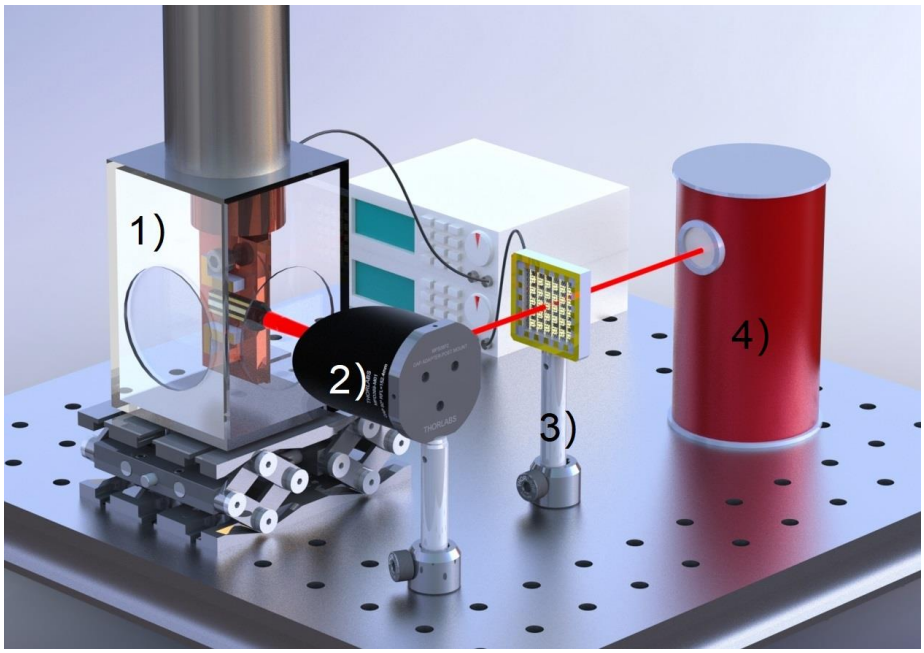

(b)

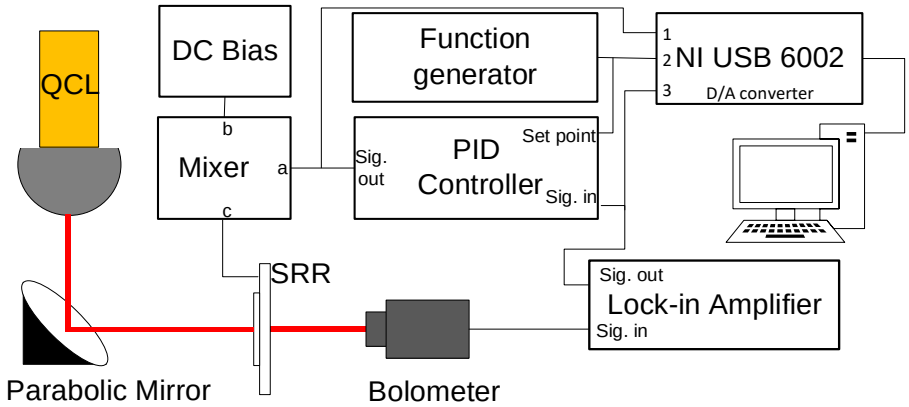

Figure 3.14 (a) Illustration and (b) schematic of the set-up for amplitude stabilization: 1) cryostat and QCL; 2) off-axis parabolic mirror; 3) SRR; 4) bolometer.

3.3.5 Detector

There are many THz detectors available to use and the Golay cell is one of the most commonly used detectors. It can work at room temperature and is a very compact device

though it can only work at very low frequencies (below 500 Hz, above which the signal to noise level is low). The bolometer is chosen here for its high S/N ratio and relatively high frequency response (up to 2 kHz), which are important features for an effective PID control. In principle it could be possible to use similar integrated devices [217], [218] as both detectors and modulators, removing the need for an external cryogenic detector and extending the PID control bandwidth. This will be discussed later in Section 6.2.2. However, in this first demonstration of amplitude stabilization a more conventional, higher responsivity cryogenic Si bolometer detector is used to allow an optimal experimental set-up.

3.3.6 PID control

A PID control loop is used to keep the transmitted power stable at the setpoint and a commercial PID controller (SIM 960 Analog PID Controller) from Stanford Research Systems is chosen due to its high bandwidth (100 kHz). It combines analog signal handling with digital control, which allows adjustment of the PID parameters and setpoint on the computer through an RS-232 interface. Additionally, the low-noise front end brings better performance to noise sensitive applications. Another useful feature is the up to 1000× settable gain, which removes the need for input preamplification. The output of the controller is a -10 V to 10 V voltage signal, which can be directly applied on the back-gate of graphene with a 20 V offset. This also eliminates the need for output signal amplification before sending the signal back to the close loop.

For a PID control loop, the choice of the PID parameters is important. A badly chosen parameter set will give a long response time or lead to oscillations (underdamped) of the controlled variable. Here, a square wave is applied on the setpoint and the PID parameters are tuned to give a quick response with no oscillations.

3.3.7 Data acquisition

In this work, three signals need to be recorded: the output power of the laser, the setpoint of the PID controller and the output voltage of the PID controller. To achieve high speed data transmission, the signals are acquired using a NI USB 6002 DAQ device with a maximum sampling rate of 50,000 samples per second and 8 analog input channels, before recorded on a computer through a LabVIEW program. As this is an NI product, it is also convenient to be integrated with the control panel for the PID controller in the same LabVIEW program.

3.4 Amplitude stabilization of a THz QCL

In this section, active amplitude stabilisation of a THz QCL with the SRR device and the system shown in Figure 3.14 will be discussed. The PID controller setpoint is fixed at a constant number, which determines the target output power of the QCL. This is performed to test the effectiveness of the SRR device in keeping the laser output power stable. During the measurement, the data acquisition rate of the programme is set to be 6000 sample/s.

3.4.1 Experimental results

Figure 3.15 summarises the key results of this measurement. In Figure 3.15, the top graph shows the time variation of the laser power transmitted through the SRR modulator. The bottom graph shows the corresponding PID controller output voltage. It can be seen that during the first 60 seconds, the PID controller is on, and the power is stabilised at around 10. At 60 seconds, the PID controller is switched off and the power starts oscillating. When the PID controller is switched on again at 153 seconds, the power returns to 10 and stabilises there.

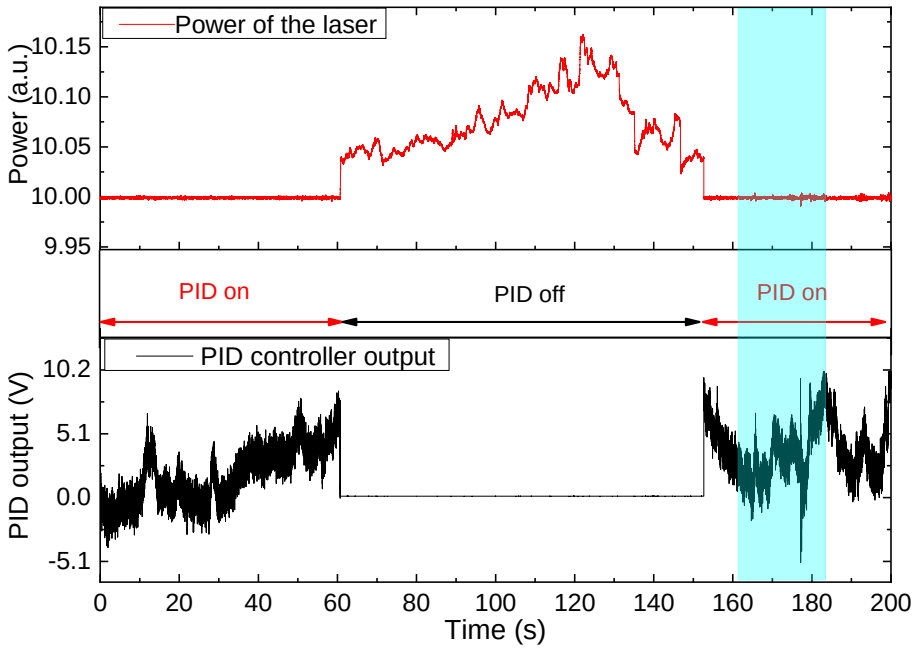

Figure 3.15 Power fluctuation of the laser (red) with the PID on (0 s to 60 s, 153 s to 200 s) and off (60 s to 153 s) and the corresponding output of the PID controller (black).

Several small spikes can be seen on the output power curve in Figure 3.15. To find out the reason for this, the figure is zoomed in within the blue-shadowed area and shown

in Figure 3.16. There are two such spikes within this time frame and they are labelled with blue shadows in the graph. As can be seen from the graphs, when there is a spike on the power curve, there is also a spike or an abrupt change on the PID controller output. This reveals that there might be some abrupt disturbances in the system, which introduce abrupt changes on the QCL output power. The response of the feedback loop is not fast enough to compensate the disruptions.

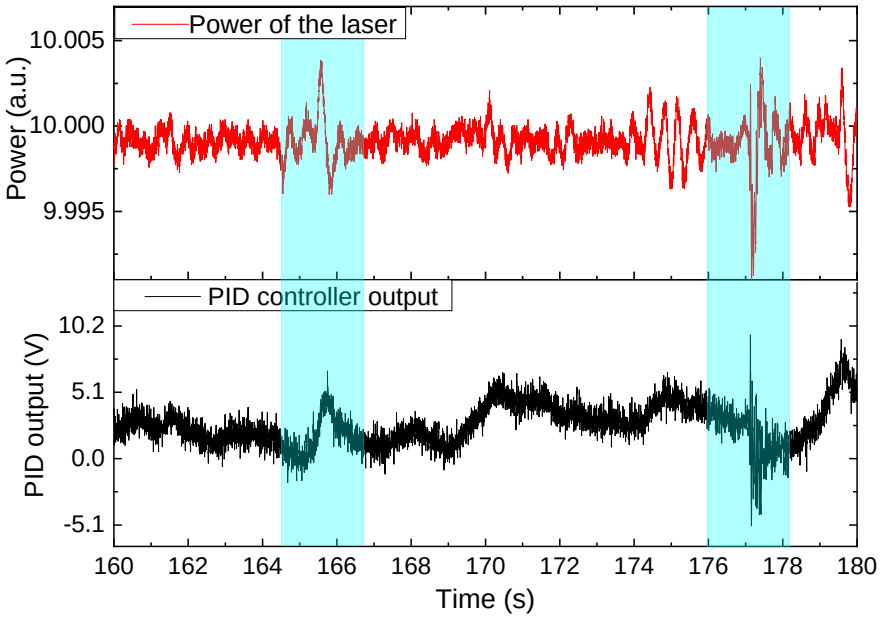

Figure 3.16 Power fluctuation of the laser (red) in the blue shaded area in Figure 3.15 and the corresponding output of the PID controller (black).

To characterize the stabilization, the QCL power is recorded in three different experimental configurations: (1) laser passing through the SRR modulator with PID (2) without PID control and (3) a free running laser (the SRR is not in the optical path). Figure 3.17 compares the stability of the power in the three aforementioned experimental conditions, which give peak-to-peak fluctuation magnitudes of 0.0043, 0.054, and 0.152, respectively. With the PID controlled SRR device switched on, the fluctuation of the QCL power is reduced from 1.52% to 0.043% of the total power, which is more than a 30-fold improvement with this non-optimized stabilisation approach. The PID control loop plus the modulator in the setup has a certain bandwidth, the high frequency fluctuations of the QCL power beyond which cannot be compensated, which is the main reason for the residual amplitude fluctuations [219].

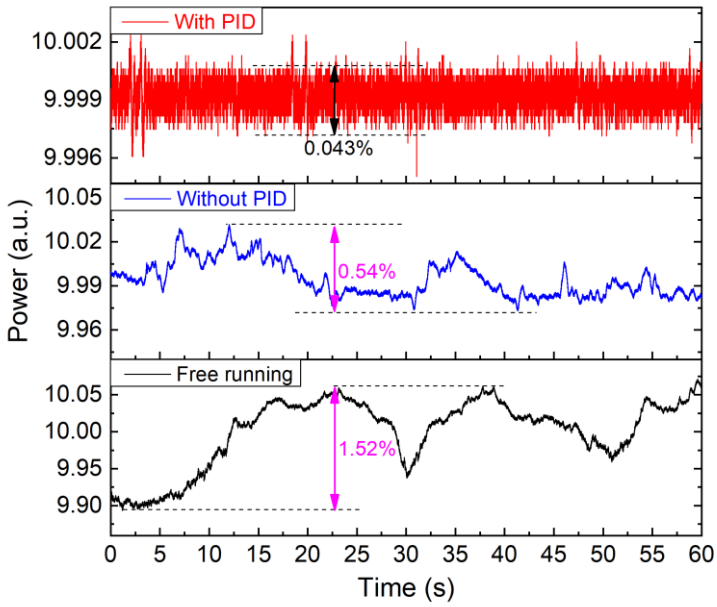

Figure 3.17 Output power fluctuation within 60 seconds of a QCL with the PID controlled SRR modulator (red), no PID control (blue), and free running (black). The power of the free running laser has been normalized to the same level as the other two traces for comparison.

3.4.2 Noise analysis in frequency domain

To analyse the noise property of the laser output power in the three different conditions in frequency domain, a fast Fourier transform (FFT) is performed for each output power waveform to get the frequency components of the noise. The sampling frequency and sampling time are 6000 Hz and 60 s, respectively. Therefore, the frequency bandwidth is 3000 Hz and the frequency resolution is 1/60 Hz. 0 Hz components are removed for all the waveforms to magnify the visibility of the components at the remaining frequencies. The noise levels show very different characteristics at low frequency range (<5 Hz), middle frequency range (from 5 Hz to 100 Hz) and high frequency range (≥100 Hz), thus they are analysed separately. The amplitudes of the frequency components are converted to the percentage of the average output power, which is labelled as P_{QCL}, in all the graphs for comparison.

In all three situations, noise is mainly distributed in the low frequency range, as shown in Figure 3.18 (amplitudes of the low frequency components are much higher than the high frequency ones). This indicates the existence of temporal drift in the system, the cause of which might be the oscillation of the optical bench, usually sub hertz.

For a free running laser and the laser system without PID control loop, the low frequency components have higher amplitudes (larger than 0.02% the amplitude of the average output power) compared to the PID controlled laser. When the PID control loop is used, the amplitudes of all the low frequency components have been reduced below

0.01% the amplitude of the average output power. This shows the system's ability to suppress low frequency noise.

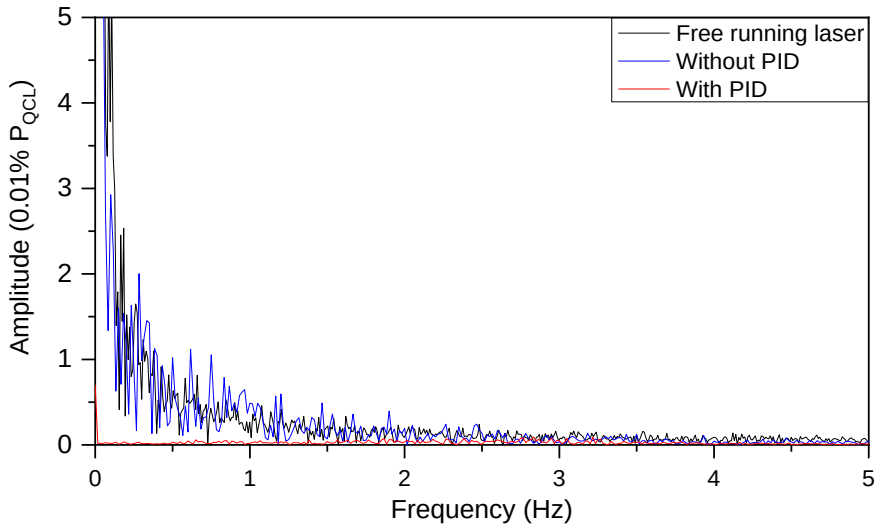

Figure 3.18 Low frequency (<5Hz) components from the Fourier transform of the output power with a free running laser (black), a laser with a PID controlled SRR modulator (red), the same laser with the SRR modulator but no PID control (blue).

The amplitudes of the middle frequency range components in the three situations are displayed in Figure 3.19. When the SRR device is put into the system (with or without PID control loop), it introduces noise at 50 Hz and 60 Hz (they only exist for the system with SRR device) into the system. The 50 Hz noise might appear due to the electrical noise in the system as it is at the line frequency. Similarly, there are also noise components at 100 Hz, 150 Hz, 250 Hz, etc, which are all multiples of 50 Hz. The origin of the 60 Hz noise needs to be further investigated.

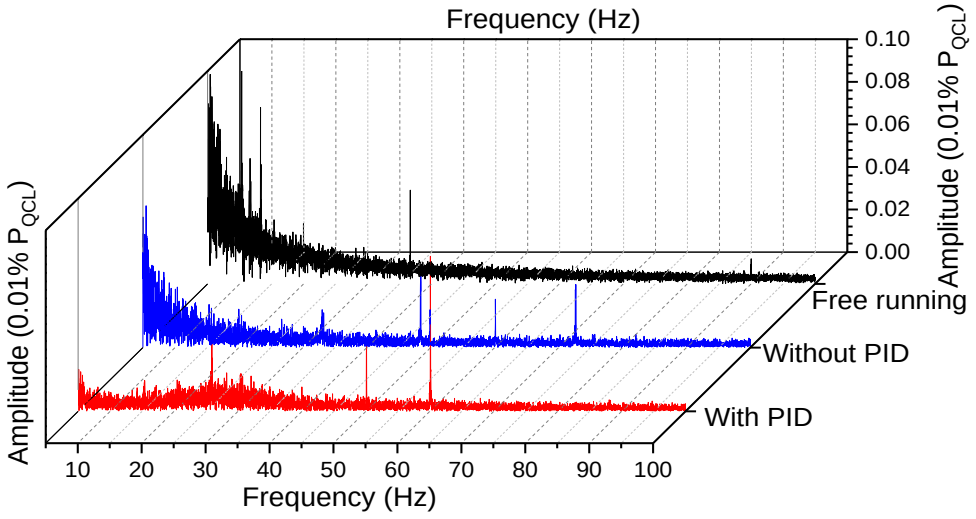

Figure 3.19 Middle frequency (5 Hz to 100 Hz) components from the Fourier transform of the output power with a free running laser (black), the laser with PID controlled SRR modulator (red), laser with the SRR modulator but no PID control (blue).

In the high frequency range, as shown in Figure 3.20, the noise distribution of the system without PID and with PID are similar, with some high amplitude components which cannot be seen for the free running laser. This indicates putting the SRR device into the optical path introduces high frequency noise into the output power. What is interesting is that there is a small burst of noise at a certain high frequency range for all of them (1400-1800 Hz for the free running laser and 2000-2600 Hz for the other two). The reason of this cannot be easily explained at the scope of this work and needs further investigation.

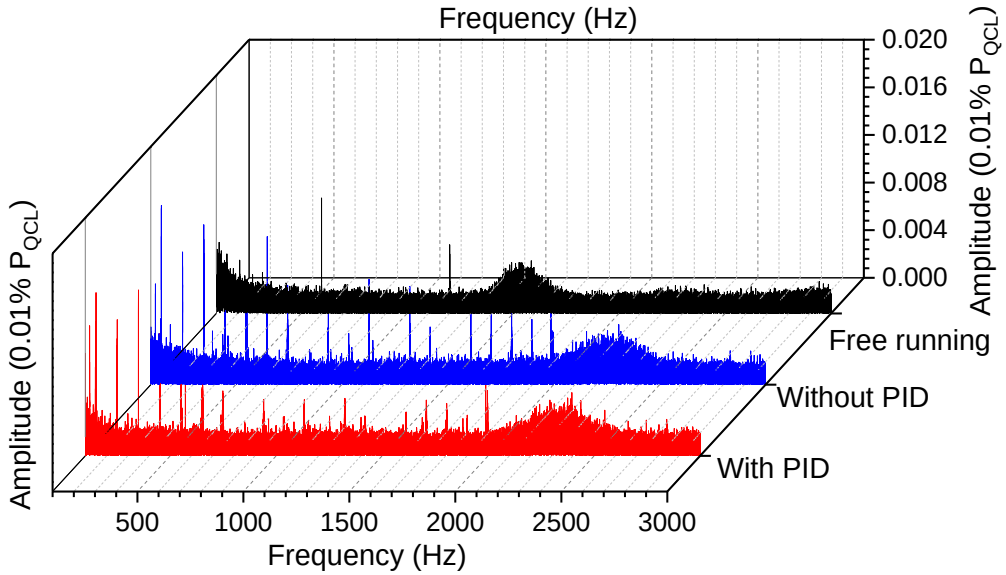

Figure 3.20 High frequency (>100 Hz) components from the Fourier transform of the output power with a free running laser (black), laser with PID controlled SRR modulator (red), laser with the SRR modulator but no PID control (blue).

3.4.3 Evaluation of the amplitude stability of a THZ QCL-Allan variance

The Allan variance (AVAR), also known as two-sample variance, is a measure of frequency stability in clocks, oscillators and amplifiers. It is named after David W. Allan and expressed mathematically as $\sigma_y^2(\tau)$. It is defined as

$$\sigma_y^2(\tau) = \frac{1}{2\tau^2}\left\langle \left(x_{n+2} - 2x_{n+1} + x_n \right)^2 \right\rangle , \tag{3.12}$$

where $\langle \ldots \rangle$ denotes the expectation operator, τ is the observation period and x is the data point of a time series. Figure 3.21 is a typical Allan Variance plot [220]. Different sources of noise can be identified on this plot from the slope of the plot, as shown in Figure 3.21.

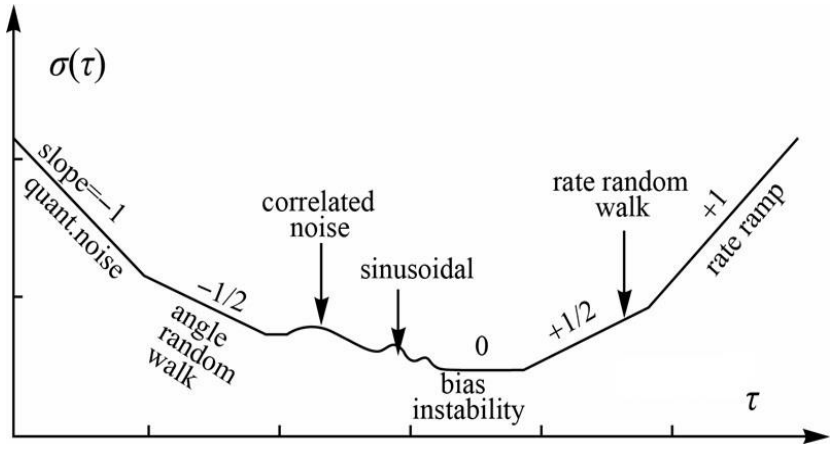

Figure 3.21 Different noise processes on an Allan Variance Plot, from [220] © 2008 IEEE.

To evaluate the stability of the system under the three different conditions (free running, through the SRR device without PID control and laser system with PID control), the Allan Variances of the laser output power in these three conditions are calculated, with the results shown in Figure 3.22.

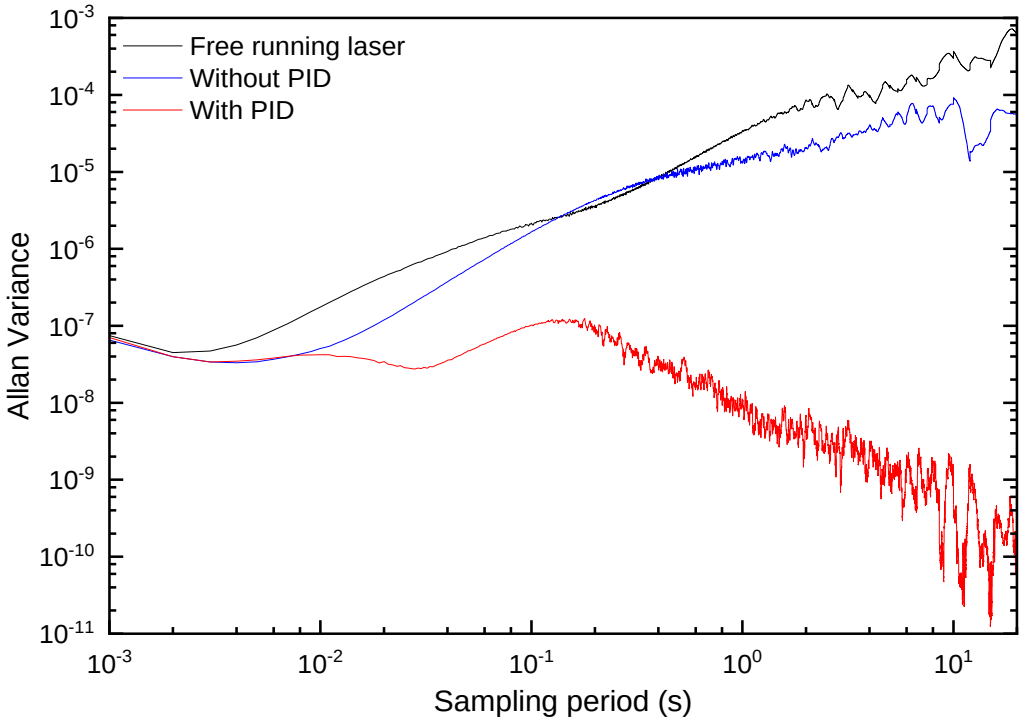

Figure 3.22 The Allan Variance of the laser output power under three different conditions: free running (black), transmitted through the SRR device without PID control (blue) and with PID control (red).

The first minimum point on the plot is called the Allan time, which determines the longest observation time for a system before the noise builds up. As can be seen, the Allan Variance plots of a free running laser (black) and a laser without stabilization (blue) are very similar. However, when the SRR device is put into the optical path, the Allan time increases slightly, due to the small aperture on the device, which filters out some of the low frequency and middle frequency noise from the output power, as shown in Figure 3.18 and Figure 3.19. Both plots become unstable at around 0.4 s. For a stabilised laser with PID control, the Allan Variance plot is very different from the previous two. The Allan time is increased from about 2 ms to about 30 ms, which is 14 times longer and means that the output power is more stable with the PID control loop. There is still room for further optimisation by reducing bias instability of the QCL (electronic noise in practice and the flat part on the plot). Apart from that, this noise analysis does not separate the noise from the lock-in and the detector, which are all subject to electronic noise and temperature change. On all three plots, the random walk noise (with a 1/2 slope) exists. Considering that the laser is a multimode laser, this may be due to the frequency instability of the QCL and can be further improved by adding frequency stabilisation onto the system.

3.5 Active amplitude control of a THz QCL

Another application of this system is to actively control the output power of a THz QCL. To test its capability for this, different waveforms are superimposed onto the PID voltage setpoint, and the corresponding laser output power is recorded.

A 1 Hz square wave, given by a function generator, is applied onto the setpoint first and the amplitude and offset of the square waves are 0.011V and 5.188V, respectively. Figure 3.23 shows the response of the system to it. As can be seen, the output of the PID controller is also a square wave with the same frequency as the setpoint, but with an inverted phase. This is due to the negative feedback of the PID loop: a higher feedback signal gives lower transmittivity and thus lowers the transmission power. The QCL power follows the waveform of the setpoint with the same amplitude and frequency. There are some oscillations on the output power, which might be attributed to the variation in setpoint. This active control is effective for a time frame longer than 3 minutes, as shown in Figure 3.23 (b), making it suitable for experiments in spectroscopy and communications. The time variation of the PID controller output also reveals the fluctuation of the QCL power with respect to time.

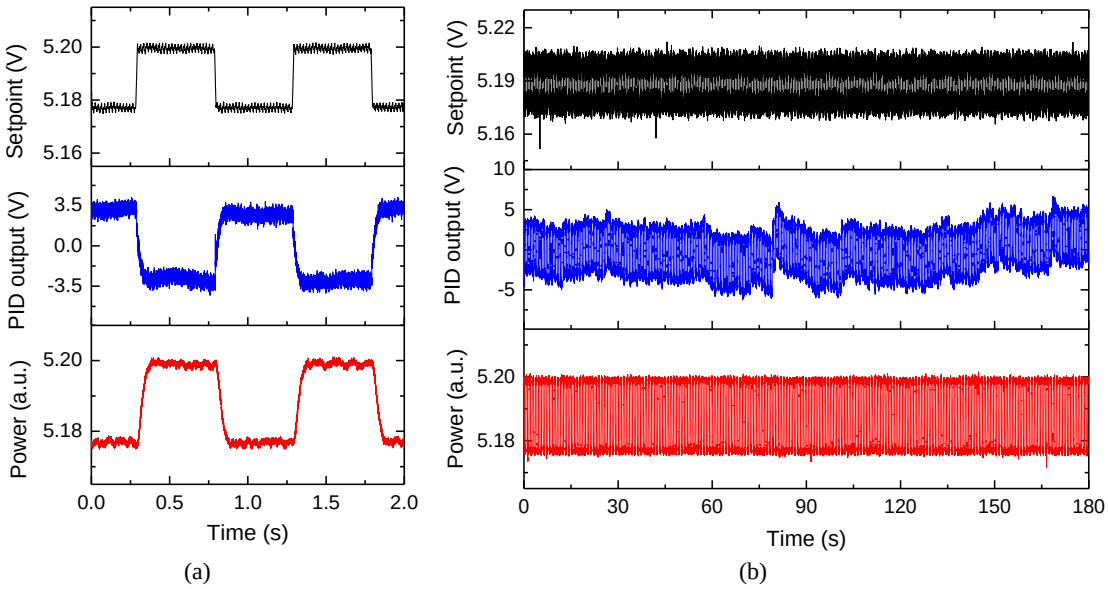

Figure 3.23 Time variation of the PID controller setpoint, the PID controller output and the power of the QCL when a square wave is applied as the power setpoint: (a) in 2 seconds; (b) in 180 seconds.

The response of the system to several other waves have been measured as well with the results shown in Figure 3.24. For both a sine wave and a triangle wave input, the output power can follow the same waveform, which further demonstrates the system's potential to generate THz signal with an arbitrary waveform.

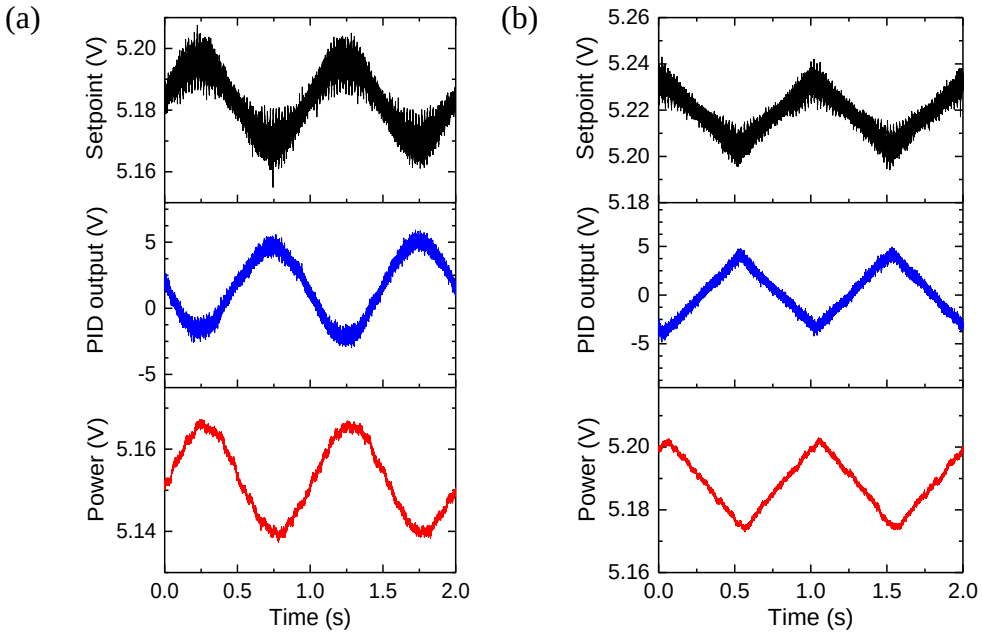

Figure 3.24 Response of the QCL output power to (a) a sine wave and (b) triangle wave.

3.5.1 The stability of the setup

As an amplitude stabilisation setup, the stability of the setup itself is essential for a robust system. Measurements have been done over multiple days without any realignment to test the stability of the system when it is in an ambient environment. The active power control is done three days after the power stabilization measurement with the results displayed in Figure 3.25. When the PID is on in both measurements, the power can be set to the setpoint, which confirms the system's stability for both applications.

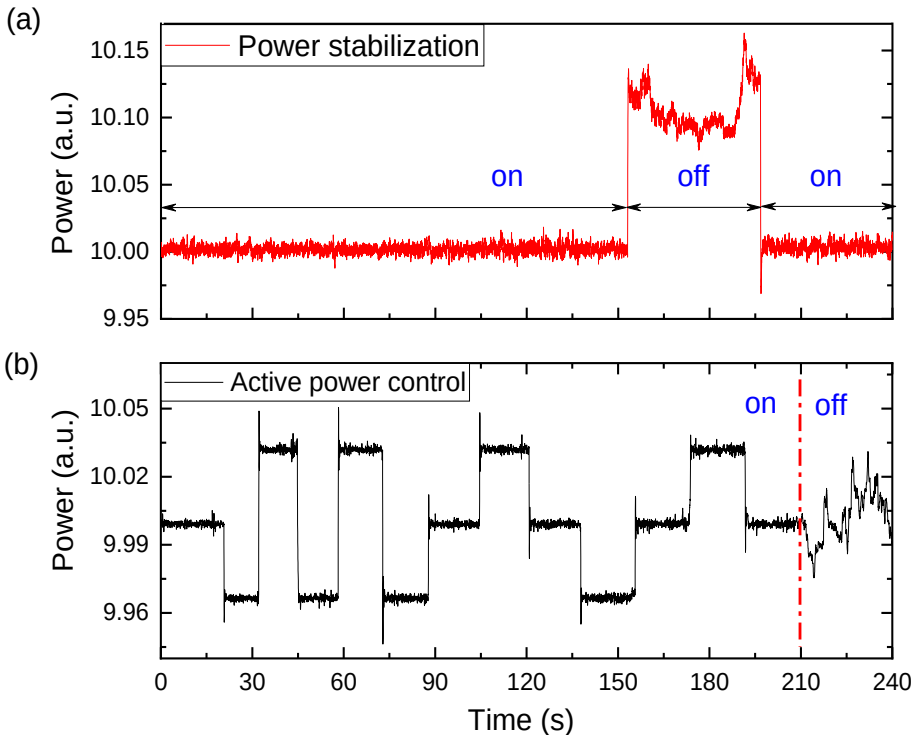

Figure 3.25 Measurement results over two different days without realignment. (a) shows the results for amplitude stabilization while (b) shows the active power control with the system after three days.

3.6 Amplitude stabilization with an external cavity configuration

To achieve a high modulation depth (of up to 100% [53]), an external cavity configuration is explored, as the modulation of the SRR device can be amplified by the external cavity due to the Fabry–Pérot effect. A schematic of the external cavity configuration is shown in Figure 3.26. In this configuration, the THz QCL (QCL-G) is totally suppressed from lasing by a silicon lens with an antireflection coating (18 μm parylene C) on it. The SRR device works as a reflectivity tunable mirror, forming an external cavity with the suppressed laser. A parabolic mirror is used to focus the light

onto the SRR array, and the output power is measured from the other QCL facet with a bolometer. By tuning the reflectivity of the SRR device, the gain of the external cavity, and thus the output power can be modulated.

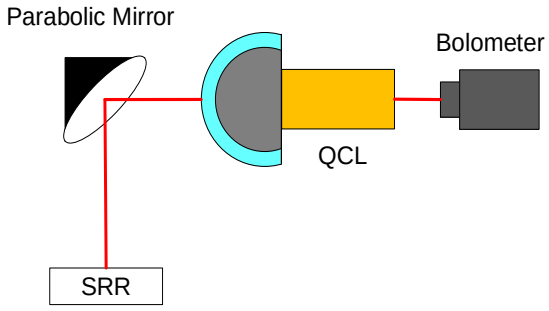

Figure 3.26 Schematic for the external cavity configuration

The same device in the transmission setup is used here as the modulator. Figure 3.27 shows the output power of the external cavity QCL at different bias current in three different feedback conditions. When there is no feedback, the QCL does not lase. When either a gold coated mirror or the modulator is used as a feedback element, the lasing is restored. The output power of the mirror feedback QCL is almost twice as high as the one of a modulator feedback QCL. The threshold current for the modulator feedback QCL is 100 mA higher than its counterpart. This is because at 2.85 THz, the reflectivity of the mirror and the modulator is around 99.7% and 70%, respectively. Therefore, the feedback from the modulator will be weaker compared with the mirror.

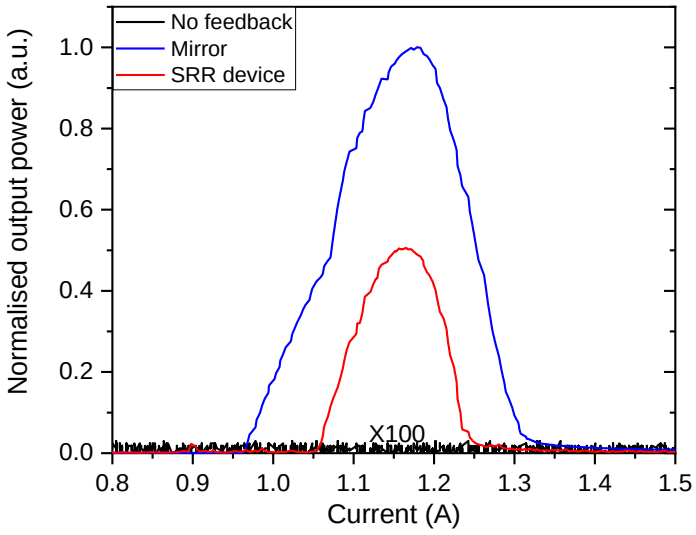

Figure 3.27 Power-current-response of the external cavity QCL in three different situations: without feedback (black) and with feedback from a gold coated flat mirror (blue) and the SRR device (red).

To test the modulation ability of the SRR device, the output power of the external cavity QCL is measured when the back-gate voltage is changed from -10 V to 60 V, with the result shown in Figure 3.28. A 20% modulation is achieved with 30 V voltage change and the Dirac point is at 39 V, consistent with the previous results for the transmission scheme. The modulator is then put into a feedback loop similar to the one used in Section 3.3.6 but with different PID parameters. However, it is difficult to keep the feedback loop stable due to the instability of the external cavity, which is sensitive to the alignment and any mechanical vibrations will introduce fluctuations onto the laser output power.

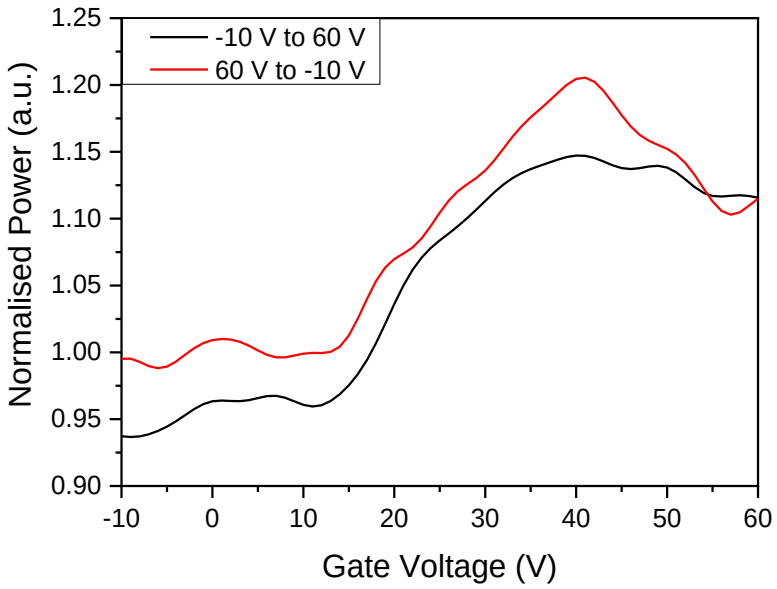

Figure 3.28 Normalised output power of the laser when the back voltage of SRR device in the external cavity is changed from -10V to 60 V (black) and from 60V to -10V (red).

Figure 3.29 shows the output power drift of the QCL with feedback from a gold-coated flat mirror and the SRR device, which shows the long-period instability of the setup. Even for the feedback from the mirror, the output power fluctuates significantly but the peak power stays around the same value, which reveals that mechanical instability exists in the setup. When the SRR is used as the feedback element, the fluctuation becomes more severe as the surface area of the SRR device is much smaller than the mirror and close to the spot size of the QCL (the device size is $3\ \text{mm} \times 3\ \text{mm}$ and the beam size is about $1.5\ \text{mm} \times 1.5\ \text{mm}$), which makes it more sensitive to alignment. The output power changed to a new value at around 300 s, which might due to mode hopping and is undesired for amplitude stabilisation.

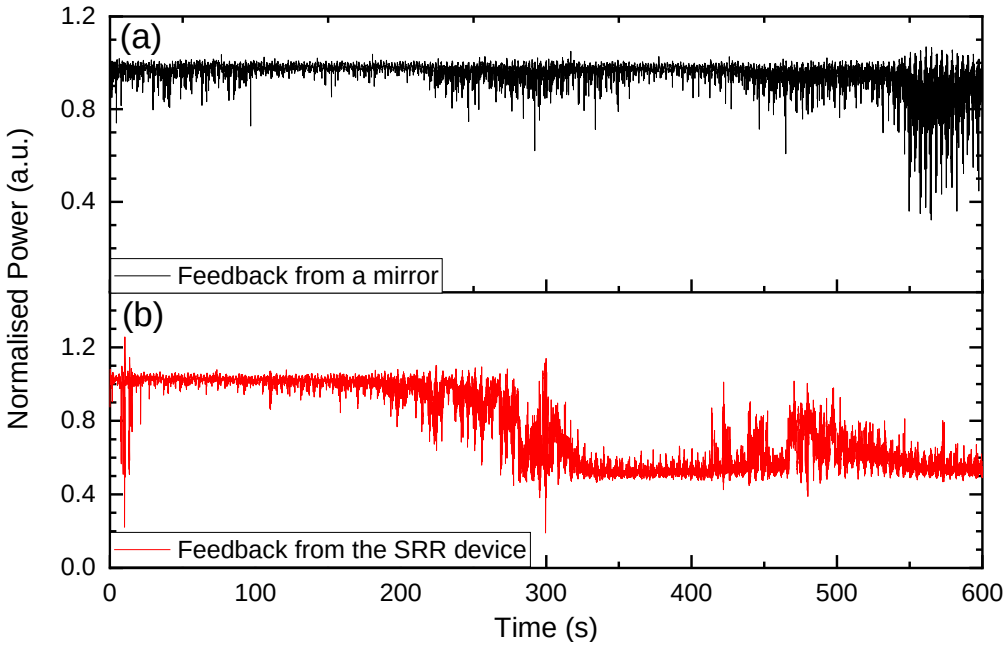

Figure 3.29 The output power fluctuation of the laser with feedback from (a) a gold coated flat mirror, (b) the SRR device.

To improve this, a pinhole with a diameter of 1 mm is put in front of the SRR device. As shown in Figure 3.30, the amplitude of fluctuations reduces significantly with the pinhole and the long period drift is not present as well.

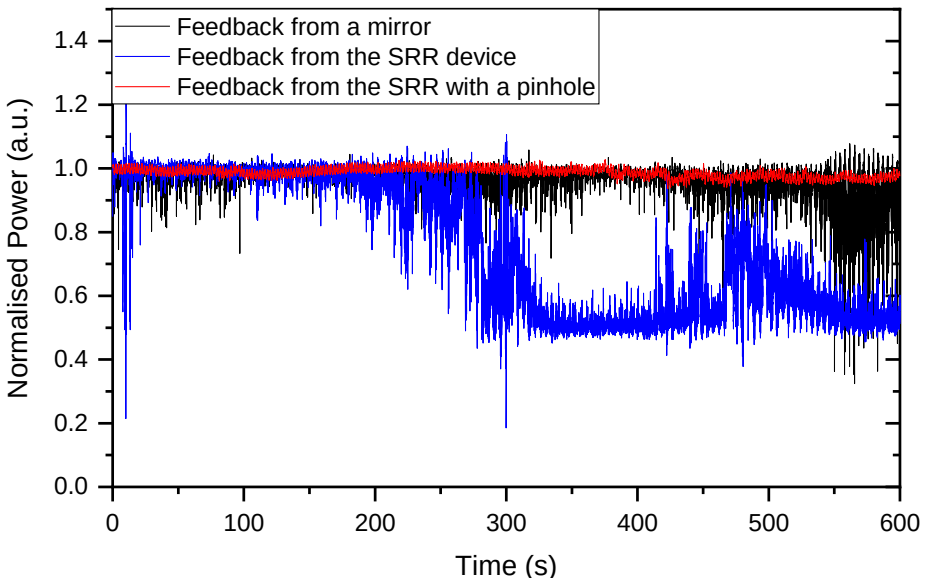

Figure 3.30 The output power fluctuation of the external cavity QCL with feedback from a gold coated flat mirror (black), the SRR device (blue) and the SRR device with a pinhole in front (red).

However, as shown in Figure 3.31, even with the pinhole, the fluctuation amplitude is still about 10% of the output power, which is not suitable for output power stabilisation. There are several causes for the instability: the vibration induced by the pump used to evacuate the cryostat, the air currents and mode hopping of the laser, etc., which can all be resolved with an improved setup in a closed environment with active vibration isolation employing a single mode laser. As this is a proof of concept, these optimisations have not been carried out but could be an interesting project for future research.

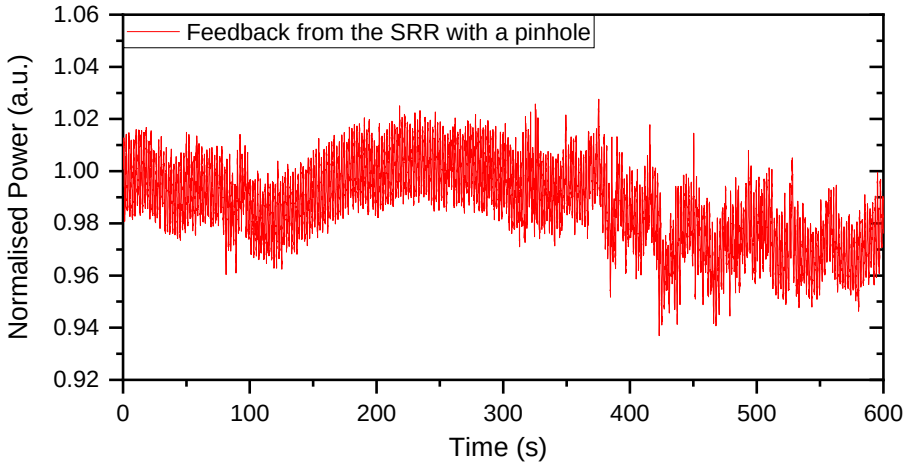

Figure 3.31 The output power fluctuation of the external cavity QCL with feedback from the SRR device with a pinhole in front.

3.7 Conclusion and future work

In this chapter, amplitude stabilization of a 2.85 THz single-plasmon QCL with a graphene loaded SRR amplitude modulator has been demonstrated.

An SRR device has been designed for modulation purposes with COMSOL simulations. The device is then tested with a TDS system, which demonstrates a good agreement between measured transmission spectra and simulation results and confirms the expected resonance frequency and modulation ability.

The modulator works at room temperature and is capable of 2.7% modulation of the transmitted laser power, corresponding to a voltage setpoint at 20 V with a 20 V (peak to peak) AC voltage superimposed. This modulation is sufficient to be used for effective laser amplitude stabilization, despite the fact that there is significant room for optimization of the demonstrated system. The magnitude of the fluctuation in laser power is reduced from 1.52% to 0.043%. The efficiency, flexibility and robustness of

this approach have also been demonstrated using several active control configurations for the QCL output, without affecting the amplitude stability.

The noise of the output power in different situations has also been analysed through FFT in frequency domain and the stability has been evaluated with Allan Variance in terms of observation time, which all prove a reduction of noise and improvement of amplitude stability with the PID feedback loop.

In addition, a higher modulation depth (20%) has been achieved with an external cavity configuration and has been exploited for amplitude stabilization. However, due to the instability of the external cavity induced by vibrations in the experimental environment, a stable feedback loop cannot be achieved. It may be possible to overcome this in the future by improving the mechanical stability of the system.

Furthermore, for some metamaterial structures, like the dipole antennas, they can be used for both modulation and detection of THz radiation [205][218]. Therefore, it is possible to use one such devices as an integrated device for amplitude stabilisation so that no extra detector is needed, and a more compact system can be achieved, which will be further discussed in Section 6.2.2.

Chapter 4
THz scattering-type scanning nearfield optical microscopy (s-SNOM)

Over time, there has been a lot of effort to develop techniques for improving the resolution of an optical microscope. With the advent of nearfield imaging technique, the resolution has been brought below the diffraction limit [221]. Especially for scattering-type scanning nearfield optical microscopy (s-SNOM), it has achieved nanometre resolution from the visible to THz frequency range [222], which allows us to study many phenomena: plasmonic resonance in nano-structures [223]–[226], optical properties of solid-state and two-dimensional materials [227], [228], inspection and mapping of quantum objects [229], to name a few. In this chapter, the theory of nearfield imaging is discussed and an s-SNOM operating at THz frequency range is developed based on a tuning fork system and a THz QCL.

4.1 Motivation

By definition, microscopy is the science of investigating small objects and structures using a microscope. Therefore, increasing the resolution to be able to see smaller features has always been the goal for the research in this field. After conventional microscopy was established in the 17th century, the resolution of an optical microscope has been improved considerably and it has been adopted in applications from medicine and chemistry, to physics and other technologies. However, for a conventional optical microscope, the highest resolution it can achieve is fundamentally determined by the diffraction limit because of the wave nature of light.

4.1.1 The diffraction limit of a classical optical microscope

In a classical optical microscope, the resolution is fundamentally limited by the diffraction of light, which was first realised by German physicist Ernst Abbe. He found that the ultimate resolution of an imaging system is not constrained by the equipment quality, instead by the aperture of its optics and the wavelength of the light source [230].

Because of diffraction, for a system using light with wavelength λ, traveling in a medium with refractive index n and converging to a spot with half-angle θ, the resolution limit $d_{\min}$ is given by

$$d_{\min} = \frac{\lambda}{2n\sin\theta} = \frac{\lambda}{2\mathrm{NA}} \tag{4.1}$$

where $\mathrm{NA} = n\sin\theta$ is called the numerical aperture of the objective. From equation (4.1), in air, because n=1, the highest resolution that can be achieved will be $\lambda/2$.

The fundamental limiting factor is still the wavelength of the light. To increase the resolution, a shorter wavelength should be used, however, this results in a high photon energy, which may damage the sample. Besides, in some situations, to get more information of a sample, optical images at different wavelengths need to be taken. In this case, a system having similar resolution at different wavelengths would be useful.

At the same time, the numerical aperture can be increased by increasing the refractive index; this can be achieved by filling the space between the sample and the objective with high refractive index ($n>1$) liquid, such as water (n=1.33) or Cedar Oil (n=1.51) or placing a hemispherical lens with high refractive index in contact with the sample. However, as can be seen, the resolution improvement of these approaches is still highly limited by the variation range of the refractive index.

In life science, fluorescence microscopy has been developed to push the resolution towards the diffraction limit. It uses fluorescence and phosphorescence instead of, or in addition to, scattering, reflection, and attenuation or absorption of light, to study the properties of organic or inorganic substances [231]. For a fluorescence microscope, the resolution is usually determined by the spot size of the light. To reduce the focal spot size, several concepts emerged during the mid-20th century: confocal [232], 4Pi and I^5M microscopy [233], [234], the resolution of which can be better than 100 nm. However, as the spot size is limited by diffraction, they still cannot break the diffraction limit.

4.1.2 Beyond the diffraction limit: far-field approaches

To further improve the optical resolution, several techniques that could overcome the diffraction limit have been developed, which can be classified into two groups: far-field approaches and nearfield approaches. For far-field approaches, the optical signals (typically fluorescence) are collected at a normal working distance while the nearfield techniques operate in proximity to the sample and collect evanescent signals that decay rapidly but contain extra information about the sample [235].

For a far-field fluorescence microscope, breaking Abbe's barrier is about discerning an arbitrary number of densely packed and similarly labelled features within a $\lambda/2n$ circle, which is not limited by diffraction and possible if the features can be recorded sequentially. If the markers of each feature can be successively transferred to a signal-giving "bright" state A, while keeping the other markers in a state B that is "dark" [236], reading out the bright ones allows assembly of a sub-diffraction image, provided that their coordinates are known.

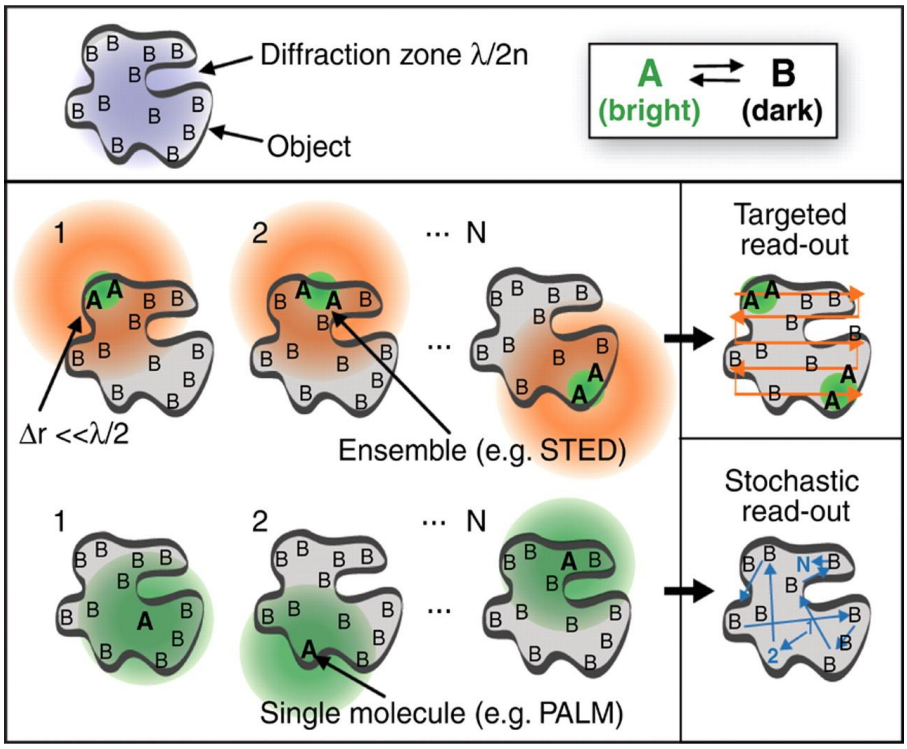

Figure 4.1 Principle of microscopy using targeted signal switching or stochastic single-molecule switching, from [237]. Reprinted with permission from AAAS.

Two ways of signal switching are possible: targeted readout mode and stochastic readout mode, the principle of which is displayed in Figure 4.1. Stimulated emission depletion (STED), ground state depletion (GSD) and saturated pattern excitation microscopy (SPEM) are based on the targeted readout concept. In targeted readout mode, one of the two states (here A) is established at a sub-diffraction-sized spot at the position of a zero to read out an unknown number of fluorophore molecules. The image is assembled by deliberate translation of the zero.

In photoactivatable localization microscopy (PALM) and stochastic optical reconstruction microscopy (STORM), the stochastic readout mode is adopted and a single switchable fluorophore from a random position within the diffraction zone is

switched to a stable state A, while the other molecules remain in state B. The coordinate is calculated from the centroid of the diffraction fluorescence spot measured by a pixelated detector. The coordinate pops up stochastically depending on where the interrogated marker molecule is located.

For both approaches, a specific state is established in a region ($\lambda/2n$) to characterize the features from this region [237] and the resolution is determined by the size of this region, which is defined by a single molecule.

4.1.3 Beyond the diffraction limit: nearfield approaches

Aside from fluorescence, surface plasmons (those that are either excited on the metallic surface or localized in a small metallic tip) also provide a method of overcoming the diffraction limit of light, which opens the door for nearfield approaches.

On a metallic surface, surface plasmon polaritons (SPP) travel along the surface as an evanescent wave and the travelling speed is lower than the light speed. If the frequency of the plasmon is the same as the frequency of the light, the wavelength of the surface plasmon will be smaller than that of the light [238]. In this way, a shorter wavelength is achieved without changing the refractive index or using a short wavelength light source. Based on this principle, several techniques that can overcome the diffraction limit of the light source have been developed. The SPP on a gold thin film were used for subwavelength imaging and the 502 nm line of an argon-ion laser was used to excite the SPP [239]. The superlens phenomenon has been used for super resolution imaging as well [104]. The resolution of such systems is mainly determined by the wavelength of the SPP, which is usually below 100 nm for visible light.

Inspired by scanning microscopy, such as SEM, and scanning tunnelling microscopy (STM), scanning nearfield optical microscopy (SNOM) has been developed by combining the interaction mechanisms of optical microscopy with the high resolution of scanning probe methods [240]. The SNOM techniques can be classified into two groups depending on whether an aperture is used or not, namely aperture SNOM and apertureless SNOM.

The idea of aperture SNOM was first presented in 1972 [241], and its resolution has been improved significantly since then. In aperture SNOM, a small aperture, through which the sample is illuminated, is placed near the sample surface. The aperture creates a sub-wavelength size light source, not limited by diffraction but determined by the aperture size [242]. When scanning the aperture across the sample, the optical field at each scanning point is probed with sub-wavelength spatial resolution [243], which is then combined to form the optical image of the sample. As the size of aperture is limited

by the fabrication technique and also determines how much light can transmit through the aperture, it cannot be extremely small. Therefore, the resolution of such a system, which is determined by the aperture size, cannot be as high as the apertureless SNOM.

In apertureless SNOM, a nano-sized probe (usually with diameter of several or tens of nanometre) scans the sample surface to form an image with a resolution much better than the diffraction limit [244]. Compared to the SPP on a metallic surface, there is no propagation of SPP in the tip because of its small size, and hence losses related to the retardation of SPP do not exist [238]. Therefore, the resolution of the microscope is comparable to the size of the confined field, which is the same as the size of the probe. As the scattered light from the probe is measured, apertureless SNOM is also called scattering-type SNOM (s-SNOM).

4.2 Principle of the s-SNOM

An s-SNOM is a combination product of a scanning probe microscopy (SPM) and optical imaging. Figure 4.2 shows a basic experimental setup of the s-SNOM, in which an Atomic Force Microscope (AFM) is used as a base instrument to scan across the sample in proximity to a tip to get the topography. The tip region is illuminated by a focused light beam and the scattered light is recorded by a detector to give an optical image of the sample. For an s-SNOM to operate, there are usually four things to consider: how to get the topography; how to understand the optical contrast; how to reduce the background noise and how to increase the signal to noise ratio of the system, which will be discussed in this section.

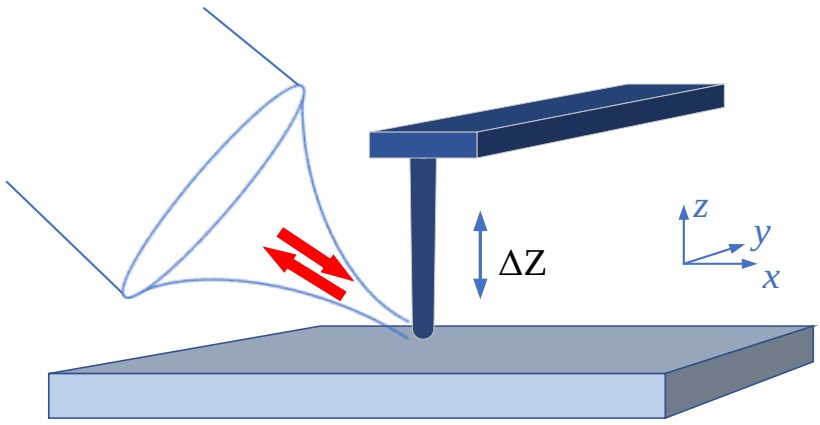

Figure 4.2 The principle of an s-SNOM

4.2.1 Topography image

In an s-SNOM, a SPM captures the topography image of the sample. It can achieve nanoscale resolution by scanning a sharp probe across a sample and recording the topography as a function of tip position. The first SPM was invented by Binnig *et al.* in the form of Scanning Tunnelling Microscopy in 1982 [245]. Soon after that, they invented the AFM in 1986 [246], which has since become one of the most widely used SPMs. Most of the s-SNOM systems in the literature use it as the base setup. The AFM is a combination of the principles of the scanning tunnelling microscope and the stylus profilometer. It incorporates a probe that does not damage the surface. The operation principle of an AFM is shown in Figure 4.3. A sharp tip is scanned across the sample surface and it follows contour B to maintain a constant force between the tip and the sample with a feedback loop. Depending on which feedback mechanism is used, the AFMs can be classified into mainly two groups: cantilever-deflection AFM and tuning fork AFM.

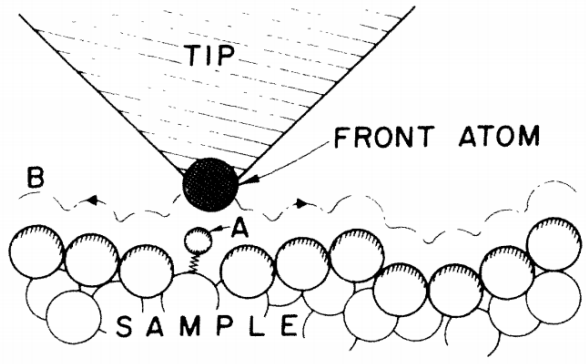

Figure 4.3 Operation principle of an AFM, reprinted figure with permission from [246] Copyright (1986) by the American Physical Society.

In a cantilever-deflection AFM, the tip is mounted at the end of a flexible cantilever, which will deform when the force between the tip and sample changes due to the sample topography or vibrations in the system. A feedback loop keeps the force constant by changing the tip height, which reflects the topography of the sample. The force between the tip and sample needs to be measured as a feedback signal. The most commonly used method for measuring the force in a cantilever system is the beam deflection measurement [247]. Figure 4.4 shows the principle of this method [248]. Here, a laser beam is reflected off the back of the cantilever and collected by a position-sensitive detector (PSD) consisting of two or four closely spaced photodiodes, whose output signal is passed to a differential amplifier. Bending of the cantilever results in the

difference of the amount of light collected by different photodiodes, producing an output, which is proportional to the deflection of the cantilever and used as the feedback signal. In this method, the tip is dragged across the sample surface, therefore, it is called contact mode [246], [249].

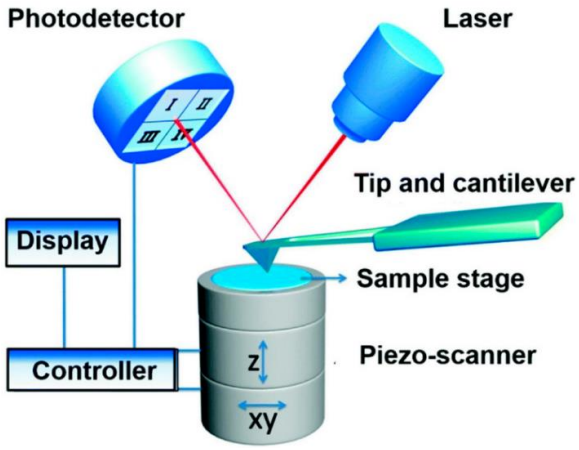

Figure 4.4 A schematic of the beam deflection method, from [248], reprinted with permission under Creative Commons Attribution License.

In many situations, to protect the sample, it is necessary to keep a small distance between the tip and sample surface. One possible way of doing this is to drive the cantilever with a piezoelectric actuator so that it oscillates at its mechanical resonance frequency in proximity to the sample with a few nm oscillation amplitudes, which is sensitive to interaction forces between the tip and the sample and varies when these forces change [250]. As a result, the oscillation amplitude can be monitored with the beam deflection method as well and it is used as the feedback signal here. This method is called the non-contact mode.

When working in an ambient environment, a liquid meniscus layer of water will develop on most samples. In this case, it is difficult to keep the tip close enough to the sample surface to detect the force change without colliding it. To overcome this, tapping mode was developed [251], in which the cantilever is driven to oscillate up and down at or near its resonance frequency with the amplitude varying from several nm to 200 nm . The amplitude and frequency of the driven signal are kept constant, which gives a constant oscillation amplitude of the cantilever when there are no external perturbations. Changes of topography will induce an oscillation amplitude change, which can be measured in the same way as in non-contact mode and is used as the feedback signal.

Cantilever-deflection AFM is the most commonly used AFM nowadays. However, it presents issues when scanning in a dark environment is needed during the measurement as a laser is needed for the tip position measurement. Therefore, a feedback mechanism without using a laser is needed, and a tuning fork offers the ability to measure the tip position without any other external elements. Furthermore, if measurements at cryogenic temperature need to be done, the compactness of the tuning fork system makes it suitable to operate in a very limited space. The final goal of this work is to build a cryogenic system that could measure semiconductor devices at low temperature. Therefore, the tuning fork AFM has been chosen for our system, which will be discussed in detail in Section 4.4.

4.2.2 Tip-sample nearfield interaction

The main difference of an s-SNOM from an AFM is that there is an optical nearfield interaction between the tip and sample when the tip region is illuminated by a laser, which is also the reason why an optical image can be obtained. Several models have been developed to understand the optical nearfield interaction. For a qualitative explanation of the material contrast, the point-dipole model is usually used. Here it is assumed that the shaft of the tip does not affect the way that a sample influences the nearfield between the tip and the sample, and the tip is simplified as a polarizable sphere which can be inscribed at its apex [252]–[254].

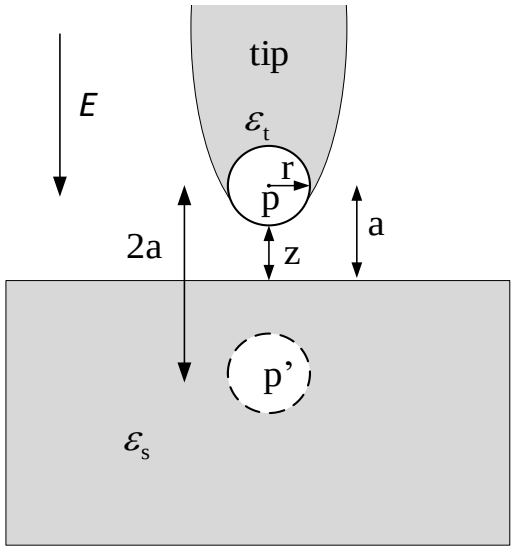

Figure 4.5 Modelling of the tip-sample nearfield interaction. The tip is modelled as a polarized sphere with radius *r* sitting above the sample surface at a distance of *a*. The relative permittivity of the tip and the sample are and ε_s, respectively. *E* is the input electric field. Reproduced with permission of [253], permission conveyed through Copyright Clearance Center, Inc.

Figure 4.5 shows the basic idea of this model, in which the tip is modelled as a polarised sphere with radius r ($r \ll \lambda$) and relative permittivity ε_t sitting above the sample surface at a distance of a. Therefore, the polarizability of the tip can be calculated as [254]

$$\alpha = 4\pi r^3 \frac{\varepsilon_t - 1}{\varepsilon_t + 2} \tag{4.2}$$

When applying an electric field in the sample area, only the component of electric field that is perpendicular to the sample surface will introduce a strong nearfield interaction because of the antenna effect of the tip shaft. Figure 4.6 gives the surface charge density distribution on the tip when it is illuminated with a plane wave polarized either perpendicular or parallel to the tip axis. As can be seen, when the electric field is parallel to the tip axis, there is a field enhancement, while there is no field enhancement in the other polarization [221]. As a result, here only the component of electric field that is perpendicular to the sample surface will be considered. The sphere becomes polarized with dipole moment $p = \alpha E$, so that the electric field of the induced tip dipole can be described as

$$E_{\text{tip}} = \frac{p}{2\pi(z+r)^3} \quad . \tag{4.3}$$

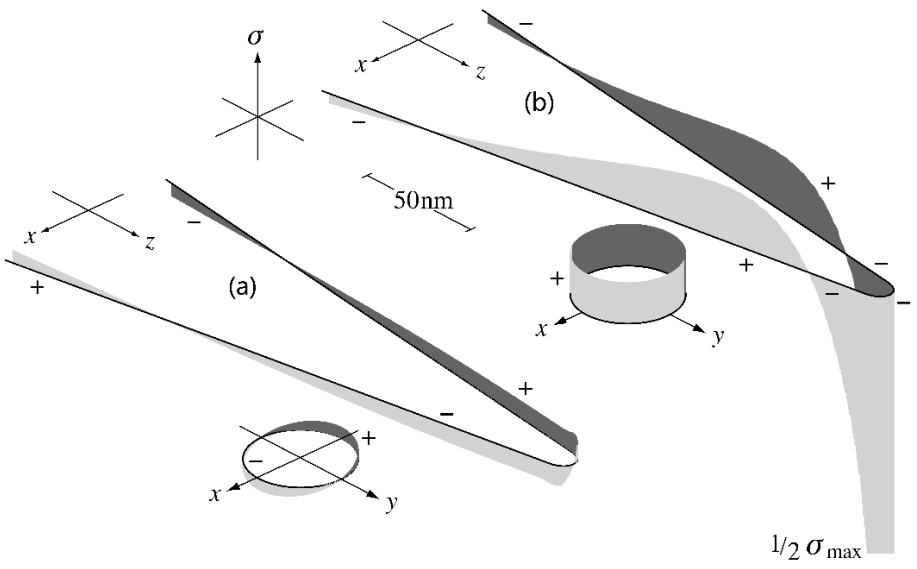

Figure 4.6 Nearfield interaction induced surface charge density when a tip with 5 nm tip radius is illuminated by an 810 nm plane wave with the polarization perpendicular to the tip axis (a) and parallel to the tip axis (b). The surface charges form a standing wave in each case. In (a) the surface charge wave has a node at the end of the tip, whereas in (b) there is a large surface charge accumulation at the foremost part, responsible for the field enhancement [221].

This electric field will induce surface charges in the sample, which sits below the tip with relative permittivity ε_s. To simplify the calculation, the sphere is replaced by a point dipole of the same direction and equal strength, located in the centre of the sphere. In the electrostatic approximation, the nearfield between the tip dipole and the sample can be described by a 'mirror' point dipole inside the sample at a distance of $2(z+r)$ from the tip dipole, with its direction parallel to the tip dipole and a dipole moment $p' = \beta p$ [5], where

$$\beta = \frac{\varepsilon_s - 1}{\varepsilon_s + 1} \tag{4.4}$$

is the dielectric surface response function [253] or surface reflection factor [254] of the sample. The incident field of the tip dipole is enhanced by this image field so that it becomes:

$$p = \alpha\left(E + \frac{p'}{16\pi(z+r)^3}\right) = \frac{\alpha E}{1 - \frac{\alpha\beta}{16\pi(z+r)^3}} = \alpha' E \quad , \tag{4.5}$$

where

$$\alpha' = \frac{\alpha}{1 - \frac{\alpha\beta}{16\pi(z+r)^3}} \, . \tag{4.6}$$

The total field of the tip-sample system is the superposition of the tip field and image dipole field, which is

$$p_{\text{total}} = p + p' = p(1+\beta) = \alpha'(1+\beta)E \quad . \tag{4.7}$$

As a result, the effective polarizability of the tip-sample system will be

$$\alpha_{\text{eff}} = \alpha'(1+\beta) = \frac{\alpha(1+\beta)}{1 - \frac{\alpha\beta}{16\pi(z+r)^3}} \quad . \tag{4.8}$$

According to scattering theory, the scattered field from a point dipole is proportional to its polarizability, therefore

$$E_{\text{sca}} \propto \alpha_{\text{eff}} E \, , \tag{4.9}$$

where E_{sca} is the scattered field and also the signal to be measured. During a measurement, the input field is usually constant, thus the optical signal is directly determined by α_{eff}. According to equation (4.8), the effective polarizability is

determined mainly by the sample material β, the tip material and shape α, and the distance between the tip and the sample z, the influence of which on the performance of an s-SNOM will be discussed in the following sections.

The point dipole model can only give a qualitative explanation of the nearfield signal. For a better quantitative explanation and prediction of optical contrast, the finite dipole model was introduced [255], [256], which takes the elongated shape of the tip into account and the tip is treated as a prolate spheroid much smaller than the wavelength. It is found that the tip nearfield can be much better described by a finite dipole consisting of point charges Q_0 and $-Q_0$ rather than by the field of a point dipole. This model gives a good quantitative prediction of the optical contrast in an s-SNOM measurement but involves more mathematical complexity. For the purpose of understanding the principle of s-SNOM, the point dipole model is enough to give direct conclusions of practical significance, which as a result will be used in further discussions.

4.2.3 Optical contrast

It is revealed from equation (4.8) and (4.4) that, the sample affects the nearfield interaction only through the relative permittivity ε_s taken at the illumination wavelength. Although the tip material and size as well as the distance z also influence the nearfield signal, during an imaging process, they should be constant. As a result, the optical contrast of an s-SNOM is determined only by the local permittivity of the sample.

4.2.4 Background scattering elimination

In equation (4.8), both α and β are generally complex numbers. Therefore, the effective polarizability α_{eff} will be a complex number as well.

$$\alpha_{\text{eff}} = A_{\text{eff}} e^{i\phi}, \tag{4.10}$$

where A_{eff} is the relative amplitude and there is generally a non-zero phase shift ϕ between the incident and the scattered light. Considering a practical situation where the sample material is silicon with relative permittivity = 15 and the tip sphere is gold, with radius a = 10 nm and relative permittivity = -106000 + 193000i (at 3 THz) [257], the change of amplitude and phase of the effective permittivity is shown in Figure 4.7. As can be seen, at large distance, both the amplitude and phase does not change much but they increase dramatically when the distance is smaller than the tip radius.

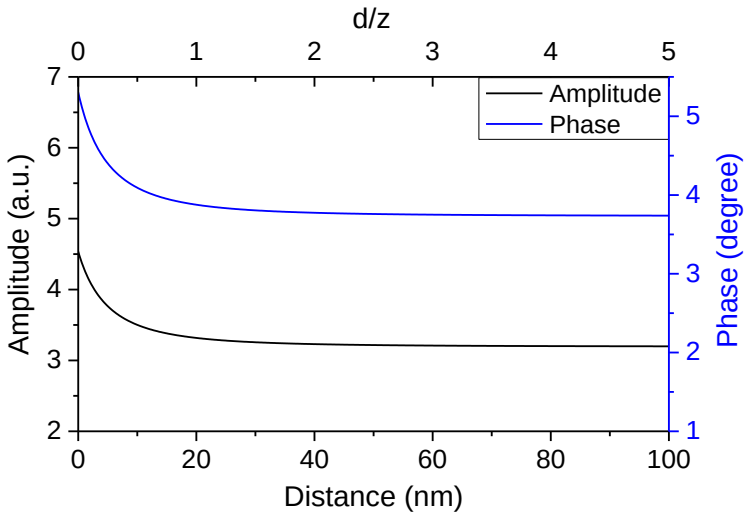

Figure 4.7 Calculated nearfield scattering amplitude A_{eff} and phase ϕ versus the distance d between the tip sphere and the sample.

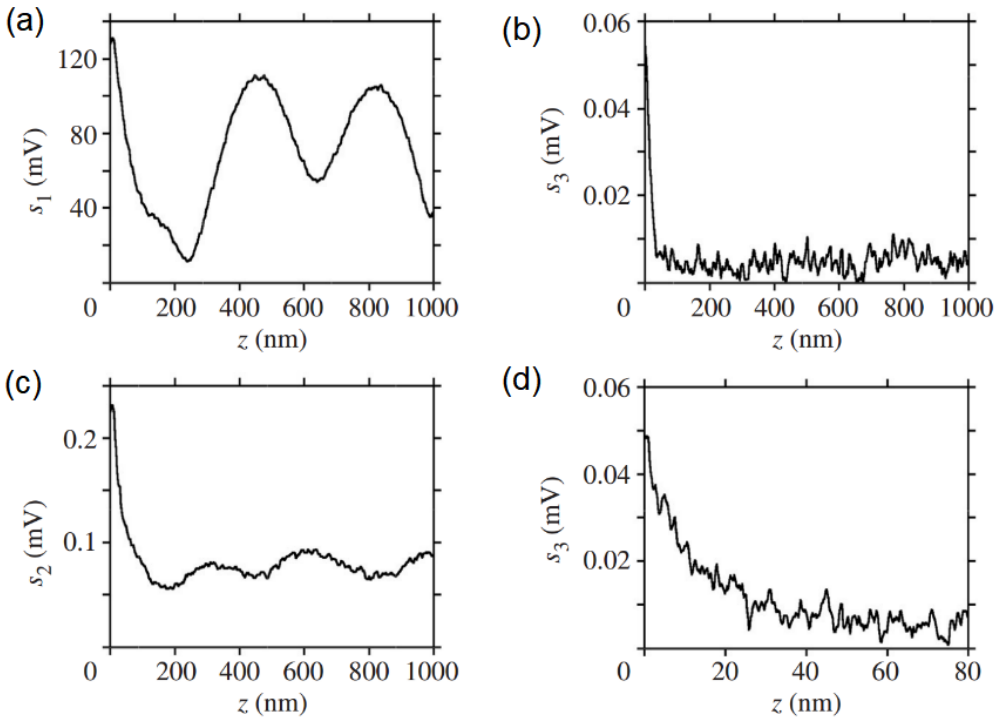

Figure 4.8 Experimental s-SNOM amplitude versus distance z between Pt tip and Si sample, for n = 1-3 demodulation orders (tip radius a ≈ 20 nm, tapping amplitude Δz ≈ 20 nm, wavelength λ = 633 nm). (a) first order demodulation; (b)second order demodulation; (c) third order demodulation; (d) third order demodulation within a smaller distance range. Reproduced with permission of [253], permission conveyed through Copyright Clearance Center, Inc..

In s-SNOM, when the tip is illuminated by a light source, the physical size of the beam spot causes reflections from either the tip shaft or the sample surface, which introduce a massive background noise. To get the real isolated optical signal out, a way to suppress the background noise needs to be developed. The nonlinear dependence of α_{eff} on the distance, as shown in Figure 4.7 offers us a solution. By modulating the distance between the tip and sample, the real optical signal will be modulated at the same frequency while the background signal doesn't change much. Due to the nonlinearity of the nearfield signal, demodulating the overall signal at high order harmonics will eliminate the background signal. Figure 4.8 gives the amplitude of the nearfield signal taken in an experiment at different harmonics, which shows that the choice of a high order harmonics eliminates the background, and also steepens the nearfield response [253].

4.2.5 Field enhancement

The s-SNOM not only has the advantage of high resolution, but also gives a highly enhanced field intensity near the probe, owing to the resonance of localized SPP. The enhancement factor strongly depends on the shape and the size of the probe. Figure 4.9 shows several commonly used probe structures designed for high field concentration [238].

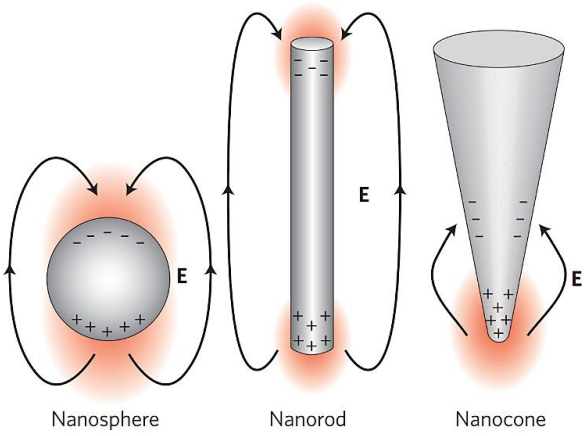

Figure 4.9 Illustration of some commonly used probe structures showing field enhancement, reprinted by permission from [238] © 2009, Springer Nature

4.3 THz nearfield imaging

Most microscopy techniques mainly work well in visible or infrared. However, with the development of knowledge and technology in mid-infrared, far infrared, and even

longer wavelengths (THz), microscopes that can work in these long wavelength ranges are needed to understand some interesting phenomena that can only happen in these ranges. A special advantage of s-SNOM over any other form of optical microscopy is that it can work with mid-infrared and even longer wavelength light illumination [253]. In fact, for metals the conductivity increases monotonically with wavelength in the infrared, which will enhance the antenna performance of the metal tip, giving it a better performance in the long-wavelength or THz spectral regions.

THz imaging is appealing in several areas. In biomedical research fields this non-ionizing radiation has been used for diagnostics, due to its capability of discriminating between healthy and cancerous tissues [258]. Besides, many materials which are opaque in visible or infrared are transparent to THz radiation [259], such as some plastics, cardboard and ceramics, etc, making THz radiation suitable for package inspection, quality control and non-destructive testing. In addition, the longer wavelength of THz waves enables greater penetration into substances, for example in the detection of skin cancers below the surface. Also, many chemicals exhibit unique spectral fingerprints in the terahertz range, which can be used for identification and chemical analysis.

The combination of THz radiation with nearfield imaging opens a wide range of research possibilities. In semiconductor physics, THz nearfield imaging has proved to be a viable tool for inspection of integrated devices with sub-wavelength resolution [229]. It is well known that THz radiation is sensitive to the doping level of semiconductor devices. Accordingly, it can be implemented for the inspection and mapping of quantum objects even when covered by a dielectric layer, as an alternative and/or complementary technique to photoluminescence techniques. It can also be used for nanoscale chemical materials identification via molecular vibrational spectroscopy [260]–[263], polariton mapping in 2D materials [223], [224], [226], [264]–[266], and studies of metal–insulator transitions [267], [268] and strongly correlated quantum materials [269], [270].

4.3.1 THz aperture SNOM

Like in other frequency ranges, nearfield imaging in THz spectral range was first demonstrated with an aperture type setup by Hunsche *et al.* in 1998 [242], which is shown in Figure 4.10. The whole system is based on a THz TDS system. By focusing the THz radiation onto a tapered metal tip with a small exit aperture and scanning a sample in the nearfield of this aperture, a spatial resolution of better than $\lambda/4$ was demonstrated.

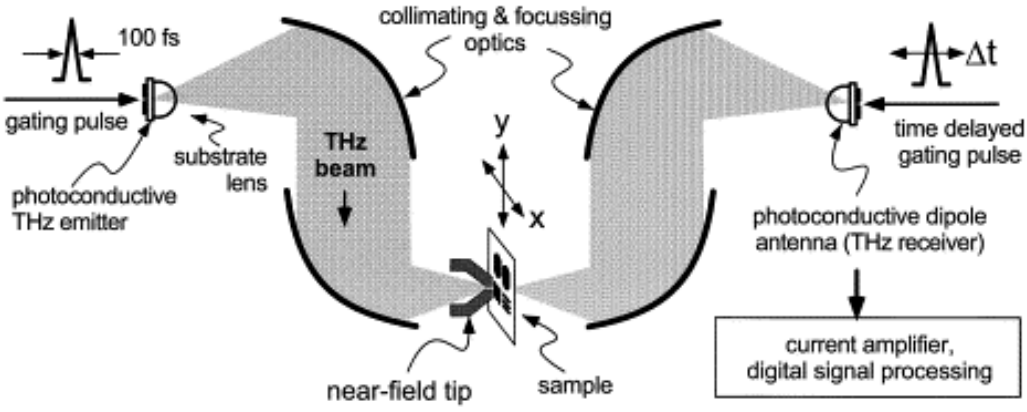

Figure 4.10 THz nearfield imaging using a tapered metal tip with a small exit aperture, reprinted from [242], Copyright (1998), with permission from Elsevier.

3 years later, a collection mode THz nearfield imaging setup was developed by Mitrofanov *et al.* [243]. As shown in Figure 4.11, instead of putting a small aperture on the scanning tip, a nearfield probe, which consists of a small aperture in a metallic screen and a photo-conducting antenna, was used and the sample was illuminated by a uniform THz beam with a spot size larger than the sample. A 7 μm (11.67 λ/1000) resolution was achieved at 0.5 THz with this setup. The spatial resolution of the conventional aperture type nearfield setup is determined by the aperture size. However, the usable aperture size is limited by the strong reduction of light transmission through the aperture, which was found by Bethe and Bouwkamp to follow a power law: $T \sim d^6$ (d is the diameter of the aperture) [271]. Recently, a new THz nearfield probe with THz nanodetectors embedded in the aperture region has been developed [272]. With this detector, evanescent THz field, which does not follow the six-power dependence, is converted into a detectable electrical signal at the nanoscale and detected.

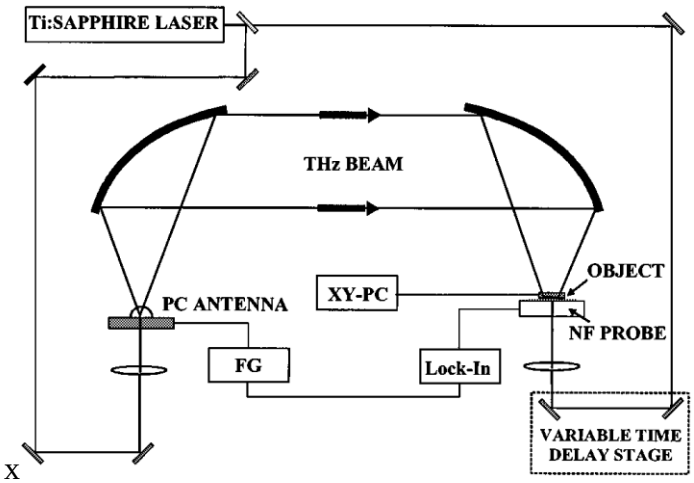

Figure 4.11 Schematic diagram of a collection mode terahertz nearfield imaging setup, from reference [243] © 2001 IEEE.

4.3.2 THz apertureless SNOM

The first THz s-SNOM was demonstrated by Kersting *et al.* in 2003 based on a THz TDS system [273]. The setup is shown in Figure 4.12, where the THz beam is focused to the diffraction limit onto the surface of the sample and part of the incident radiation is scattered and absorbed by the tip-surface system. The transmitted THz radiation is detected either by electro-optic sampling or with a bolometer. They achieved a spatial resolution of 150 nm (λ/1000) for 2.0 THz pulses.

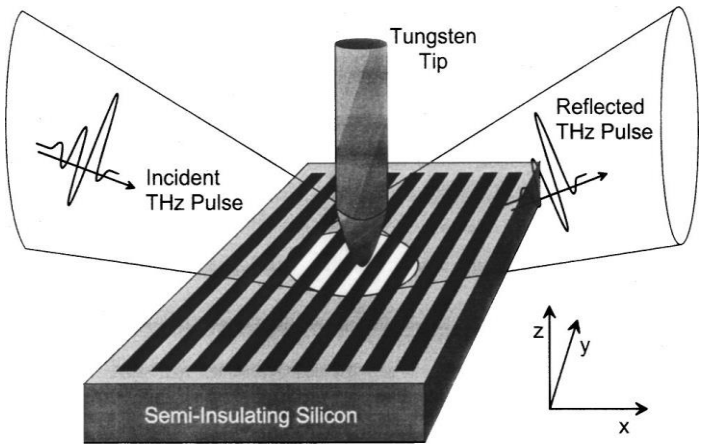

Figure 4.12 Setup for the first demonstration of THz s-SNOM, reprinted from [273], with the permission of AIP Publishing.

Since then, with the advancement of THz sources and detectors, many other THz s-SNOMs with different light sources (gas laser [229], THz QCL [274]–[276], THz TDS [277], etc.) and detection methods (direct measurement of scattering light [229], [253], [273], self-detection [274], [276], etc.) have been developed. The resolution has improved significantly as well. A spatial resolution of 40 nm at 2.54 THz was achieved by Hillenbrand *et al*. in 2008 with a continuous-wave CH_3OH gas laser, which is the first time to achieve a better than λ/1000 resolution within the THz range [229]. They imaged a semiconductor transistor and demonstrated simultaneous THz recognition of materials and mobile carriers in a single nanodevice, which opens the door to quantitative studies of local carrier concentration and mobility at the nanometre scale.

4.3.3 THz nearfield imaging with a QCL

QCL based THz nearfield imaging techniques can also be classified into two groups as with other nearfield imaging techniques: aperture type and scattering type. An aperture based system was first demonstrated by Degl'Innocenti *et al.* in 2009, with the setup shown in Figure 4.13 [278]. In this setup, a square aperture was placed in

proximity (4 μm) to the sample and a THz QCL lasing at 105 μm was used as the light source. A λ/10 resolution has been achieved with this setup. A nearfield imaging setup has also been developed with the nearfield probe in reference [272] and a 3.4 THz QCL.

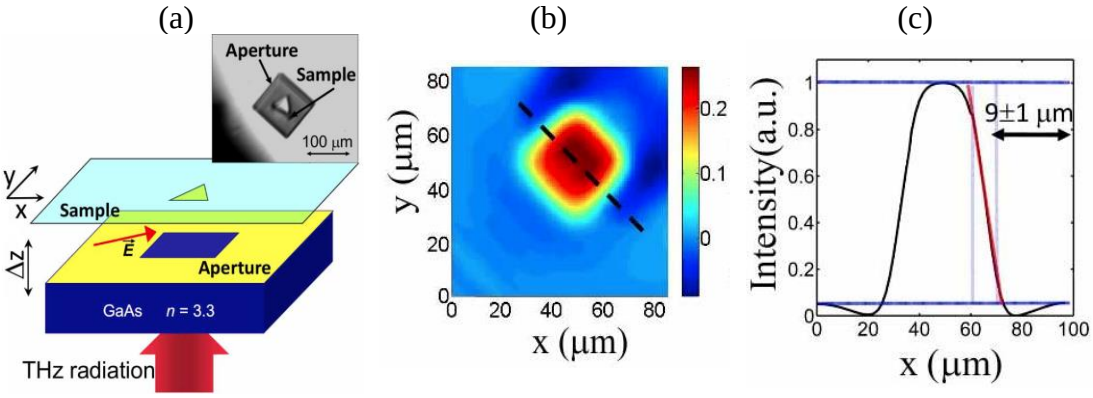

Figure 4.13 A differential nearfield scanning optical microscope. (a) Experimental setup; (b) image of a square metallic evaporation; (c) line profile extracted from the dashed line in (b). Adapted from reference [278] © 2009 Optical Society of America.

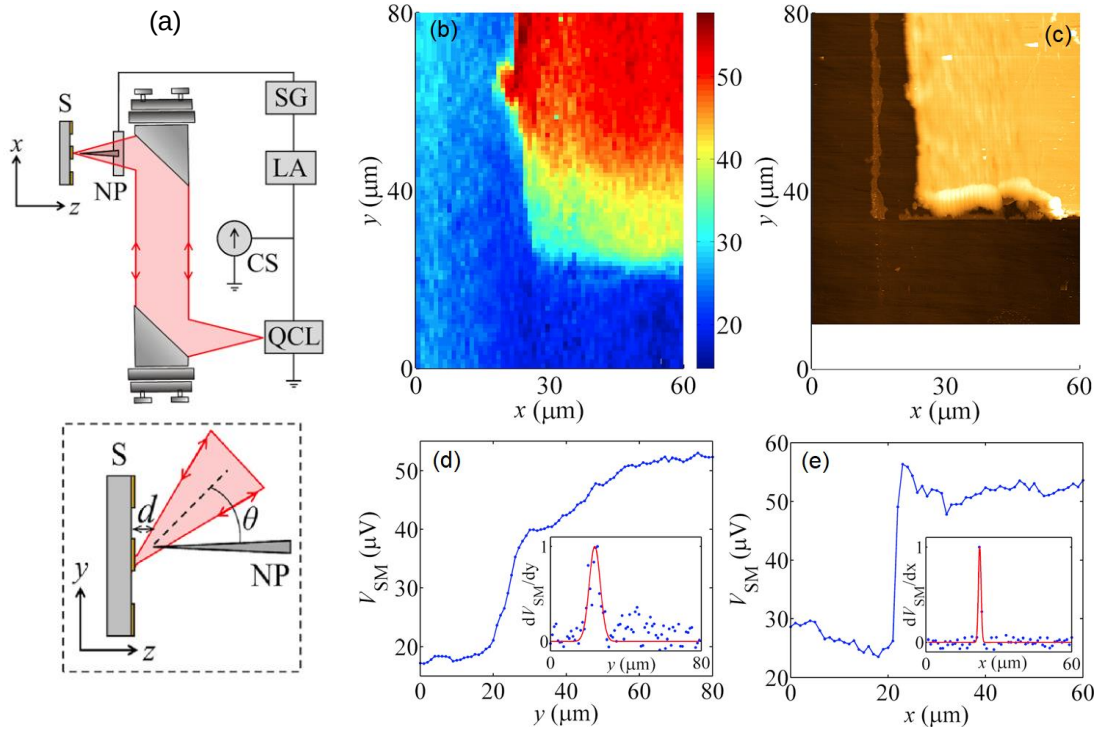

Figure 4.14 An s-SNOM with a THz QCL. (a) Schematic of the setup; (b) THz image of a rectangular region of 115-nm-thick gold deposited on a quartz substrate; (c) the corresponding topography image; (d) and (e) are the edge response functions in the x and y directions. Reprinted from [274], with the permission of AIP Publishing.

To achieve a higher resolution, a THz s-SNOM was developed with a QCL by Dean *et al.* in 2016 [274]. The schematic of the setup is shown in Figure 4.14, where the light from a 2.53 THz QCL is focused onto the tip of a horizontally oriented platinum-iridium needle using a pair of off-axis parabolic reflectors, with the beam axis forming a 50° elevation angle relative to the needle shaft. Here, the needle is kept at a constant height and the sample is scanned to get the THz response image. The scattered signal from the tip-sample nearfield interaction is detected with a self-mixing scheme, where the voltage perturbation of the QCL due to the external feedback from the scattering signal is measured. As no external detector is needed, the system can be very compact. With this setup, 1 μm (8.43 λ/1000) and 7 μm (59 λ/1000) resolutions have been achieved in the x and y directions, respectively.

4.4 Tuning fork based AFMs

Tuning forks have long been used as pitch standards for musical instruments. They were first introduced to quartz crystal resonators as a frequency standard in 1928 [279]. After they were applied on wrist watches in the late 1960s, they soon largely replaced the mechanical pendulums or springs as the dominant resonators for wrist watches [280], [281]. Economic and practical considerations within the watch industry have helped to shrink their size such that they are now appropriate as AFM sensors. Like piezoresistive sensors [282], quartz tuning forks have the advantage of self-sensing, therefore, the use of optics is not necessary and operation in ultrahigh vacuum and low temperatures are easily implemented [283]–[285], which is helpful for SPM. The tuning fork was first used as the position sensor for an AFM in 1988 [286], not long after the invention of the AFM itself. The past three decades have seen a significant improvement of the quartz tuning fork performance and the development of a wide range of applications based on it. This section will discuss the principle of a tuning fork as a distance sensor and how it can be incorporated into an AFM.

4.4.1 Theory of the quartz tuning fork

The basic principle of a tuning fork is familiar to musicians or physicists [281], [287]: it is a resonator composed of two prongs connected together at one end, and its resonance frequency is determined by its geometry and material. In a quartz tuning fork (QTF), the prongs are made from quartz with electrodes subsequently deposited on the surface [288], [289]. Using the piezoelectric material (quartz) makes it possible to replace the mechanical excitation of a tuning fork with an electronic excitation thanks

to the piezoelectric effect, which also allows direct measurement of the oscillation properties of the tuning fork, like amplitude and frequency, through the voltage.

A preliminary analytical study of the tuning fork can be performed by approximating the right half-section of a QTF as an L-shape bar and then its frequency is analysed by a cantilever beam model with Sezawa's theory which accounts for the effect of the clamped position of tuning fork base [290]–[295]. According to the theory, the resonance frequency of the tuning fork is given by

$$f = \frac{\alpha^2}{2\pi L^2}\sqrt{\frac{EI}{\rho A}} \tag{4.11}$$

where α is the eigenvalue of the boundary condition equation, L is the length of the probe, E is the Young's modulus, ρ is the mass density, I ($bh^3/12$) is the moment of inertia and A is the cross-sectional area. b is width and h is the height of the cross-section of the cantilever beam. An even simpler model, in which it is assumed that each prong of the tuning fork behaves as a clamped beam, can give a reasonably accurate prediction of the resonance frequency of the tuning fork. A set of resonant frequencies are established and the angular frequency for the first resonant mode is approximately described as [281]

$$\omega_0 = \frac{1.76a}{L^2}\sqrt{\frac{E}{\rho}} \tag{4.12}$$

where ω_0 is the resonant frequency and a is the thickness of the prong. For a standard commercial QTF, ω_0 is usually around 32 kHz.

As a resonator, the oscillation of the tuning fork can be described by a mechanical model, which has an equivalent electric model as a series resistor-inductor-capacitor circuit [296], [297], as shown in Figure 4.15. The tuning fork is modelled as a damped resonator in the mechanical model and its equation of motion is

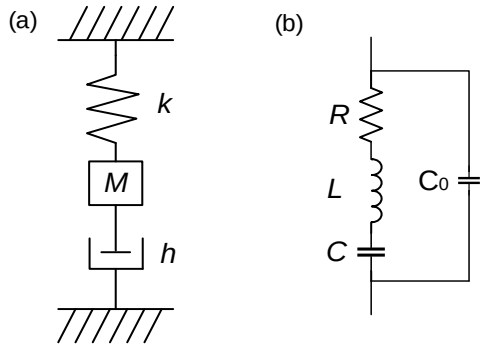

Figure 4.15 Mechanical model of the tuning fork as a damped resonator and (b) equivalent circuit model

$$mx(z,t)+h(z)x(z,t)+k(z)x(z,t)=\mathbf{F}\,, \tag{4.13}$$

which can be also expressed as equation (4.14), where x is the oscillation of the tuning fork, z is the distance between the tip and sample surface, γ is the damping constant, ω_0 is the resonance frequency, and F is a constant driving force.

$$mx(z,t)+m\gamma(z)x(z,t)+m\omega_0^2(z)x(z,t)=Fe^{-i\omega t} \tag{4.14}$$

The stead-state solution for equation (4.14) will be

$$x(z,t)=\frac{F/m}{\omega_0^2(z)-\omega^2-i\gamma(z)\omega}e^{-i\omega t}\,, \tag{4.15}$$

which is a Lorentzian function with a Q-factor

$$Q(z)=\frac{f_0(z)}{\Delta f(z)}=\frac{\omega_0(z)}{\sqrt{3}\gamma(z)}\,, \tag{4.16}$$

where Δf is the FWHM of the resonance. As can be seen, both the oscillation amplitude x and the Q factor are dependent on the distance z. During the oscillation, the movement of the left prong and the right prong will cancel out at the centre. This means there is no centre-of-mass movement and results in a very high Q factor, which is typically of the order of 10^3–10^4 at ambient conditions and can be several orders of magnitude higher in vacuum.

4.4.2 Tuning fork as a force sensor for AFM

QTFs have been widely used as force sensors for SPM [282]–[286], [298]–[306]. In an AFM, when the probe (tuning fork with tip attached) approaches the sample surface, two forces will be influenced: the dissipative friction force associated with the second term in equation (4.14) and a reactive elastic force due to the third term in equation (4.14). Both of them are contributed from two parts: a static part which is determined by the physical properties of the tuning fork and a near-field interaction induced contribution. To get the interaction part of the damping factor, the oscillation equation (4.15) at a resonant condition can be used, which gives

$$\gamma(z)=\gamma_{\text{stat}}+\gamma_{\text{int}}(z)=\frac{F/m}{\omega_0(z)x_0(z)}\,, \tag{4.17}$$

with x_0 being the oscillation amplitude. If $z\to\infty$, $\gamma_{\text{int}}(z)$ should go to zero. As a result

$$\gamma_{\text{int}}(z) = \gamma_{\text{stat}}\left(\frac{\omega_0(\infty)x_0(\infty)}{\omega_0(z)x_0(z)} - 1\right). \tag{4.18}$$

The third term in equation (4.13) gives the relationship between the mass and the stiffness $k_{\text{stat}} = m\omega_0^2(\infty)$. By combining this with equation (4.14), the friction force can be calculated as

$$F_{\text{int}}^{\text{friction}}(z) = m\gamma_{\text{int}}(z)\omega_0(z)x_0(z) = \left(1 - \frac{\omega_0(z)x_0(z)}{\omega_0(\infty)x_0(\infty)}\right)\frac{k_{\text{stat}}x_0(\infty)}{\sqrt{3}Q(\infty)}\ . \tag{4.19}$$

As the resonant frequency ω_0 changes much slower with distance than the amplitude x_0, $\omega_0(z)/\omega_0(\infty)$ can be dropped from the term in the bracket. In addition, the voltage V due to the induced charge at the surface of the tuning fork is directly proportional to the oscillation amplitude [221] and thus

$$F_{\text{int}}^{\text{friction}}(z) = \left(1 - \frac{V(z)}{V(\infty)}\right)\frac{k_{\text{stat}}}{\sqrt{3}Q(\infty)}x_0(\infty) \tag{4.20}$$

The elastic force can be obtained in a similar way as

$$F_{\text{int}}^{\text{elastic}}(z) = k_{\text{int}}(z)x_0(z) = \left(\frac{\omega_0^2(z)}{\omega_0^2(\infty)} - 1\right)k_{\text{stat}}x_0(z) \tag{4.21}$$

In a realistic case, for instance, a 32 kHz tuning fork, with spring constant $k_{\text{stat}} = 40\text{kN/m}$ and a quality factor with attached tip being $Q(\infty) \approx 1200$, oscillates at an amplitude of $x_0(\infty) = 10$ pm. An amplitude change of 10% will give $F_{\text{int}}^{\text{friction}}$ of about 20 pN, which is much weaker than for the 5 Hz induced frequency shift $F_{\text{int}}^{\text{elastic}}$ (amplitude ~110 pN) [221].

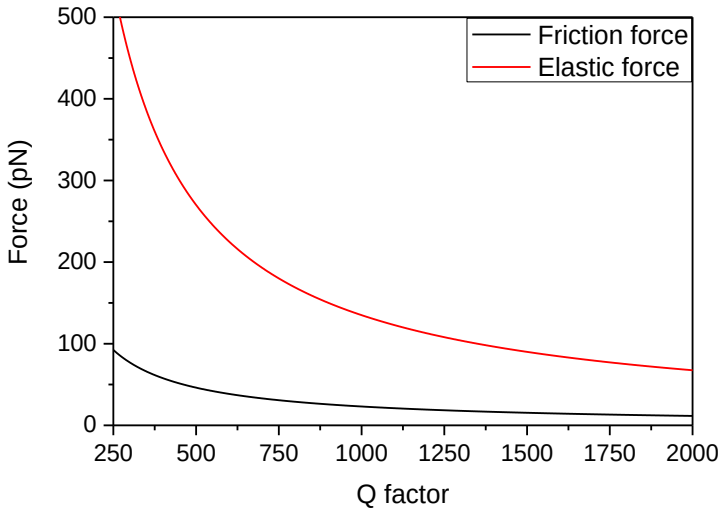

Figure 4.16 Fraction force and elastic force experienced by a tuning fork as a function of the Q factor

Figure 4.16 shows the trends of friction force and elastic force when the Q factor changes, showing that the elastic force is larger than the friction force. Therefore, measuring the friction force will give a higher sensitivity. However, measurements of $F_{\text{int}}^{\text{friction}}$ rely on measurements of amplitude variations which are inherently slow for high Q-factors. As a result, measurements of frequency shifts and thus of $F_{\text{int}}^{\text{elastic}}(z)$ represents a good compromise between sensitivity and speed.

4.4.3 Tip-sample distance control

When the tip is approaching the sample surface, both the elastic and friction force will increase, which will give a larger *k* and γ. As a result, ω_0 will increase and x_0 will decrease, since $\omega_0 = \sqrt{k/m}$ and $x_0 = F/(m\omega_0\gamma)$. The ratio of $x_0(z)/Q(z)$ is independent of *z* [221], so that as the probe gets closer to the surface, a reduction in the oscillation amplitude always corresponds to a proportional drop in the Q factor. Therefore, the distance between the tip and sample surface can be measured by monitoring either the oscillation amplitude or the frequency of the tuning fork, which can then be used as a feedback signal to keep the tip sample distance constant through a negative feedback loop, as shown in Figure 4.17. In the feedback loop, the oscillation amplitude or frequency is first measured and compared to the setpoint, which generates an error signal. After the error signal is transformed into voltage signal and amplified, it is applied on the piezo positioner, which will move the tip to a new height and change the oscillation amplitude or frequency. Therefore, every time the tip-sample distance changes, the feedback loop will take the tip to a new height to keep the distance constant.

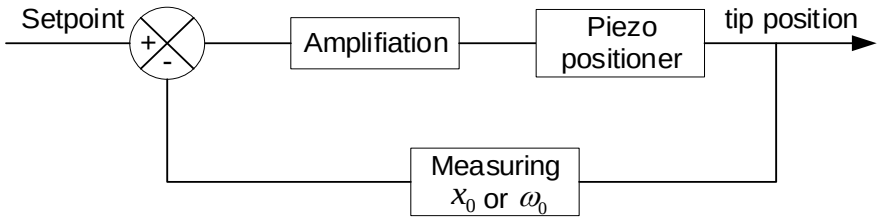

Figure 4.17 Schematic of a feedback loop used to control the tip sample distance

4.4.4 Response time

For an SPM, the response time of the tip position to the tip-sample distance change is an important parameter, which will determine the achievable scanning speed. For a resonator, the response time is mainly determined by its Q factor: the higher the Q factor of a system, the longer it takes to respond to an external signal. On the other hand, a

high Q-factor is a prerequisite for high sensitivity. As a result, a compromise is needed to adjust the parameters of a tuning fork used for probe–sample distance control so that there is sufficient sensitivity to prevent probe or sample damage and the response time is sufficiently short to guarantee reasonable scanning speeds. The steady state solution of the tip oscillation (equation (4.15)) can be expressed in terms of amplitude and phase

$$x(t) = x_0 \cos(\omega t + \varphi_0) \ . \tag{4.22}$$

where the amplitude is

$$x(z) = \frac{F/m}{\sqrt{\left(\omega_0^2(z) - \omega^2\right)^2 + \omega_0^2(z)\omega^2/3Q^2(z)}} \tag{4.23}$$

and the phase is

$$\varphi_0 = \tan^{-1}\left(\frac{\omega_0 \omega}{\sqrt{3}Q(\omega_0{}^2 - \omega^2)}\right) . \tag{4.24}$$

When the tip-sample distance *z* is changed, the resonant frequency ω_0 will change to new values ω_0' at t=0. The new solution can be found through equation (4.14) with proper boundary conditions to be [307]

$$x(t) = x_0' \cos(\omega t + \varphi_0') + x_t e^{-\omega_0' t/(2\sqrt{3}Q)} \cos(\omega_t t + \varphi_t) \ . \tag{4.25}$$

The solution consists of a steady-state term (left) and a transient term (right). x_0' and φ_0' are the new steady-state amplitude and phase, respectively, while x_t, ω_t and φ_t are the corresponding parameters of the transient term, which are adjusted to fit the boundary conditions. The oscillation amplitude will be

$$\left|x(t)\right| = \sqrt{x_0'^2 + x_t{}^2 e^{-\omega_0' t/(\sqrt{3}Q)} + 2x_0' x_t e^{-\omega_0' t/(\sqrt{3}Q)} \cos[(\omega_t - \omega)t + (\varphi_t - \varphi_0')]} \ . \tag{4.26}$$

To illustrate how the Q factor will affect the response time, a numerical simulation is performed with equation (4.26) , which gives the oscillation amplitude evolution of a 32 kHz tuning fork with different Q factors after an abrupt change in tip sample distance, with the result shown in Figure 4.18. It can be seen from equation (4.26) that it takes about $2\sqrt{3}Q$ oscillations for the tuning fork to reach a new steady state and the response time of a tuning fork is given by

$$\tau = \frac{2\sqrt{3}Q}{\omega_0'} \cong \frac{2\sqrt{3}Q}{\omega_0} \tag{4.27}$$

For a tuning fork with a Q factor of 500 (most of the tuning fork used in our system has a Q factor around 500), the response time is about 200 ms. As a result, if the oscillation amplitude is used for feedback, the bandwidth of the feedback loop will be very low

and the scanning speed will be very slow, especially for high Q factor tuning forks. To overcome this, the frequency modulation method was proposed, which utilizes the resonant frequency as the feedback signal. In an ideal situation, the resonant frequency will change immediately upon a perturbation. It takes at least one oscillation period to measure the frequency of an oscillation, which is a much shorter period compared to the time of $2\sqrt{3}Q$ oscillations. Therefore, in this thesis, the frequency shift is used as the feedback for tip-sample separation control. The frequency shift can be measured using a Phase Lock Loop (PLL) [289], [308], [309], which needs several oscillations to track the relative phase of a signal compared to a reference.

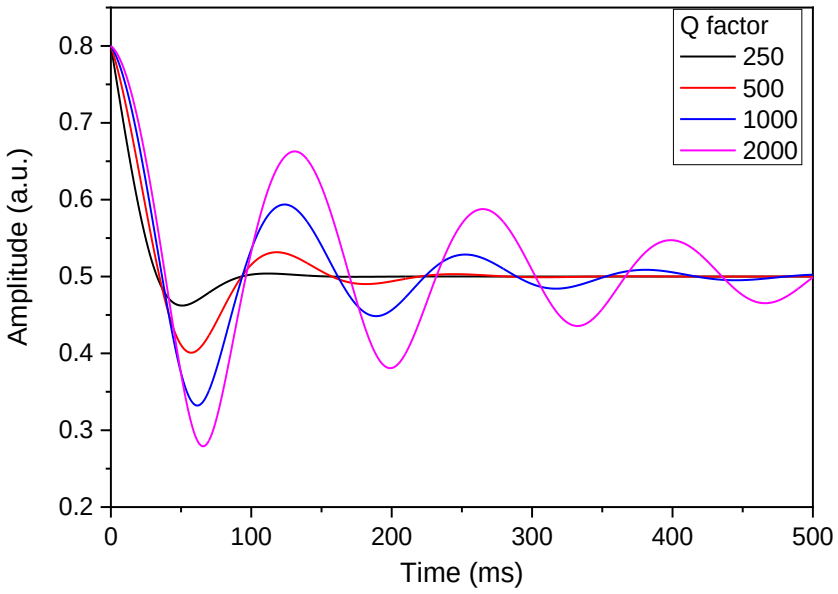

Figure 4.18 The oscillation amplitude of a tuning fork with different Q factors. The resonant frequency is 32 kHz, and the Q factor varies from 250 to 2000, which are the typical Q factor value of the tuning forks used in this work.

4.5 Experimental setup

Considering the advantages of the tuning fork system for low temperature operation, self-sensing as well as compactness, the QTF based AFM has been used in this work as a base platform for the THz s-SNOM. The home-built system mainly contains two parts: the optical part and the AFM part. Figure 4.19 shows a 3-dimensional model of the whole setup. The optical part gives the optical image of the sample and includes a THz QCL, a cryostat for cooling the THz QCL and two parabolic mirrors for focusing the light on the probe. The AFM gives the topography of the sample and includes a scanning stage, a QTF tip sample distance control system and a vibration isolation platform.

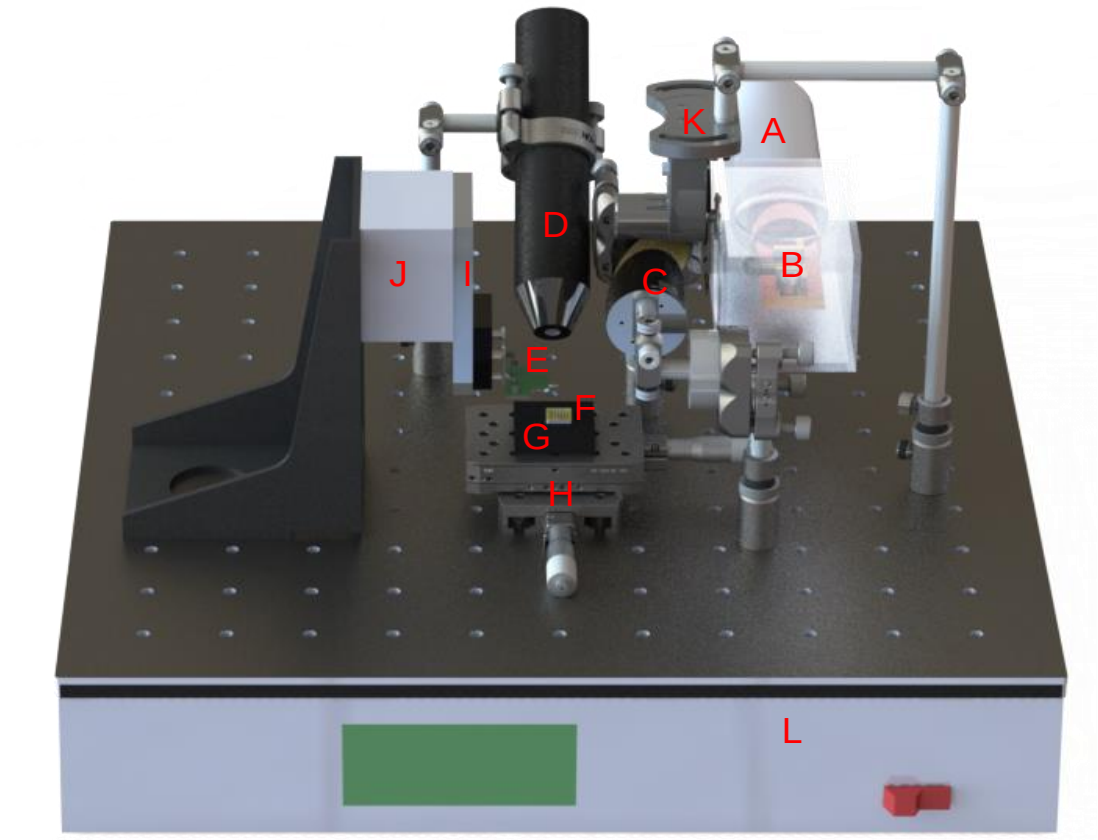

Figure 4.19 A 3-dimensional model of the experimental setup: A- cryostat; B- THz QCL; C-parabolic mirrors; D- microscope; E- tuning fork with tip; F- sample; G- *xy* nano scanner; H- *xy* coarse positioner; I- z nano positioner; J- z micro positioner; K- mechanical chopper; L- active isolation platform

The principle of the setup is illustrated in Figure 4.20 (a). The laser light is collimated and focused by two 2-inch f/1 off-axis parabolic mirrors with ~30° incident angle. When the beam is illuminating the metallic tip, a positive change in the laser power is detected due to the feedback of the scattered light from the tip. A higher feedback in the laser cavity corresponds to a reduced bias measured on the QCL, as schematically shown in Figure 4.20 (b) and also in Figure 4.21 (a). The apparatus is then arranged for the collection of the scattered light with a self-detection method, which will be discussed later.

The topography of the sample is recorded by a home-built AFM and the sample is scanned in the xy plane. For each xy position, measurements are recorded for both the height of the tip, yielding the surface topography, and the signal from the lock-in amplifier, corresponding to the THz scattered signal and yielding the THz image.

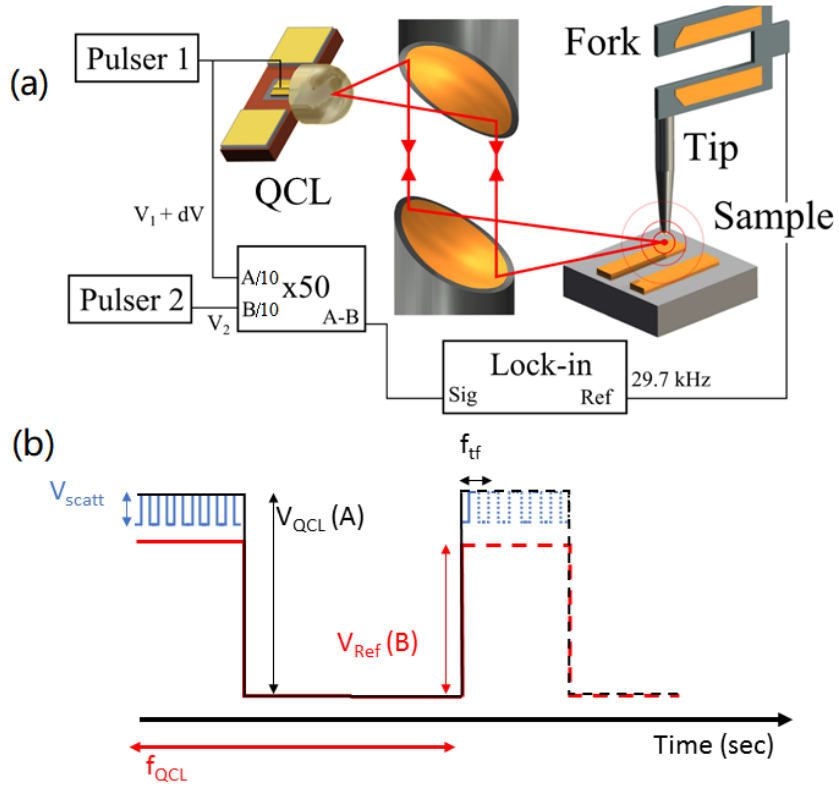

Figure 4.20 (a) Schematic of the experimental setup. The tuning fork oscillation frequency is set as the reference frequency of the lock-in amplifier. The tip/tuning fork system operates in tapping mode. The input of the lock-in amplifier is given by the amplified voltage difference between the bias applied to the QCL and another, frequency synchronized, pulse. (b) Acquisition scheme with the self-mixing technique. The scattered light into the cavity yields a reduction in the QCL bias V_{QCL} oscillating at the reference frequency of the tuning fork f_{tf}. This is compared to the bias of a second pulser V_{Ref} before being amplified.

4.5.1 Light source and self-detection

The light source for this THz s-SNOM is a 2.85 THz QCL (QCL-H in Appendix A). The QCL is fabricated with a single plasmon waveguide and has a bound-to-continuum active region design. In order to enhance the sensitivity of the system, as well as the collection of the scattered light, a silicon lens is attached to the QCL with an 18.5 µm thick antireflection parylene coating. The lens mounting has two primary aims: increasing the collection efficiency of the back-scattered light, and increasing the cavity mirror loss, rendering the device more similar to a quantum cascade amplifier [155]. By carefully attaching the lens to the facet of the laser using a layer of PMMA, the emission can be strongly reduced but not fully suppressed. Partially suppressed laser emission is needed in order to align the beam onto the metallic tip. The QCL is operated in a continuous flow liquid helium cryostat with the temperature kept at 5 K. The LIV characteristics of the device with and without feedback from a gold coated flat mirror

and the original laser without anti-reflection coating are presented in Figure 4.21 (a). Its spectrum is displayed in Figure 4.21 (b). The laser is operated at the current density corresponding to the maximum emitted power and mounted into the cryostat such that the E-field has a polarization component along the tip shaft as only this component can excite strong nearfield interaction. The optical path is finely adjusted in order to have a maximal back-scattered signal into the cavity.

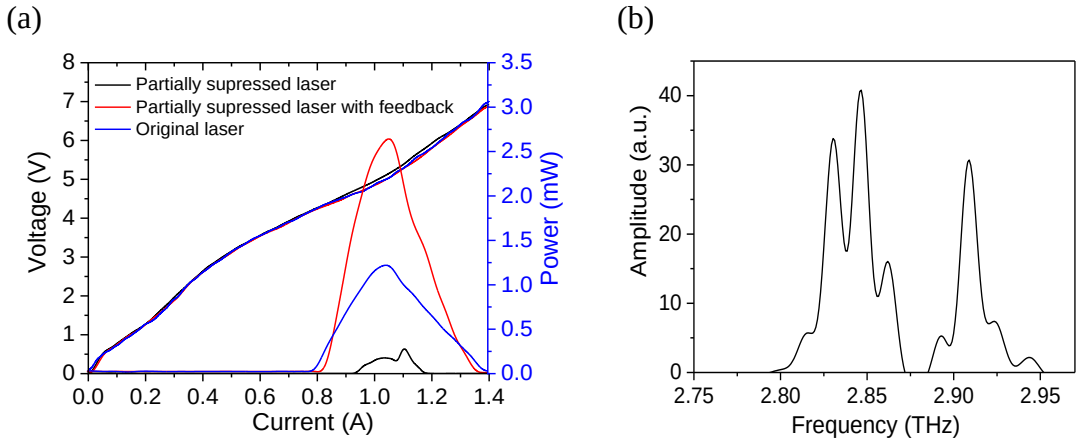

Figure 4.21 (a) LIV curve and (b) spectrum of the THz QCL used in the setup

The detection method for the THz scattered light used here is a self-mixing scheme, which is reported in Figure 4.20 (b). To amplify the small voltage perturbation V_{scatt} on the laser bias V_{QCL} caused by the scattered light, it is first subtracted with an identical pulse V_{Ref} synchronized to the repetition rate of the QCL f_{QCL}, kept fixed to 2 kHz with 10% duty cycle. The voltage difference between the two pulses V_1 and V_2 in Figure 4.20 (a) needs to be kept as low as possible in order to use the minimum sensitivity scale on the lock-in amplifier, thus minimizing the noise. The voltage difference has been magnified in Figure 4.20 (b) for clarity. The difference in voltage is then amplified and fed to the lock-in amplifier which takes the resonant frequency of the tuning fork f_{tf} as its reference. The amplitude of the output signal from the lock-in amplifier is finally taken as the THz signal.

In this system, the self-mixing effect is in a different regime compared with the one discussed in Chapter 2. Here, as the QCL is only partially suppressed from lasing and the feedback signal (scattering light) from the scanning tip is very weak (< 1 nW) compared to the QCL output power (around 0.2 mW), the system operates in a weak feedback regime like the normal self-mixing arrangement. Therefore, the self-mixing signal is dependent on both the laser frequency and the optical path length, which determine the phase difference of the laser filed between the internal cavity and the external cavity.

4.5.2 Topography measurement

Topography data obtaining with the s-SNOM is measured using a home-built tuning fork AFM. Several key elements are needed for building an AFM: a tuning fork with tip attached, controllable stages for adjusting the probe height and scanning the sample, and a microscope for monitoring the probe position, along with associated illumination. A feedback loop is also needed for keeping the tip-sample distance constant. In addition, software is needed for acquiring the data for tip height as a function of xy coordinates.

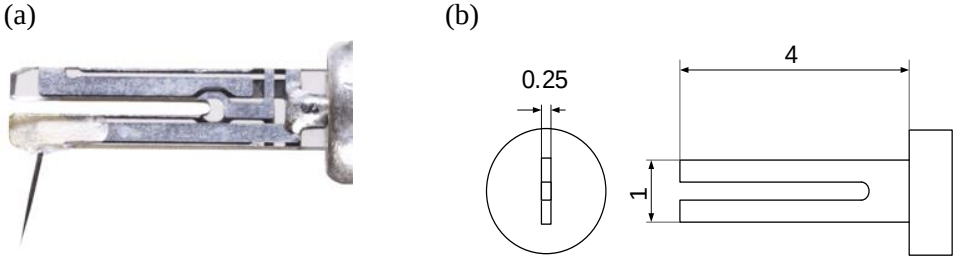

Figure 4.22 (a) A photo of the tuning fork and (b) its dimensions

The tuning forks used in the setup are from a commercial company (Mad City Labs, Inc.) and have dimensions of 4×1×0.25 mm, as shown in Figure 4.22. The tuning fork, which has a typical resonant frequency of ~30 kHz, incorporates a tungsten tip, with a 2 mm length, 80 μm diameter, and a <50 nm tip radius. The tuning fork is mounted on a probe board, which has two configurations depending on the tuning fork oscillation direction: shear force and normal force. In this work, as the tapping mode will be used, the normal force configuration will be adopted and the tuning fork oscillates in the direction perpendicular to the sample surface, as shown in Figure 4.23 (a), which produces the modulation for background noise elimination.

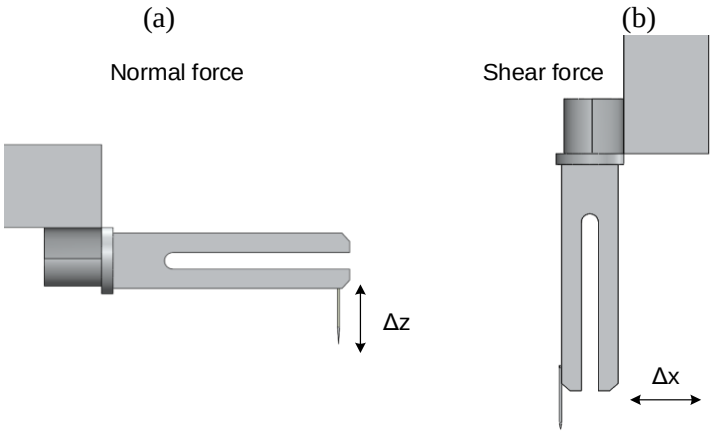

Figure 4.23 Two configurations of the tuning fork with a tip attached: (a) normal force and (b) shear force

The whole probe board/tuning fork module is then attached on a nano-positioner (NANO-OP65 from Mad City Labs, Inc.) with 65 µm travel range and 0.13 nm minimum step-size. A micro-positioner (SPM-MZ from Mad City Labs, Inc.) with a 25 mm travel range and 95 nm minimum step-size is used to bring the tip close to the sample surface with a distance within the travel range of the nano-positioner. When the system is brought into close proximity to the sample surface, the tuning fork resonance is damped, such that the amplitude, frequency or phase can be used as a feedback signal to keep a constant tip-sample distance, typically between 30 nm and 100 nm.

For sample scanning, two piezoelectric stages (from Physik Instrumente Ltd) with 250 µm travel range in each direction and 0.4 nm minimum step size are employed. Two manual positioners (from Thorlabs Inc.) with 12 mm of travel and 100 nm minimum step-size are used to roughly adjust the position of the sample before a scan.

To be able to see the probe height and roughly the scanning area by eye, an optical microscope is constructed using a CMOS camera with 2048×2048 pixels over a 1 $inch^2$ detection area, coupled with a ×10 objective lens. The microscope is connected to the computer so that its captured image can be shown in real time on the screen. It is positioned at a ∼45◦ angle with respect to the vertical, to allow both the probe and sample to be in the field of view once the probe is within 50 µm from the surface.

The feedback loop is fulfilled with a commercial controller (MadPLL from Mad City Labs, Inc.), which can use either oscillation amplitude, frequency or phase as a feedback signal. The controller records the tip height as well. A LabVIEW program records the height value at each point during a snake scan to form the topography.

For many measurements, the sample is not level when it is scanned. As a result, there is usually a tilt on the topography image. This does not have any influence on the THz image as the THz signal is only determined by the distance between the tip and the sample, which is always kept constant. However, for the topography image, it will deteriorate the image contrast, and some fine structures might be buried within this tilt. To increase the topography image contrast, a flattening process is performed for all the topography images. To remove the tilt, two lines are chosen near the two edges on the image in the y direction. The tip height is then averaged along the two lines, with average values of A and B. The difference of them (A-B) is then divided by the number of the lines between them L_n to give the slope in the y direction (A-B/ L_n). All the lines in the y direction is recalculated by taking the first line as a reference and removing the tilt. For instance, for a data point x in the n_{th} line, it will be recalculated as $x' = x - \mathrm{n} \cdot (\mathrm{A\text{-}B}/\mathrm{L_n})$. The same processing is also applied to the lines in the x direction.

4.5.3 Exemplary measurement results

A typical measurement example is showed in Figure 4.24, taken by Dr. Robert Wallis. This picture reports (a) the optical micrograph of the sample, (b) the topography and (c) the THz scattered image. The scanned sample area is a $14\ \mu m \times 9\ \mu m$ rectangle, which consists of metallic features over a SiO_2 substrate. The sample has two overlapping metallic areas. The metallic region defined with optical lithography (Ti/Au 10/500 nm) is reported in blue. The metallic area fabricated with electron beam lithography (Ti/Au, 80/20 nm) is indicated in green.

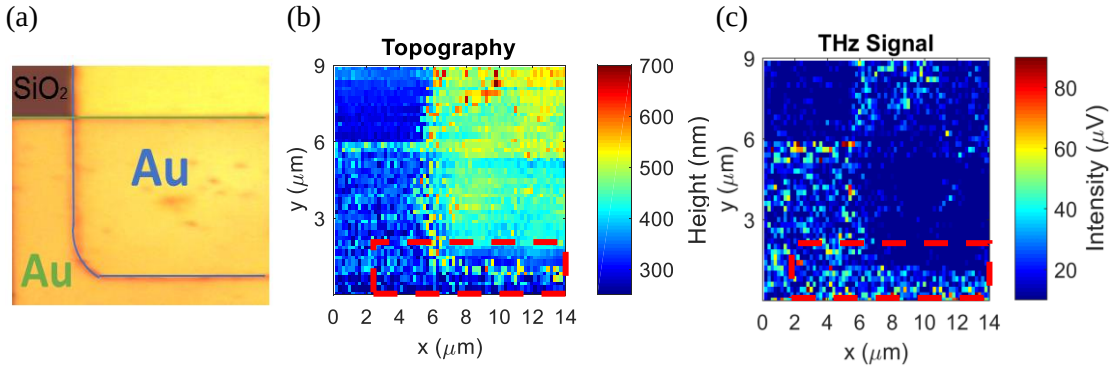

Figure 4.24 (a) Optical microscope image, (b) topography and (c) THz image of an exemplary sample, modified from [275]. The THz signal is taken at the resonance frequency of the tuning fork.

Assuming that the relative permittivities are 3.9 for SiO_2 and -106000 + 193000i for the Au features [214], [257] respectively and the W-tip has an apex radius of ~ 40 nm and ε_{tip} of – 37817.448-i 60952.753 [213], the effective polarizability α_{eff} of the nearfield interaction at different areas can be calculated with equation (4.8) for different tip-sample distances, as shown in Figure 4.25. It shows a reduced polarizability, hence scattering efficiency, for the dielectric substrate SiO_2 with respect to the Au area. Also, a nearfield effect can only be observed when the distance between the tip and sample is smaller than 40 nm, comparable to the tip radius.

The THz image presented in Figure 4.24 (c) shows comparable values for the scattering signals on the SiO_2 and the thicker Au evaporation. In contrast, the THz signal recorded over the metallic evaporation obtained via E-beam lithography, corresponding to the horizontal stripe, presents a significantly increased signal in comparison with them. The scattering signal intensities in the SiO_2 and E-beam Au area are averaged in the two area respectively, which gives an average intensity of 8.5 µV and 20 µV. Therefore, the THz signal on E-beam gold is 2.35 times the one on SiO_2, which is much higher than 1.3, the number calculated using equation (4.8) and reported in Figure 4.25.

This might be attributed to the increased roughness, as also shown by the topography, and uniformity of this area. The induced dipole itself and the tip radius have sizes comparable to the roughness and to the total thickness of this metallic layer which might interact efficiently with the total scattering [310]. At the same time, the $(z+r)^3$ dependence in the effective polarizability's denominator causes the distance behaviour of the signal to steepen with increasing demodulation harmonic [311]. This will introduce discrepancy between the measured and calculated signal ration as well as only the first harmonic signal is recorded.

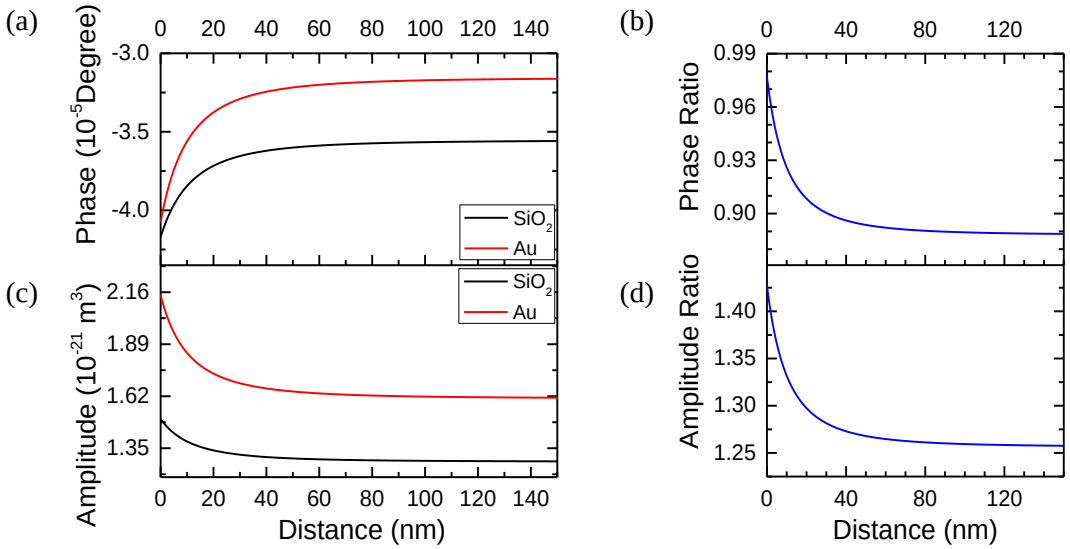

Figure 4.25 Effective polarizability calculated for the different sample materials shown in Figure 4.24. Au features tend to increase the effective polarizability in comparison with dielectric materials. (a)/ (c) are the phases/amplitudes of the effective polarizability with the sample material being SiO_2 or Au; (b)/(d) are the ratios of the effective polarizability phases/amplitudes between Au and SiO_2.

A second scan over the red rectangular area of Figure 4.24 has been recorded with a 100 nm step-size and the topography and corresponding THz signal are reported in Figure 4.26 (a) and (b), respectively. Several profiles have been extracted from the dashed area of Figure 4.26 (b), to measure the resolution, which, as shown in Figure 4.26 (c), is calculated to be ~ 78 nm, by using the 10%-90% criterion. This corresponds to a spatial resolution of ~ λ/1200, which is comparable to the resolution achieved at these frequencies with a methanol gas laser [229], but obtained with an emitting source with < mW emitting power and without the need of an extra detecting element. At the same time, this system yields an improvement of more than 10 times compared to similar nearfield systems implementing THz QCLs [272], [278].

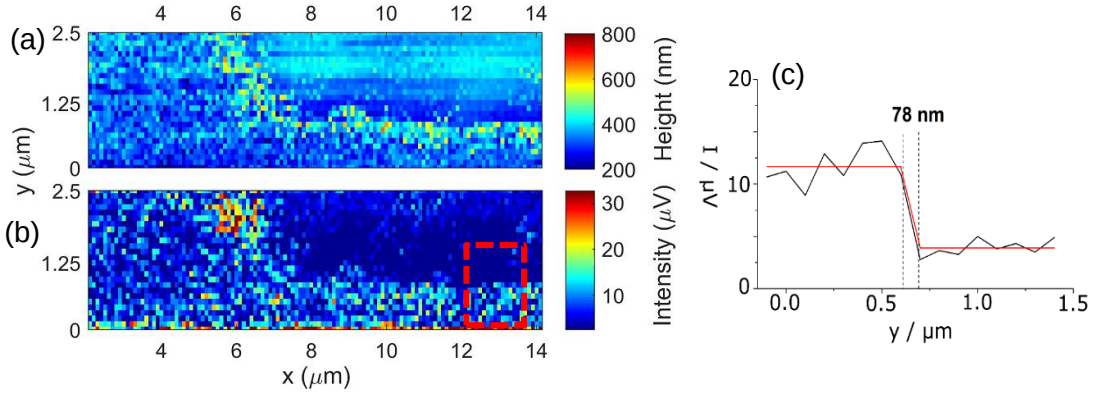

Figure 4.26 Topography (a) and THz image (b) acquired with 100 nm step-size of the metallic features shown in Figure 4.19 (a). From the profiles extracted in the dashed area in (b) it was possible to obtain an estimation of the spatial resolution of the system (c), calculated to be 78 nm, which is better than $\lambda/1000$, modified from [275]. The THz signal is taken at the resonance frequency of the tuning fork.

4.6 Topography improvement

As a first demonstration of an s-SNOM based on tuning fork AFM and a THz QCL, the setup is put on a rigid optical bench, which does not have oscillation isolation and is operated in an ambient environment. It is stable enough to scan a sample with large height contrast in topography but struggles to measure finer structures as it is even difficult to get a faithful topography of the sample with this setup. If the topography resolution is not sufficiently high, it is impossible to get a high resolution on the THz image. Therefore, several measures have been taken to increase the stability of the system, and thus the topography resolution. I would like to acknowledge the help from my colleague Nikita Almond for the work finished in this section.

4.6.1 Acoustic vibration isolation

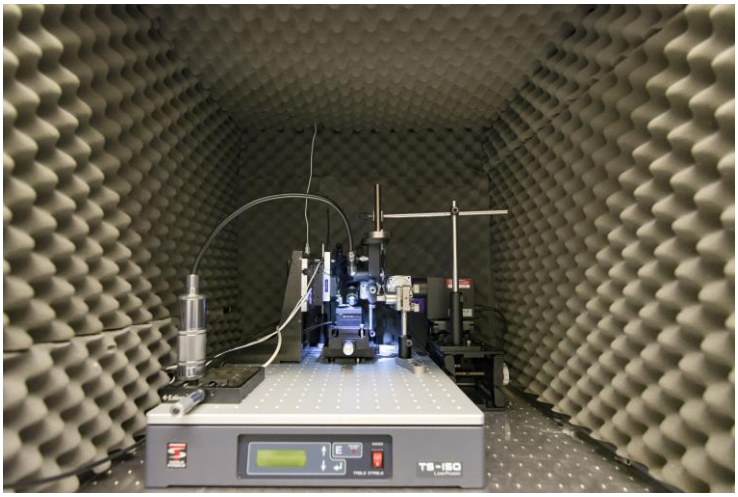

Figure 4.27 Sound isolation box for the THz s-SNOM

The first thing to do is reducing the air current, which can be achieved by putting the whole setup in a closed box. A sound isolation box (SIB), shown in Figure 4.27, is made to reduce both the air current and the vibrations induced by sound waves, as usually seen in an AFM setup. The box is made with plastic panels with an aluminium frame. Sound absorption foam is put on the panels to absorb external sounds.

Figure 4.28 compares the tip oscillation amplitude before and after using the SIB. As can be expected, a drop in the amplitude is seen (from 200 nm to about 100 nm). Without the SIB, there is a long-time drift on the tip position, which is reduced with the SIB as well. For all the future measurements, they will be conducted with the SIB. In the future, the SIB will be sealed for nitrogen purge, so that the influence of the water vapor can be reduced, which might increase the sensitivity of the system as the water absorption of the THz scattering signal will be reduced.

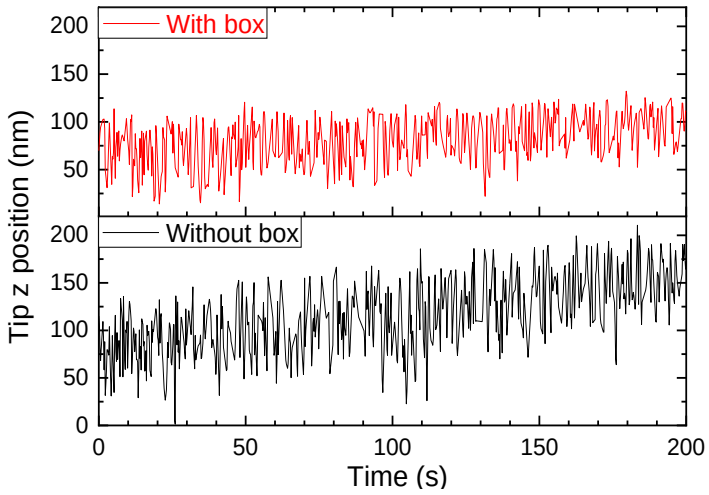

Figure 4.28 The oscillation of the tip with (red) and without (black) the sound isolation box.

4.6.2 Mechanical vibration reduction with passive isolation

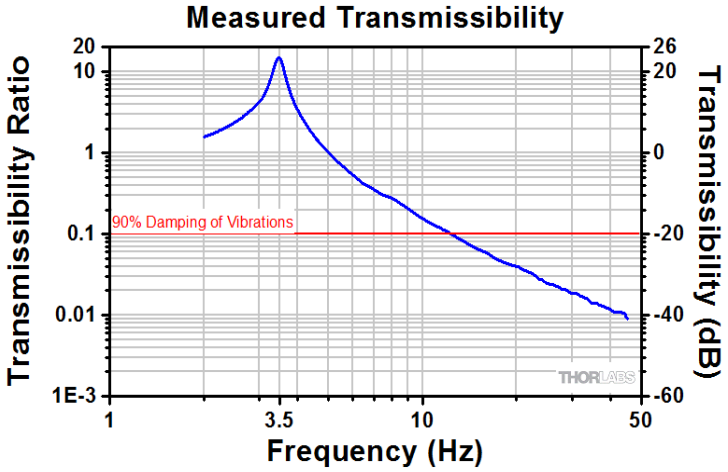

Figure 4.29 Transmissibility curve of the PTT600600 IsoPlate Support Plate, from [312].

The setup initially sits on a rigid optical bench, which does not provide any vibration isolation. To reduce the mechanical vibration, the setup is moved from the rigid optical bench onto a floating optical bench, which uses pneumatic vibration isolators with automatic re-leveling and tie bar flange as table supports. The isolators can isolate 94% of the vibration at 5 Hz and 98% of the vibration at 10 Hz [313]. However, two of the isolators are broken, therefore, the floating optical bench can only provide passive vibration damping. Because of the large mass, it cannot isolate high frequency vibrations. To improve the damping at high frequency, a passive isolation platform PTT600600 IsoPlate Support Plate from Thorlabs is put between the floating optical bench and the setup. The transmissibility curve of it is shown in Figure 4.29. As can be seen, the vibration can be reduced by 90% above 11 Hz.

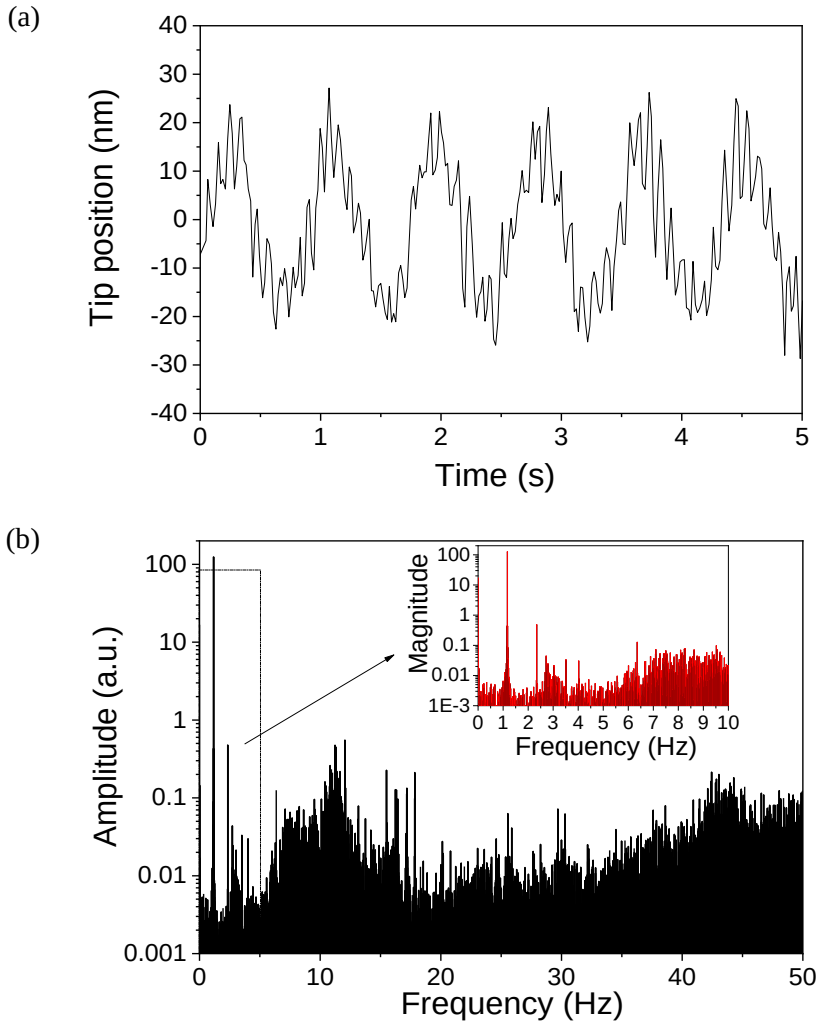

Figure 4.30 The oscillation of the tip when a passive isolation platform is used on a floating table: (a) Tip position versus time; (b) Fourier transform of waveform. For FFT, the sampling rate and sampling time are 100 Hz and 50 s, respectively, which give a 0.02 Hz frequency resolution and a 50 Hz bandwidth.

The tip position over time is recorded in this configuration, which is shown in Figure 4.30 (a) and gives an about 50 nm oscillation amplitude. The tip position is Fourier transformed to analyse the frequency domain properties of the oscillation, as shown in Figure 4.30 (b). There is a very large component at about 1.2 Hz. Vibrations at around 2.4 Hz, 3.6 Hz also exist in the system. They are suspected to originate from the slow oscillation of the optical bench as the resonance frequency of the pneumatic vibration isolators for bench supporting is around 1 Hz. The Thorlabs passive isolation platform can only suppress high frequency noises while the low frequency component remains. Furthermore, there is still a considerate amount of high frequency vibration left.

To evaluate the resolution of the new configuration, two calibration samples (grating structures with different heights on a Si substrate with 3 µm period) have been measured: one with a grating height of 108 nm and the other 20 nm. The results are shown in Figure 4.31. Both graphs have been flattened. For the 108 nm sample, even if the topography is not good, the structure of a grating can still be seen. However, for the 20 nm high sample, it is even hard to see the grating structure. As a result, to see features with a height contrast around 20 nm, the stability of the setup needs to be further improved. An obvious approach is to eliminate or reduce the amplitude of the 1.2 Hz noise and its high order harmonics.

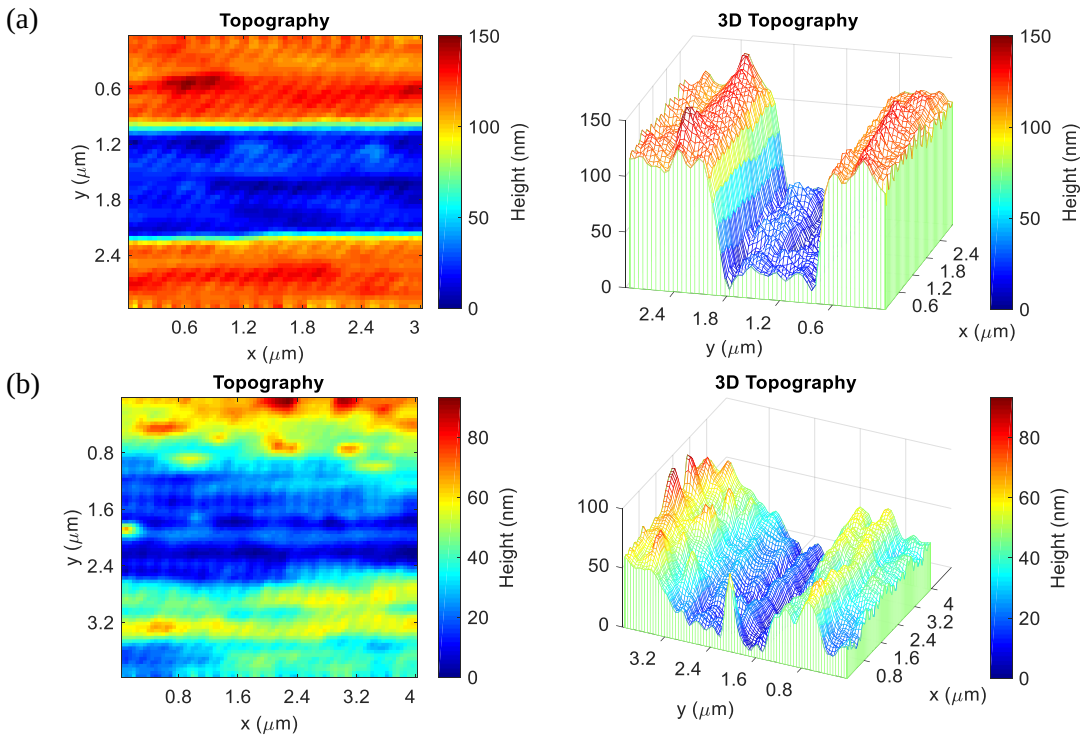

Figure 4.31 Topography of a (a) 108 nm high grating and (b) 20 nm grating when the system is on a passive oscillation isolation platform.

4.6.3 Mechanical vibration reduction with active isolation

To further reduce the high frequency vibrations as well as the effect of the 1.2 Hz noise and its high order harmonics, an active isolation platform (AIP) TS-150/LP is purchased from HWL Scientific Instruments GmbH and put underneath the setup. The whole system is still put on the floating optical bench. The transmissibility curve of the AIP in the vertical direction is shown in Figure 4.32. As can be seen, it can reduce 68 % and 99% vibration at 2 Hz and above 10 Hz, respectively. It can also reduce the 1.2 Hz vibration by 35%.

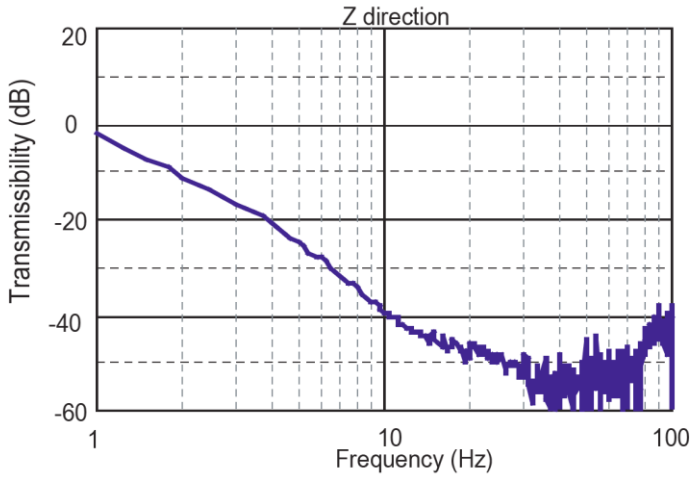

Figure 4.32 Vertical transmissibility curve of the TS-150/LP active vibration isolation system, from [314].

It can operate in three different modes, the definition of which is listed in Table 4.1. The first mode is off/off mode, when the AIP is not powered. In this case, the AIP is locked and functions as a rigid support, which means it provides no vibration isolation. The second mode is on/off mode, when the AIP is powered but the active isolation is off. The AIP is unlocked and can provide passive isolation. In the last mode, the AIP is powered, and the active isolation is switched on. This is the normal operation mode of the AIP and it provides active isolation in this case.

Table 4.1 Three operation modes of the TS-150/LP AIP

Operation mode	AIP	Active isolation	Isolation
off/off	off	off	no
on/off	on	off	passive
on/on	on	on	active

To evaluate the effect of the AIP, the tip position is recorded when the AIP works in three different operation modes. The results are displayed in Figure 4.33 (a) and their Fourier transforms can be seen in Figure 4.33 (b).

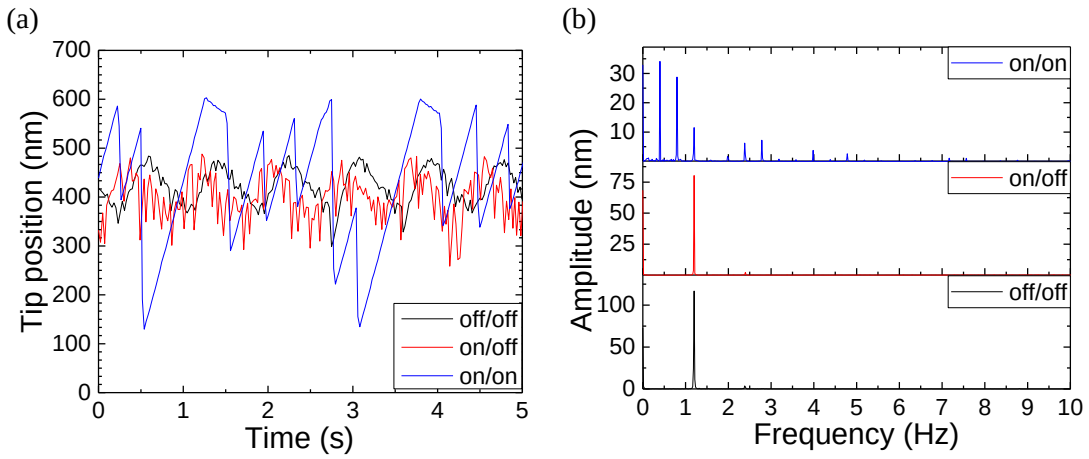

Figure 4.33 (a) The oscillation of the tip position and (b) its Fourier transform in three different conditions when the system is put on an active oscillation isolation platform, which is on top of a floating optical bench: the platform is off (black line), the platform is on but the active isolation is off (redline) and the platform is on with active isolation (blue line). For FFT, the sampling rate and sampling time are 100 Hz and 50 s, respectively, which give a 0.02 Hz frequency resolution and a 50 Hz bandwidth.

In the off/off mode, the oscillation amplitude is about 180 nm and there is a strong 1.2 Hz component in the spectrum. In the on/off mode, the oscillation amplitude does not change much compared with the one in the off/off mode, but the component at 1.2 Hz becomes smaller, which means the AIP can compensate part of the 1.2 Hz noise even when just being used as a passive platform. However, when the active isolation is turned on (the on/on mode), the tip starts to oscillate with a 500 nm amplitude, which is unexpected. Thankfully, however, the 1.2 Hz component reduces further. When looking at the frequency domain, two sub-Hz components pop up with large amplitudes and some higher frequency components are generated as well. One possible reason of this is that the new frequency components are generated when the AIP is fighting with the 1.2 Hz noise induced by the floating table as its ability to compensate low frequency noise is limited.

To prove that the instability of the tip height is caused by the fighting between the AIP and the floating optical bench, the whole system is moved from the floating optical bench back to the rigid one. The tip position is then recorded in the same three operation modes as on a floating optical bench, with the results shown in Figure 4.34 (a). In the off/off mode, the tip oscillation amplitude is about 80 nm. In frequency domain, there are four peaks, one at low frequency (<3 Hz) and one each at 8 Hz, 12 Hz and 19 Hz.

When the AIP operates as a passive platform, the oscillation amplitude is reduced to about 50 nm because the noises at low frequency and 12 Hz have been compensated as can be seen from the frequency domain. When the active isolation is turned on, the oscillation amplitude is further reduced to about 10 nm, which is comparable to some commercial AFMs. In the frequency domain, most of the high frequency components are eliminated and there is only slightly low frequency component left.

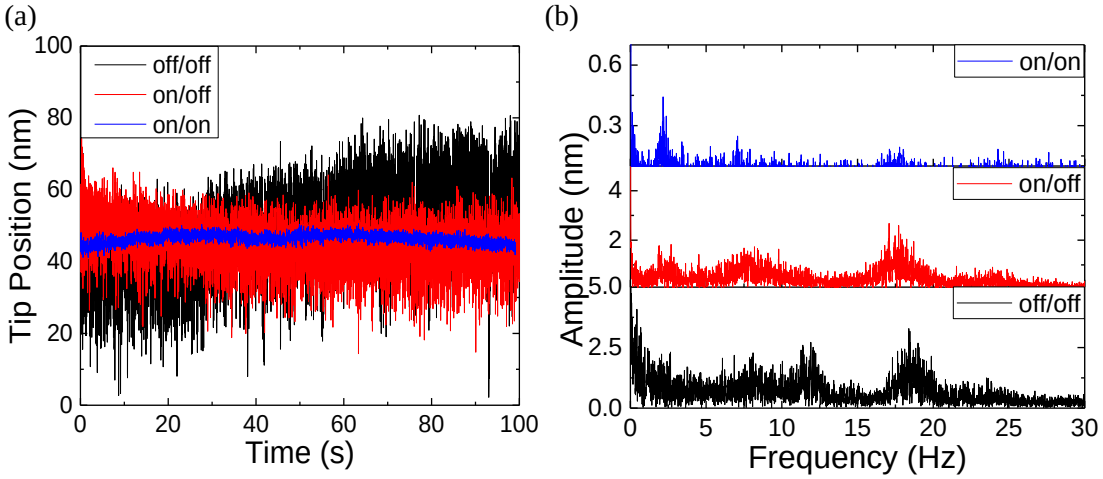

Figure 4.34 (a) The oscillation of the tip position and (b) its Fourier transforms in three different conditions when the system is put on an active oscillation isolation platform, which is on top of a rigid optical bench: the platform is off (black line), the platform is on but the active isolation is off (redline) and the platform is on with active isolation (blue line). For FFT, the sampling rate and sampling time are 100 Hz and 50 s, respectively, which give a 0.02 Hz frequency resolution and a 50 Hz bandwidth.

A scan is then performed on the previously measured 20 nm high grating calibration sample in two operation modes: with (on/on) and without (on/off) active isolation. The results are shown in Figure 4.35. The tilts in the two graphs have been removed. When the active isolation is off, the grating feature could be seen but not obviously due to several ups and downs on the surface. When the active isolation is on, the feature of a grating could be clearly seen, and the surface is smooth. Besides, the difference between the height of the grating pitch given by this measurement and given by a commercial AFM is very small.

Vertical resolution can now be better than 10 nm, achieved by covering the system with a sound isolation box and using an active isolation platform on a rigid optical bench, as well as isolating the vibrations of the vacuum pump from the optical bench. This provides a suitable platform for attaining THz images. However, a good topography does not guarantee an efficient THz signal and other measures need to be implemented to improve the sensitivity and SNR of the THz signal.

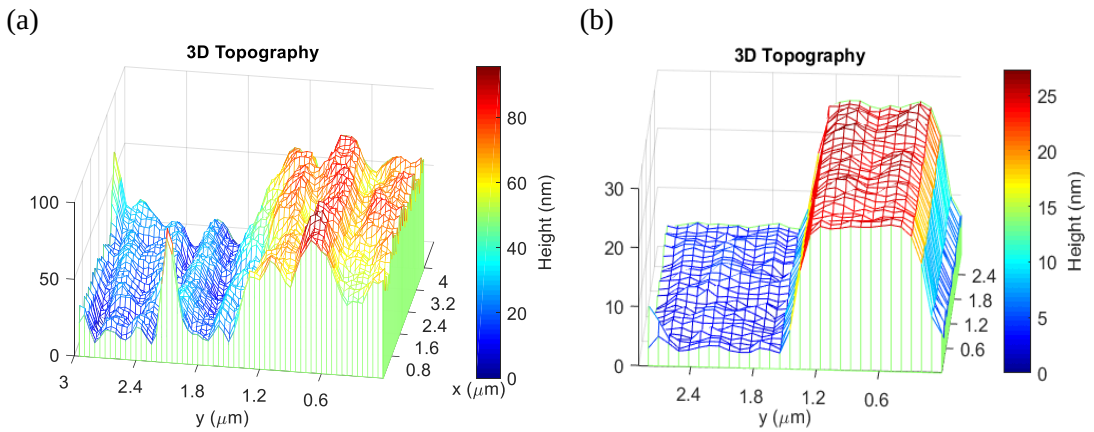

Figure 4.35 Topography of the same calibration sample in two conditions: (a) without active isolation; (b) with active isolation. The calibration sample is a grating structure on silicon with a height of 20 nm.

4.7 Electronic noise reduction

Several sources of electronic noises exist in the original s-SNOM setup, which deteriorate the SNR of the system. To detect the small scattering signal and enhance the sensitivity of the system, the electronic noise needs to be reduced as well. Figure 4.36 gives a schematic of the electronic configuration of the setup. Two pulsers are gated by the same function generator at 980 Hz so that two synchronised pulses can be produced. The repetition rate of the two pulses are the same (1 kHz). One pulse (from pulser 2) is used to bias the QCL while the other (from pulser 1) is set as a reference signal. The terminal voltage of the QCL is subtracted from the reference signal and then amplified by the differential amplifier, the output signal of which is then detected at the tuning fork resonant frequency with a lock-in amplifier.

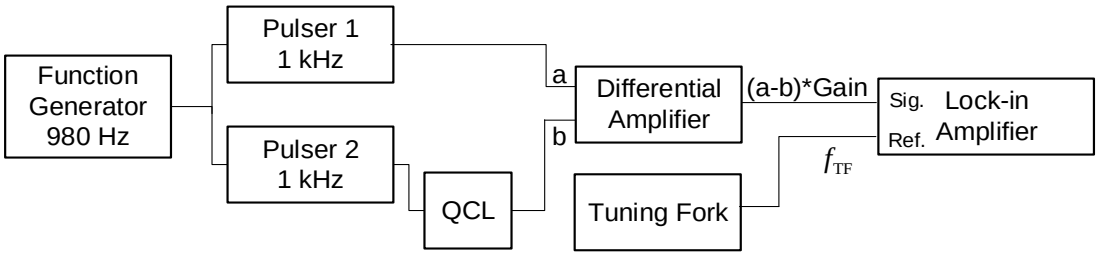

Figure 4.36 Schematic of the electronic configuration for the s-SNOM setup. There are two pulsers, one of which is used to produce the bias for the QCL and the other one produces a reference voltage. They are gated by the same function generator. The output of pulser 1 and the terminal voltage of the QCL are fed into a differential amplifier with the output detected by a lock-in amplifier to get the modulated signal at the tuning fork resonant frequency.

Several modifications have been performed to reduce the electronic noise. To analyse the origin of electronic noises, the waveforms of the four most important voltage signals are recorded with a digital oscilloscope, as shown in Figure 4.37. As can

be seen, since the frequency of the gate voltage is set only slightly lower than the frequency of the two pulses, only one pulse can be generated by the pulsers during one gating period.

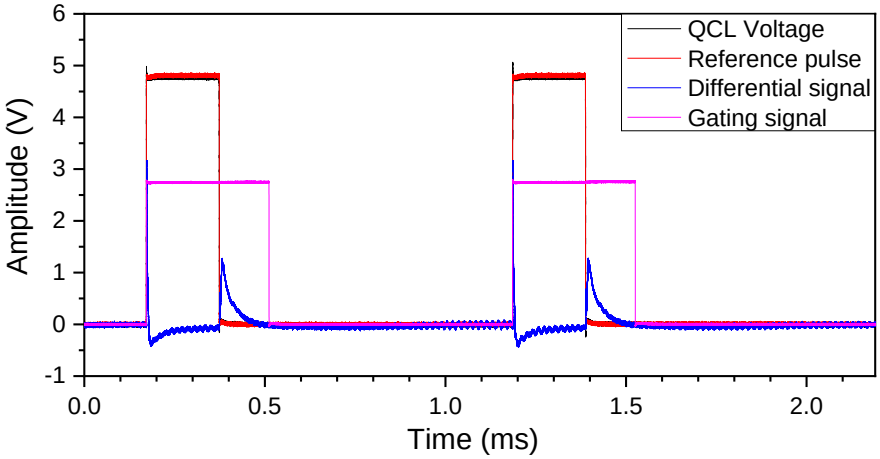

Figure 4.37 The waveforms of four voltage signals for a SNOM measurement

4.7.1 Reference pulse synchronisation

If zooming in just to the falling edges of the voltages, it can be seen that the bias pulse for the QCL and the reference pulse from the second pulser are out of sync (with different durations), shown in Figure 4.38 (a).

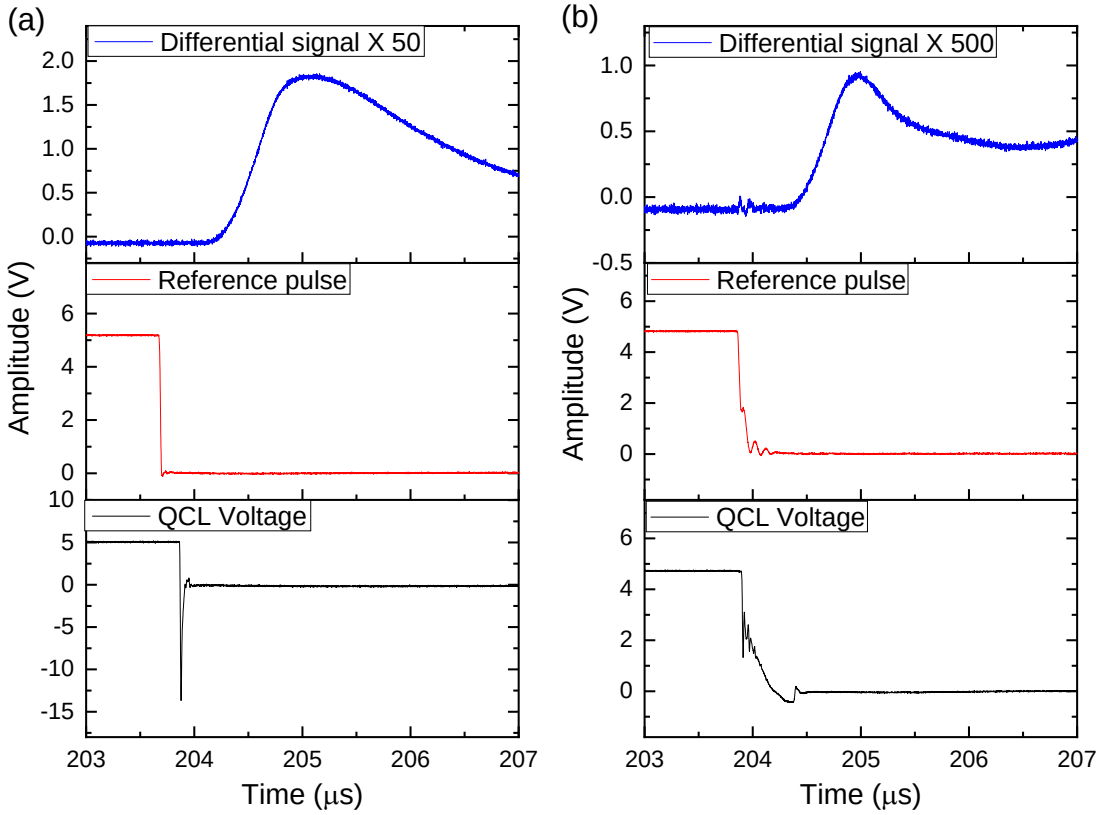

Figure 4.38 Falling edges of the waveforms for the QCL voltage and the reference pulse and the corresponding end part of the waveform for the differential signal: (a) before improvement; (b) after improvement.

The rise times, frequencies and amplitudes of the two pulses might be slightly different from each other as well. As the differential signal from the two is taken as the THz signal, any difference between the two will generate an output signal. Therefore, minimising the difference between the two pulses is important for getting a smaller background noise. To achieve this, the trigger voltages for the two pulsers are adjusted so that they will generate two pulses at the same time point. After this, the two pulses start to rise at the same time, as shown in Figure 4.39 (a). Furthermore, the frequency and the duty cycle of the reference pulse is adjusted to get the same pulse duration. As shown in Figure 4.38 (b), the falling edges of the reference pulse and the QCL voltage almost overlap with each other in time after this modification.

4.7.2 Impedance matching of the QCL

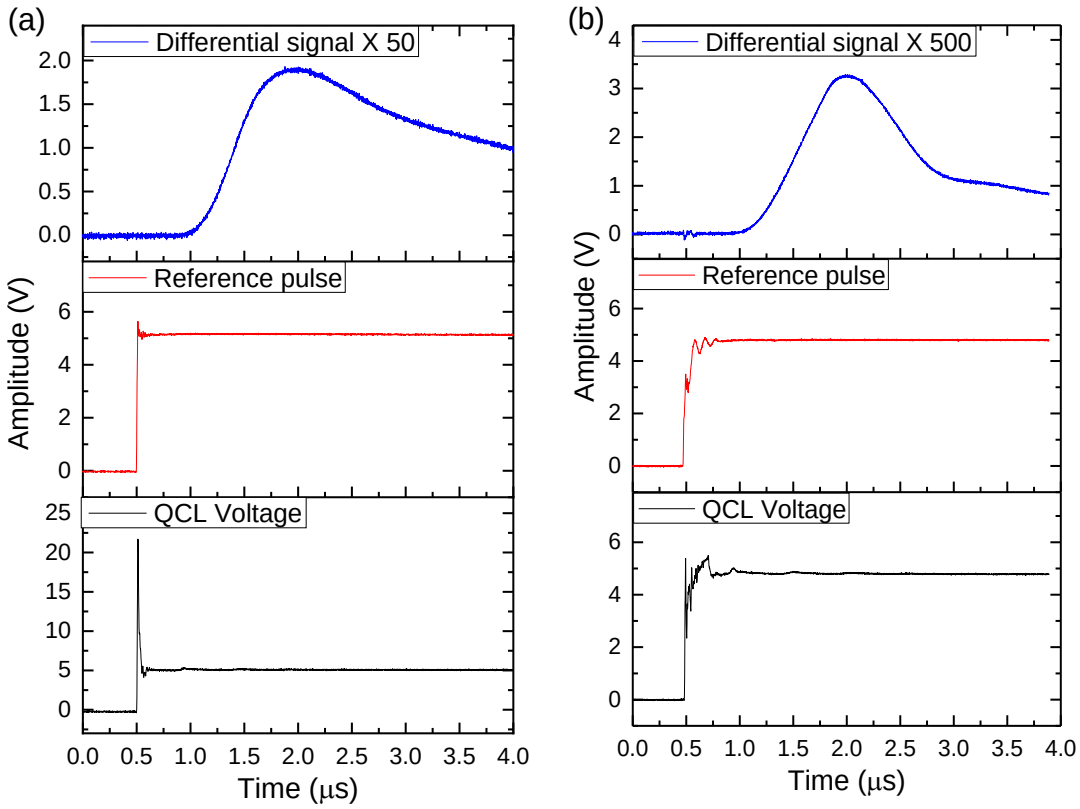

Figure 4.39 Rising edges of the waveforms for the QCL voltage and the reference pulse and the corresponding beginning part of the waveform for the differential signal: (a) before improvement; (b) after improvement.

In addition, as the resistance of a THz QCL is usually much smaller (around 10 Ω) than the coupling resistance of the electronic instruments (usually 50 Ω), there is a large impedance mismatch between them. This will generate a spike on the QCL voltage when the QCL is switched on and off, as shown in the bottom graphs in Figure 4.38(a)

and Figure 4.39 (a). The two spikes introduce a large noise into the THz signal, which is acquired by monitoring the QCL voltage. To overcome this, an equivalent circuit, which consists of a resistor and a Zener limiting diode and is designed and made by my colleague Wladislaw Michailow, is connected to the QCL and the reference load to reduce the effects of impedance mismatch. By adjusting the resistance of the variable resistor on the reference path, the reference path can be balanced. In this way, the spike on the QCL voltage is largely reduced, as shown in Figure 4.38(b) and Figure 4.39 (b).

Another measure that could reduce the system noise is optimising the cable lengths. Preferably, short cables should be used as they introduce less resistance into the corresponding electrical paths. In the cases where long cables need to be used, another cable with the same length should be used for the reference path.

These modifications give a significant reduction in electronic noise, by more than 50 times (the number is calculated by comparing the background signal without THz light measured with the lock-in amplifier before and after the improvement) and allow for an increased gain to be used on the differential amplifier, 20 times (1000×) what was previously possible (50×).

Recently, a method for conditioning the self-mixing signal of a THz QCL imaging system has been reported [315], as shown in Figure 4.40. The QCL voltage pulse is first time-gated to remove the leading and the trailing edges, as shown in Figure 4.40 (c), therefore, the spikes caused by impedance mismatch is not a problem anymore. A linear

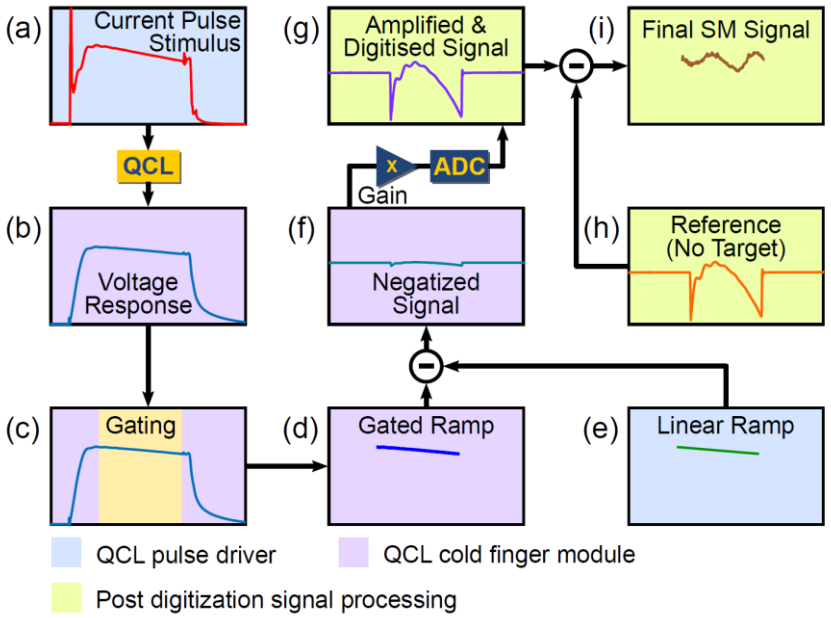

Figure 4.40 Signal conditioning by removing the leading and the trailing edges of the pulse. A perfect voltage ramp is digitally synthesised and subtracted in analog hardware from the truncated pulse to get the self-mixing signal, from [315].

voltage ramp with the same slope is then digitally synthesised and subtracted from the truncated pulse with analog hardware. The resulting signal is amplified and recorded. A reference signal is taken with the system before a measurement when there is no optical feedback. During the measurement, this reference signal is subtracted from the measured real-time signal to get the self-mixing signal. This method removes not only the noise introduced by impedance mismatch but also all the artefacts in the QCL bias circuit. Therefore, this can be implemented in our setup in the future to further reduce the electronic noise.

4.8 Conclusions

In this chapter, a THz s-SNOM based on self-mixing technique using QCLs and a tuning fork AFM has been demonstrated. A 78 nm resolution, corresponding to $<\lambda/1000$, has been achieved with a QCL emitting around 2.85 THz. The sensitivity of this approach has been further enhanced by partly suppressing the lasing action and simultaneously increasing the collection efficiency with an antireflection coated lens attached to a laser facet.

Several measures, including adding a sound isolation box, isolation of the pump vibration and utilisation of an active isolation platform, have been implemented to improve the topography of the system, which reduces the amplitude of the tip oscillation from about 150 nm to below 10 nm.

In addition, several optimisations have been done on all the electronic connections to reduce the electronic noise including reference pulse synchronisation, QCL impedance matching and cable length optimisation. The resulting background electronic noise is reduced by more than 50 times and a higher gain can be used on the differential amplifier, giving a higher sensitivity and SNR.

The research represents significant progress in the field of THz microscopy and paves the way to unique investigations of semiconductor devices, quantum objects, bidimensional materials and biological samples.

Chapter 5
Application of the THz s-SNOM

As a research tool, the s-SNOM lends researchers the ability to look at the optical properties of devices or samples with nanometre resolution. At THz frequency range, this makes it possible to study the THz response of a variety of materials, varying from semiconductors [316] and metamaterials [317] to lowdimensional materials [318]–[320], and from quantum dots [321]–[323] to biological samples [324]. It can reveal resonances caused by excitonic, plasmonic, and/or vibrational energy states, as the critical length scale for these physical phenomena lies between 10 nm and 10 μm [325], [326], which cannot be reached by conventional far-field imaging due to the diffraction limit. In this chapter, the THz s-SNOM will be used to study several physical phenomena within THz nanostructures and to characterise the optical property of metamaterials.

5.1 State of art

An s-SNOM can reveal optical information of a sample with nanometre resolution. One important application of this is the study of the fundamental properties of nano scale resonant structures. For instance, it can be used to study the fundamentals of length scaling and the coupling effect between adjacent antenna segments of optical antennas, which has been demonstrated in the infrared by Olmon *et al.* [327]. Here, an infrared s-SNOM with a CO_2 laser (λ = 10.6 μm) and interferometric homodyne detection was used to investigate the resonances of linear gold wire antennas designed for the mid-infrared by probing the z direction nearfield component. Figure 5.1 (a) and (b) are the topography graphs of two antennas with different lengths (2 μm and 3.4 μm) while Figure 5.1 (c) and (d) are corresponding optical images, which reveal that the dimers with individual segments optically coupled across a small gap have a resonant behaviour emerging from a superposition of individual monomer modes, reminiscent of a linear quadrupole. The coupling between the two segments is mainly manifested by resonant effects due to the current-field and local field enhancement effects, which are all determined by the separation of the segments.

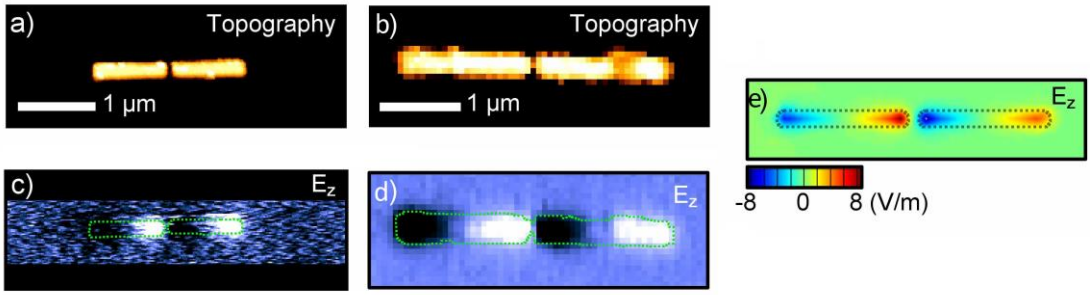

Figure 5.1 Mid-infrared s-SNOM imaging of optical antenna modes. (a) and (b) are the topographies of two single gap antennas and (c) and (d) are the corresponding nearfield images. (e) is the numerical simulation result for the 3.4 μm antenna dimer in (b) and (d). Adapted from reference [327], © 2010 Optical Society of America.

Similar measurements have been done with two-photon luminescence micro-spectroscopy [328]. The evolution of the modal field with wavelength, both in the gap and along the two coupled gold nanowires forming the antenna, is directly visualized in Figure 5.2. At resonance (730 nm), the luminescence for the gap area is enhanced by at least 80 times. A dynamical charge redistribution due to the nearfield coupling between the two arms has been observed as well. These provide fundamental information of antenna structures and criteria for optimisation of similar structures to get a strong coupling effect and resonant interaction, which are essential for modulation and detection purposes. THz s-SNOM has the potential of getting similar information for antennas resonating at THz frequency range.

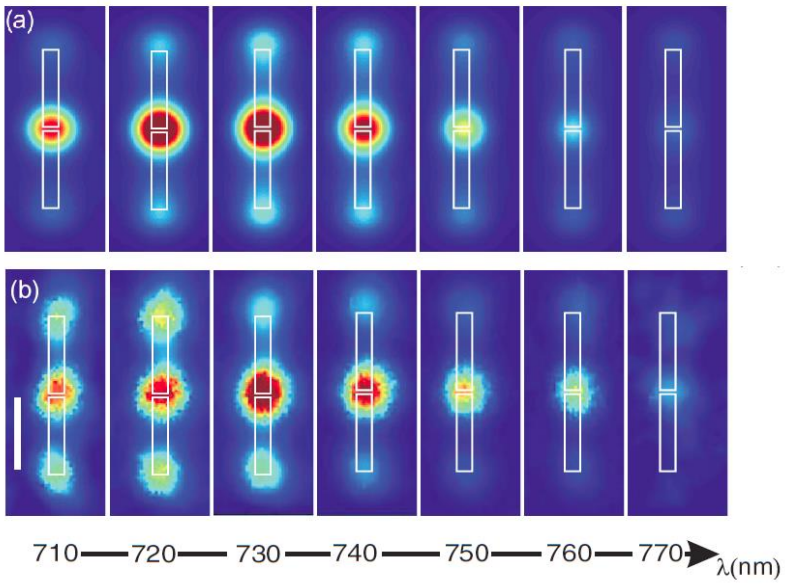

Figure 5.2 Evolution of the modal field with the incident light wavelength over a single gap antenna: (a) the computed electric field amplitude distribution and (b) the measured field distribution with two-photon luminescence micro-spectroscopy (scale bar 500 nm). Adapted with permission from [328]. Copyright (2008) by the American Physical Society.

At the same time, the s-SNOM is a useful tool to study plasmonic resonance of graphene, which can be utilised to manipulate optical fields and the energy flow of light through plasmon polaritons [329], [330]. This is essential for information and communication technologies. Real-space imaging of plasmon fields in a graphene nano structure (tapered graphene ribbon on the carbon-terminated surface of 6H-SiC [331]), has been demonstrated with a 9.7 µm s-SNOM [224]. A diagram of the setup is shown in Figure 5.3 (a) and Figure 5.3 (b) gives the nearfield image , where fringes parallel to the edge of the ribbon in its wider axis can be seen. This was explained to be the interference pattern between the backward and forward propagating plasmons, which is confirmed by numerical calculation of the local density of optical states, as shown in Figure 5.3 (c). Furthermore, by changing the gate voltage applied to the tapered graphene ribbons on a Si/SiO_2 (300 nm) substrate, plasmonic switching and active control of the plasmon wavelength has been achieved, as shown in Figure 5.3 (d).

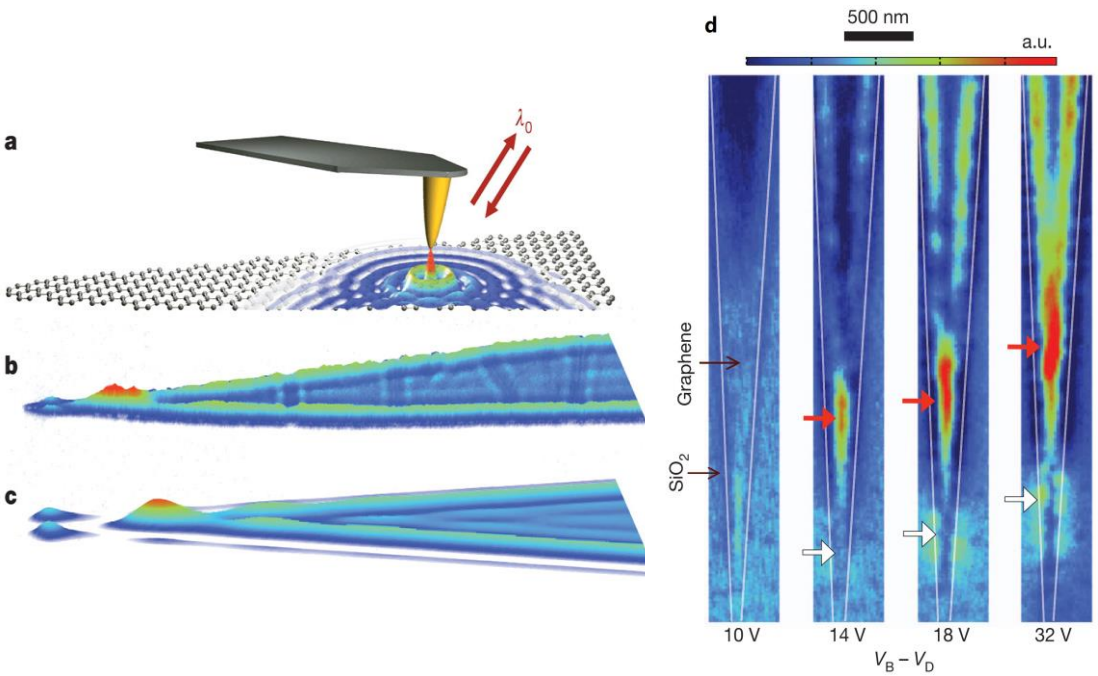

Figure 5.3 Imaging propagating and localized graphene plasmons with an infrared s-SNOM. (a) Diagram of the experimental setup. (b) Nearfield image. (c) The calculated local density of optical states. (d) Plasmonic switching and active control of the plasmon wavelength by electrical gating, reprinted with permission from [224] © 2012, Springer Nature.

Similar research has been done for graphene nanoribbons on a Al_2O_3 substrate, where mode patterns of surface plasmons and edge plasmons have been observed [332]. When graphene is etched into different shapes, it will act as a nanoresonator, which will support a set of plasmonic sheet modes at different frequencies [226]. A nano graphene

disc on a SiO_2 substrate supports different modes when the size changes. The modal profiles of graphene disks with a diameter changing from 50 nm to 450 nm has been imaged by an s-SNOM, as shown in Figure 5.4 (a), which is confirmed by numerical simulations in Figure 5.4 (b). It is also found that, for the same graphene disk, it supports different modes at 11.06 μm and 11.31 μm wavelengths.

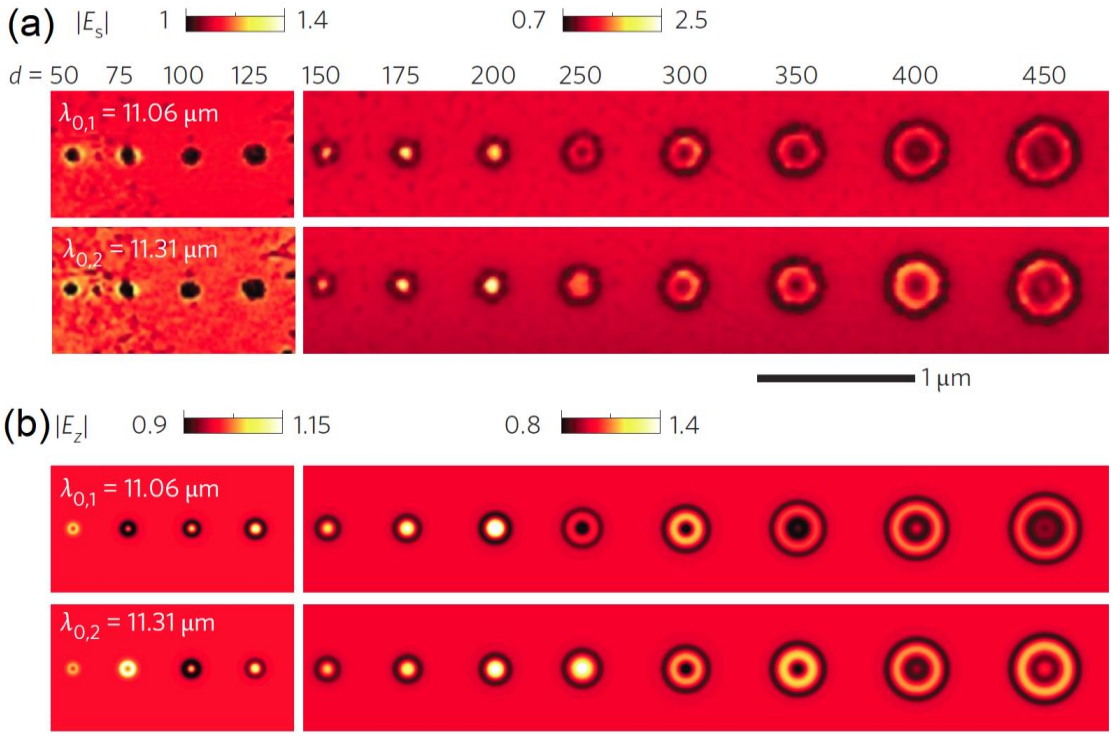

Figure 5.4 Nearfield image of plasmons in tailored disk graphene nanoresonators. (a) s-SNOM image of the sheet plasmon modes on the graphene nano-disc and (b) corresponding simulated plasmon modes, adapted with permission from [226] © 2016, Springer Nature.

For plasmonic applications, graphene with high mobility is needed as it can support plasmons with a long lifetime. To evaluate the mobility of a graphene sheet, it is necessary to know the layer information as the electrical [333], [334] and magnetic properties of graphene, such as mobility and conductivity, are highly influenced by the number of layers and the stacking structure, which can bring drastic changes in band structures [333], [335]. For samples on a conducting substrate or in freestanding conditions, high-resolution electron microscopy [336] and scanning tunnelling microscopy [337] can successfully visualize stacking domains and their boundaries with about 1 nm resolution. Other conventional far field spectroscopy [333], [338] and Raman spectroscopy [339]–[341] can be used to get the stacking information for samples on a dielectric substrate but the resolution is relatively low (about 1-10 μm).

The s-SNOM offers an approach to producing a nanometre resolution image of the layer structure for few-layer graphene on a dielectric substrate. Figure 5.5 shows an s-SNOM image of the stacking structures of few-layer graphene [342]. The topography and visible light (633 nm) nearfield image can only give the layer information while the infrared (3.39 μm) nearfield image can differentiate between the different stacking structures of triple-layer graphene.

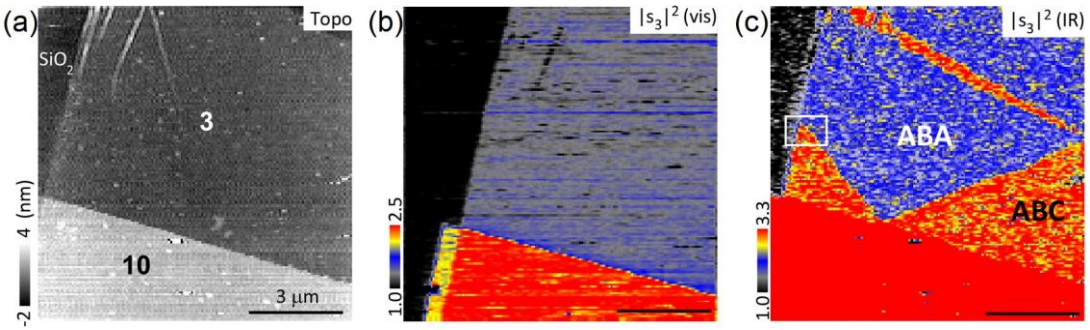

Figure 5.5 Infrared s-SNOM imaging of the stacking structures of few-layer graphene: (a) Topography; (b) visible light (λ = 633 nm) nearfield image; (c) infrared (λ = 3.39 μm) nearfield image. Adapted with permission from reference [342]. Copyright (2015) American Chemical Society.

Compared to light at other frequency ranges, THz radiation has several unique properties: low energy, transparency to many materials and great penetration, as discussed in Section 4.3. The combination of the last two allows us to image features below the surface of a thin layer of THz transparent material. Because the tip is separated from the material which will contribute to the nearfield effect by a layer with finite thickness, the nearfield signal will not be as strong as when there is no encapsulation layer present. One example is imaging a gold grating embedded in a dielectric layer [277], as shown in Figure 5.6. The THz nearfield microscopy used here is based on an atomic force microscope and THz time-domain spectroscopy, shown in Figure 5.6 (a). The AFM topography just shows a flat surface while the grating feature is clearly seen on the THz image. The time evolution of the THz signal can also be acquired with this system. It is also found that first order demodulation at the AFM tip resonant frequency on the lock-in amplifier is preferred for subsurface imaging, especially for nanostructures embedded in thick films because the first-order demodulation has the longest interaction length, and a lateral resolution comparable to higher-order demodulation.

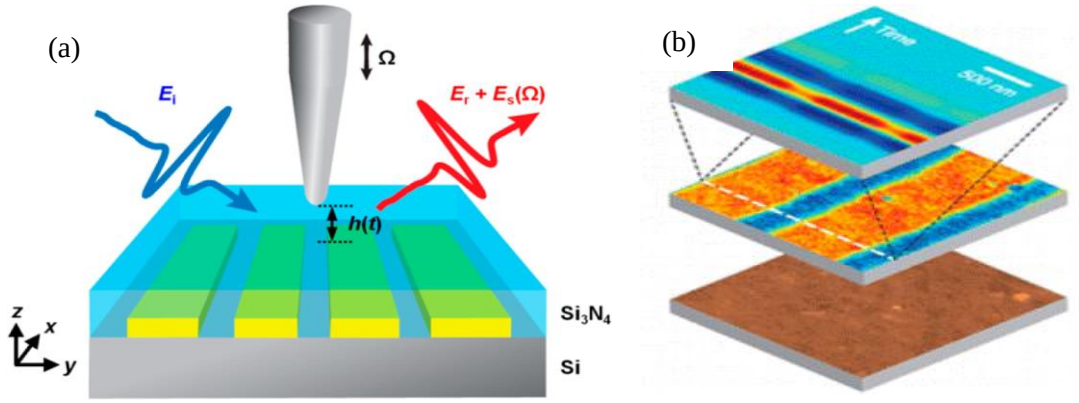

Figure 5.6 Subsurface nanoimaging of a metallic grating embedded in a dielectric film: (a) experimental setup; (b) from bottom to top are topography, THz image and spatiotemporal image of the dot line on THz image. Adapted with permission from reference [277]. Copyright (2015) American Chemical Society.

Because of their low energy, THz photons can excite molecular vibrations and phonons, as well as electrons of non-metallic conductors [1], [2]. As a result, THz s-SNOM also offers intriguing possibilities for material and device characterization of semiconductor devices at nanometre resolution. Simultaneous THz recognition of materials and mobile carriers with a 40 nm resolution in a semiconductor transistor has been demonstrated with a 2.54 THz s-SNOM, as shown in Figure 5.7 (c). In contrast to the IR image in Figure 5.7 (b), the THz image can also reveal the highly doped poly-Si gate ($n \approx 10^{19}$ cm^{-3}) and the highly doped Si regions ($n \approx 10^{19}$ cm^{-3}) just below the metallic NiSi source and drain contacts. This can facilitate the optimization of growth for low mobility materials, which has been difficult to achieve due to the lack of information on dopant distribution and junction properties [229].

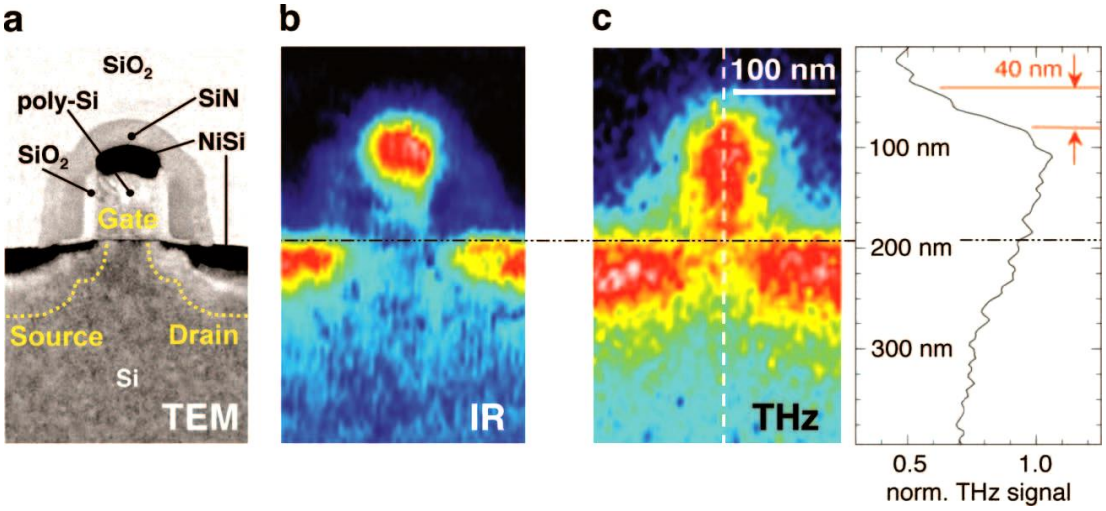

Figure 5.7 Carrier density imaging with an s-SNOM. (a) Transmission electron microscopy (TEM) image, (b) Infrared ($\lambda \approx 11$ μm) s-SNOM image and (c) 2.54 THz s-SNOM image of a single transistor, adapted with permission from [229]. Copyright (2008) American Chemical Society.

An infrared s-SNOM, using a CO_2 laser with wavelength $\lambda = 10.6$ μm, has been used to map free-carriers in axially modulation-doped silicon nanowires, as shown in Figure 5.8 (a). Figure 5.8 (b) shows the AFM topography and nearfield signal from a nanowire encoded with alternating sections of boron-doped and intrinsic silicon, demonstrating that infrared s-SNOM is sensitive to both p-type and n-type free-carriers for carrier densities above $\sim 1 \times 10^{19}$ cm^{-3} [343]. The THz s-SNOM also has the potential to achieve the same function as it has been demonstrated to be sensitive to mobile carrier concentrations in the range 10^{17}-10^{18} cm^{-3} [229]. Therefore, THz nearfield microscopy enables quantitative studies of local carrier concentration and mobility at the nanometre scale and potentially the characterization and optimization of optoelectronic properties in a wide range of semiconducting materials and nano-structured devices.

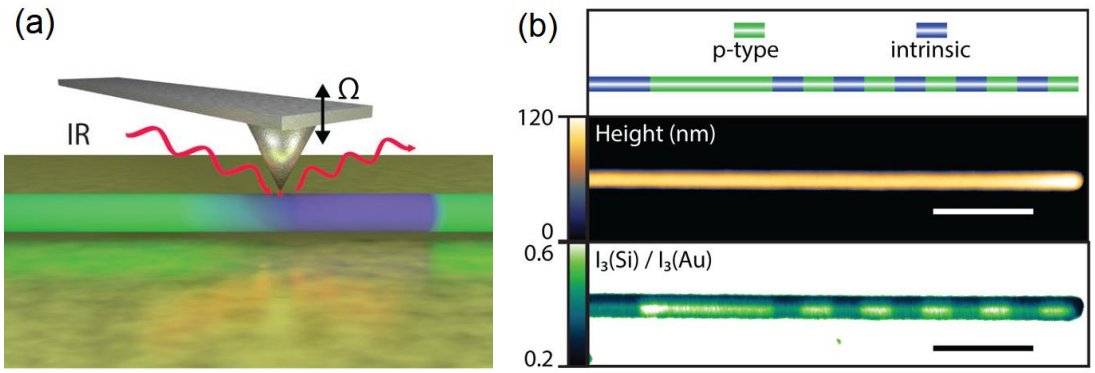

Figure 5.8 Free-carrier mapping in Multijunction Silicon Nanowires (SiNW) with an infrared s-SNOM. (a) schematic of the experimental setup. (b) from top to bottom are a schematic of SiNW doping profile, topography and nearfield infrared image normalized to Au of a representative SiNW sample. Scale bar: 1 μm. Adapted with permission from [343]. Copyright (2017) American Chemical Society.

5.2 Experimental configurations

All the measurements in this chapter are performed on the home-built THz s-SNOM discussed in Chapter 4. For the surface emitting photonic crystal (SEPHC) QCL and the dipole antenna array, they are measured with the setup before the topography improvement and electronic noise reduction discussed in Section 4.6 and 4.7 , which is named V1 s-SNOM. The measurements with the indium tip in Section 5.7.4 are performed with the V1 s-SNOM as well. For the other measurements, they have all been conducted with the improved setup, which is named V2 s-SNOM.

The light source for the two setup versions is the same THz QCL (QCL-H in Appendix A), with the LIV and spectra shown in Figure 4.21. The LIV of the QCL did

not change much during all the measurements. Figure 5.9 shows its LIV after the Si lens dropped off and was reattached on it. The LIV looks similar compared to the one shown in Figure 4.21 with the threshold current and dynamic range close to their counterparts. The QCL is operated in pulsed mode at 2 kHz with 10% duty cycle. The temperature of the cryostat is kept at 5 K. The current of the QCL is kept at 1 A to get the maximum output power.

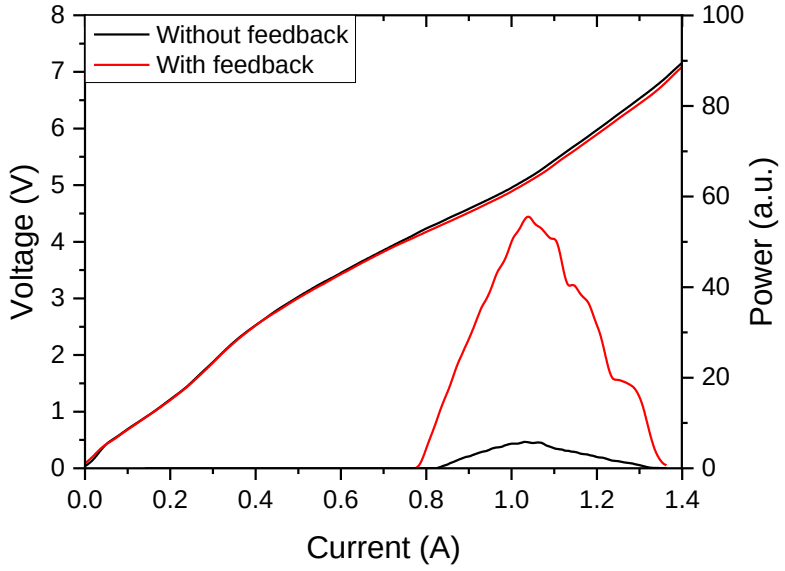

Figure 5.9 LIV of QCL-H when it is partially suppressed with the AR coated SI lens (without feedback) and with feedback from a gold coated flat mirror (with feedback).

The detection method used is the self-mixing detection discussed in Section 4.5.1. For all the measurements, the amplitude signal from the lock-in is taken as the THz signal. The integration time of signal is usually 300 ms. If other integration time is used, it will be specified for that measurement.

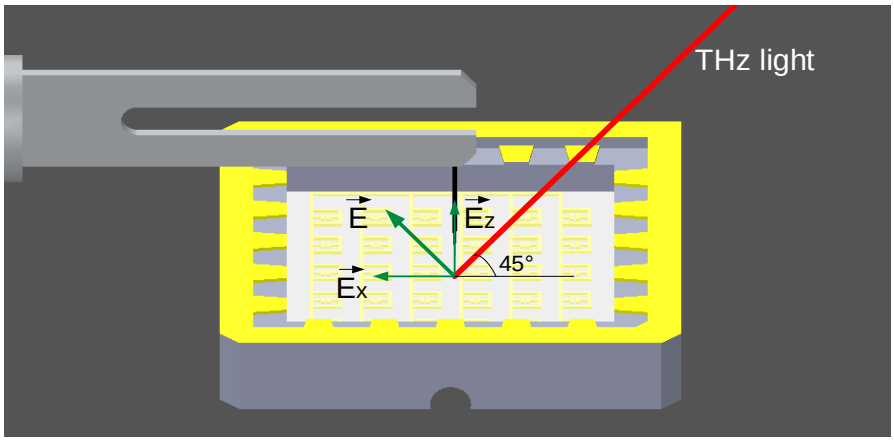

Figure 5.10 The illumination geometry of the system

For all the measurements in this Chapter, the light illustration geometry is the one shown in Figure 5.10. The THz light goes on the sample with a 45-degree angle. Its polarisation is indicated by the green arrow $\vec{E}$. Therefore, it has components in both x $\overrightarrow{E_x}$and z directions $\overrightarrow{E_z}$. The z component will introduce field concentration when it illuminates the scanning tip, which will give a contrast on the THz image between areas with different material susceptibility. The x component will apply an electric field on the sample in the x direction. If the sample has a resonant structure, both of them exist during a s-SNOM measurement. The overall THz signal is the summary of the two.

5.3 Electric field mapping of a SEPHC QCL

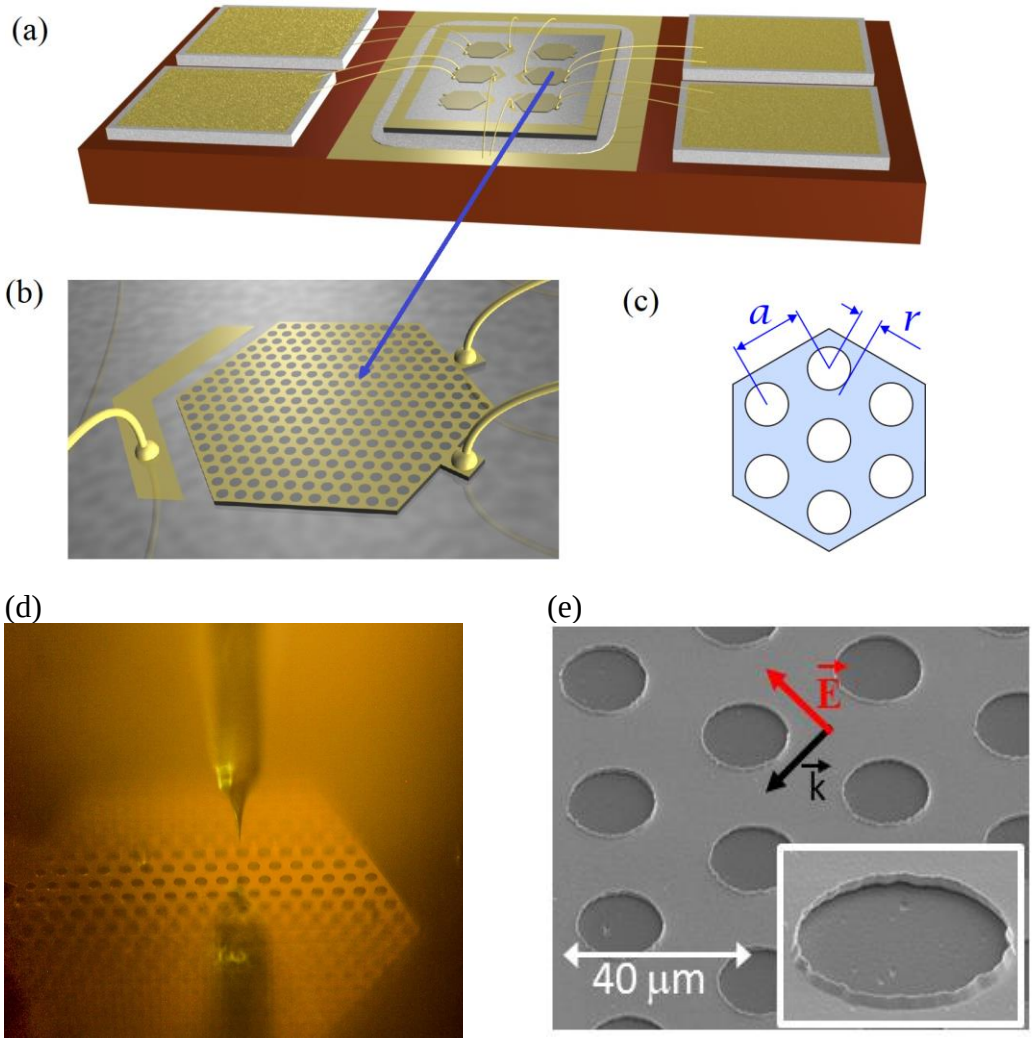

Figure 5.11 Information of the SEPHC QCL sample. (a) Schematic of a chip holding six SEPHC QCLs; (b) a single SEPHC QCL; (c) definitions of the lattice parameters r and a; (d) optical photo of the tip-sample system and (e) SEM micrograph of the sample. (a), (b) and (c) are adapted from [59].

To explore the potential of the V1 s-SNOM, it is first used for mapping the plasmonic resonances supported by resonant metallic features. A SEPHC QCL [344] based on triangular arrays of holes and emitting around 2.85 THz is chosen since its emission overlaps well with the s-SNOM frequency. The interest in this sample, which is used as a passive element at room temperature, stems from its patterned metallic top contact area, and the relative plasmonic resonances supported. Figure 5.11 (a) shows a schematic of the sample, which is a chip holding 6 SEPHC QCLs on it. The structure of a single SEPHC QCL can be seen in Figure 5.11 (b), the top contact of the laser is patterned with a photonic crystal structure. The frequency response of the photonic crystal is mainly determined by two geometric parameters *a* and *r*, which are defined as the distance between the centres of two holes and the radius of the holes, as shown in Figure 5.11(c). For this sample, *a* and *r* are 38 μm and 10 μm, respectively. Figure 5.11 (d) gives an optical microscope image of the tip and sample in the s-SNOM while Figure 5.11 (e) shows a SEM micrograph of the top contact for the SEPHC QCL. The depth of the holes is about 0.6 μm. Due to the lift-off process during the fabrication, the borders of the holes present significant sharp ripples, as shown by the SEM of the inset in Figure 5.11 (e).

5.3.1 Simulation results of the dipole resonance on the SEPHC QCL

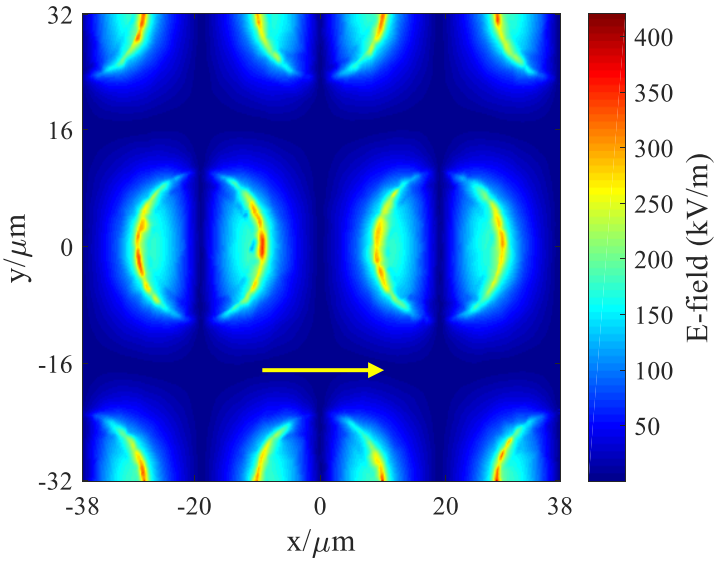

Figure 5.12 Absolute number of the normalized E-field z component at 2.85 THz simulated with COMSOL Multiphysics for THz light incident as depicted in Figure 5.7 (b) and power density of $2\times10^{-4}\,\mathrm{W/\mu m^2}$ with the polarization direction indicated by the yellow arrow.

The patterned metallic surface of the QCL supports dipole modes because of the periodical microcavity structures on it. To analyse the electric field distribution, a COMSOL Multiphysics simulation is performed with the electric field and wave vector of the input light in the directions shown in Figure 5.11 (e). The input power of the electric field is 1 W (power density of $2\times10^{-4}\,\mathrm{W/\mu m^2}$). Here, the z component of the electric

field is analyzed as only this component has a strong nearfield interaction with the tip, as shown in Figure 4.6. Besides, for the THz s-SNOM, the absolute value instead of the real value of the electric field is recorded because of the signal acquisition method used. Therefore, for all the simulations in this chapter, the absolute value of electric field z component will be calculated. The simulation result for the SEPHC QCL is displayed in Figure 5.12, which includes the topological feature of a raised lip around the hole and shows that the resonant plasmonic modes supported at 2.85 THz have two distinct peaks for each microcavity along the direction of the incident E-field.

5.3.2 The s-SNOM measurement results

The sample is then scanned in the V1 THz s-SNOM. The scanning area is a $50\ \mu m \times 50\ \mu m$ square and the step size is 0.5 μm. A 500 ms delay is added into each step of the measurement to get a stable THz signal. The overall scanning time is about 90 mins. The measurement parameters are summarised in Table 5.1. Figure 5.13 (a), (c) report the topography and the retrieved THz scattered signal acquired simultaneously while Figure 5.13 (b), (d) display the corresponding 3-dimensional images. The THz light is polarised in the x direction. All the topography images have been flattened in this chapter with the method discussed in Section 4.5.2.

Table 5.1 THz-s-SNOM measurement parameters for the SEPHC QCL

s-SNOM	Area ($\mu m \times \mu m$)	Step size (μm)	Delay time (ms)	Integration time (ms)	Scanning time (min)
V1	50×50	0.5	500	300	90

The topography of the SEPHC QCL is consistent with the SEM micrograph, showing a metal triangular lattice of holes along the two directions. The image has been smoothed over 3 points and in some points the tip lost contact with the surface, resulting in missing rows, which have been substituted with the first neighbouring points. This operation did not affect the THz signal and also had marginal effects on the topography. To get the depth of the holes and also the difference between the THz signal in x, y directions, four line profiles have been extracted along the two corresponding lines (shown in Figure 5.13 (a), (c)) in two directions with the results shown in Figure 5.14. The topography line profiles reveal that the height of the holes is around 0.6 μm, which is consistent with the design specifications for the microcavities. The ripples due to the lift-off are also correctly recorded by the s-SNOM topography and can be seen on the line profiles in Figure 5.14 (a), (b), which gives a height of about 300 nm for the ripples.

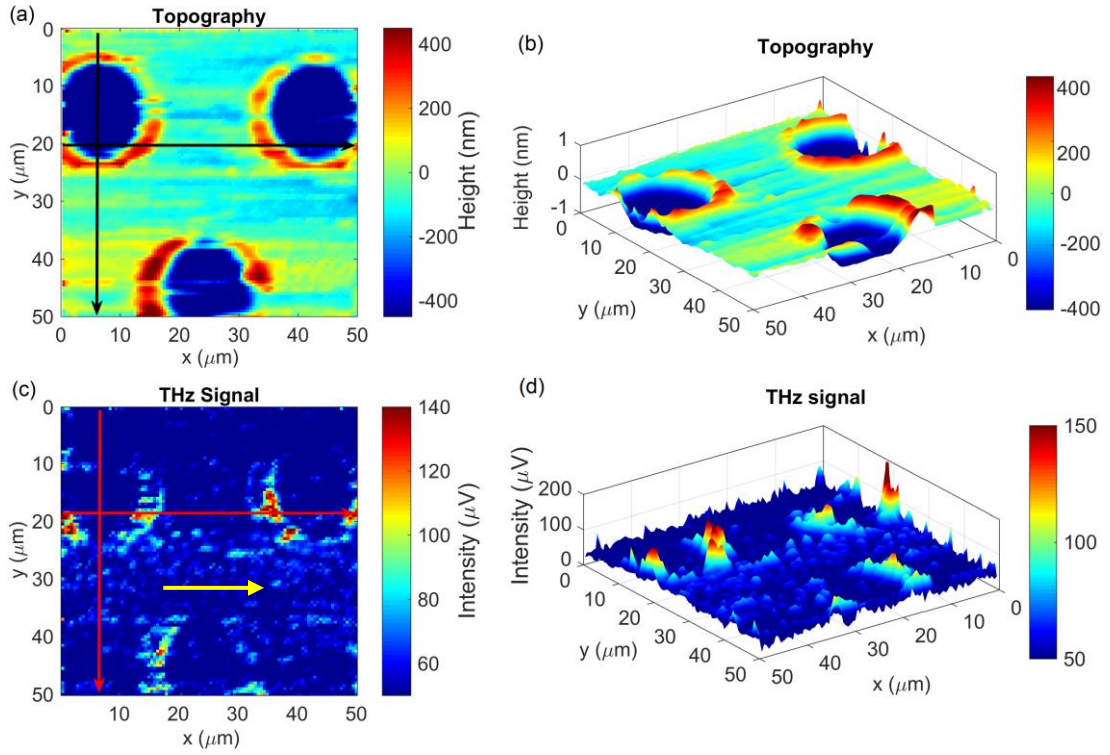

Figure 5.13 THz s-SNOM scanning results of the SEPHC laser: (a) Topography, (b) topography in 3D, (c) THz image and (d) THz image in 3D. The step size is 0.5 µm. The light polarization direction is indicated by the yellow arrow

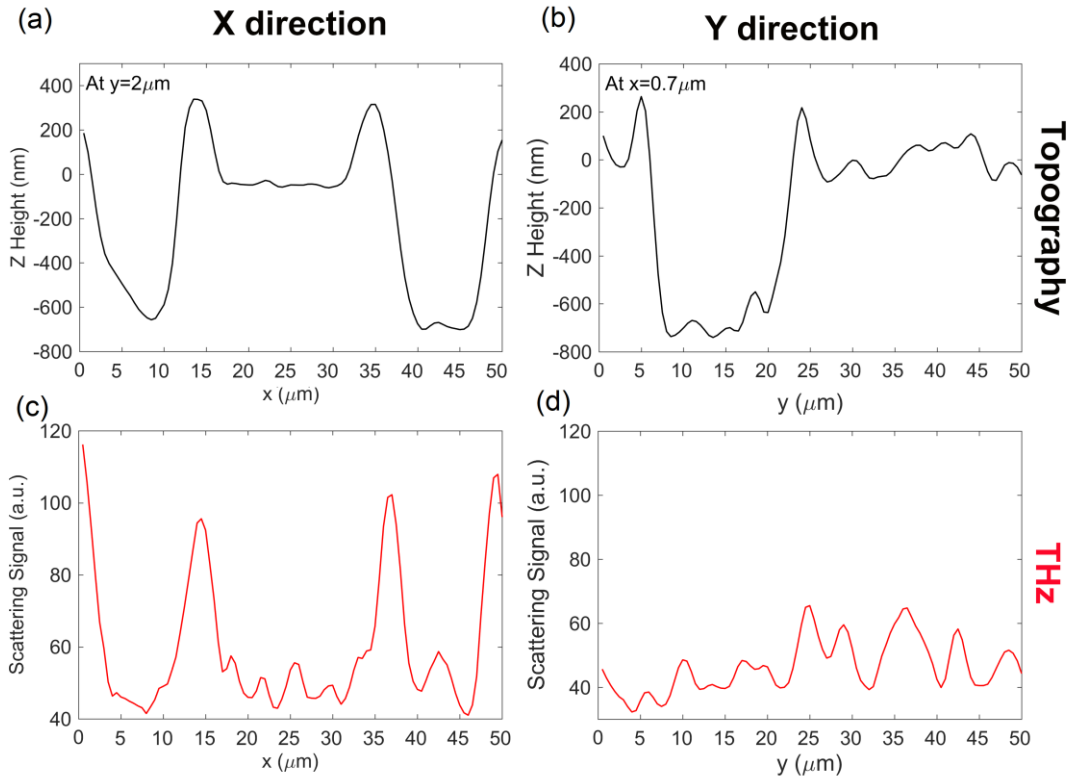

Figure 5.14 Line scan profiles of the s-SNOM image (topography (a), (b) and THz (c), (d)) of the SEPHC QCL in x and y directions.

The THz image (shown in Figure 5.13 (c), (d)) and the corresponding profiles (shown in Figure 5.14 (c), (d)) in contrast to the topography, exhibit an asymmetry in the vertical direction with respect to the horizontal one. In particular, two annular peaks are evident along the polarization direction, in good agreement with the simulations presented in Figure 5.12. This is consistent with the resonant plasmonic modes supported by the photonic crystal metallic structure.

The sample is then rotated by 30 degrees to the left and scanned again with the THz light polarised in the direction indicated with the yellow arrow in Figure 5.15 (also rotated by 30 degrees to the left). The measurement parameters are in Table 5.2. Figure 5.15 shows the recorded topography as well as the THz image. As can be seen, when the sample and the light polarisation are rotated by 30 degrees, the THz response is rotated correspondingly by 30 degrees as well. This further confirms the simulation result as displayed in Figure 5.16, which shows that the plasmonic resonance is always along the light polarisation direction.

Table 5.2 THz-s-SNOM measurement parameters for the SEPHC QCL in 30 degree

s-SNOM	Area (μm × μm)	Step size (μm)	Delay time (ms)	Integration time (ms)	Scanning time (min)
V1	60 × 60	1	500	300	33

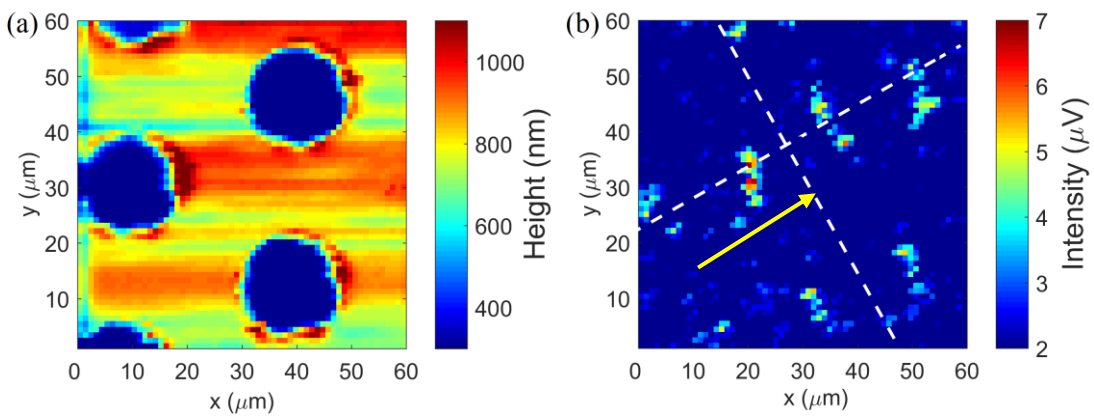

Figure 5.15 THz s-SNOM scanning results of the SEPHC laser when it is rotated by 30 degree to the left: (a) Topography, (b) THz image. The polarization of the light is in the direction indicated by the yellow arrow. The step size is 1 μm.

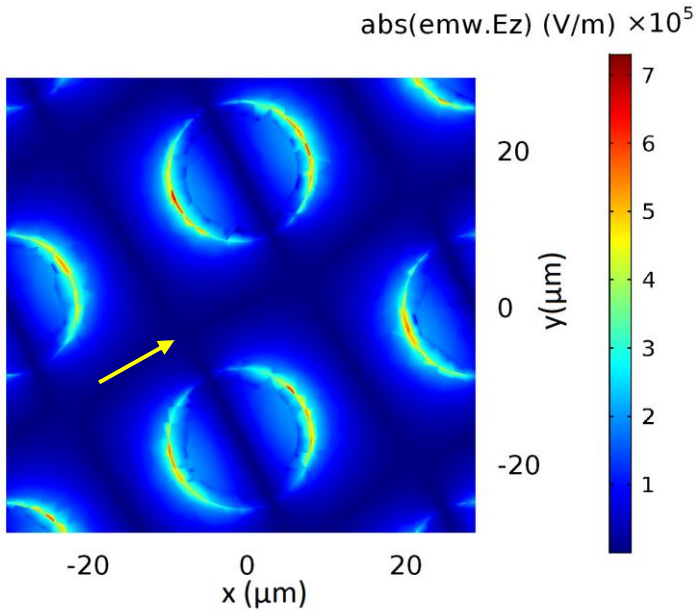

Figure 5.16 Absolute number of the normalized E-field z component at 2.85 THz simulated with COMSOL Multiphysics for THz light incident as depicted with the yellow arrow and power density of $2\times10^{-4}\,\mathrm{W/\mu m^2}$.

5.4 Plasmonic resonance of a dipole antenna array

THz s-SNOM, as a uniquely sensitive approach, also allows the retrieval of dielectric/plasmonic modes supported in buried resonant structures at these frequencies, as discussed in Section 5.1. Here it is used to image the plasmonic resonance of a dipole antenna array buried underneath a dielectric layer, which will help us to better understand the working principle of the device and give directions on improving its performance.

5.4.1 Structure of the antenna array

The sample under investigation is similar to the one reported in reference [218]. Figure 5.17 (a) shows a schematic of the sample. Arrays of planar antennas are connected in series, which are then all joined together by graphene squares. Since the antennas are finally connected to the source and drain pads, they not only provide the plasmonic resonance capable of concentrating the light in the gap region, but also act as electrodes, thus efficiently collecting all the photocurrent contributions arising from the illuminated graphene areas. The whole structure is fabricated on a SiO_2/Si substrate. The geometry of the antenna array is shown in Figure 5.17 (b). The antenna length L is adjusted so that the antenna array will resonate at 2.85 THz. The antenna width W, gap width g and lateral spacing Δx are 1 μm, 0.3 μm and 1.75 μm, respectively.

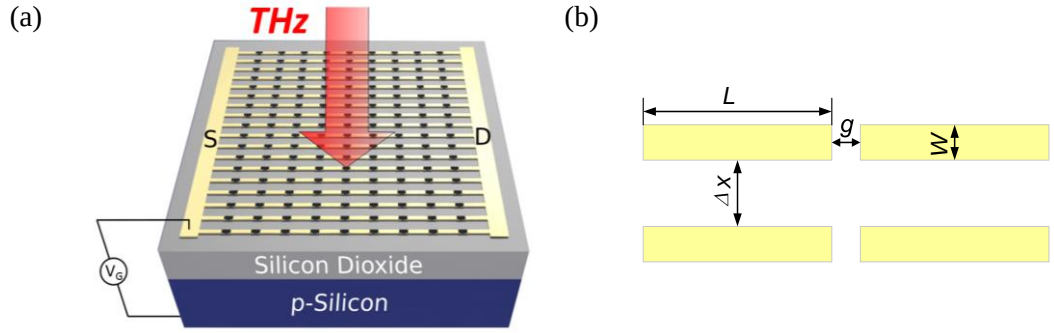

Figure 5.17 (a) A schematic of the antennas array coupled to graphene, modified from [218]; (b) a schematic of the antenna array geometry.

5.4.2 COMSOL simulation

Before fabricating the sample, COMSOL simulations are undertaken to find the optimal size for the antennas, which would resonate at 2.85 THz, the same as the operating frequency of the s-SNOM. The average energy at the gap between the antennas for three antenna arrays with different antenna lengths (18 µm, 19 µm and 20 µm), and resonant frequency around 2.85 THz are simulated. Figure 5.18 gives the simulated results, which reveal that the three arrays present resonances at 3.05 THz, 2.89 THz and 2.75 THz, respectively. Therefore, the 19 µm antenna array hits the right resonant frequency.

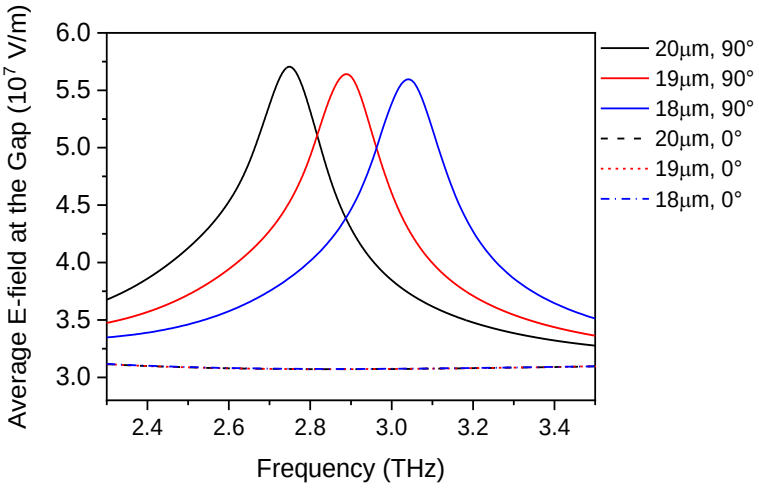

Figure 5.18 Average electric field at the gap between two antennas for different antenna sizes and different light polarizations. 90° and 0° represent the polarization of the light along the antenna axis and perpendicular to the axis, respectively.

To have a rough understanding of what is expected to appear on the nearfield image, the electric field distributions of the 19 µm antenna array when incident light is

polarized in two directions are simulated with COMSOL Multiphysics with a 1W input power (power density of $2.59\times10^{-3}\,\mathrm{W/\mu m^2}$). The results are shown in Figure 5.19.

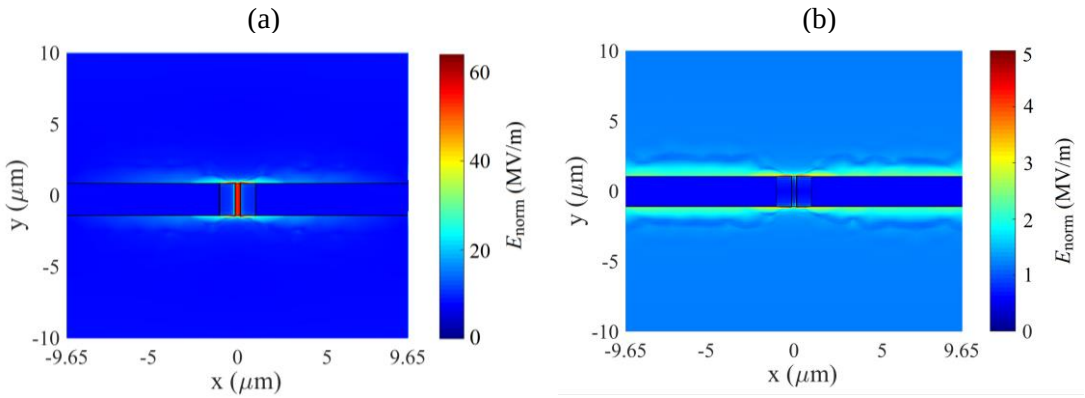

Figure 5.19 E-field distribution at 2.85 THz for the antennas from COMSOL simulation at different light polarizations with an input power density of $2.59\times10^{-3}\,\mathrm{W/\mu m^2}$. (a) parallel to x axis; (b) perpendicular to x axis. A graphene square at the gap area (as shown in Figure 5.20) is included in the simulation.

When the polarization is parallel to the main axis of the antennas, a concentrated electric field presents at the gap area, which is about 60 MV/m. When the polarization is rotated by 90° thus perpendicular to the main axis, there is no concentrated field at the gap area anymore. Instead, only a slightly stronger electric field can be seen at the edge of the antennas compared to other regions. The average electric field at the edge area is about 3 MV/m, which is 20 times weaker compared with the previous situation.

5.4.3 Fabrication of the sample

The 19 μm antenna array is then fabricated by my colleague Long Xiao with a similar procedure discussed in Section 3.2.3. Monolayer graphene, grown by CVD [345] is first transferred onto a SiO_2/Si substrate (300 nm/525 μm thick) and selectively etched in an oxygen plasma chamber after an electron beam lithography in order to define an array of graphene squares. Each square has an area of 9 μm^2. The antenna array is then fabricated via electron beam lithography, Ti/Au metal evaporation (14/91 nm) and lift off. The gap between two antenna arms is about 300 nm. The graphene squares are designed in the position to short the gap between the antenna arms.

In order to reduce the hysteresis [346] and bring the Dirac point to bias voltages lower than 100-120 V, which has been observed in previous strongly p-doped samples, a conformal dielectric layer (100 nm of Al_2O_3) is deposited on top of the sample via ALD in stop-flow mode using H_2O/TMA precursors, thus encapsulating the graphene [347]. Due to this dielectric layer, other imaging techniques or s-SNOM at other frequency ranges cannot get information from underneath it. However, the strong

penetration ability of THz radiation makes the THz s-SNOM a unique tool to study such samples. Figure 5.20 gives the SEM micrograph of one pair of antennas on this sample.

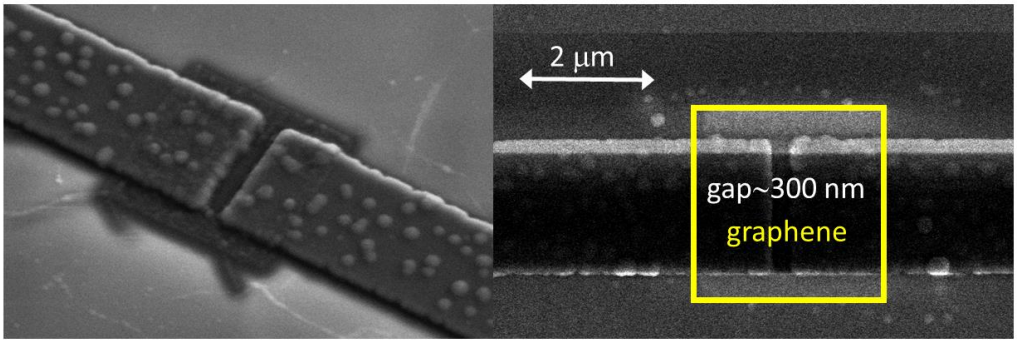

Figure 5.20 SEM micrograph of one pair of antennas on the fabricated sample.

5.4.4 Transmission spectrum measured by TDS

To further confirm the resonant frequency of the sample, it is tested in a THz TDS (Menlo) system. Figure 5.21 shows its transmission spectra when the incident light has different polarization directions. A resonant dip at about 2.75 THz (0.14 THz lower than the simulation result) can be seen when the light is polarized along the main axis while there is nearly no resonance present when the polarization is perpendicular to the main axis. The transmission of data is normalised using the SiO_2/Si substrate as a reference. The normalised transmission at 2.85 THz is about 20% and 50% for the parallel and perpendicular polarisations.

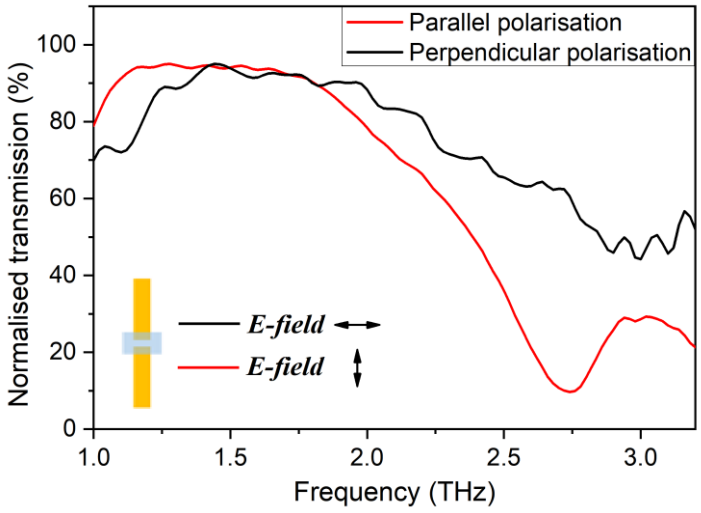

Figure 5.21 Transmission spectra of the 19 μm antenna array with two different light polarisations measured with THZ TDS.

5.4.5 THz response with the SNOM

The antenna array is then imaged with the V1 s-SNOM when no gate voltage is applied on it. In the following two measurements, all the parameters, apart from the scanning area, are kelp the same. The scanning area for the light polarisation along the antenna main axis is $4\ \mu m \times 3.5\ \mu m$. For the polarisation perpendicular to the antenna axis, the scanning area is $14\ \mu m \times 4.5\ \mu m$. The other parameters are shown in Table 5.3.

Table 5.3 THz-s-SNOM measurement parameters for the antenna array

s-SNOM	Step size (μm)	Delay time (ms)	Integration time (ms)
V1	0.1	500	300

When the orientation of the incident light polarization is along the antenna main axis, the THz image and the corresponding extracted profile, shown in Figure 5.22 (c), (d) respectively, present a strong E-field enhancement in the gap area. This is in good agreement with the simulation result reported in Figure 5.19 (a). The line profile is obtained by averaging all the lines from 1 μm to 2 μm in the x direction.

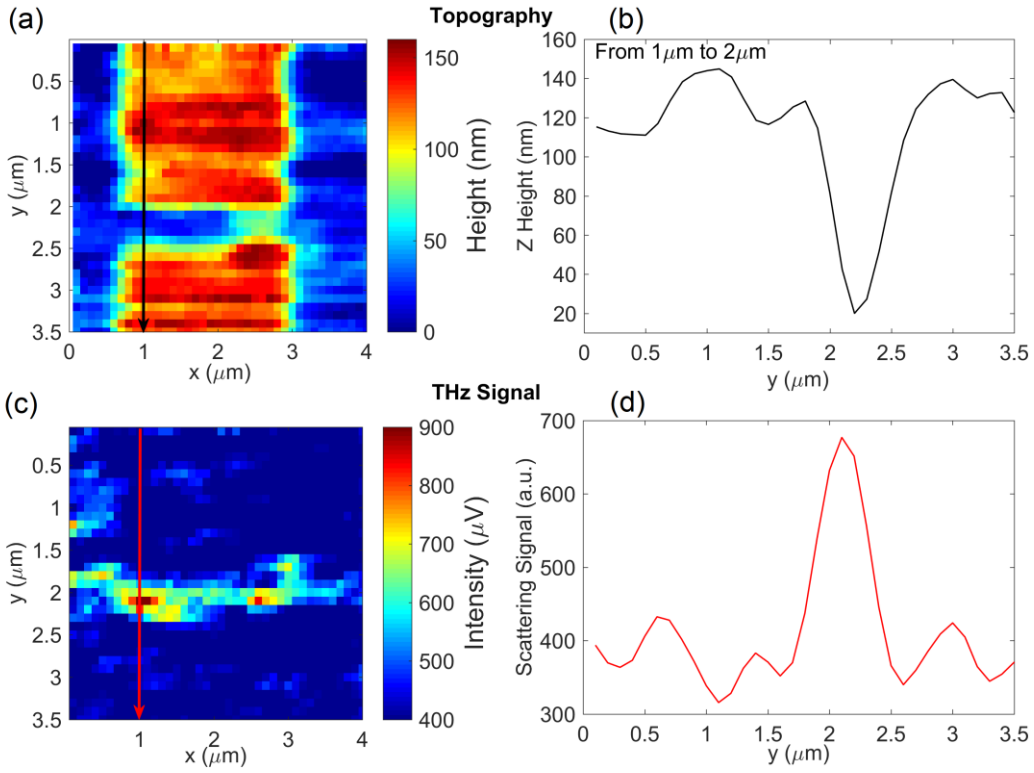

Figure 5.22 Plasmonic resonance with the E-field polarized along the major axis of the antennas. (a) Topography of the resonant elements with about 300 nm gap. (b) Extracted line profile of the same element. (c) THz signal and corresponding profile (d) showing a strong E-field enhancement in the gap region. The step size is 100 nm.

In contrast, when the sample is scanned with the light polarization perpendicular to the main axis of the antenna, a weak THz signal is still observable at the boundary between the metallic antennas and the dielectric, as shown in Figure 5.23 (b), but no resonant enhancement of the E-field is observed in the gap. It can also be seen that the scattering signal is much weaker (around 85 μV), as shown in the line profile in Figure 5.23 (b), compared to the one with the light polarization parallel to the antenna axis (700 μV at the gap area). The line profile is obtained by averaging all the lines from 1.5 μm to 2 μm in the y direction.

After measuring the antenna array as a static device, another attempt is made to measure it in the s-SNOM as a dynamic device, the reflectivity of which can be tuned by back gating. However, when applying a back-gate voltage, the leakage current goes across the device is very high (around 1 mA), which makes it unsuitable to act as a dynamic device. New samples which can be backgated with the same geometry will be designed and fabricated in the future.

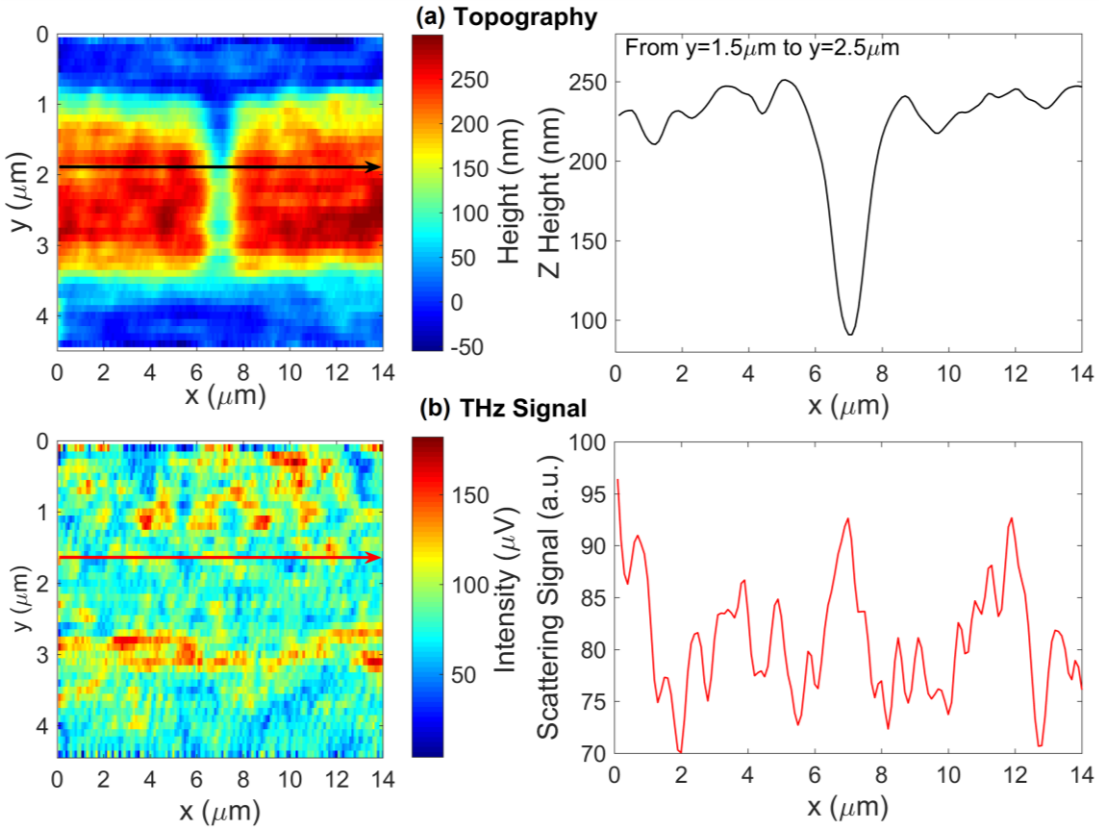

Figure 5.23 Topography (a) and corresponding THz image (b) of the antenna device with the E-field polarized perpendicular to the major axis of the antennas. The profiles extracted show that there is no resonance in the gap, as the polarization of the incoming radiation cannot excite the main plasmonic resonance.

5.5 Electric field mapping of a split-ring resonator

The THz s-SNOM is then used to image the electric field distribution of a device with a slightly more complicated geometry. Here, it is the SRR device used for amplitude modulation in Chapter 3. Being able to map the electric field distribution will help people to better understand the mechanism of the modulation. The structure and geometry of the device are shown in Figure 3.3. This device is covered by a large single sheet of graphene; therefore, it will damp the resonance of the resonator and give a less concentrated electric field, meaning a lower THz signal for the s-SNOM measurement.

5.5.1 COMSOL simulations

Before undertaking s-SNOM measurements, the electric field distribution within a single split-ring resonator with a nominal size *a* of 12.8 μm is simulated with COMSOL Multiphysics with an input power of 1 W (power density of $1.8\times10^{-3}\,\mathrm{W/\mu m^2}$). The simulated distributions for the absolute value of the electric field z component are shown in Figure 5.24 (a) and Figure 5.24 (b) for different input electric field directions, which are the THz signal distributions expected to see in the s-SNOM measurement.

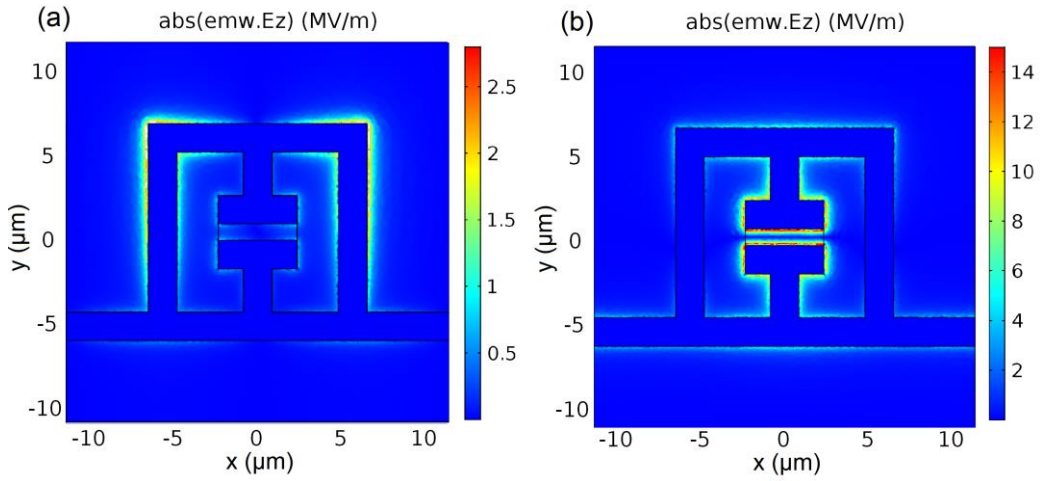

Figure 5.24 The distribution of absolute value of the E-field z component on an SRR with the polarization of light in: (a) *x* direction; (b) y direction

When the input electric field is in the x direction, the electric field is stronger at the edges of the arms on the two sides. In contrast, when the electric field is in the y direction, a field concentration can be seen within the gap area. It can also be seen from the simulation that, the SRR has a lower field concentration at the gap area compared to the antenna as the average electric field at the gap for the SRR is 5 MV/m while the one for the antenna array is about 60 MV/m. Considering the input power density for

the antennas array is 1.44 times the one for the SRR, the electric field at the gap of the antennas is about 8.33 times the one for the SRR, which is almost an order of magnitude stronger. Therefore, a higher sensitivity is necessary to get the information of the electric filed distribution of the SRR device.

5.5.2 SNOM measurement results

The device is first measured with the V1 s-SNOM before all the modifications for topography improvement have been undertaken. Figure 5.25 shows the results for one measurement. The quality of the topography is poor with a large variation on the height. The height of gold SRR structure is about 100 nm. However, the variation of the height in the topography image is more than 200 nm, more than twice of its real height. On the THz image, no clear signal can be seen, which is expected considering the quality of the topography. The conclusion is that the system is not stable enough to measure samples with a small variation on height. Therefore, an upgrade of the system, which is discussed in Section 4.6 has been done to improve the topography.

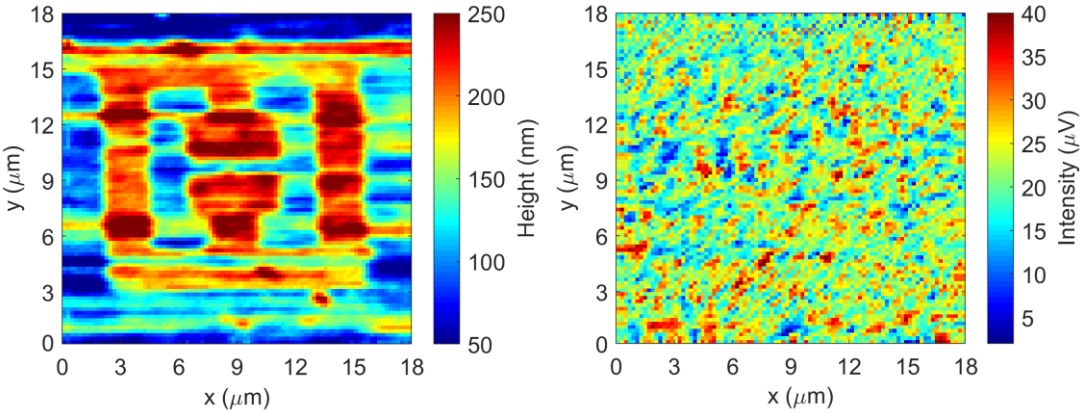

Figure 5.25 (a) The topography and (b) THz image of an SRR with the V1 s-SNOM when the light polarization is in y direction. Step size of this measurement is 200 nm.

After the upgrade of the system, the same SRR device is scanned in the V2 s-SNOM with the light polarized in the x direction (perpendicular to the capacitive gap) and the other parameters as shown in Table 5.4.

Table 5.4 THz-s-SNOM measurement parameters for the SRR

s-SNOM	Area (μm×μm)	Step size (μm)	Delay time (ms)	Integration time (ms)	Scanning time (min)
V2	16×16	0.2	500	300	54

Figure 5.26 (a) and (b) shows the recorded topography as well as the THz image. The topography is significantly improved compared to the one taken with V1 s-SNOM and gives the height of the gold on the device as about 110 nm, which is consistent with the design specification (100 nm). The SRR feature can be seen clearly and the surface of the metal looks flat. On the THz image, a strong signal can be seen at the gap region, which reveals a concentrated electric field there, in good agreement with the simulation result. Line profiles are extracted for both the topography and THz images in Figure 5.25 (a) and (b). The correlation of the gap on the topography and a reduced scattering signal on the THz image can be seen on the line profiles shown in 5.25 (c) and (d). As the electric field is only concentrated at the gap region in this situation, it reveals that large area graphene is not necessary for modulation. This gives us a direction for improving the performance of the SRR device as a modulator because small area graphene introduces smaller capacitance, which results in a higher modulation speed.

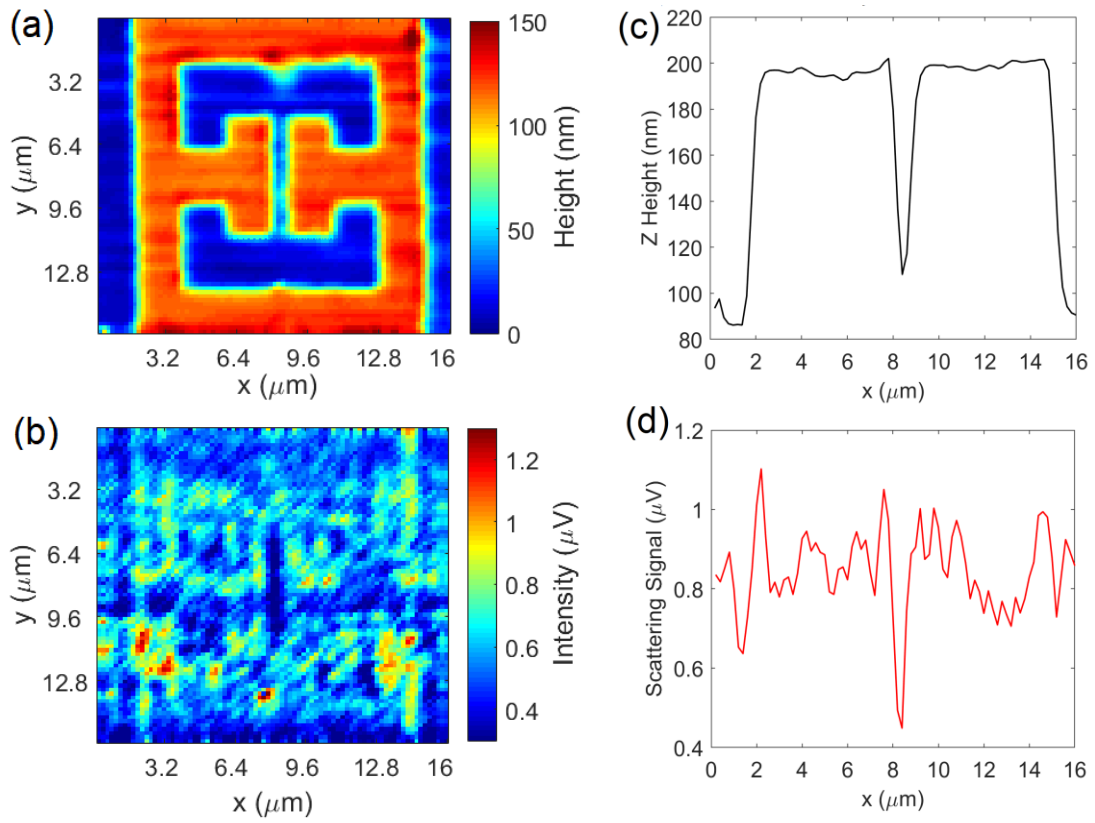

Figure 5.26 The topography and THz image of an SRR when the light polarization is perpendicular to the gap: (a) topography; (b) THz image. There is a strong signal at the gap area. Step size of this measurement is 200 nm. (b) and (d) are the corresponding line scan profiles by averaging all the lines from 7 μm to 9 μm in the y direction.

It needs to be pointed out that an inverted signal is seen here because the phase difference between the feedback signal from scattering and the internal laser field is close to 180 degree. The voltage perturbation is dependent on the optical path length, which determines the phase difference, as shown in Figure 5.27 [348]. Therefore, when the phase difference is 180 degree, the system operates in a similar condition as the valley position on the blue curve. The scattering signal gives a destruction interference to the laser field, which means a stronger nearfield interaction will give a smaller signal.

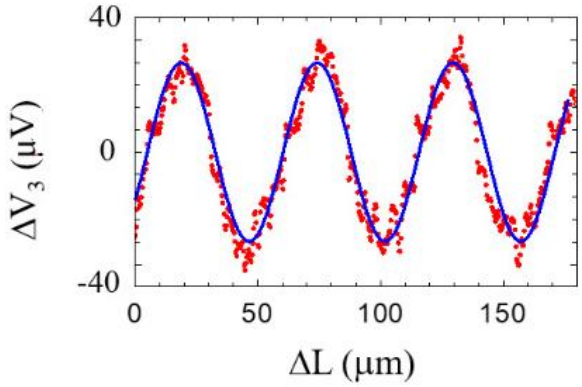

Figure 5.27 Self-mixing induced modulation from a Au surface of the voltage drop across the QCL at the third demodulation order, as a function of ΔL. Reprinted with permission from [348], © 2018 Optical Society of America.

The sample is then rotated by 90 degrees so that the polarization of the THz light is parallel to the gap and scanned in the V2 s-SNOM. All the scanning parameters are the same with the previous measurement. The topography gives the same height for the metal, as shown in Figure 5.28 (a) and also confirmed by the line profile in Figure 5.28 (c). The THz response is displayed in Figure 5.28 (b), which shows the outline of the SRR geometry and a slightly stronger electric field on the side arms, which is also consistent with the simulated result. On the x direction line profiles in Figure 5.28 (c) and (d), a correlation can also be seen between the gold structure on the topography image and the THz scattering signal. On the y direction line profiles, the gap can be seen on the topography line scan but there is no correlated signal on the THz line scan, as shown in Figure 5.29. As a result, this non-resonant response will not make a big contribution to the modulation as the electric field is not confined at the gap area. This explains why this device can only modulate the light when it is polarized perpendicular to the gap.

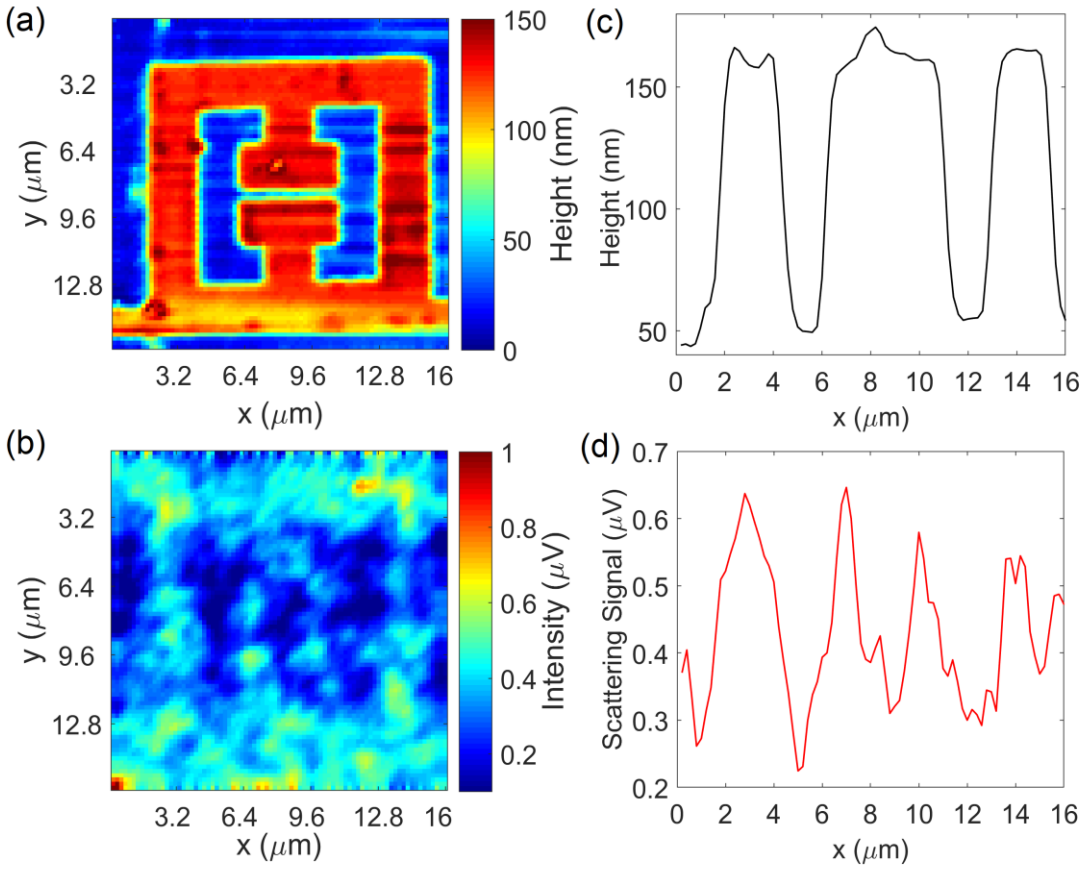

Figure 5.28 The topography and THz signal of an SRR when the light polarization is parallel to the gap: (a) topography; (b) THz image. Step size of this measurement is 200 nm. (b) and (d) are the corresponding line scan profiles by averaging all the lines from 6 μm to 8 μm in the y direction.

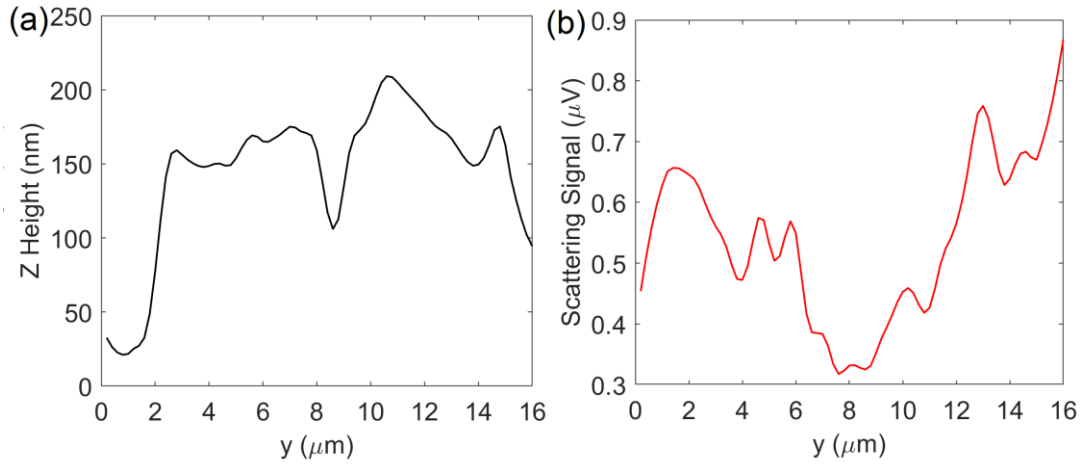

Figure 5.29 Line profiles for (a) topography in Figure 5.28 (a) and (b) THz image in Figure 5.28 (b) in the y direction. They have been taken by averaging all the lines from 7 μm to 9 μm in the x direction on the two images.

5.6 Metasurface Fractal-Cross Absorbers

Following on the resonant structures, a metasurface sample has been measured in the THz s-SNOM. The device is similar to the one reported in reference [349]. It is a broadband metasurface THz absorber with fractals as the base geometry, as shown in Figure 5.30. Two fractal features (level 1, shown in Figure 5.30 (a), and level 3, shown in Figure 5.30 (b)) are distributed periodically on the substrate, which consists of three layers: Si, metal (Ti/Au) and polyimide. The fractal cross behaves as a resonator here. Fractals with different orders will resonate at different frequencies. Therefore, combining fractals of several different orders together will generate a broadband resonance. To optimise the design, it is essential to know which resonant modes exist for fractals with different orders or sizes, and the s-SNOM has the potential to image the resonant modes supported by this structure.

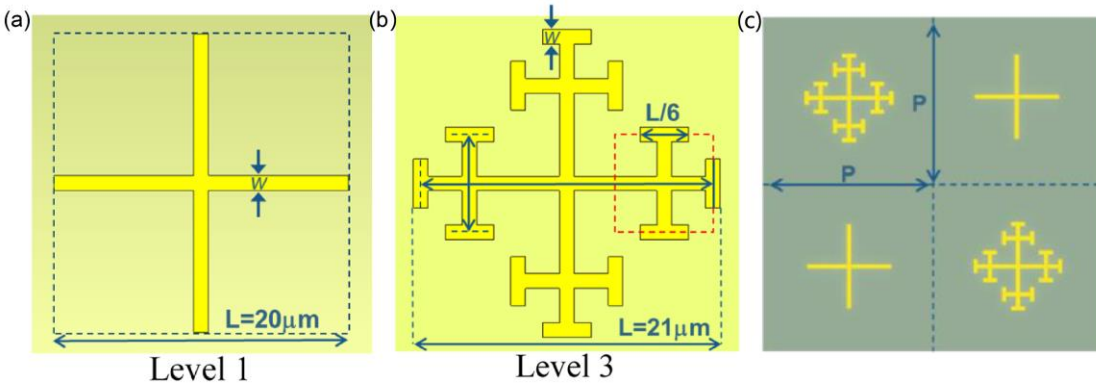

Figure 5.30 Geometry of the metasurface sample. (a) the geometry of the level one fractal; (b) the geometry of the level three fractal; (c) the layout of the fractals on the metasurface. Line width w =1 μm for all structures. Modified with permission from [349]. Copyright (2017) American Chemical Society.

5.6.1 COMSOL simulation

COMSOL simulations are performed to get the response of one unit of the periodical feature when it is illuminated by a plane wave at 2.85 THz in two directions (0° and 45°). Here 0° means the polarization of the light is parallel to the y axis in Figure 5.31. As shown in Figure 5.31 (a), when the light is polarised along one axis of the cross, it excites a resonance mode along this direction. A strong electric field exists at the edge of its arm in the excited direction while a weak electric field exists on the other arm. Because of the symmetry of the sample, it will have the same response if it is rotated by 90°. When the sample is rotated by 45°, the electric field of the light will have an equal component in both the x and y directions. Therefore, a symmetric electric field

distribution is expected, as confirmed by the simulation result in Figure 5.31 (b). Also, the electric field is stronger at the edge of the cross branches while the electric field in the centre of both fractals is nearly zero.

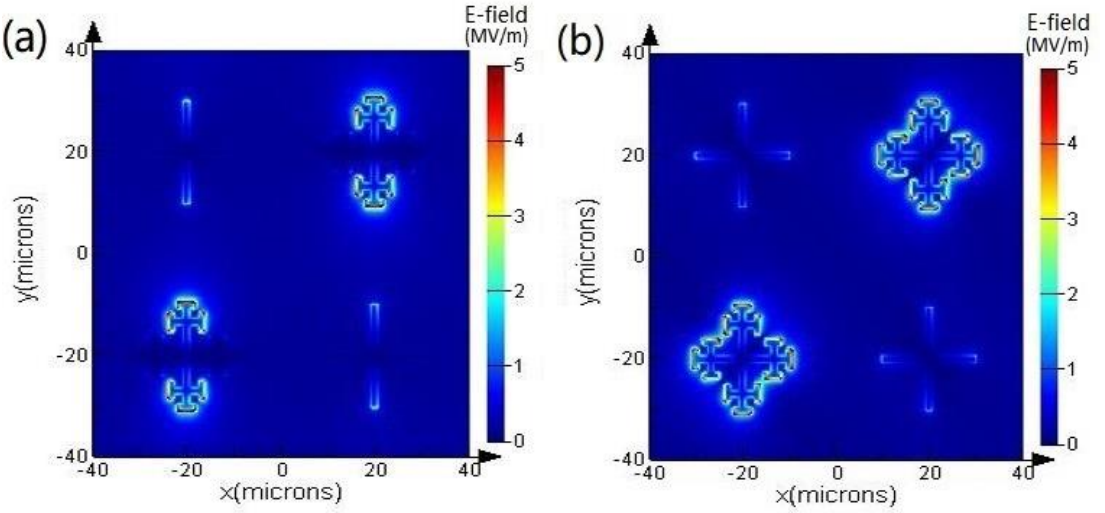

Figure 5.31 Simulated electric field distribution on the sample when the light is incident in (a) 0° (parallel to the y axis); (b) 45°, simulated by Yash D. Shah from University of Glasgow. The input power of the electric field is 1 W.

5.6.2 THz s-SNOM measurement results

As discussed in the previous section, the metasurface has different responses when the incident light is polarised in different directions. To prove this, it is imaged in the V2 s-SNOM.

5.6.2.1 Polarization of the incident light

Only two situations (0° and 45°) need to be considered here because of the symmetry of the geometry. The sample is first scanned with the light polarised along one of the cross arms, here in the y direction. The scanning parameters are displayed in Table 5.5. As can be seen from Figure 5.32 (a), the topography reveals the geometry of the fractal cross clearly and an asymmetry can be seen on the THz image. There is a strong THz signal along the y direction while not much signal can be seen along the x direction, which means there is a strong electric field along the y direction while the electric field along the x direction is negligible. This is in good agreement with the simulation result shown in Figure 5.31 (a). When the sample is rotated by 45°, the asymmetry is broken, and similar levels of signal is recorded in both directions. For three 3rd order fractals, the electric field is higher on the high order branches and lower in the centre, which again is consistent with the simulated results. However, for one 3rd order fractal (bottom

left), the electric field at the centre of the fractals is of similar strength with the one at the edge of all the branches, which might be an artefact of the THz signal. Further investigation is needed to find the reason for this mismatch between the COMSOL simulation and THz s-SNOM image.

Table 5.5 THz-s-SNOM measurement parameters for Figure 5.32

Polarisation	Area (μm×μm)	Step size (μm)	Delay time (ms)	Integration time (ms)	Scanning time (min)
0 degree	80.4×80.4	0.6	500	300	150
45 degree	84×84	0.6	500	300	165

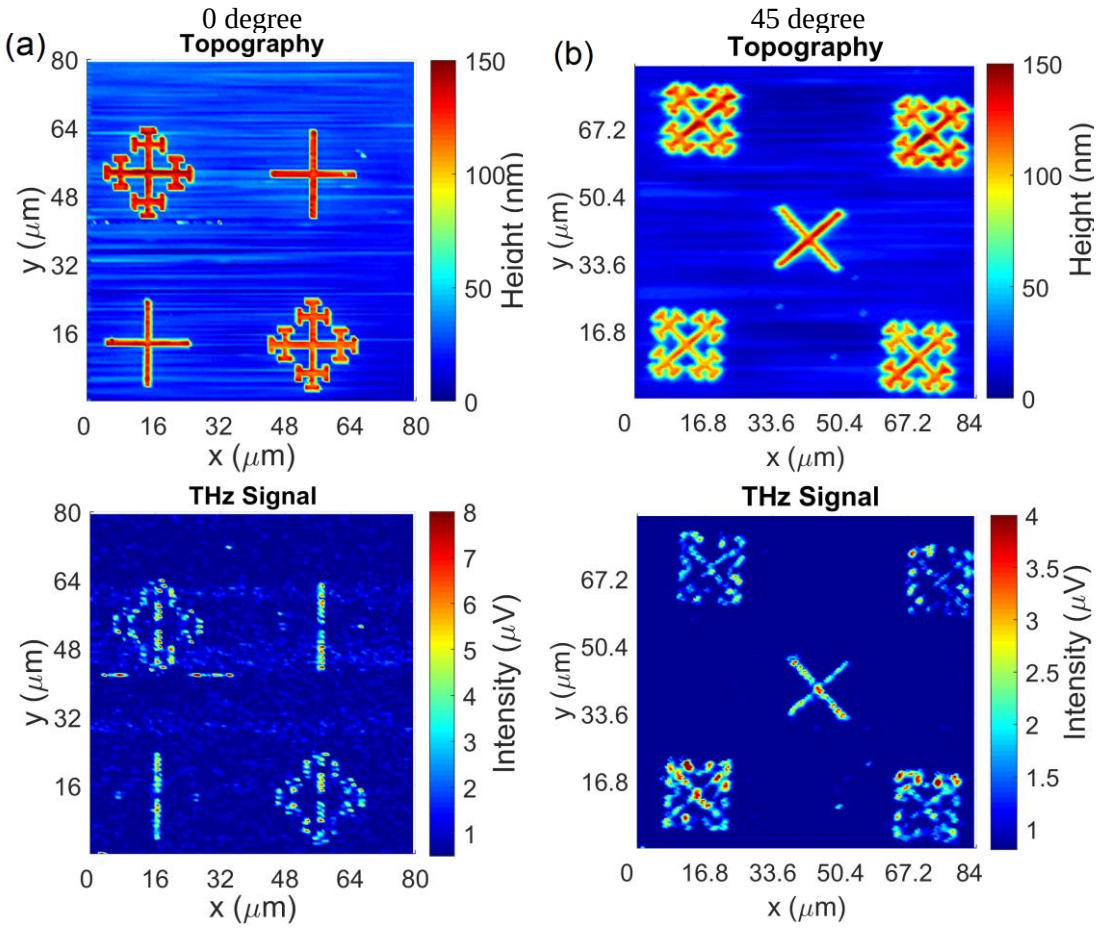

Figure 5.32 THz s-SNOM results of the absorber in two scanning directions: (a) 0°; (b) 45°. The top graphs are topographies and the bottom ones are THz images.

5.6.2.2 QCL power

Usually, the THz QCL in the s-SNOM setup is operated at the bias current where it gives maximum power (1 A for this QCL). When the operating current is increased from 1 A to 1.2 A, the power of the QCL drops because the energy bands starts to misalign, as can be seen from Figure 4.21 (a). For the metasurface, this means the incident electric field becomes weaker, which will give a reduced THz signal. This has been observed during our measurement. Three scans are performed when the operating current of the QCL is changed from 1 A to 1.2 A. The other scanning parameters are kept the same for all the scans and are displayed in Table 5.6. From the results in Figure 5.33, it can be seen that the THz response becomes weaker when the operating current is increased. The signal nearly halves when the current is increased to 1.2 A, which is expected as the power of the QCL drops from 2.5 mW to 1.1 mW, as can be seen from Figure 4.21 (a).

Table 5.6 THz-s-SNOM measurement parameters for different QCL currents

Polarisation	Area (μm×μm)	Step size (μm)	Delay time (ms)	Integration time (ms)	Scanning time (min)
45 degree	22.2×22.2	0.3	500	300	50

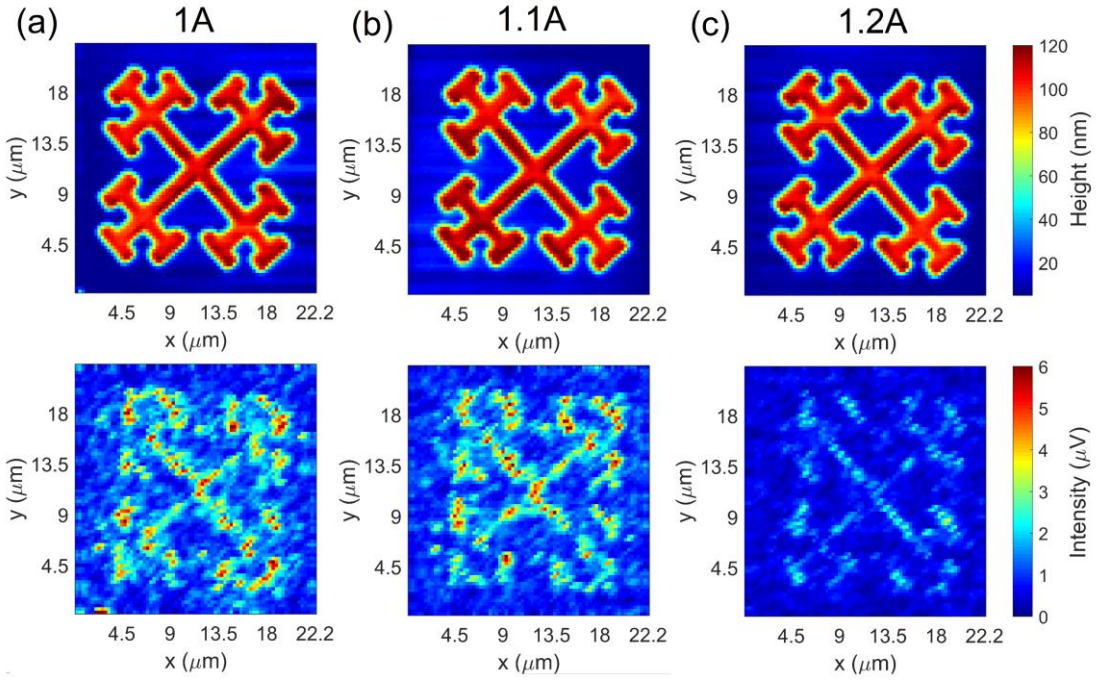

Figure 5.33 THz s-SNOM results of the absorber in 45° scanning direction, with different operating currents of the THz QCL: (a) 1 A; (b) 1.1 A and (c) 1.2 A. The top graphs are topographies and the bottom ones are THz images.

5.6.2.3 Integration time

During the measurement, it is found that the signal integration time chosen on the lock-in amplifier has a large effect on the SNR ratio of the THz signal. In principle, a longer integration time shall give a larger SNR at the cost of the scanning speed. As a result, it is useful to find an integration time that could give a reasonable SNR and scanning speed at the same time. Here, the same feature is imaged by the s-SNOM with the integration time being 30 ms, 100 ms and 300 ms. The corresponding step delay times for these three measurements are set to 60 ms, 200 ms and 600 ms, respectively. The other measurement parameters (scanning area, step size) are the same as the scans in the last section and the QCL is operated at 1 A. The measurement results are displayed in Figure 5.34. As can be seen, for all the measurements, the quality of the topography looks nearly the same. This means that 60 ms is already long enough for the tip to settle down when the height of the sample changes. Therefore, if the sensitivity of the nearfield is high enough, the scanning speed of the s-SNOM can be higher than 160 Hz. However, for the THz image, the image quality looks very different at different integration times. At 30 ms, the SNR is too low to see a clear signal. When the integration time is increased to 100 ms, it can already give a reasonable SNR. Therefore, 100 ms is a suitable compromise between the scanning speed and the system SNR for future measurements.

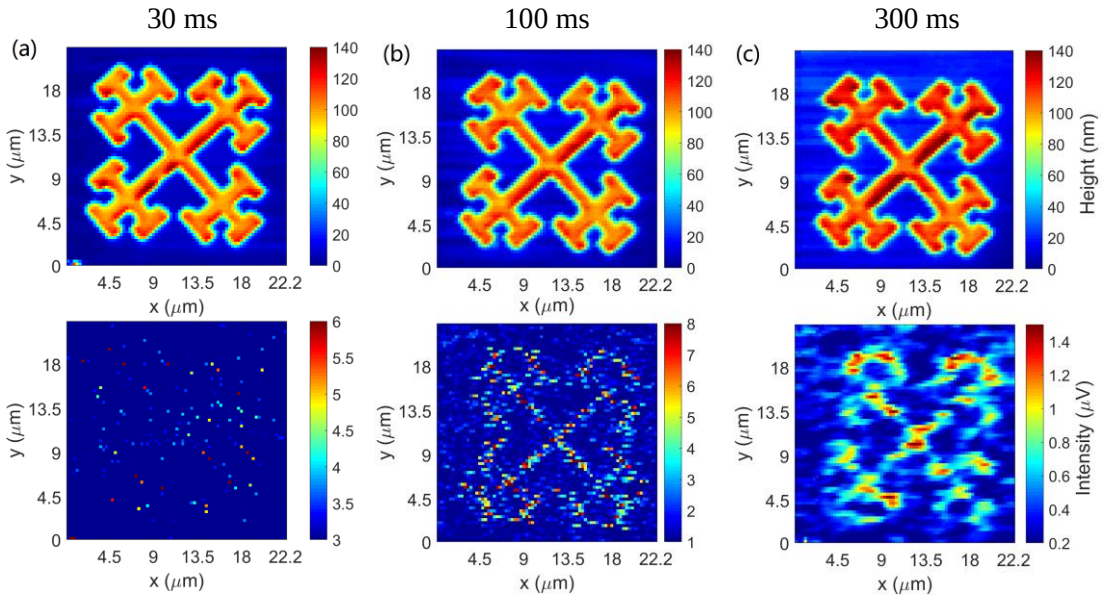

Figure 5.34 THz s-SNOM results of the absorber in 45° scanning direction and different integration times on the lock-in amplifier: (a) 30 ms; (b) 100 ms and (c) 300 ms. The top graphs are topographies and the bottom ones are THz images.

5.7 Tip material and geometry

Apart from THz nanoimaging of functional devices, the system can also be used to analyse how to improve the contrast of the THz image. For instance, it can be used to find an optimum material or geometry for the tip. According to equation (4.2) and equation (4.8), the material of the tip has an influence on the nearfield interaction. Therefore, it is necessary to investigate which material can help to give a larger optical response. For nearfield interaction, the most important optical property of the tip is the relative permittivity ε_t . As this property is frequency dependent, it is essential to find which materials have a smaller real part of ε_t at THz frequency range as a smaller real part will give a larger effective polarizability.

At the same time, scanning tips with resonant structures can enhance the field concentration within the tip apex area, which can be achieved by exploiting the lightning rod effect or adiabatically compressing an electromagnetic wave propagating along a long, tapered metal wire [4], [350], [351]. For the normal cone shaped tips, it is found that a large field enhancement can be achieved when the length of the tip is close to the wavelength of the light source [352], [353]. The resonant length can be calculated as $L = \lambda/2\gamma$, here L is the tip length, λ is the wavelength of the light source and γ is the geometric factor depending on the geometry and material of the tip.

5.7.1 Optical properties of several materials at THz frequency range

To analyse the influence of optical properties of the tip material on the nearfield signal, the amplitude and phase of the effective polarizability α_{eff} for several different tip-sample systems have been calculated with the equation (4.8). The relative permittivity of several metal materials is displayed in Table 5.7.

Table 5.7 Relative permittivity of several materials at 3 THz [213][354]

Material	Tungsten	Gold	Silver	Titanium
$\varepsilon_{\text{real}}$	-37817.448	-106000	-133710	-6495.0594
$\varepsilon_{\text{imag}}$	60952.753	193000	218450	15728.015

Among these four materials, tungsten, gold and silver are commonly used at THz frequency range and there are commercial tips available either with the material or coated with the material. Therefore, these three materials have been used in this calculation. The sample has been chosen to be Au on SiO_2 , which is the most commonly used material system for our devices. The calculated results are shown in

Figure 5.35, from which it can be seen that the amplitudes of α_{eff} for different materials are nearly the same. This is expected as the real parts of ε_t for these metals are all large negative numbers, which gives a nearly equal to 1 value for the amplitude of $(\varepsilon_t - 1)/(\varepsilon_t + 2)$. Thus, the tip material almost has no effect on the amplitude of α_{eff}.

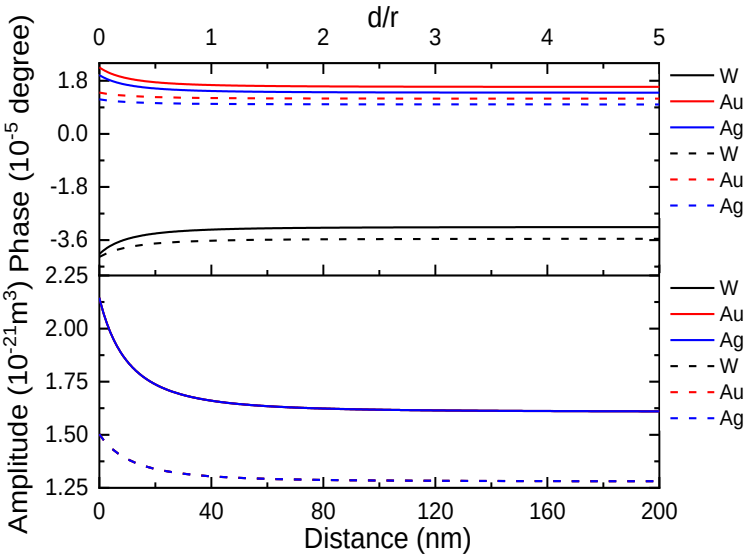

Figure 5.35 Effective polarizability α_{eff} of the tip-sample system. The solid lines are for the Au sample while the dashed lines are for SiO_2 sample. The bottom graph shows the amplitudes of α_{eff} and the top graph gives the phase changes for different tip materials.

However, the situation is quite different for the phase. For different tip materials, the phase changes are different, as shown in the top graph in Figure 5.35. Since the self-mixing effect is phase sensitive, a larger phase difference will also give a stronger signal. As can be seen from Figure 5.36, for the same material group, Au and Ag give a larger phase change compared to W. As a result, Au and Ag tips or Au- and Ag-coated tips are preferred for THz s-SNOM.

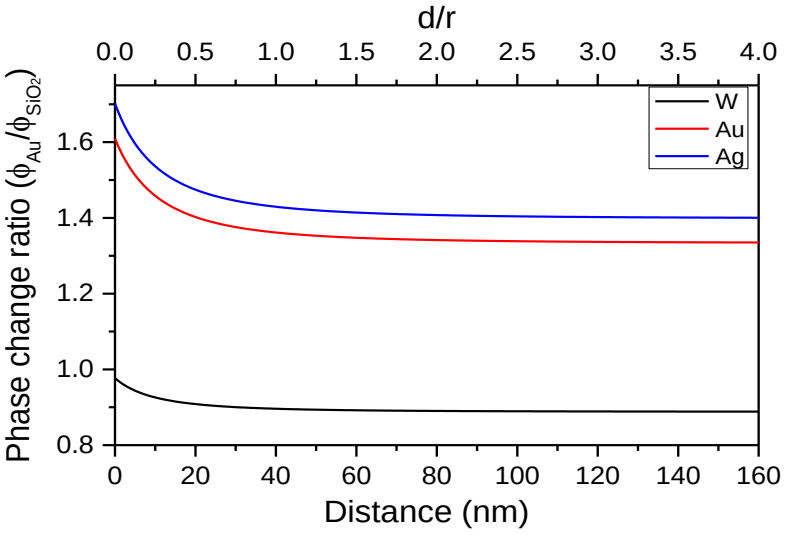

Figure 5.36 The phase contrast between Au and SiO_2 for different tip materials

5.7.2 Gold coated tungsten tip

As discussed in the last section, because a gold tip can introduce a higher phase change difference between Au and SiO_2 compared to a tungsten tip, for samples with Au features on a SiO_2 substrate, the gold (or gold coated) tip can give a better contrast. This has been further confirmed by imaging gold features on a SiO_2/Si substrate with a gold coated tungsten tip.

Firstly, the stability of the tip is evaluated by recording the topography of a sample with a simple structure. Here, a gold coated tungsten tip from Nanonics is incorporated into the V2 s-SNOM. The Q factor of the probe and the tip radius are similar to the tungsten tips used before. Therefore, a similar topography resolution shall be expected, which is confirmed by recording the topography of a gold corner on a SiO_2/Si substrate, shown in Figure 5.35 (a). The scanning parameters are displayed in Table 5.8. A line profile extracted from it gives a resolution of about 50 nm, which can be improved by reducing the step size. Also, for current applications, a 50 nm step size is small enough to reveal the necessary information as the smallest feature scanned is at least 100 nm in size. The line profile gives the thickness of gold as 75 nm, which is consistent with the result from an AFM measurement. It also shows that the gold surface is flat on the topography, which indicates a low tip oscillation amplitude during the measurement.

Table 5.8 Scanning parameters for Figure 5.35

s-SNOM	Area (μm×μm)	Step size (μm)	Delay time (ms)	Scanning time (min)
V2	2×2	0.05	200	6

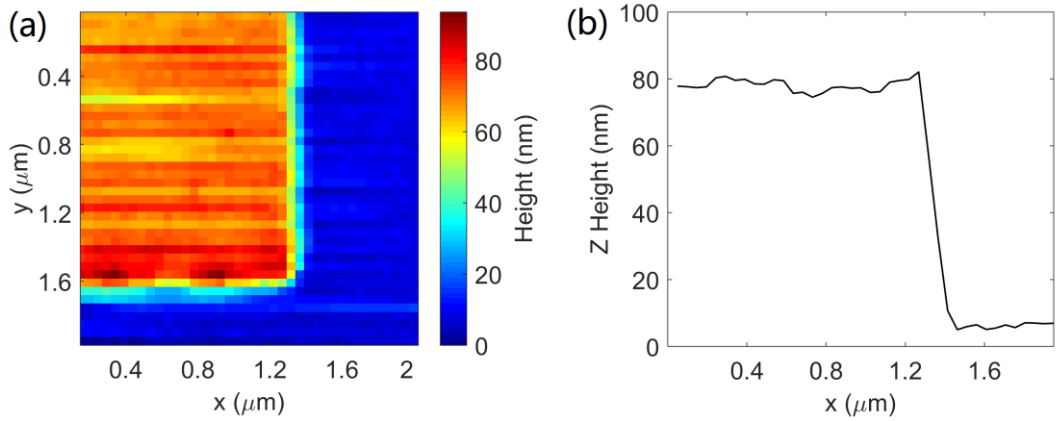

Figure 5.37 Topography of a gold corner on SiO_2/Si substrate with a gold coated tungsten tip. (a) topography; (b) a line profile extracted from the topography graph along the x direction at y=1 μm.

Then, the tip is used for imaging a more complex structure: a coupled resonator. The sample measured here consists of Au resonators on a SiO_2/Si substrate. The resonators are out of resonance with the QCL frequency (new resonators will be designed to work at 2.85 THz in Chapter 6). Therefore, it is only expected to see a contrast between Au and SiO_2. A s-SNOM scan is performed with the parameters shown in Table 5.9. Figure 5.38 (a) shows the topography of the resonator, which has very sharp contrast at the geometry boundaries, further confirming that a high resolution can be achieved with this gold coated tip. The yellow region is the Au feature and it is expected to have a stronger THz response, as can be seen from the THz image shown in Figure 5.38 (b), which looks blurred. One possible reason for this is that the sensitivity of the THz response is not high enough to produce a sharp contrast, which can be attributed to a non-optimal alignment of the optical path.

Table 5.9 Measurement parameters for Figure 5.38

s-SNOM	Area (μm×μm)	Step size (μm)	Delay time (ms)	Integration time (ms)	Scanning time (min)
V2	21×18	0.3	200	100	15

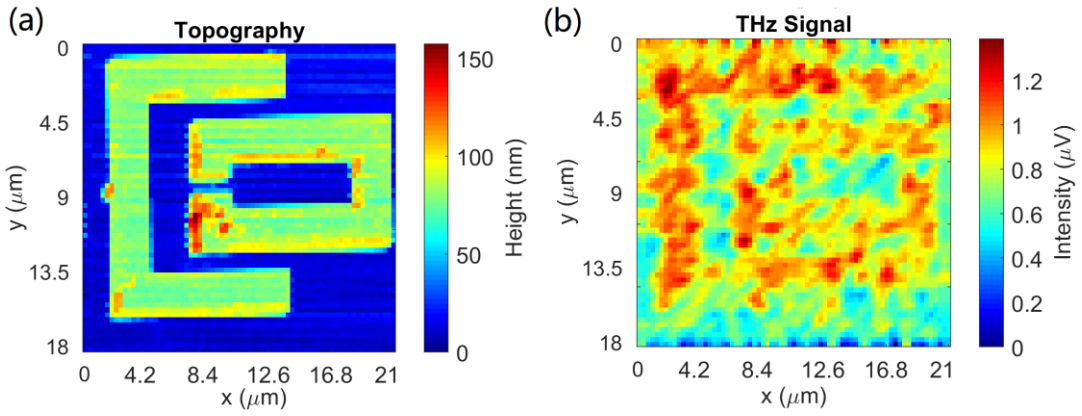

Figure 5.38 Topography and THz image of a coupled resonator recorded by the s-SNOM with the gold coated tungsten tip. (a) topography; (b) THz image.

The performance of the gold coated tungsten tip and a bare tungsten tip is compared by measuring the same feature. The sample measured is a gold feature (100 nm thickness) on a SiO_2/Si substrate. During the optical alignment, the gold coated tungsten tip used in the last measurement is crashed onto the sample due to an unexpected vibration on the optical bench. It is then replaced by a second gold coated tip with a

tuning fork of larger size. The second probe does not work stably in the system, as can be seen from the topography taken with it in Figure 5.39 (a). Despite the bad topography, the THz contrast between Au and SiO_2 can still be seen, as shown in Figure 5.39 (c). The same feature is then imaged with a tungsten tip. The scanning parameters for the two measurements are all the same apart from the step size, which is 0.5 µm for the tungsten tip and 1 µm for the gold coated tungsten tip. The THz signal integration time is 100 ms and the step delay is 200 ms. Figure 5.39 (b) and (d) give the topography and THz image taken with the tungsten tip. Compared with the images taken with the gold coated tip, the topography looks better, but the contrast of the THz image is slightly worse. Also, the THz signal is much lower when the tungsten tip is used.

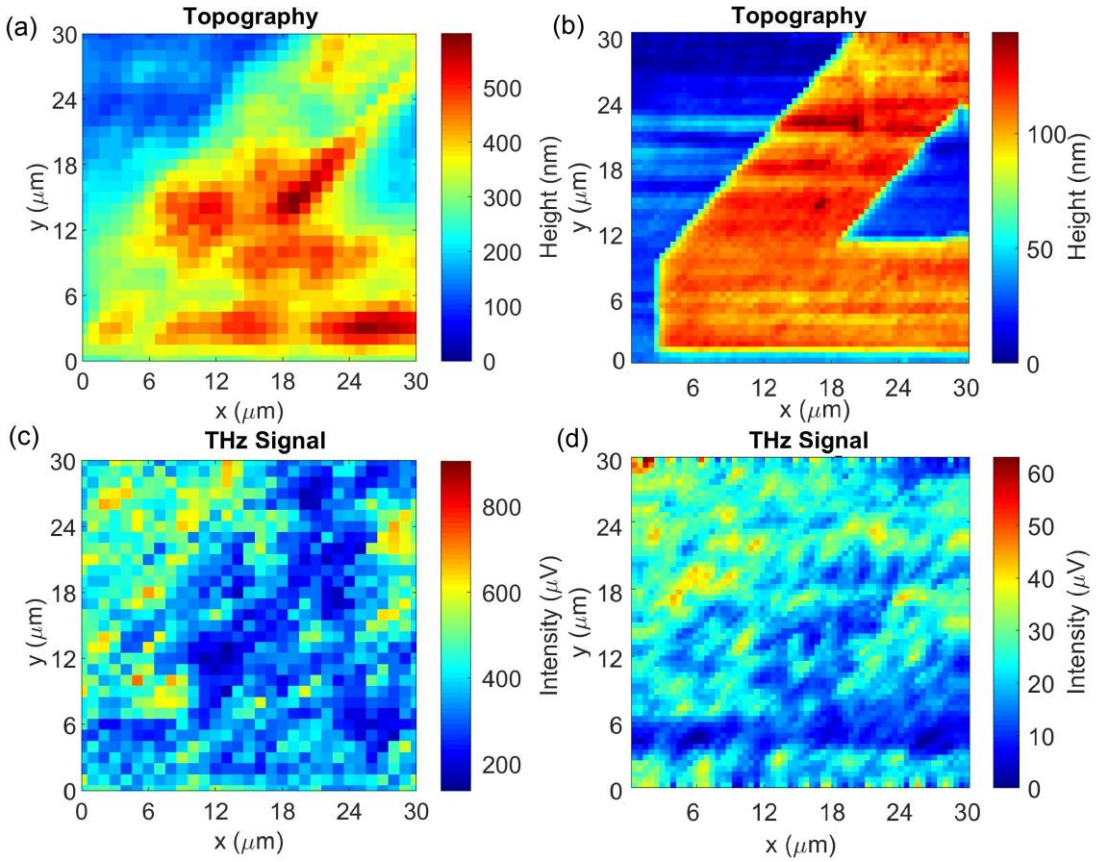

Figure 5.39 THz s-SNOM images of a gold feature on a SiO_2/Si substrate with a tungsten tip and a gold coated tungsten tip. The thickness of gold is 100 nm. (a) and (c) are the topography and THz image measured with the gold coated tungsten tip; (b) and (d) are the corresponding images taken with the tungsten tip. The large height variation on the topography with the gold coated tip in figure (a) is due to the instability of the tuning fork.

Furthermore, a large area scan is performed for a gold letter "Z" on a SiO_2/Si substrate. The scanning parameters are summarised in Table 5.10. The topography is still not good, as can be seen from both Figure 5.40. However, the THz contrast between

the gold and SiO_2 is very strong, which is even better than the contrast of the topography image, as shown in Figure 5.40 (a). The QCL light is then attenuated with a piece of paper, the transmission of which is about 40 %. Therefore, the THz signal will be 16% the one without attenuation as the THz light passes through the paper twice. When the THz light is attenuated with the paper, the THz contrast becomes much weaker (150/100 for SiO_2/Au compared to 250/50 when there is no attenuation), which is expected and can be seen from Figure 5.40 (b).

Table 5.10 Measurement parameters for Figure 5.40

s-SNOM	Area (μm×μm)	Step size (μm)	Delay time (ms)	Integration time (ms)	Scanning time (min)
V2	70×70	1	200	100	17

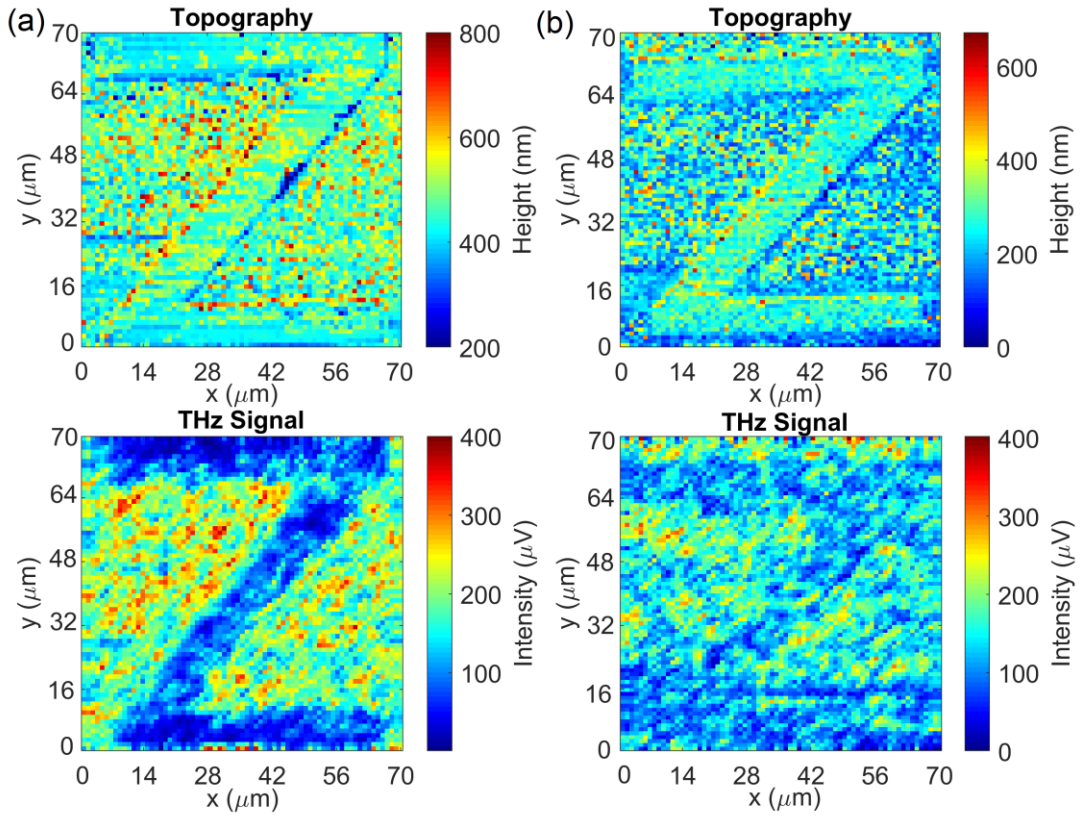

Figure 5.40 THz s-SNOM images of a gold letter "Z" on SiO_2/Si substrate measured with a gold coated tungsten tip at two conditions. The top ones are topography graphs and the bottom ones are THz images. (a) the THz light is not attenuated; (b) the THz light is attenuated with a layer of thin paper.

5.7.3 Tip geometries

The sensitivity of the THz s-SNOM is mainly determined by scattering efficiency of the tip in coupling the nearfield interaction at the tip apex into the far-field [355]. It has been demonstrated that the scattering efficiency can be improved if the length of the tip is comparable to the wavelength of the light being scattered, when the tip behaves as a resonant dipole antenna [356]. Such a tip is called a resonant tip. To study the influence of the tip geometry on its scattering efficiency, a traditional non-resonant tungsten tip and a resonant indium tip are compared. The tungsten tip is from Mad City Labs, Inc, which is the tip generally used in the setup as it is highly compatible with their MadPLL control system. The resonant indium tip is from Oleg Mitrofanov's group in UCL. Indium is chosen here as it is very easy to fabricate into a tip shape on the tuning fork.

Table 5.11 Geometric parameters of the tungsten and indium tip

Tip	Tungsten tip	Indium tip
Length	~2 mm	50-150 μm
Radius	< 50 nm	50-100 nm

Both tips are metal wire tips with similar shapes. The length of the tungsten tip is much longer than the THz wavelength while the one of the indium tip is much shorter and close to the resonant length of THz radiation. The detailed numbers are displayed in Table 5.11. The SEM pictures of exemplar tips are shown in Figure 5.41.

(a) (b)

Figure 5.41 SEM micrographs of (a) a tungsten tip and (b) an indium tip, from [357] [352].

5.7.4 Resonant tip: indium tip

An indium tip is incorporated into the V1 s-SNOM and tested. It is similar to the one reported in reference [352] and fabricated directly onto a bare quartz tuning fork by Thomas Siday from UCL. The tuning fork with indium tip is then incorporated into our THz s-SNOM. During the first attempt, the PID control loop could not detect it when the tip is approaching the sample surface. As a result, the tip crashes onto the sample surface. One potential reason for this is that the tuning fork with indium tip attached has a much larger Q factor (3000) compared to the one with a tungsten tip attached (200-1500) as the indium tip has less mass than the tungsten tip. A larger Q factor means a slower response. In addition, the PID loop is optimized for Q factor between (100-1500) and might not be able to keep a probe with a Q factor of 3000 stable on the sample surface.

To overcome this, two measures have been taken. The first one is to reduce the Q factor of the tuning fork by damping it with a larger mass, which can be achieved by attaching more indium on the tuning fork. After several attempts, the Q factor of the tuning fork with tip, which could be measured directly by its response to an excitation signal with the MadPLL setup and software, is reduced from 3000 to 800, which is within the optimum working range of the PID loop. The second measure is to adjust the PID parameters of the feedback loop when the tip is on the sample surface. With these two improvements, the tip can stay on the sample surface stably enough for a topography measurement. However, during this process, the tip crashes onto the sample surface several times and becomes blunt with a radius around 1 μm, which is estimated from the optical microscope image.

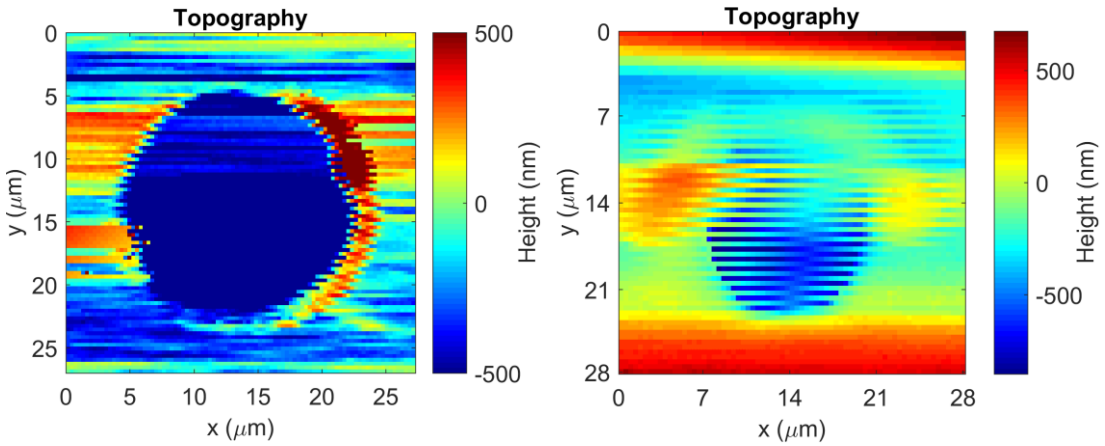

Figure 5.42 Topography of a hole on the THz QCL shown in Figure 5.11 with (a) a tungsten tip, (b) an indium tip

One of the microcavity on the surface of the SEPHC QCL in Section 5.2 has been scanned with the indium tip and the topography is compared with the topography of a similar hole acquired with a tungsten tip, shown in Figure 5.42 (a). With such a tip radius, it is difficult to get a good topography, as displayed in Figure 5.42 (b). It has also been found that the tip is degrading during the scanning and becomes blunter, which indicates that the tip might still have been touching the sample surface at some point within the scanning process. One possible explanation for this is that the tip is too soft and the elastic force it experiences when approaching the sample surface is much smaller than the one for the tungsten tip. As a result, a larger gain might be necessary for the feedback loop in this case.

After the topography comparison, the THz image of a gold corner on a GaAs substrate is taken with the indium tip. Its topography is shown in Figure 5.43 (a), in which the bottom left is gold and the top right is GaAs. A clear contrast can be seen between the gold and GaAs area (a higher signal at the gold area).

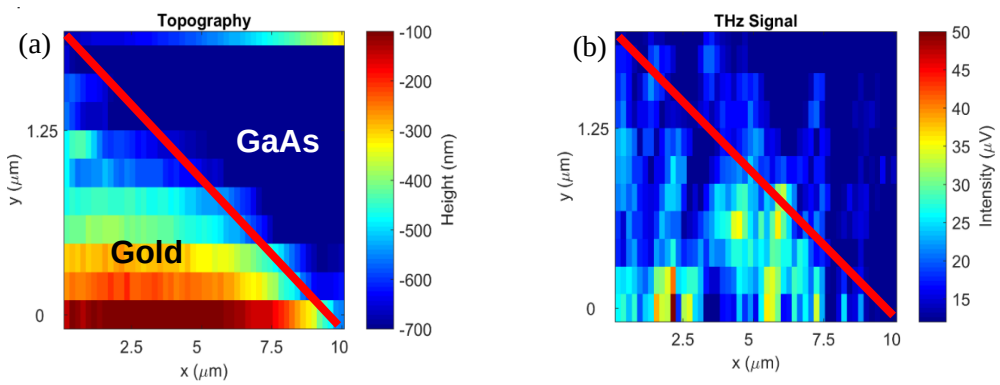

Figure 5.43 THz s-SNOM results of a gold feature (300 nm) on a GaAs substrate with the indium tip. (a) Topography; (b) THz image. The red line is the boundary between gold feature and GaAs substrate.

5.8 Metamaterial samples for THz s-SNOM characterization

Graphene loaded metamaterials are promising devices for amplitude [97], frequency [358] and polarization [359] modulation of THz radiation. To optimise the performance of such devices, it is necessary to have a good understanding of their working principles, which can be studied with the THz s-SNOM. The measurements in the previous sections can only give a qualitative explanation for the working principle of these devices. To quantitatively characterise the performance of such a device, a more systematic study needs to be performed. In this section, two graphene loaded metamaterial devices, SRR and the coupled resonator, with different parameter variations have been designed with

COMSOL simulations and fabricated to study the influence of these parameters on the THz properties of them. These two geometries have been chosen because they have been demonstrated to have the ability to modulate the amplitude or frequency of a THz QCL[97] [358], which are essential for many THz applications.

5.8.1 Split-ring resonators

For an SRR, its optical properties are mainly determined by four structural parameters: the nominal size *a*, line width *f* , gap width *e*, and metal thickness *t*, as shown in Figure 5.44. They determine the inductance, resistance and capacitance in the LRC model of an SRR. The relationship between these parameters and the resonance frequency as well as average electric field at the gap region has been studied with COMSOL simulations. Here, the thickness of metal is kept as a constant value (100 nm) and the power of the input electric field is 1 W for all the simulations. The SRR is put on a SiO_2/Si substrate. The details about the simulation and the parameters used for the simulations have been discussed in Section 3.2.2. The average electric field is obtained by averaging the electric field over the gap area (the red area in Figure 5.44), which takes into account all the three components of the electric field. It indicates how strong the field concentration is at the gap area, which is an important parameter for an SRR array if it is to be used as a modulator.

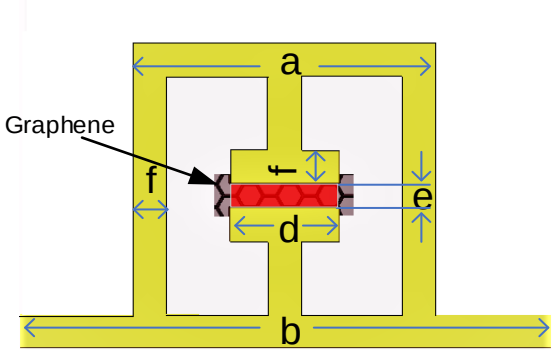

Figure 5.44 Schematic of the SRR geometry and the area over which the electric field is averaged. In the simulations, it is averaged over the red area in the centre of an SRR unit cell. Monolayer CVD graphene is put at the gap area.

5.8.1.1 Nominal size *a*

For an SRR, the resonance frequency is in reverse proportion to its nominal size because a larger size gives a smaller inductance, which leads to a lower resonance frequency. This is confirmed by the simulation results, as shown in Figure 5.45. In this simulation, the line width ratio L_w (L_w= *f*/*a*) and the gap width *e* are kept constant,

0.08 μm and 1 μm, respectively, only the nominal size *a* has been changed from 10 μm to 14.5 μm, which results in a resonant frequency shift from 3.2 THz to 2.1 THz. The results also show that the average electric field at the gap does not change when the line width and the gap width stay the same. The resonant frequency/wavelength for different nominal sizes are extracted from Figure 5.45 and plotted in Figure 5.46. As can be seen, the relationship between the nominal size *a* and the frequency (*f*)/wavelength (λ) can be fitted with a reciprocal/linear function, which can be used to predict the optimal nominal size for a given resonant frequency.

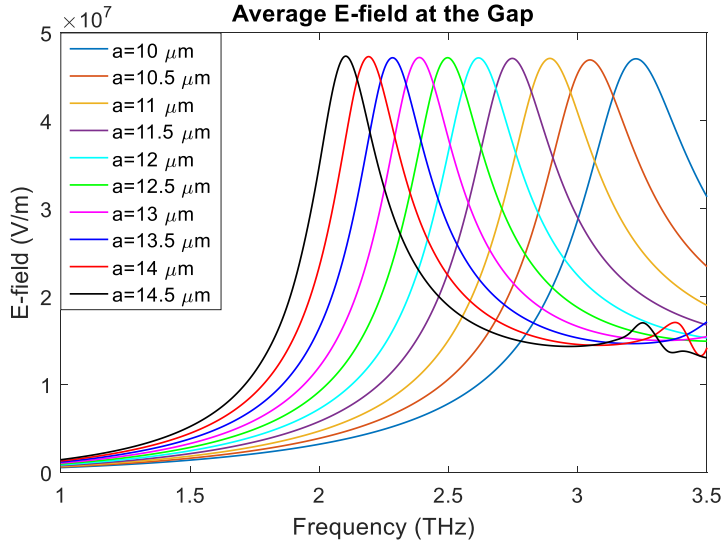

Figure 5.45 Average electric field at the capacitive gap for SRRs with 10 different sizes (the nominal size *a* varies between 10 μm to 14.5 μm) from COMSOL simulations.

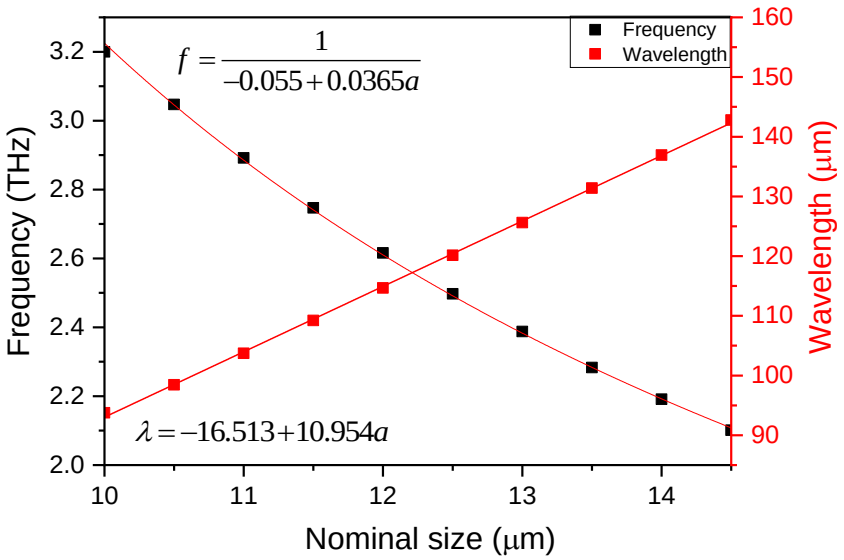

Figure 5.46 The resonance frequencies and the corresponding wavelengths for SRRs with different nominal size *a*. The relationship between the nominal size *a* and the frequency (*f*)/wavelength (λ) is fitted with a reciprocal/linear function.

5.8.1.2 Gap width and line width ratio

The influence of two other variables, line width ratio L_w and gap width e on the resonant frequency and average electric field is then studied. The resonant frequency and average electric field are simulated with the nominal size a kept constant as 10 μm. The line width ratio L_w and gap width e are increased from 0.07 a to 0.09 a and 0.2 μm to 0.4 μm, respectively. The simulation results are plotted in Figure 5.47. As can be seen, both the line width ratio and the gap width have influence on the resonant frequency and the average electric field. A larger line width gives a blue shift on the resonant frequency and a lower average electric field. For the gap width, it has a large effect on the average electric field. When the gap width is halved, the average electric field has more than doubled, which is reasonable as the same energy is concentrated in a smaller area. The increase of the gap size also gives a blue shift on the resonant frequency because it will increase the capacitance of the device.

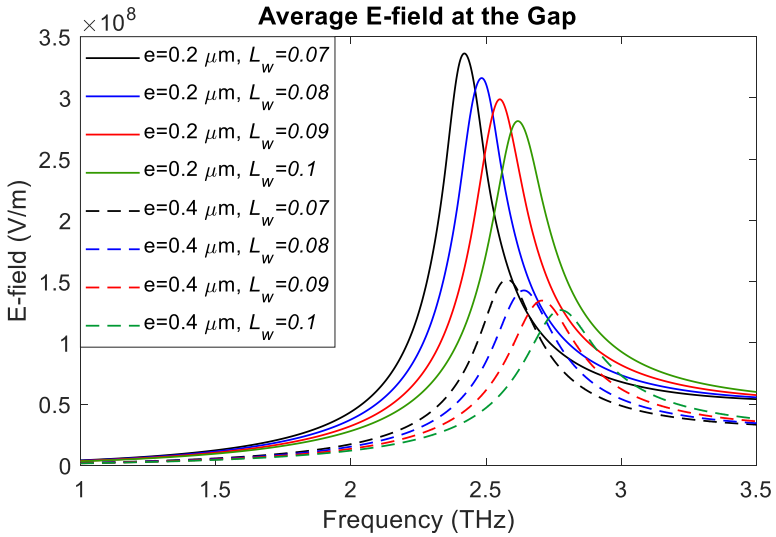

Figure 5.47 Average electric field at the capacitive gap for SRRs with 2 different gap sizes: 0.2 μm (solid line) and 0.4 μm (dashed line) from COMSOL simulations. The arm width is increased from 0.07 a to 0.1 a. Here, e is the width of the gap while L_w is the line width ratio.

The influence of the gap size is then investigated further as the variation range of it is much larger compared to the line width ratio. Besides, compared to the line width ratio, the gap size has a much larger influence on the average electric field at the gap area within its variation range. Here, both the nominal size a (10 μm) and the line width ratio L_w (0.09) of an SRR are kept constant while the gap width is increased from 50 nm to 1000 nm, with the results shown in Figure 5.48 (a). To get the relationship between the gap size and the average electric field as well as the resonant frequency,

nonlinear fits of the simulated average electric field (E_{gap}) and resonant frequency (f) at the gap area with the gap size is performed, as shown in Figure 5.48 (b). The average electric field increases almost linearly and slowly with the gap size reducing when the gap is wider than 400 nm. After the gap size is reduced to smaller than 400 nm, it goes up exponentially when the gap size is further reduced. A higher average electric field means a more concentrated field, which is beneficial if the device is used for modulation purposes. At the same time, the resonant frequency changes in a similar way. As can be seen from Figure 5.48 (a), it does not change much when the gap is broader than 400 nm and a big shift happens when the gap size is further reduced. Therefore, several parameters can be adjusted when designing an SRR to meet a certain resonant frequency and strength.

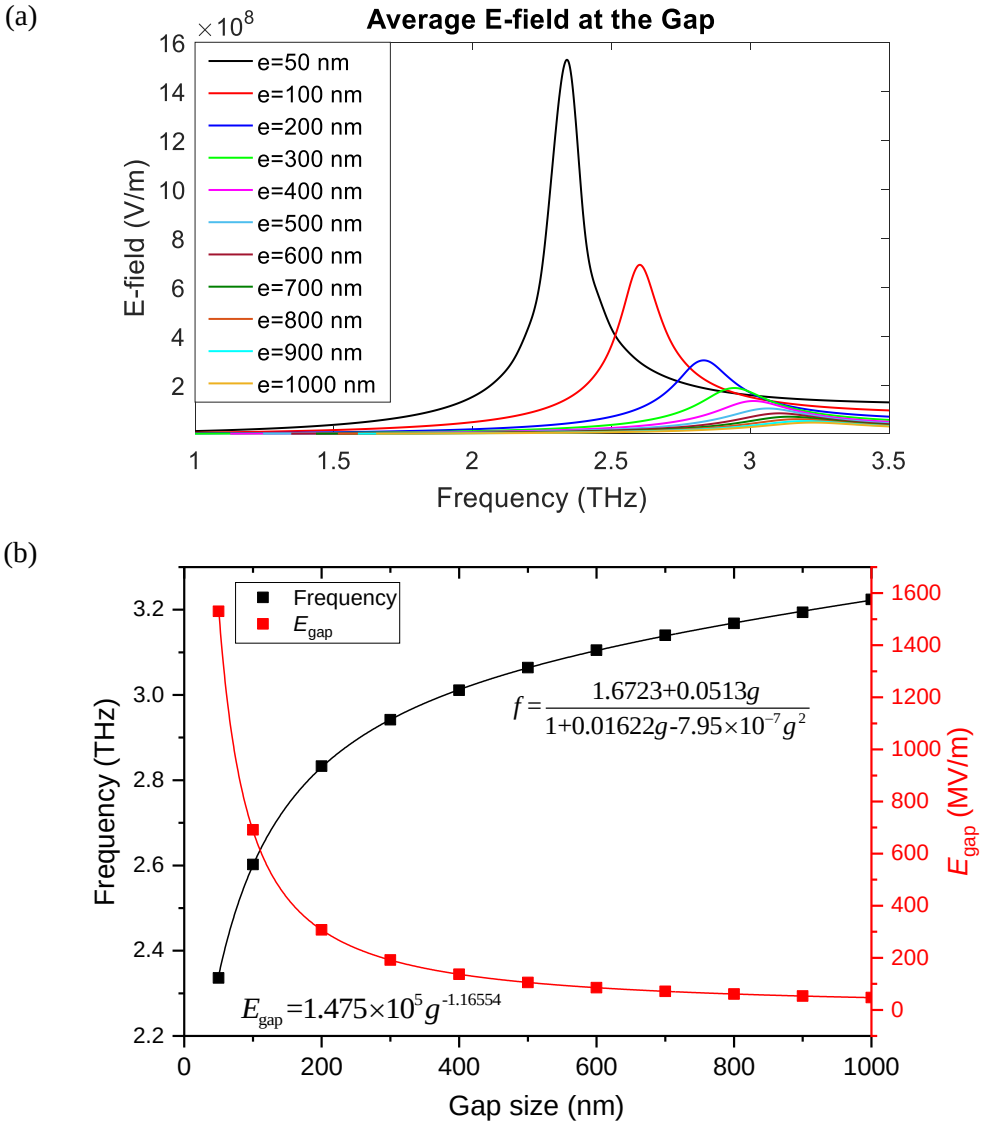

Figure 5.48 COMSOL simulation results of average electric field at the gap for different gap separations. (a) The resonant curves of an SRR with different gap sizes. (b) Nonlinear fits of the relationship between the gap size and the average electric field/resonant frequency.

5.8.1.3 Electric field distribution for different gap size

The electric field distribution of an SRR with different gap sizes has been simulated as well, as shown in Figure 5.49. The nominal size of the SRR is 10 μm and the line width ratio L_w is 0.09. When the gap size is large (>500 nm), the charges mainly distribute around the edges of the two ring arms. When the gap size is reduced, the charges are squeezed, which gives a higher average electric field at the gap area.

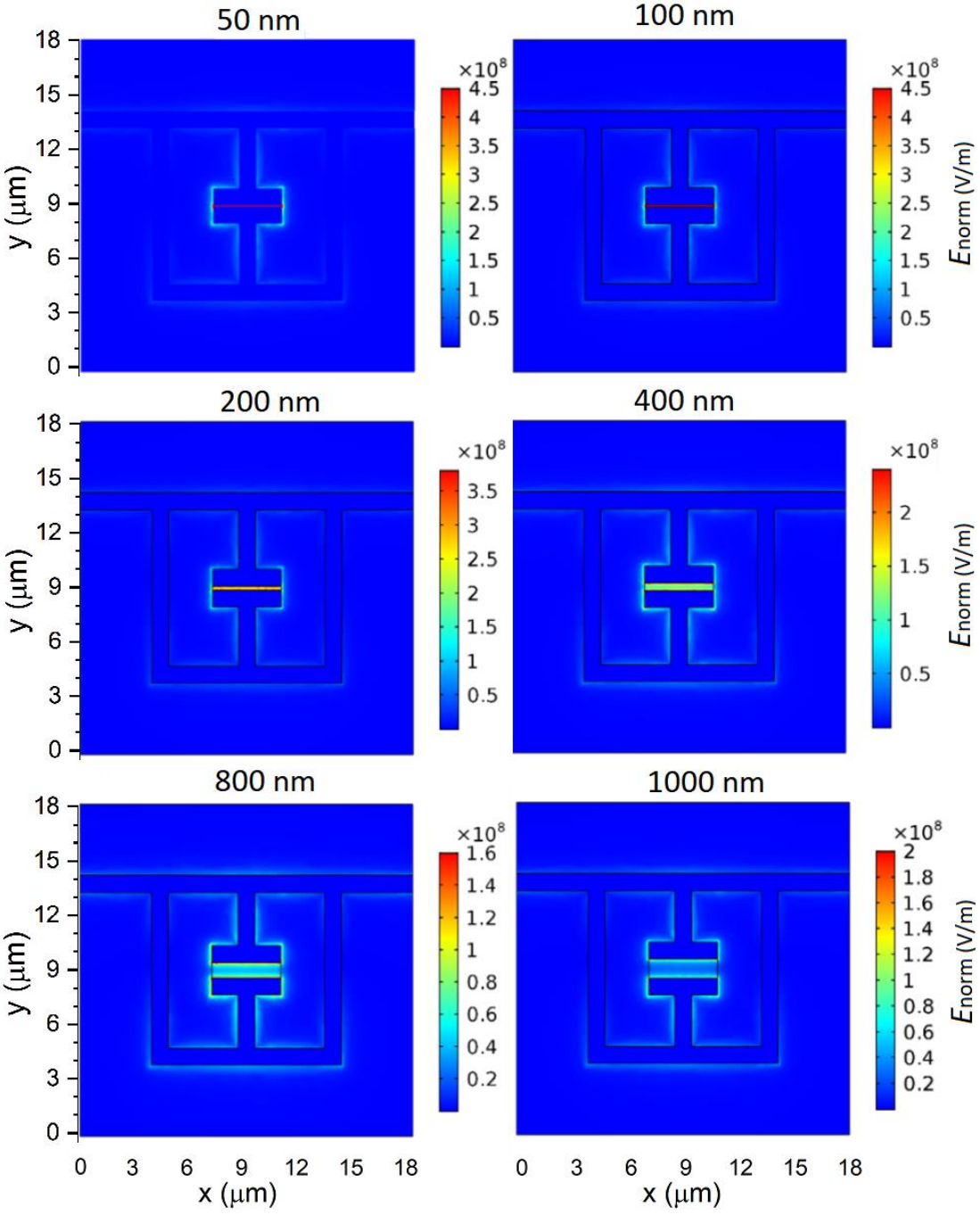

Figure 5.49 Electric field distribution of SRRs with different gap sizes (from 50 nm to 1000nm) from COMSOL simulations when they are illuminated by a 1 W light field with the polarization in y direction.

5.8.1.4 Array of SRRs with different geometric parameters

After the simulation study, an array of SRRs with different structural parameters is then designed, as shown in Figure 5.50 and is called patterned SRR array in this thesis. From the bottom to the top, the nominal size reduces from 14.5 µm to 10 µm. From the left to the right, the gap size decreases from 1 µm to 100 nm. The minimum gap size is chosen as 100 nm as this is the smallest gap that can be easily fabricated with E-beam lithography if the thickness of metal is about 100 nm. If the gap size is smaller than this, it becomes difficult to do the lift-off after the evaporation. The line width ratio L_w is kept constant so that a comparison can be made between two SRRs with all the same parameters but different nominal sizes or gap sizes.

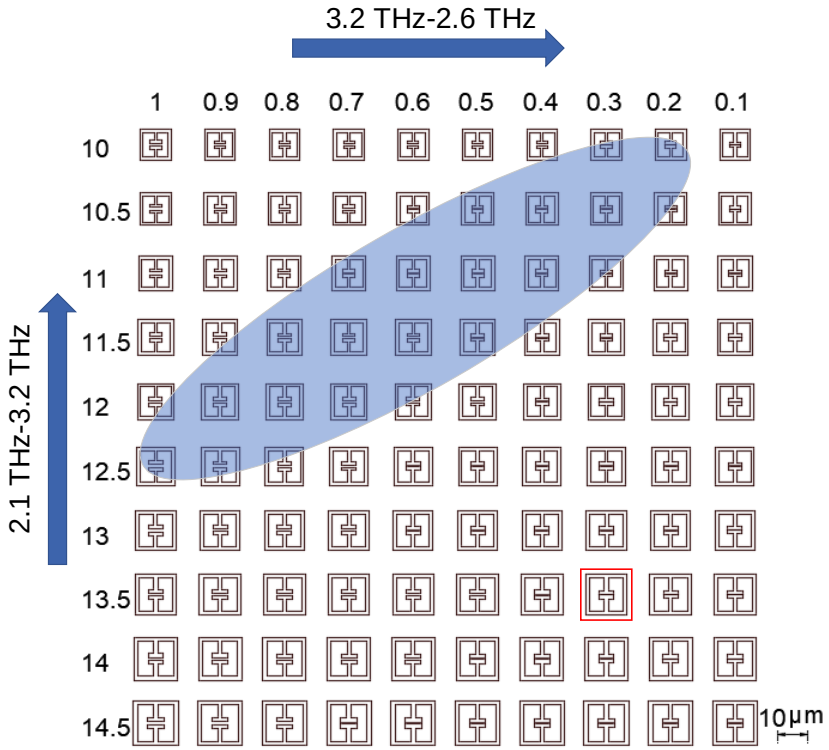

Figure 5.50 Layout of the device for SRRs with different parameters, unit: µm. The nominal size *a* of the SRRs varies from 10 µm to 14.5 µm while the gap size *e* decreases from 1 µm to 0.1 µm.

When keeping the gap size *e* fixed at 1 µm and reducing the nominal size *a* from 14.5 µm to 10 µm, the resonant frequency increases from 2.1 THz to 3.2 THz. If *a* is kept fixed at 10 µm while *e* is reduced from 1 µm to 0.1 µm, the resonant frequency reduces from 3.2 THz to 2.6 THz. Therefore, different combinations of the nominal size and the gap size give the SRR array a spectral coverage from 1.8 THz to 3.2 THz, which covers the frequency range of all the THz QCLs currently used in the research group.

This device can be used for three different experiments. Firstly, it can be used to study the modal field evolution if a THz s-SNOM scan is performed on the SRRs on a vertical line (different nominal sizes but same gap size). As the frequency of the THz QCL used in the s-SNOM is fixed, when scanning on SRRs with different nominal sizes, it will go through different resonant conditions: close to resonance, on resonance and then off resonance. It is equivalent to sweeping the laser frequency for the same SRR.

Secondly, a large scan can be taken on the whole area to find the SRR that gives the strongest THz response at the light source frequency. If the laser source is 2.85 THz, this will help to find the optimal nominal size and gap size for an SRR array to have a very strong resonance at 2.85 THz. On the current SRR array, according to the simulation results, all the SRRs in the blue-shadowed area have a resonant frequency around 2.85 THz.

Furthermore, another array with the same layout but rotated by 90° is put next to the previous array. Therefore, two SRRs with the same geometric parameters but orientations perpendicular to each other can be imaged in the same scan to study the influence of the light polarisation on the electric field distribution.

5.8.1.5 Large area SRR arrays for THz TDS measurements

Apart from the areas of SRRs with different sizes, two arrays of SRRs with single nominal size and gap size are put on the sample for THz TDS characterisations, so that the validity of the simulation results can be evaluated by comparing the TDS measurement results with the simulated ones. The parameters of the SRRs for these two devices are displayed in Table 5.12. They are designed to have resonant frequencies at 2.2 THz and 3.1 THz, respectively.

Table 5.12 Parameters of SRRs for TDS characterisation

	Nominal size	Line width	Gap width	Designed resonant frequency
SRR1	13.5 μm	1.08 μm	0.3 μm	2.2 THz
SRR2	9 μm	0.72 μm	0.2 μm	3.1 THz

5.8.1.6 SRR Sample layout

Both the patterned SRR array and the large area SRR array are put on the same sample. It is divided into 4 small rectangular areas, which are labelled as (a), (b), (c), (d) in Figure 5.51. The size of each area is 1.1 mm × 1.6 mm, which is large enough for TDS measurements.

Area (a) is filled with the patterned SRR array shown in Figure 5.50 with two orientations. 90-degree patterned array (patterned array rotated by 90 degrees) and patterned array are put on this area in alternate lines, starting from the top with the 90-degree patterned array. 20 arrays in total are filled into this area.

Area (b) is covered by a patterned SRR array similar to the one shown in Figure 5.50 but with the nominal size of the SRR varying from 9 μm to 13.5 μm with a 0.5 μm step. The gap size is still changed from 1 μm to 0.1 μm with a 0.1 μm step. The SRRs in this area cover a resonant frequency range between 3.5 THz and 2 THz. For area (a) and area (b), 60% of the patterned arrays have graphene at the gap area of the SRRs and the corresponding SRRs are connected to the bonding pads (areas with purple outline in Figure 5.51) with gold wire, so that the graphene can be gated.

Area (c) and area (b) are filled with a large area array of SRR1 and SRR2, with 58×77 and 41×54 SRRs, respectively. All the SRRs have graphene in the gap area and they are all connected to the bonding pads. Therefore, these two areas can work as gated devices.

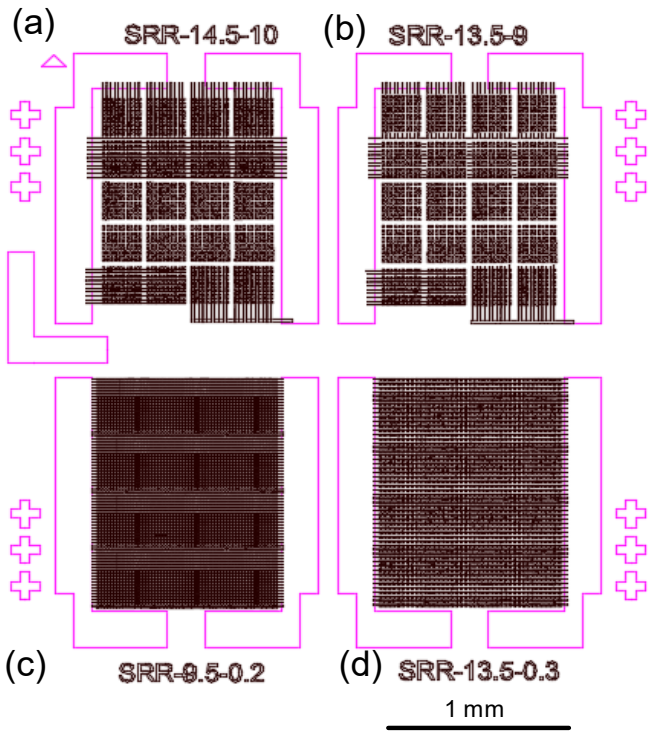

Figure 5.51 The layout of the graphene loaded SRR device

5.8.1.7 Sample fabrication

The sample is then fabricated in a similar way as discussed in Section 3.2.3 with the same substrate. The difference for fabrication of this sample is that the graphene is put on the sample after the SRR metallisation. Therefore, it is suspended on top of the metal

structure instead of sitting underneath it. As discussed in Section 5.5.2, when illuminated by a light field, most of the electric field concentrates at the gap area of the SRR, therefore, small area graphene rectangles with a comparative size to the gap area are used for this sample and put at the gap area, as shown in Figure 5.42. A monolayer graphene is first transferred onto the sample, which already has the SRRs on it. The graphene squares are then defined with an E-beam lithography step. The relative position between the graphene square and the SRR is crucial. Therefore, several alignment marks are put on the sample with the same E-beam lithography step for the SRR evaporation to align the E-beam pattern for graphene squares to the gold SRRs. Negative E-beam resist (MA-N 2410) is used here as the part illuminated by electron beam needs to remain. After the development, the square at the gap area of a SRR is still covered with resist while the other areas are not. The uncovered graphene is then etched away with oxygen plasma. An SEM image of a 13.5 µm SRR (in area (d)) is taken after the graphene etching, and graphene remains at the gap area, as indicated by the red arrow.

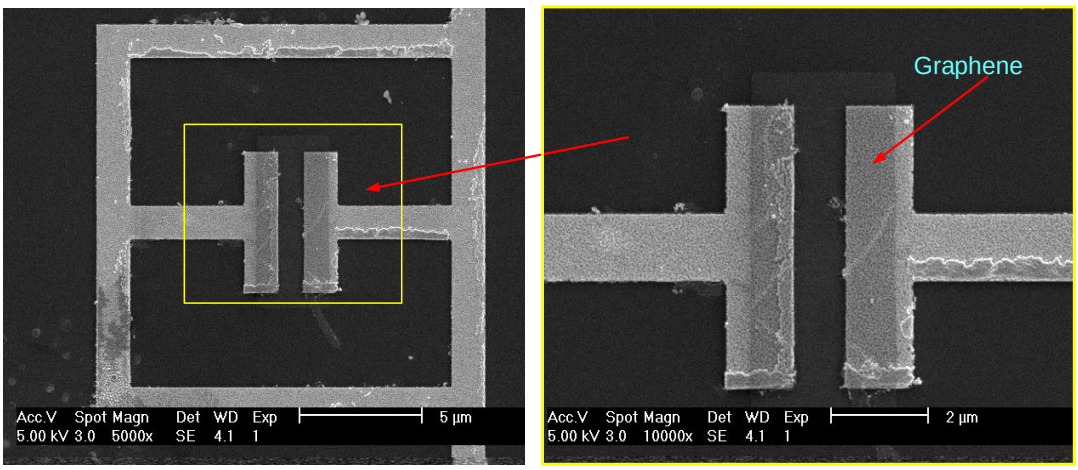

Figure 5.52 A SEM image of the 13.5 µm SRR array after the graphene etching. There is only graphene at the gap area. The graphene is in electrical contact to the gold feature.

5.8.1.8 TDS measurements

The transmission spectra of these two devices are measured with THz TDS after the SRR metallisation and before the graphene transfer, Figure 5.53 shows the comparison between the simulated transmission spectra of the devices and the ones measured with the TDS. The simulated resonant frequencies are slightly higher than the measured ones (60 GHz for SRR1 and 20 GHz for SRR2). The reason might be that the geometry and material properties parameters used in the simulation are not exactly the same compared with the ones of the fabricated devices. This confirms that the simulations are valid.

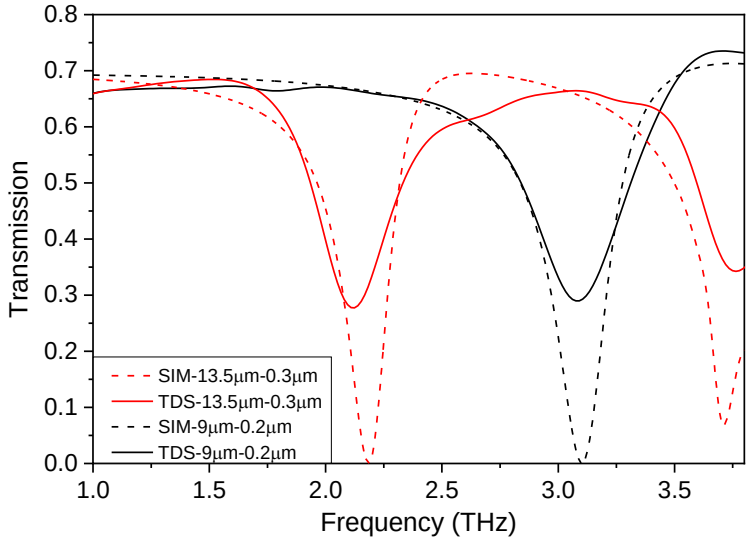

Figure 5.53 COMSOL simulation (dashed lines-SIM) and TDS measurement (solid lines-TDS) results of the transmission spectra for the two SRR devices on the sample: SRR1 (red), SRR2 (black).

5.8.2 Coupled Resonators

The second interesting geometry to study with the THz s-SNOM is the coupled resonator (CR), which is also called electromagnetically induced transparency (EIT) device. The geometry of a CR is shown in Figure 5.54, which is based on the design in reference [358]. A single coupled resonator consists of two individual resonators (a dark resonator and a bright resonator) sitting next to each other. Here, *a* is the nominal size of the CR, and all the other parameters are related to it with the ratio in Figure 5.54. All the CRs in this section are scaled based on this template.

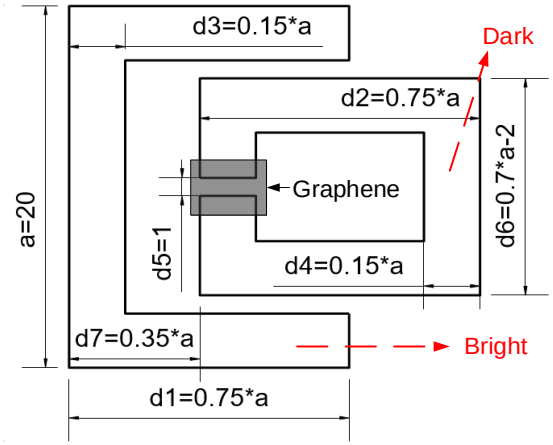

Figure 5.54 Template of the CR design. The dimension unit is μm. A small graphene rectangle is put at the centre gap area (gray area in the graph).

5.8.2.2 Three resonant modes

A coupled resonator array with a connecting wire on it usually has three resonant modes, as shown in Figure 5.55. The properties of these three modes of a coupled resonator array with a 0.81 scale (a nominal size of 16.2 μm) are displayed in Table 5.13. The first resonant mode appears as a result of the connecting wire, which has the lowest resonant frequency and much weaker resonant strength compared to the other two modes. The two other modes are a result of the nearfield capacitive coupling between the individual resonances of the dark resonator and the bright resonator, which are split into two hybridized modes, with a low frequency "bonding" resonance at 1.75 THz and a high frequency "anti-bonding" resonance at 2.35 THz. These two modes also have different electric field distributions. For bonding modes, the carries concentrate at both the side gaps and the centre gap, therefore a high electric field is present in these regions as well. For anti-bonding mode, the carries only concentrate at the centre gap, where the highest electric field exists. A summary of the information for these three modes can be seen in Table 5.13.

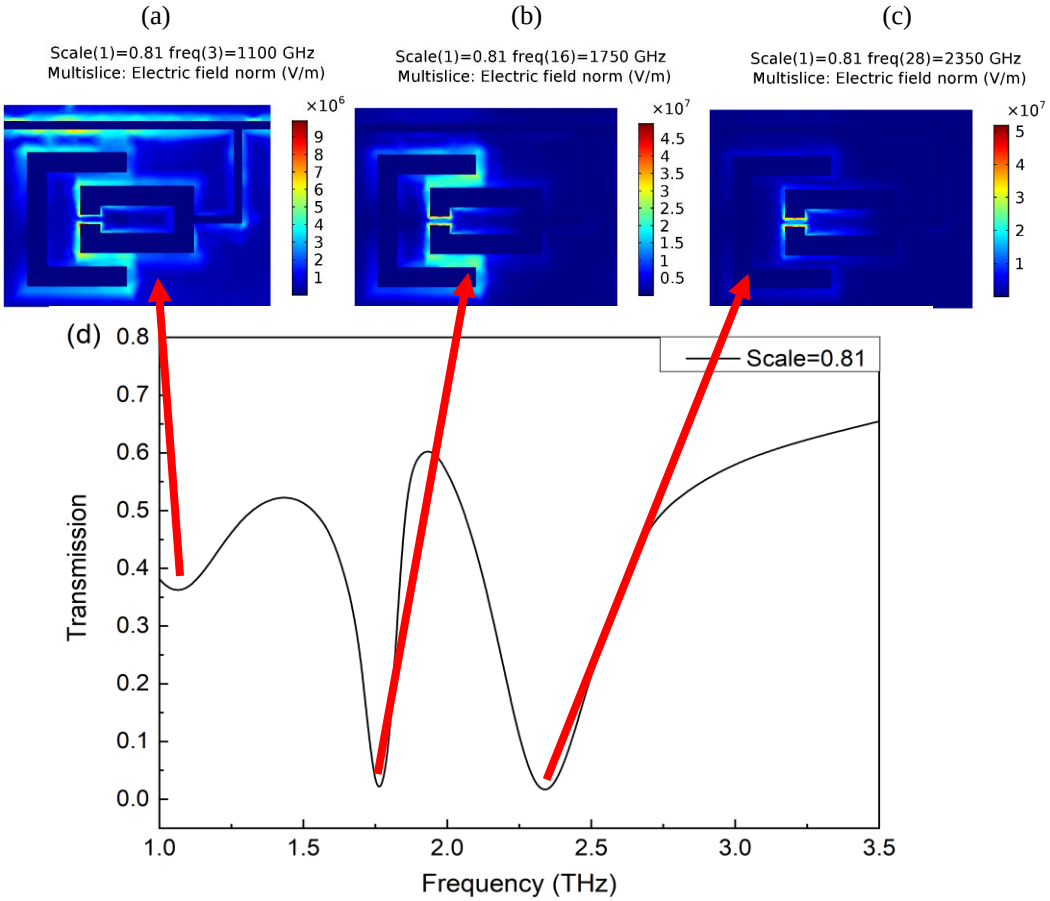

Figure 5.55 Electric field distribution of a CR (0.81 scale) with a connecting wire when it resonates at different modes. (a) connecting wire mode; (b) bonding mode; (c) anti-bonding mode. (d) The transmission spectrum of the CR from COMSOL simulation. There is no graphene at the center gap area for this simulation.

Table 5.13 Properties of three resonant modes for the coupled resonator with a 0.81 scale

	Mode 1	**Mode 2**	**Mode 3**
Frequency (THz)	1.1	1.75	2.35
E_{max} **region**	Connecting wire	All three gaps	Centre gap

5.8.2.3 Overall size/Scale

Compared with an SRR, more variable parameters have influence on the optical properties of a CR: the sizes of the bright and dark resonators, the distances (vertical distance and horizontal distance) between them and gap size of the bright resonator. Here, the CR shown in Figure 5.54 is used as a template and it is scaled to other sizes to get different resonant frequencies. Figure 5.56 gives the transmission spectra of CRs with scales from 0.4 to 0.7 and a fixed gap size (0.4 μm for both the centre gap and the side gaps), which cover a spectral range from 1.8 THz to 3.7 THz for the bonding mode and 2.6 THz to 5.1 THz for the anti-bonding mode.

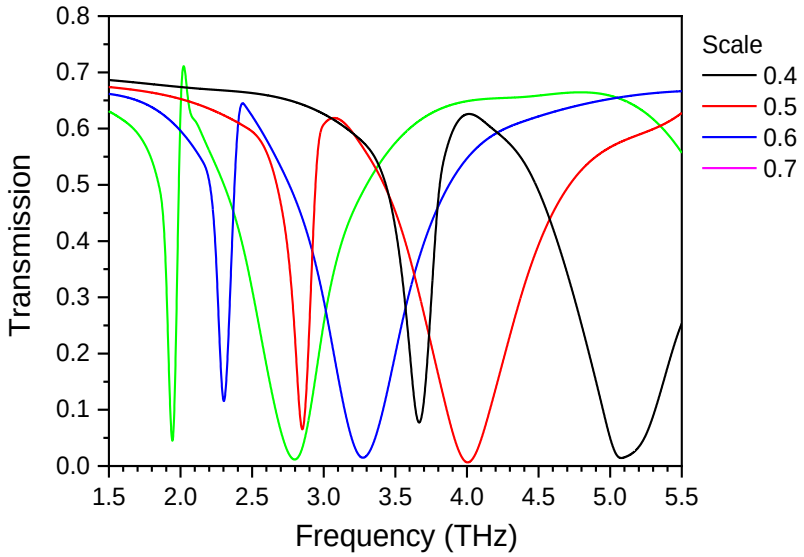

Figure 5.56 Transmission spectra for CRs with different sizes and a fixed gap size from COMSOL simulations.

To investigate how the resonant wavelengths for the two modes changes with the CR scale, they are extracted from the simulation results and plotted in Figure 5.57. The centre gap size and the side gap size are kept fixed (0.4 μm for both). A linear fitting can be performed to the resonant wavelength with scale for both modes, which means

both resonant wavelengths increase linearly when the CR scale is increased. It can also be seen that the change slope with scale for the anti-bonding mode is higher than the bonding mode (254.9 compared to 163.8 for the bonding mode). This means, when increasing the CR scale, the resonant wavelength of the anti-bonding mode increases faster than the bonding mode.

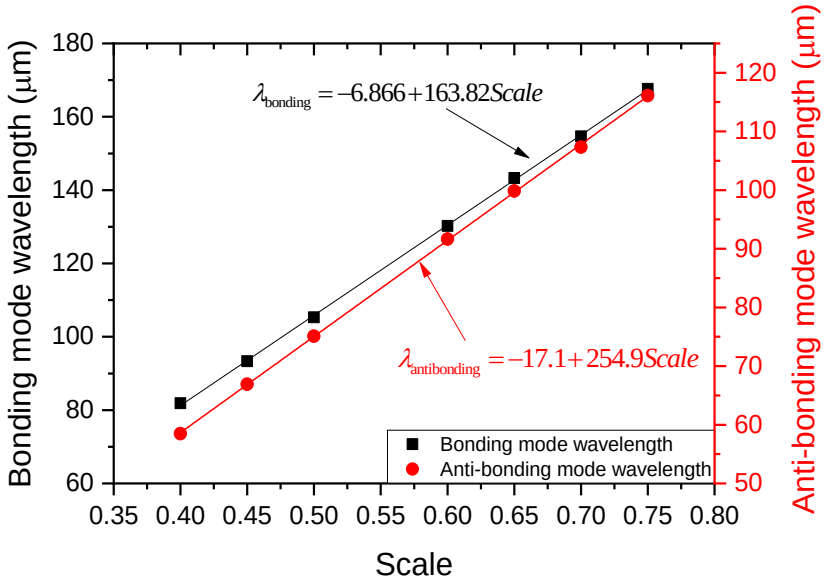

Figure 5.57 The relationship between the resonant wavelengths of the two modes and the CR scale. Linear fittings are performed for both modes.

5.8.2.4 Central gap size

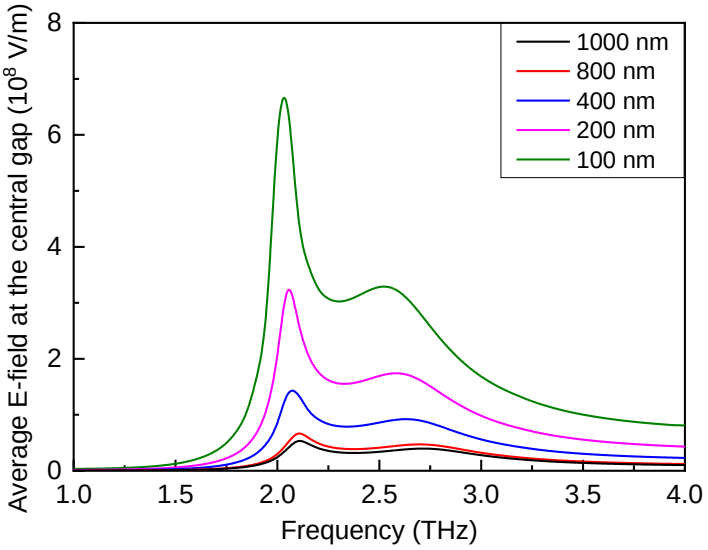

Figure 5.58 Average electric field at the central gap for CR with a fixed scale and a fixed side gap size but different central gap sizes from COMSOL simulations. The scale of the CR is 0.65 and the side gaps are 0.4 μm.

The influence of the centre gap size is studied as well. Here, the scale and the side gap size of the CR are kept constant (0.65 and 0.4 μm, respectively), while the centre gap size is reduced from 1000 nm to 100 nm. The simulation results in Figure 5.58 show that a smaller gap size gives a higher field concentration, thus a higher electric field at the gap region. However, the gap size does not have an obvious influence on the resonant frequency of the bonding mode. For anti-bonding mode, the resonant frequency is blue-shifted when increasing the centre gap size.

Two CR arrays (array a and array b) with different scales and gap sizes are then designed, as shown in Figure 5.59. The scales of the CRs are chosen such that their anti-bonding mode resonant frequencies (for array a) or bonding mode resonant frequencies (for array b) are between 2 THz and 3 THz. The scales and gap sizes are labelled in Figure 5.59 for both devices.

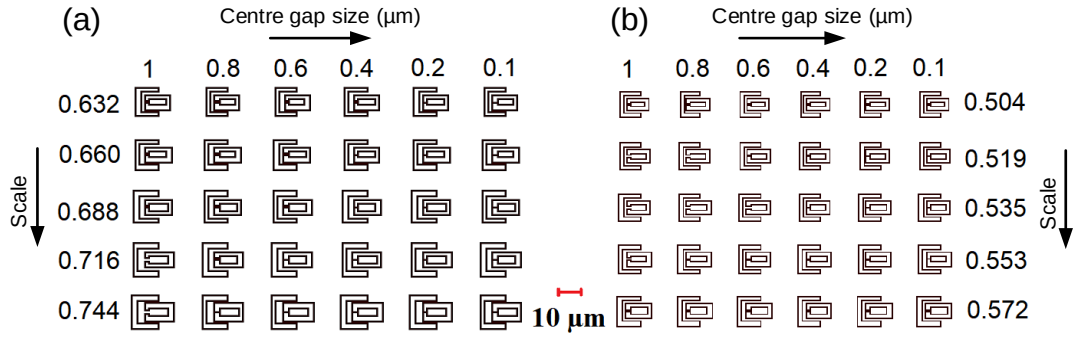

Figure 5.59 Layouts for the CR arrays with CRs of different sizes and gap sizes. For the CRs on the left side (array a), their anti-bonding modes locate between 2 THz and 3 THz. For the CRs on the right side (array b), their bonding modes are between 2 THz and 3 THz. For each CR row, the center gap size varies from 1 μm to 0.1 μm (1 μm, 0.8 μm, 0.6 μm, 0.4 μm, 0.2 μm, 0.1 μm).

5.8.2.5 Large area CR arrays for THz TDS measurements

Two devices are also designed with large area CR arrays, which have the anti-bonding and the bonding mode at around 3 THz, respectively. The geometric parameters and the corresponding simulated resonant frequencies for the two arrays are displayed in Table 5.14. The side gap is 0.4 μm for both devices.

Table 5.14 Parameters of CR arrays for TDS characterisation

	Scale	Centre gap	Anti-bonding mode frequency	Bonding mode frequency
CR1	0.67	0.4 μm	4.10 THz	3.10 THz
CR2	0.487	0.4 μm	2.92 THz	2.20 THz

5.8.2.6 CR sample layout

The device a, device b, CR1 and CR2 are then fabricated on the same chip with the SRR sample discussed in the previous section in the same process, which is called CR sample in this thesis. The layout for the CR sample is displayed in Figure 5.60. It is very similar to the SRR sample layout and also have four 1.1 mm×1.6 mm areas. Area (a) and area (b) are filled by array a and array b with two orientations. Area (c) and area (d) are covered by CR1 and CR2 with the number of CRs being 36×48 and 50×66, respectively.

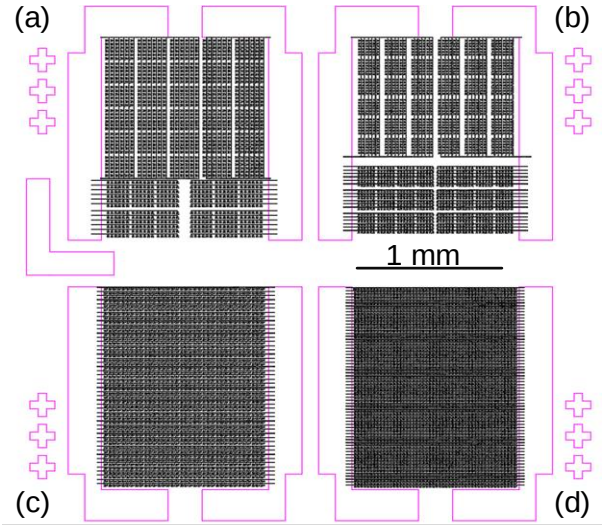

Figure 5.60 Layout of the CR sample. (a) array a in two orientations; (b) array b in two orientations; (c) CR1 and (d) CR2.

5.8.2.7 TDS measurements

The transmission spectra of the two large area devices CR1 and CR2 are measured with THz TDS after the metallisation of the CRs. The results are shown in Figure 5.61, where the COMSOL simulation results and the TDS results are compared. For both CR1 and CR2, the resonant frequencies of the bonding mode (2.095 THz and 3.065 THz) agree well with the simulated results (2.190 THz and 3.078 THz) while the resonant frequencies of the anti-bonding mode are about 150 GHz higher than the simulated ones. It can also be found that, the frequency differences between the two modes for the two devices are larger compared with the COMSOL simulations. The frequency difference is mainly determined by the resonant frequency difference and the coupling strength between the bright and the dark resonators. Therefore, either the simulation gives an inaccurate resonant frequency or the coupling between the two resonators is not modelled properly. Further investigations are needed to find out the reason behind this.

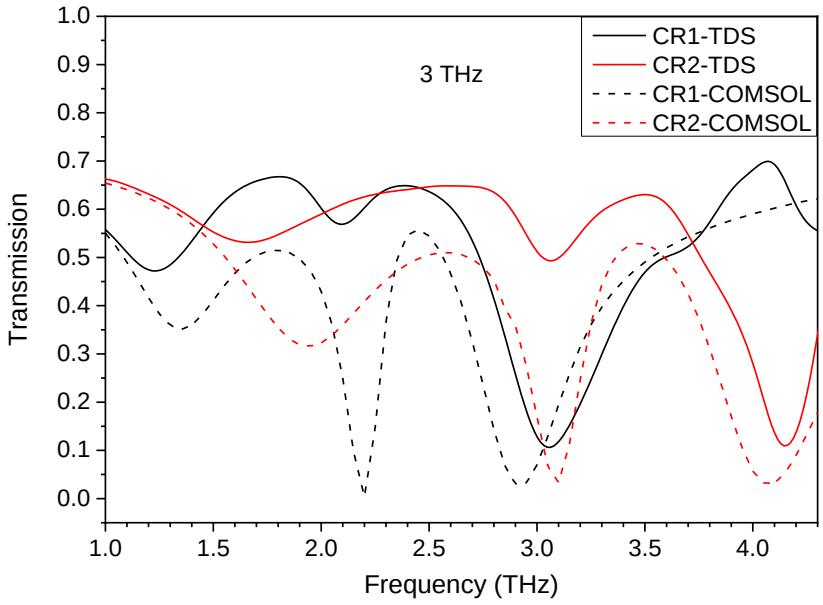

Figure 5.61 COMSOL simulation and TDS measurement results of the transmission spectra for the two large area CR devices on the sample, which are designed to have a bonding mode or anti-bonding mode at around 3 THz.

5.8.3 Section conclusion

In this section, THz metamaterials with varied geometric parameters have been designed and fabricated to study the influence of different geometric parameters on the optical properties of the metamaterial devices systematically. Two widely used metamaterial structures (SRR and CR) for THz applications are studied with COMSOL simulations. Two parameters are mainly considered here: the nominal size and the gap size.

The COMSOL simulations give a systematic prediction on the influence of the geometric parameters. For both structures, the resonant wavelength is proportional to the nominal size. As to the gap size, a larger gap size will blue shift the resonant frequency. The gap size is also the main influence factor of the average electric field at the gap area. When the gap size is larger than a critical number (400 nm here for the SRR device), the average electric field increases almost linearly and slowly with the gap size reducing. After the gap size is reduced smaller than the critical number, the average electric field goes up exponentially with the gap size further reduced. The determining factors of the critical number need to be further investigated. Therefore, a compromise needs to be made between a good field concentration and ease of fabrication when determining the gap size for these devices.

In addition, the transmission spectra of two large area SRR arrays and two large area CR arrays are measured with THz TDS. The results show that COMSOL simulations give a good prediction of the resonant frequencies with about 50 GHz frequency difference between the TDS data and simulated data.

Due to time constraints, THz s-SNOM measurements of these devices have yet been conducted and need to be finished in the future. Therefore, the next step is to map the electric field distribution in our THz s-SNOM setup to study the evolution of the mode profile when changing the geometric parameters or the graphene conductivity (changing the gate voltage). This study will facilitate understanding of the working mechanism of these devices and give directions to optimise the device designs.

5.9 Conclusion

In this chapter, the THz s-SNOM has been used for different imaging applications, which demonstrate its capability for several research purposes. Firstly, it has been used to characterise several resonant structures and the plasmonic resonances within these structures have been visualised. The THz image of the SEPHC QCL shows how the electric field is concentrated in one direction at the edge and distributed in a photonic crystal structure, proving the ability of the system for recording the local electric field. The imaging of the dipole resonance of the wire antennas confirms the effectiveness of the COMSOL simulation and demonstrates the subsurface imaging ability of the THz s-SNOM. For the SRR device, the electric field distribution mapping reveals the operation principle of the device as a modulator.

The contrast of the images of the SRR device is not great, which reveals the necessity of further improving the THz sensitivity of the system. To achieve this, two measures have been taken. Firstly, a different tip material, gold, has been tested to see the influence of tip material on the THz contrast. Both theoretical calculation and THz s-SNOM measurement prove that the gold coated tungsten tip can give a higher THz contrast compared to the bare tungsten tip. The second approach is using resonant tips, and an indium tip with a length close to the THz wavelength has been tested in the s-SNOM. The THz contrast still exists despite the poor topography due to the softness of the material. Therefore, resonant tips with harder materials or an optimised PID feedback loop for soft tips should be explored in the future.

On top of that, the influence of the integration time has been studied, and it shows that the 100 ms integration time gives a good compromise between the scanning speed and the THz image contrast.

Two graphene loaded metamaterial samples are finally designed to study the influence of the geometric parameters on the resonance frequency and field concentration effect of two metamaterial geometries, SRR and CR. The study shows that COMSOL simulations can give close predictions of the metamaterial resonant frequencies and several geometric parameters (nominal size, line width ratio and gap size) can be tuned for an SRR to meet a certain resonant frequency. It also shows that the gap size needs to be reduced below a certain number to be able to see a strong field concentration effect. The results give a direction for optimisation of the performance of metamaterial devices to meet certain application needs.

Chapter 6
Conclusion and perspectives

THz technology is a relatively new and fast-growing research field with many advancements during the last several decades. However, there are still many scientific or technological problems to be solved in this field. In this chapter, the contribution of this work to the THz world in terms of spectroscopy, modulation and nearfield imaging will be summarised. On top of that, further research based on work in this thesis and several new ideas about research in the THz field will be proposed.

6.1 Conclusion

In this thesis, three important applications of THz technologies (gas spectroscopy, amplitude stabilization and nearfield imaging) have been studied and experimentally achieved with THz QCLs. Technologies related to these three applications have been discussed as well.

6.1.1 THz gas spectroscopy

In Chapter 2, a gas spectroscopy setup based on self-mixing with an external cavity THz QCL has been demonstrated. To achieve this, two technologies have been studied and developed. Firstly, a THz QCA was developed from a THz QCL by attaching an AR coated Si lens. Secondly, a differential detection method based on self-mixing of an external cavity QCL was used to detect the small voltage perturbation signal. Compared with normal detection methods, it provides a faster and more sensitive response. To achieve broadband spectroscopy, a broadband THz QCA and a frequency tuning element are needed. Two approaches for achieving a broadband THz QCA have been proposed: broadband AR coating and the two lenses configuration. For frequency tuning, a broadband external cavity THz QCL was demonstrated with a Littrow grating, which could give 103 GHz frequency tuning around the central frequency of ~2.9 THz with a grating angle change of 1.1 degree.

6.1.2 Active control of THz radiation

With the advancement of THz modulators, it becomes possible to actively control the amplitude, frequency as well as polarization of THz radiation, which are the key technologies for many THz applications such as communication, imaging, etc. Chapter 3 presented an active amplitude control and stabilization setup with a 2.85 THz QCL. The amplitude of the QCL output was modulated by a graphene loaded metamaterial array and the modulation was actively controlled with a PID feedback loop. With the active control, the system can generate THz radiation with a designed waveform (square wave and sine wave modulation have been demonstrated). The magnitude of the fluctuation in QCL output power was reduced from 1.52% to 0.043% of the total output power as well.

Furthermore, to achieve a higher modulation depth, an external cavity configuration was explored. It gave a higher modulation depth (20% compared to 2.7% of a direct transmission scheme) of THz radiation but also introduces instability into the system due to mechanical vibrations.

6.1.3 THz s-SNOM

THz s-SNOM is a powerful research tool for semiconductor physics. In Chapter 4 and Chapter 5, an s-SNOM has been developed with a THz QCL based on a tuning fork AFM. The home-built s-SNOM can record topography and THz response of a sample simultaneously and has a resolution of better than 78 nm. As a tuning fork instead of cantilever is used, the system also provides a dark environment for measurement, which is essential for many quantum devices. In addition, low temperature AFMs with tuning forks have been demonstrated before [360]. Therefore, tuning fork based s-SNOM is promising for cryogenic temperature operation as well, which is the working condition for most quantum devices.

To improve the system's performance (resolution and stability), a sound-isolation-box and an active vibration isolation platform were utilised to reduce the mechanical instability and an impedance match and pulse synchronization were performed to reduce the electronic noise.

Several THz functional devices have been studied with the THz s-SNOM after it was built. Firstly, it was used to characterise several resonant structures: a SEPHC laser and a wire antenna array. The plasmonic resonances within these structures have been visualized, which is confirmed by COMSOL simulations. Another examined sample is

an SRR array, the electric field distribution mapping of it reveals the operation principle of the device as a modulator.

To improve the sensitivity, resonant tips as well as tips with different materials have been theoretically studied and tested in the setup, which proves that the gold coated tungsten tip can give a higher THz contrast compared to the bare tungsten tip. It has also been found that a 100 ms integration time and second order demodulation can give a better contrast.

6.2 Future work

For all the work presented in this thesis, there is still clearly some room for improvement. When it comes to THz spectroscopy, frequency tunable THz sources are essential. Acoustic waves might offer a new approach to frequency tuning of a THz QCL. For active control of THz radiation, as discussed in Section 3.7, an integrated device can be used for both modulation and detection. In addition, the resolution and sensitivity of the THz s-SNOM can be further improved and it will be useful to develop a cryogenic temperature THz s-SNOM. For THz metamaterials, apart from the function as a frequency or amplitude modulator, they also have the potential of being a THz spatial light modulator, which is the key element for THz single-pixel imaging.

6.2.1 Frequency tuning of a THz QCL with acoustic waves

In conventional semiconductor lasers, the acousto-optic effect has been widely used for frequency shifting, amplitude modulation and deflection. It has also been demonstrated that this technique can be adopted in infrared QCLs [361]. A tunable infrared QCL was achieved by incorporating an Acousto-optic Modulator (AOM) in the external cavity. By changing the frequency of the AOM, the wavelength of the QCL could be tuned from 8.5 μm to 9.8 μm. Besides, the tuning frequency can reach 1 MHz. In principle, if an AOM could work at THz frequency range, it could also be used for frequency tuning in an external cavity THz QCL by modulating the feedback of the laser cavity, which provides an approach to fast frequency tuning of THz QCLs.

Figure 6.1 gives a schematic diagram of the setup that could be used for AOM frequency tuning of a THz QCL. Two parabolic mirrors and a plane mirror are placed on the optical path of a QCA to form an external cavity. Then an AOM is placed between the second parabolic mirror and the flat mirror. When the light beam goes through the AOM, a large proportion of it will be diffracted by the AOM and the diffraction angle is correlated with the frequency. Consequently, when the mirror is

fixed, only the photons with a specific frequency can be coupled back to the QCA and thus achieve self-oscillation, which is a prerequisite for lasing. By changing the modulation frequency of the AOM, the frequency of the photons that satisfy the angle condition will experience a shift, so that the frequency of the laser radiation will be tuned.

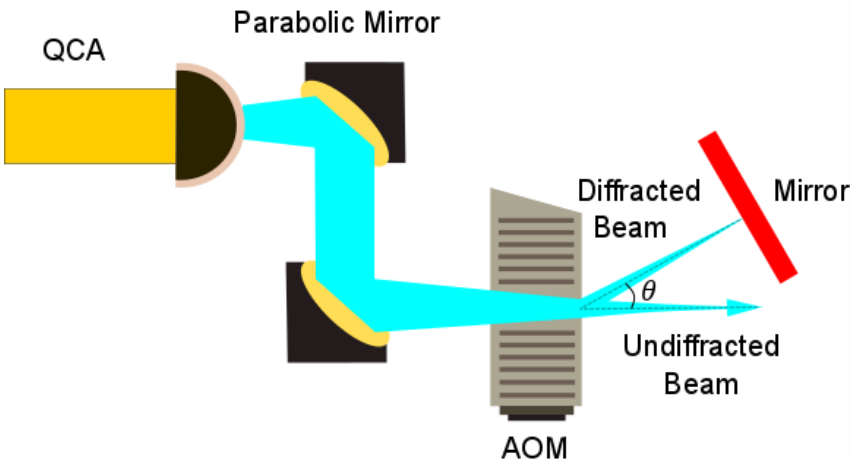

Figure 6.1 Schematic of the setup for frequency tuning of a THz QCL with an Acousto-optic Modulator (AOM). Two off-axis parabolic mirrors are employed to focus the beam on the mirror so that a maximum feedback could be gained.

Another possible approach to tuning the frequency of a THz QCL with a bulk acoustic wave is using it to modulate the thickness of semiconductor layers in the active region, which will shift the transition frequency of a QCL as well. High speed modulation of a single-plasmon THz QCL output power has been demonstrated with a single-cycle, bipolar, acoustic strain (coherent phonon) pulses generated in the Al layer deposited on the back surface by optically exciting it with ~40 fs, 800 nm pulses from a 1 kHz repetition rate Ti:Sapphire amplified laser system [362]. The acoustic pulses will induce a transient change on the voltage (or voltage modulation) across the QCL, which is shown in the bottom graph in Figure 6.2. This voltage change will then modulate the output power of the QCL, as shown in the top graph in Figure 6.2.

If a frequency tunable standing acoustic wave can be generated within the active region, the width of the quantum wells will be tunable as well, which will modulate the lasing frequency of the QCL. One problem to be solved for this approach is to find an appropriate way to generate a frequency tunable acoustic wave within the QCL active region.

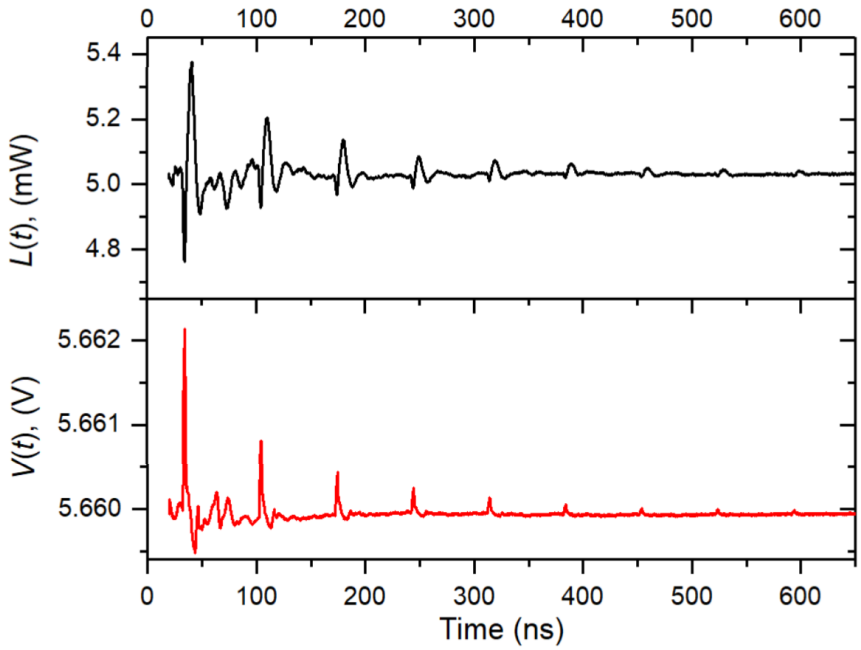

Figure 6.2 THz emission modulation with a bulk acoustic wave, from reference [362] © 2019 IEEE.

On top of bulk acoustic waves, surface acoustic waves (SAW) also have the potential to modulate the optical field of a QCL. Compared with using an AOM for frequency tuning, using SAW seems to be a more direct approach as it will provide a distributed feedback inside the laser cavity. If this can be achieved, it will be a very stable and convenient frequency tunable THz source as there is no need for an external cavity and other components.

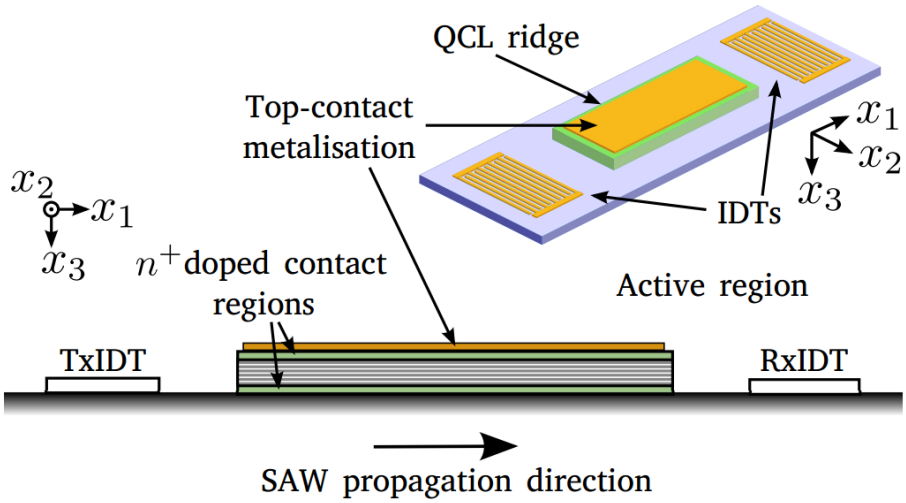

Figure 6.3 Schematic of a SAW modulated QCL, from reference [189] © 2013 IEEE.

Figure 6.3 gives a schematic of a possible configuration of a QCL with interdigitated transducers (IDTs) on top. It is now possible to fabricate the transducer of SAW on top a QCL ridge. SAW have been adopted in the field of electron transport in a semiconductor material for many years. As a result, the fabrication method of a SAW transducer on a semiconductor material substrate is mature. At present, using ZnO as the acousto-optic material, considerably strong SAW can already be produced [363]. Fabrication of it on top of a GaAs substrate has been demonstrated as well. This is also a field having attracted many researchers. Theoretical calculations and simulations have been conducted to prove the feasibility of this approach [189][364]. However, there has been no experimental demonstration of this up to now. As a result, there is still much work to do in this field.

6.2.2 Active THz radiation control with an integrated device

Because of its unique optoelectronic properties, graphene has been exploited for many photonic applications. As demonstrated in the previous sections, graphene loaded devices can be used for optical modulation. Additionally, photodetectors based on graphene, other two-dimensional materials and hybrid systems have been demonstrated as well [365]–[367]. For certain applications, such as amplitude stabilization of a laser, simultaneous optical modulation and detection are necessary or will largely reduce the size and complexity of the whole system. Therefore, building an integrated device which can be used for both modulation and detection is of great interest.

There are several possible approaches to achieving this. One such choice, which has been demonstrated by Youngblood and his colleagues [368], is a dual layer graphene device. Two layers of graphene, separated by a dielectric layer (Al_2O_3), are integrated on a planarized silicon photonic waveguide. The device is in configuration of a simple field effect transistor (FET): the bottom layer (the channel) acts as an optical absorber and can collect photogenerated carriers, while the top layer acts as a transparent gate electrode, which can tune the electrical and optical properties of the bottom graphene layer. A schematic of the device configuration is shown in Figure 6.4 (a). Figure 6.4 (b) gives the SEM micrograph of the device. Two asymmetric source and drain contacts made of titanium/gold (light blue) and palladium/gold (dark yellow) dope the graphene (light purple) to be n- and p-type, respectively. A 100 nm layer of dielectric (Al_2O_3) is put between the gate and the channel, which induces a lateral p−i−n junction, shown in Figure 6.4 (c). A near infrared photodetection responsivity of 57 mAW^{-1} and modulation depth of 64% with GHz bandwidth has been achieved with this device.

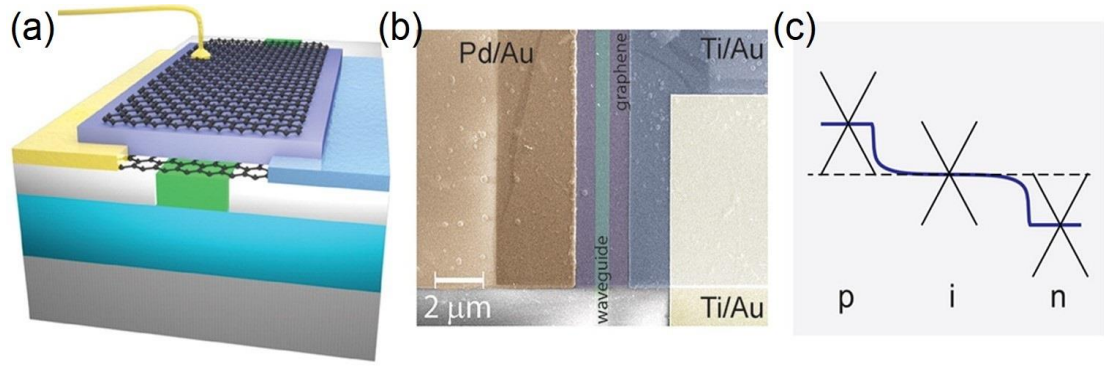

Figure 6.4 Integrated graphene modulator and photodetector. (a) Schematic illustration of the dual layer graphene modulator/detector integrated on a planarized waveguide; (b) Scanning electron microscope image of the device; (c) Illustration of the profile across the graphene channel highlighting the p–i–n junction and the built-in electric field. Adapted with permission from [368] Copyright (2014) American Chemical Society.

Another possible approach is to use a single layer metamaterial device loaded with small area graphene squares instead of a large area graphene layer, thus the graphene properties of each square can be tuned independently. The metamaterial feature array should be suitable for both detection and modulation.

This approach has been initially explored with an antenna geometry, which has demonstrated effective photodetection at room temperature around 2 THz and 2.7 THz, yielding a maximum responsivity of ~2 $\mathrm{mA \cdot W^{-1}}$ [218]. A schematic of the device is shown in Figure 6.5 (a). The Ti/Au antennas (10/65 nm) sit on top of a SiO_2/Si (300 nm/525 µm) substrate with small squares of graphene underneath the gap areas; the device can be biased with a back gate. The dimensions of the antenna geometry and the corresponding values are displayed in Figure 6.5 (b) and Table 6.1, respectively.

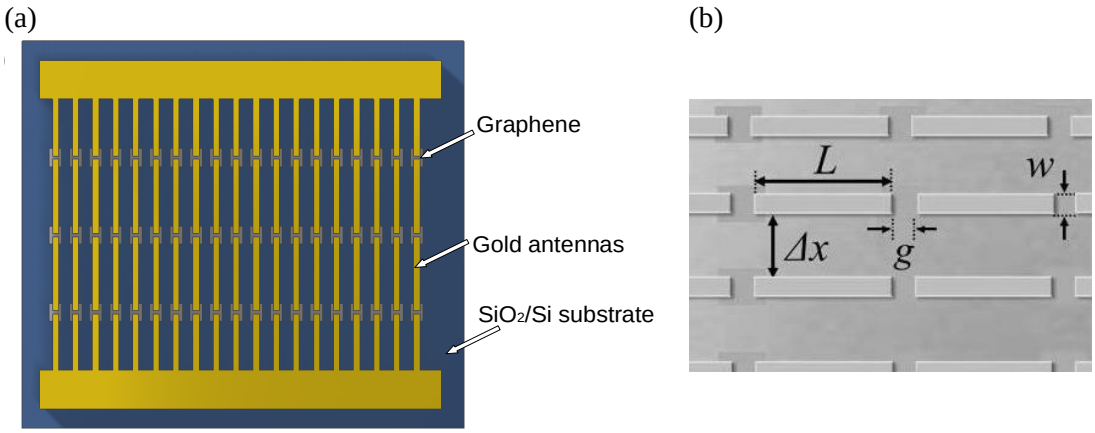

Figure 6.5 (a) Schematic of the integrated metamaterial device. (b) The geometry of the antennas. Figure (b) modified from [369].

Table 6.1 The dimension parameters for the antenna array

Name	Expression	Description
L	22.5 / 24.5 / 26.5 μm	Antenna length
w	2 μm	Antenna width
g	500 nm	Antenna gap
Δx	1.5 L	Antenna lateral spacing
t	100 nm	Antenna thickness

To get the optimal size of the antenna so that it will resonate at the QCL operating frequency, finite-element simulations have been performed with COMSOL Multiphysics to calculate the reflection spectra of antenna arrays with different antenna lengths. As shown in Figure 6.6 (a), when the length of the antennas is changed from 22.5 μm to 28.5 μm, the resonant frequency decreases from 2.35 THz to 1.86 THz. The THz QCL to be used has a central frequency of 2.25 THz, which is far away from the resonant frequency of the 28.5 μm array. Therefore, only the 22.5 μm, 24.5 μm and the 26.5 μm antenna arrays are fabricated. To further analyze the modulation ability of this device configuration, the reflection spectra of the 22.5 μm device (because it hits the right resonant frequency) at different graphene conductivities have been simulated as well with the results shown in Figure 6.6 (b). When the conductivity is increased from 0.3 mS to 0.6 mS, the reflectivity can be changed by about 8% and a 12.8 % modulation depth can be achieved.

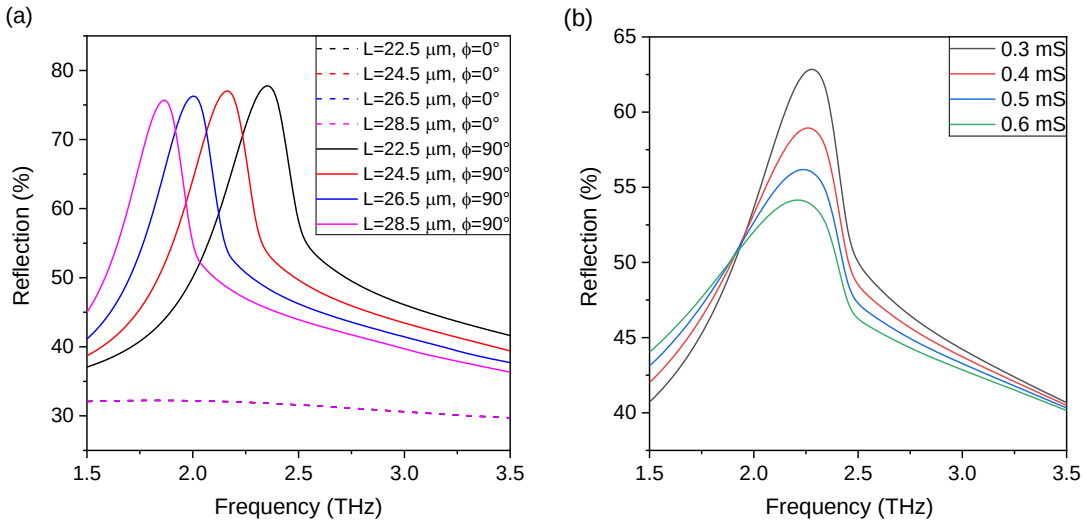

Figure 6.6 (a) The reflection spectra of the antenna array modulator with different antenna sizes and incident light directions. When ϕ=0°/90°, the light polarization is perpendicular/parallel to the main axis of the antennas. (b) The reflection spectra when the graphene conductivity is changed from 0.3 mS to 0.6 mS.

The devices have alreay been fabricated by my colleague Long Xiao with a similar procedure to the fabrication of the SRR device as discussed in Section 3.2.3. Figure 6.7 (a) gives an SEM micrograph of it. The device is first electronically tested to see whether the resistance of the graphene on the antenna arrays can be tuned by chaging the gate voltage. The back-gate on the 24.5 µm antenna array is not working, therefore, only the 22.5 µm (Antenna 1) and the 26.5 µm (Antenna 2) arrays have been measured, with the results shown in Figure 6.7 (b). The dirac point are -20V and -6 V, respectively. The diract point for Antena 2 is higer than Antenna 1, as it was exposed in air for a longer time, which will n-dope the granphene and increase the dirac point. Small area graphene graphene square in the gap between two antennas) is used for this device, the resistance measured here is the the sum of the contact resistance between the metallic antenna and graphene [369]. However, the change of it still reflects the change of the graphene resistance of all the small squares as the contact resistance of the Au antennas dose not change much when the bias voltage is changed. This graph shows that the resistance, thus the conductivity, of the graphene on the device can be tuned by changing the gate voltage. Therefore, the reflectivity of the graphene loaded antenna array can be tuned as well through back-gating.

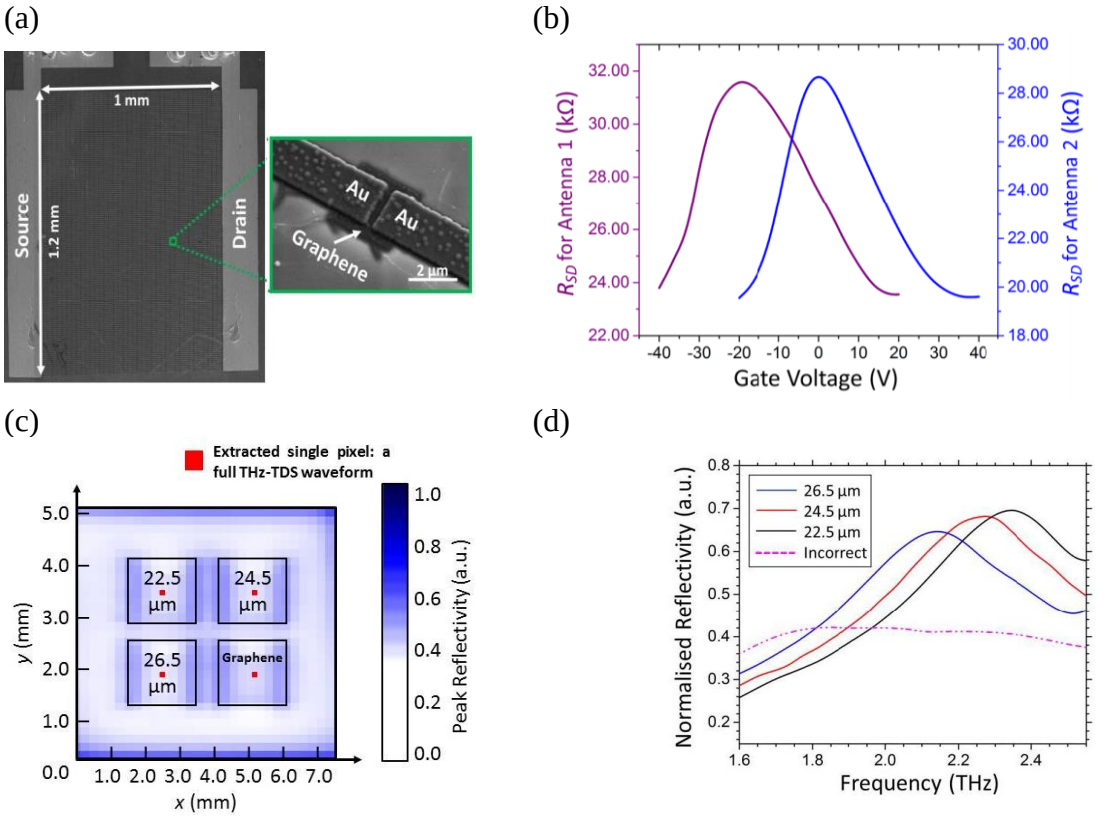

Figure 6.7 Information for the antennas device: (a) SEM micrograph; (b) The resistance of device with L = 26.5 µm for Antenna 1 and L = 22.5 µm for Antenna 2; (c) XY scan of the reflectivity of the device with THz TDS; (d) Normalised reflection spectra for the three arrays with different antenna lengths. Modified from [369].

The device is then measured in a THz TDS system to get its THz response. Firstly, an XY scan is conducted to locate the antenna arrays on the sample, with the results shown in Figure 6.7 (c). A difference can be seen between the gold electrodes and other areas as they have a much higher reflectivity. Afterwards, finer measurements are performed to get the reflection spectra of the different arrays. As can be seen from Figure 6.7 (d), the 22.5 µm, 24.5 µm and 26.5 µm antenna arrays have resonant frequencies of 2.34 THz, 2.25 THz and 2.13 THz, respectively. Idellay, the 24.5 µm antenna array should be used for further amplitude stabilisation experiment. However, as the back-gate of it is not working, the 22.5 µm antenna array will be used as the resonant frequency of it (2.34 THz) is very close to the laser frequency (2.25 THz). The next step is to test the modulation ability of the device with a THz QCL.

The device also has the potential for high speed active control of THz radiation. A low impedance path is made for the graphene to charge and discharge because the antenna arrays are directly connected to small rectangular areas of graphene and then all the antennas are connected together. In addition, small areas of graphene give a small capacitance. Small impedance and capacitance can both lead to a high modulation speed and an optical modulation cut-off frequency above 100 MHz has been achieved with this approach but a slight different geometry [205].

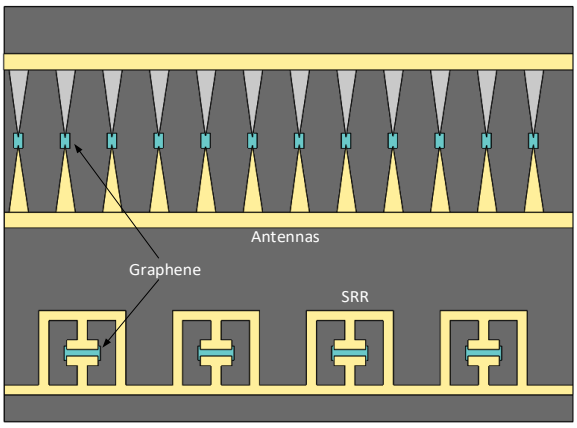

Figure 6.8 One possible configuration for an integrated device in single layer

However, the current device cannot be used in a feedback loop for both detection and modulation. When changing the bias voltage of the device, the photocurrent used for detection of the QCL power will change as well even when the QCL power stays the same. There are two ways to overcome this. The first one is a double-layered device, where the top layer is a modulator while the bottom layer is a detector. It can be designed in a similar way as the device reported in reference [368]. The second possible way of

achieving this is a hybrid device. On this device, SRRs and dipole antennas are put next to each other in alternate lines, as shown in Figure 6.8, and they can be biased independently. Therefore, the modulation and detection can be separated from each other. Both approaches can be explored if the 22.5 μm antenna array in Figure 6.7 can give a large enough modulation depth with the THz QCL measurement.

6.2.3 Frequency stabilization of a THz QCL with metamaterials

At the same time, the same principle used for amplitude stabilization in this thesis can be applied to frequency stabilization, where a frequency modulator instead of an amplitude modulator will be utilised. This approach does not need a frequency comb, or complex electronics, which will be useful for portable and applicative spectroscopic measurements.

6.2.4 Cryogenic temperature broadband THz s-SNOM

One important application of THz s-SNOM is inspection and even manipulation of quantum objects, which is also one of the final goals of building the THz s-SNOM system in this work. For many quantum objects, it only works at cryogenic temperatures. Therefore, to measure them, a cryogenic temperature s-SNOM is needed.

There are several problems to solve to achieve this. The first one is to push the QTF-based AFM to work at low temperature. Compared with room temperature, the properties of the tuning fork will be different, and the vibration isolation will be more difficult at low temperature. The second difficulty will be coupling the THz light from a THz QCL into the sample space. As the QCL needs to be cooled down with a separate cryostat, there will be at least two optical windows between the QCL and the sample, which will absorb a considerate amount of the scattering signal. At the same time, it will be more challenging to perform the alignment of the optical path.

Meanwhile, a broadband THz source is useful for THz s-SNOM measurements. It can give information of a sample at different wavelengths. The QCA based broadband external cavity QCL is a possible approach.

6.2.5 THz s-SNOM characterization of graphene loaded metamaterials

As discussed in Section 5.8, the THz s-SNOM can be used to study the modal evolution within a resonant structure and a metamaterial sample has been specially designed for this. The next step is to measure the sample with the s-SNOM and get the electric field distributions of the SRRs/CRs with different overall sizes or gap sizes. As graphene is put at the gap area for the samples, it can also be used to study how the

change of graphene conductivity will affect the electric field distribution within the resonant structure. This can be achieved by imaging the same resonator at different graphene back-gate voltages.

6.2.6 THz spatial light modulator with graphene loaded metamaterial

Spatial light modulators (SLM) are very important for many applications like imaging, adaptive optics, etc. Despite the development of THz technologies for so many years, there are still not many SLMs which can operate at the THz frequency range. Unlike for visible light, the normal liquid crystal SLM does not work well at THz frequency range. Therefore, new materials or mechanism needs to be found to spatially modulate THz radiation. One promising approach is using metamaterials, which have already been used in microwave and infrared for spatial light modulation purposes. Figure 6.9 shows a 1-bit digital metasurface operating at GHz frequency range, which has 64 pixels. The phase response of each pixel can be changed between 0 and π when the bias voltage is on and off. Therefore, a spatially patterned light beam can be generated when some of pixels are biased while the others are not.

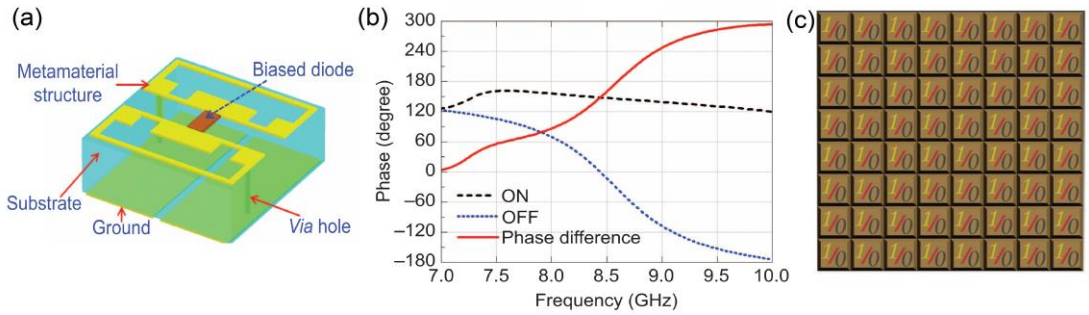

Figure 6.9 A 1-bit digital metasurface, adapted with permission from [370] © 2014, Springer Nature. (a) The structure of the metamaterial particle; (b) the corresponding phase responses of the metamaterial particle at 'OFF' and 'ON' bias voltages; (c) the pixel configuration.

A similar device has been demonstrated for mid-infrared as well, as shown in Figure 6.10. The device is a graphene loaded SRR array, which is very similar to the device used in Chapter 3 for amplitude modulation. The SRRs are divided into a 6×6 array. Each element in the array functions as a pixel and all the pixels are electronically isolated from one another so that they can be biased independently. A spatial reflection pattern of "CINT" at λ = 8.3 μm has been achieved by selectively applying 'ON' and 'OFF' gate voltages.

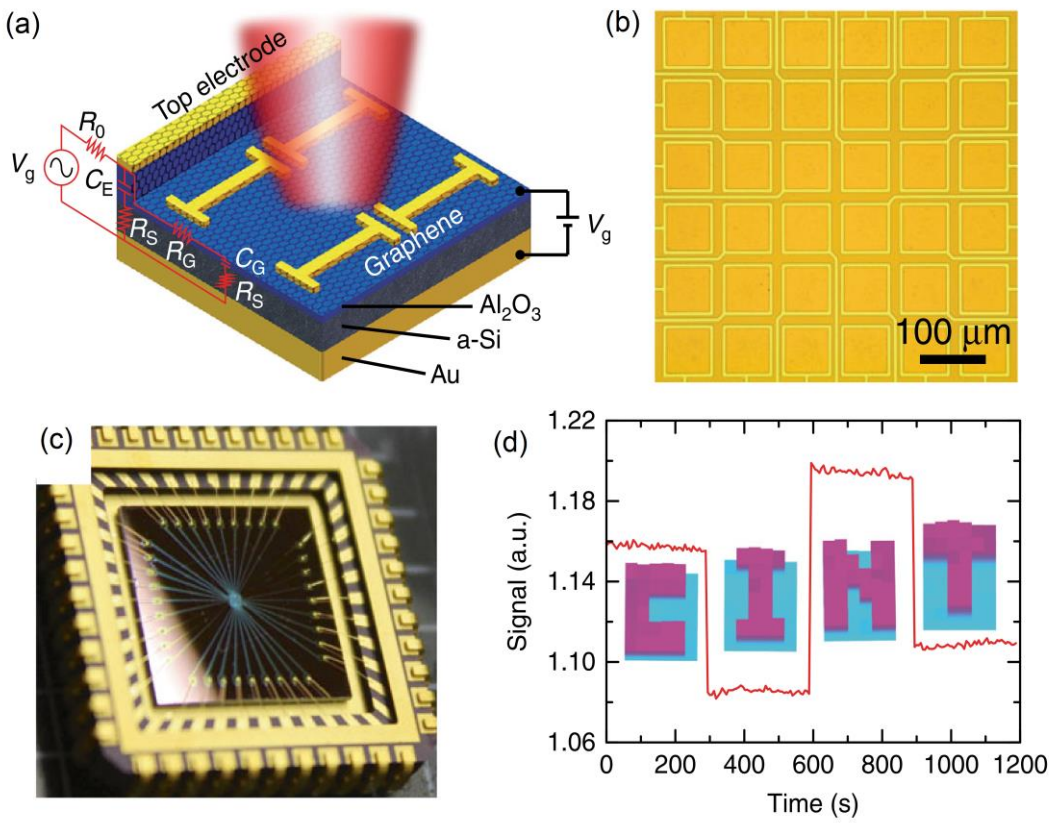

Figure 6.10 Hybrid graphene metasurface spatial light modulator for mid-infrared, adapted with permission from [371] © 2018, Springer Nature. (a) Schematic of the device; (b) the 6×6 pixel array; (c) wired bonded device on a chip carrier and (d) spatial reflection patterns of "CINT" at λ = 8.3 μm by selectively applying 'ON' and 'OFF' gate voltages.

For metamaterials, their optical properties are mainly determined by the geometric parameters. By adjusting the sizes of the aforementioned devices, they might work at THz as well. There are also many techniques for THz modulations as well, either through direct [144], [372]–[374] or indirect ways [141]. Among all these approaches, the graphene loaded metamaterials are easier to fabricate compared with other approaches and can offer a high modulation depth. Also considering the research experience in the research group on this type of devices, it will be the best choice for the first attempt. The SRR device in the Section 3.2 has demonstrated its ability for THz modulation. If the device can be divided into small pixel areas, which can be biased separately, it can be used as a THz SLM. The problem to be solved is finding a proper approach to control the gate voltages of the individual pixels independently. If 100 pixels are defined, 100 voltages need to be applied on the device separately, which will be a challenging task.

One important application of the THz SLM discussed in the previous section is single pixel imaging, which has been discussed briefly in Section 1.6.3. If the graphene loaded metamaterial device works well as a THz SLM, it can be used to generate the random THz masks, which is the key element for single pixel imaging.

References

[1] B. Ferguson and X.-C. Zhang, “Materials for terahertz science and technology,” *Nat. Mater.*, vol. 1, no. 1, pp. 26–33, Sep. 2002. doi:10.1038/nmat708.

[2] M. Tonouchi, “Cutting-edge terahertz technology,” *Nat. Photonics*, vol. 1, no. 2, pp. 97–105, Feb. 2007. doi:10.1038/nphoton.2007.3.

[3] S.-I. Kim *et al.*, “Fluorinated Organic Electro-Optic Quinolinium Crystals for THz Wave Generation,” *Adv. Opt. Mater.*, vol. 7, no. 4, p. 1801495, Feb. 2019. doi:10.1002/adom.201801495.

[4] D. M. Mittleman, “Frontiers in terahertz sources and plasmonics,” *Nat. Photonics*, vol. 7, no. 9, pp. 666–669, Sep. 2013. doi:10.1038/nphoton.2013.235.

[5] A. Madrazo, R. Carminati, M. Nieto-Vesperinas, and J.-J. Greffet, “Polarization effects in the optical interaction between a nanoparticle and a corrugated surface: implications for apertureless near-field microscopy,” *J. Opt. Soc. Am. A*, vol. 15, no. 1, p. 109, Jan. 1998. doi:10.1364/JOSAA.15.000109.

[6] R. E. Miles and M. Naftaly, “Terahertz Sources,” in *Microwave Photonics*, no. May, Chichester, UK: John Wiley & Sons, Ltd, 2009, pp. 111–129. doi:10.1002/9780470744857.ch5.

[7] T. Nagatsuma, “Terahertz technologies: Present and future,” *IEICE Electron. Express*, vol. 8, no. 14, pp. 1127–1142, 2011. doi:10.1587/elex.8.1127.

[8] D. Wu *et al.*, “Ultrabroadband photosensitivity from visible to terahertz at room temperature,” *Sci. Adv.*, vol. 4, no. 8, p. eaao3057, Aug. 2018. doi:10.1126/sciadv.aao3057.

[9] R. A. Lewis, “A review of terahertz sources,” *J. Phys. D. Appl. Phys.*, vol. 47, no. 37, 2014. doi:10.1088/0022-3727/47/37/374001.

[10] G. R. Neil, “Accelerator sources for THz science: A review,” *J. Infrared, Millimeter, Terahertz Waves*, vol. 35, no. 1, pp. 5–16, 2014. doi:10.1007/s10762-013-9999-x.

[11] G. P. Williams, “Filling the THz gap—high power sources and applications,” *Reports Prog. Phys.*, vol. 69, no. 2, pp. 301–326, Feb. 2006. doi:10.1088/0034-4885/69/2/R01.

[12] T. Kleine-Ostmann and T. Nagatsuma, “A review on terahertz communications research,” *J. Infrared, Millimeter, Terahertz Waves*, vol. 32, no. 2, pp. 143–171, 2011. doi:10.1007/s10762-010-9758-1.

[13] I. Mehdi, J. Siles, C. P. Chen, and J. M. Jornet, “THz Technology for Space Communications,” in *2018 Asia-Pacific Microwave Conference (APMC)*, 2018, vol.

2018-Novem, pp. 76–78. doi:10.23919/APMC.2018.8617235.

[14] T. Kürner, “Towards Future THz Communications Systems,” *Tstnetwork.Org*, vol. 5, no. 1, pp. 11–17, 2012. doi:10.11906/TST.011-017.2012.03.02.

[15] H. Elayan, O. Amin, R. M. Shubair, and M.-S. Alouini, “Terahertz communication: The opportunities of wireless technology beyond 5G,” in *2018 International Conference on Advanced Communication Technologies and Networking (CommNet)*, 2018, pp. 1–5. doi:10.1109/COMMNET.2018.8360286.

[16] S. Zhong, “Progress in terahertz nondestructive testing: A review,” *Front. Mech. Eng.*, vol. 14, no. 3, pp. 273–281, Sep. 2019. doi:10.1007/s11465-018-0495-9.

[17] K. Humphreys *et al.*, “Medical applications of terahertz imaging: a review of current technology and potential applications in biomedical engineering,” in *The 26th Annual International Conference of the IEEE Engineering in Medicine and Biology Society*, 2004, vol. 3, pp. 1302–1305. doi:10.1109/IEMBS.2004.1403410.

[18] P. H. Siegel, “Technology in Biology and Medicine,” *Instrumentation*, vol. 52, no. 10, pp. 0–3, 2004. doi:10.1109/TMTT.2004.835916.

[19] H. Zhan *et al.*, “Evaluating PM2.5 at a Construction Site Using Terahertz Radiation,” *IEEE Trans. Terahertz Sci. Technol.*, vol. 5, no. 6, pp. 1028–1034, Nov. 2015. doi:10.1109/TTHZ.2015.2477596.

[20] J. Liu, J. Dai, S. L. Chin, and X.-C. Zhang, “Broadband terahertz wave remote sensing using coherent manipulation of fluorescence from asymmetrically ionized gases,” *Nat. Photonics*, vol. 4, no. 9, pp. 627–631, Sep. 2010. doi:10.1038/nphoton.2010.165.

[21] E.-M. Stübling *et al.*, “Application of a robotic THz imaging system for sub-surface analysis of ancient human remains,” *Sci. Rep.*, vol. 9, no. 1, p. 3390, Dec. 2019. doi:10.1038/s41598-019-40211-7.

[22] A. D. Rakić *et al.*, “Sensing and imaging using laser feedback interferometry with quantum cascade lasers,” *Appl. Phys. Rev.*, vol. 6, no. 2, pp. 0–19, 2019. doi:10.1063/1.5094674.

[23] K. Aoki, J. Savolainen, and M. Havenith, “Broadband terahertz pulse generation by optical rectification in GaP crystals,” *Appl. Phys. Lett.*, vol. 110, no. 20, p. 201103, May 2017. doi:10.1063/1.4983371.

[24] K. Radhanpura, S. Hargreaves, R. A. Lewis, L. Sirbu, and I. M. Tiginyanu, “Heavy noble gas (Kr, Xe) irradiated (111) InP nanoporous honeycomb membranes with enhanced ultrafast all-optical terahertz emission,” *Appl. Phys. Lett.*, vol. 97, no. 18, p. 181921, Nov. 2010. doi:10.1063/1.3509404.

[25] K. Kawase, T. Hatanaka, H. Takahashi, K. Nakamura, T. Taniuchi, and H. Ito, “Tunable terahertz-wave generation from DAST crystal by dual signal-wave parametric oscillation of periodically poled lithium niobate,” *Opt. Lett.*, vol. 25, no. 23, p. 1714, Dec. 2000. doi:10.1364/OL.25.001714.

[26] K. Nawata, Y. Tokizane, Y. Takida, and H. Minamide, “Tunable Backward Terahertz-wave Parametric Oscillation,” *Sci. Rep.*, vol. 9, no. 1, p. 726, Dec. 2019. doi:10.1038/s41598-018-37068-7.

[27] D. H. Auston, K. P. Cheung, and P. R. Smith, “Picosecond photoconducting Hertzian dipoles,” *Appl. Phys. Lett.*, vol. 45, no. 3, pp. 284–286, Aug. 1984. doi:10.1063/1.95174.

[28] G. Mourou, C. V. Stancampiano, A. Antonetti, and A. Orszag, “Picosecond microwave pulses generated with a subpicosecond laser-driven semiconductor switch,” *Appl. Phys. Lett.*, vol. 39, no. 4, pp. 295–296, 1981. doi:10.1063/1.92719.

[29] H. Ito, F. Nakajima, T. Furuta, and T. Ishibashi, “Continuous THz-wave generation using antenna-integrated uni-travelling-carrier photodiodes,” *Semicond. Sci. Technol.*, vol. 20, no. 7, pp. S191–S198, Jul. 2005. doi:10.1088/0268-1242/20/7/008.

[30] T. Nagatsuma, G. Ducournau, and C. C. Renaud, “Advances in terahertz communications accelerated by photonics,” *Nat. Photonics*, vol. 10, no. 6, pp. 371–379, 2016. doi:10.1038/nphoton.2016.65.

[31] H. Ito, T. Yoshimatsu, H. Yamamoto, and T. Ishibashi, “Broadband photonic terahertz-wave emitter integrating UTC-PD and novel planar antenna,” in *Terahertz Physics, Devices, and Systems VII: Advanced Applications in Industry and Defense*, 2013, vol. 8716, no. May 2013, p. 871602. doi:10.1117/12.2015523.

[32] M. Feiginov, C. Sydlo, O. Cojocari, and P. Meissner, “Resonant-tunnelling-diode oscillators operating at frequencies above 1.1 THz,” *Appl. Phys. Lett.*, vol. 99, no. 23, p. 233506, Dec. 2011. doi:10.1063/1.3667191.

[33] G. L. Carr, M. C. Martin, W. R. McKinney, K. Jordan, G. R. Neil, and G. P. Williams, “High-power terahertz radiation from relativistic electrons,” *Nature*, vol. 420, no. 6912, pp. 153–156, Nov. 2002. doi:10.1038/nature01175.

[34] E. H. Linfield, A. G. Davies, and P. Dean, “Terahertz quantum cascade lasers — The past, present, and potential future,” in *2015 40th International Conference on Infrared, Millimeter, and Terahertz waves (IRMMW-THz)*, 2015, pp. 1–2. doi:10.1109/IRMMW-THz.2015.7327749.

[35] KAZARINOV RF and SURIS RA, “Possibility of the amplification of electromagnetic waves in a semiconductor with a superlattice,” *Sov Phys Semicond*, vol. 5, no. 4, pp. 707–709, 1971.

[36] J. Faist, F. Capasso, D. L. Sivco, C. Sirtori, A. L. Hutchinson, and A. Y. Cho, “Quantum Cascade Laser,” *Science (80-.).*, vol. 264, no. 5158, pp. 553–556, Apr. 1994. doi:10.1126/science.264.5158.553.

[37] R. Köhler *et al.*, “Terahertz semiconductor-heterostructure laser,” *Nature*, vol. 417, no. 6885, pp. 156–159, May 2002. doi:10.1038/417156a.

[38] C. Walther, M. Fischer, G. Scalari, R. Terazzi, N. Hoyler, and J. Faist, “Quantum cascade lasers operating from 1.2 to 1.6 THz,” *Appl. Phys. Lett.*, vol. 91, no. 13, p.

131122, Sep. 2007. doi:10.1063/1.2793177.

[39] W. Terashima and H. Hirayama, “GaN-based terahertz quantum cascade lasers,” in *Terahertz Physics, Devices, and Systems IX: Advanced Applications in Industry and Defense*, 2015, vol. 9483, no. May 2015, p. 948304. doi:10.1117/12.2184199.

[40] Q. Hu, “Terahertz quantum cascade lasers,” *Optics InfoBase Conference Papers*. Massachusetts Institute of Technology, 2005.

[41] L. H. Li *et al.*, “Multi-Watt high-power THz frequency quantum cascade lasers,” *Electron. Lett.*, vol. 53, no. 12, pp. 799–800, Jun. 2017. doi:10.1049/el.2017.0662.

[42] L. Bosco, M. Franckié, G. Scalari, M. Beck, A. Wacker, and J. Faist, “Thermoelectrically cooled THz quantum cascade laser operating up to 210 K,” *Appl. Phys. Lett.*, vol. 115, no. 1, p. 010601, Jul. 2019. doi:10.1063/1.5110305.

[43] B. S. Williams, S. Kumar, H. Callebaut, Q. Hu, and J. L. Reno, “Terahertz quantum-cascade laser operating up to 137 K,” *Appl. Phys. Lett.*, vol. 83, no. 25, pp. 5142–5144, Dec. 2003. doi:10.1063/1.1635657.

[44] A. Tredicucci, “Quantum Cascade Lasers,” in *Encyclopedia of Condensed Matter Physics*, Elsevier, 2005, pp. 1–9. doi:10.1016/B0-12-369401-9/01144-X.

[45] R. Koehler *et al.*, “Terahertz quantum cascade lasers,” in *2005 Conference on Lasers and Electro-Optics, CLEO*, 2003, vol. 2, p. 123. doi:10.1117/12.475764.

[46] B. S. Williams, “Terahertz quantum-cascade lasers,” *Nat. Photonics*, vol. 1, no. 9, pp. 517–525, Sep. 2007. doi:10.1038/nphoton.2007.166.

[47] G. Scalari *et al.*, “Far-infrared (λ≈87 μm) bound-to-continuum quantum-cascade lasers operating up to 90 K,” *Appl. Phys. Lett.*, vol. 82, no. 19, pp. 3165–3167, May 2003. doi:10.1063/1.1571653.

[48] L. Ajili *et al.*, “High power quantum cascade lasers operating at λ≈87 and 130μm,” *Appl. Phys. Lett.*, vol. 85, no. 18, pp. 3986–3988, Nov. 2004. doi:10.1063/1.1810217.

[49] C. Walther, G. Scalari, J. Faist, H. Beere, and D. Ritchie, “Low frequency terahertz quantum cascade laser operating from 1.6 to 1.8 THz,” *Appl. Phys. Lett.*, vol. 89, no. 23, p. 231121, Dec. 2006. doi:10.1063/1.2404598.

[50] A. Valavanis *et al.*, “Terahertz quantum cascade lasers with >1 W output powers,” *Electron. Lett.*, vol. 50, no. 4, pp. 309–311, Feb. 2014. doi:10.1049/el.2013.4035.

[51] M. I. Amanti *et al.*, “Bound-to-continuum terahertz quantum cascade laser with a single-quantum-well phonon extraction/injection stage,” *New J. Phys.*, vol. 11, 2009. doi:10.1088/1367-2630/11/12/125022.

[52] B. S. Williams, H. Callebaut, S. Kumar, Q. Hu, and J. L. Reno, “3.4-THz quantum cascade laser based on longitudinal-optical-phonon scattering for depopulation,” *Appl. Phys. Lett.*, vol. 82, no. 7, pp. 1015–1017, 2003. doi:10.1063/1.1554479.

[53] S. Fathololoumi *et al.*, “Terahertz quantum cascade lasers operating up to ∼ 200 K with

optimized oscillator strength and improved injection tunneling," *Opt. Express*, vol. 20, no. 4, p. 3866, Feb. 2012. doi:10.1364/OE.20.003866.

[54] G. Scalari, N. Hoyler, M. Giovannini, and J. Faist, "Terahertz bound-to-continuum quantum-cascade lasers based on optical-phonon scattering extraction," *Appl. Phys. Lett.*, vol. 86, no. 18, p. 181101, May 2005. doi:10.1063/1.1920407.

[55] M. Adams, "Optical waves in crystals," *IEEE J. Quantum Electron.*, vol. 20, no. 11, pp. 1294–1294, Nov. 1984. doi:10.1109/JQE.1984.1072309.

[56] B. S. Williams, S. Kumar, H. Callebaut, Q. Hu, and J. L. Reno, "Terahertz quantum-cascade laser at λ≈100 μm using metal waveguide for mode confinement," *Appl. Phys. Lett.*, vol. 83, no. 11, pp. 2124–2126, Sep. 2003. doi:10.1063/1.1611642.

[57] B. S. Williams, S. Kumar, Q. Hu, and J. L. Reno, "Operation of terahertz quantum-cascade lasers at 164 K in pulsed mode and at 117 K in continuous-wave mode," *Opt. Express*, vol. 13, no. 9, p. 3331, 2005. doi:10.1364/OPEX.13.003331.

[58] H. E. Beere and D. A. Ritchie, "Molecular Beam Epitaxial Growth of Terahertz Quantum Cascade Lasers," in *Molecular Beam Epitaxy*, Chichester, UK: John Wiley & Sons Ltd, 2019, pp. 175–190. doi:10.1002/9781119354987.ch11.

[59] O. P. Marshall, "Terahertz quantum cascade lasers: photonic crystal waveguides and high frequency bias modulations," PhD thesis, University of Cambridge, 2010.

[60] H. Yasuda and I. Hosako, "Measurement of Terahertz Refractive Index of Metal with Terahertz Time-Domain Spectroscopy," *Jpn. J. Appl. Phys.*, vol. 47, no. 3, pp. 1632–1634, Mar. 2008. doi:10.1143/JJAP.47.1632.

[61] N. Laman and D. Grischkowsky, "Terahertz conductivity of thin metal films," *Appl. Phys. Lett.*, vol. 93, no. 5, p. 051105, Aug. 2008. doi:10.1063/1.2968308.

[62] J. D. Buron *et al.*, "Graphene Conductance Uniformity Mapping," *Nano Lett.*, vol. 12, no. 10, pp. 5074–5081, Oct. 2012. doi:10.1021/nl301551a.

[63] J. D. Buron *et al.*, "Graphene mobility mapping," *Sci. Rep.*, vol. 5, no. 1, p. 12305, Dec. 2015. doi:10.1038/srep12305.

[64] P. Parkinson *et al.*, "Transient terahertz conductivity of GaAs nanowires," *Nano Lett.*, vol. 7, no. 7, pp. 2162–2165, 2007. doi:10.1021/nl071162x.

[65] T.-I. Jeon and D. Grischkowsky, "Nature of Conduction in Doped Silicon," *Phys. Rev. Lett.*, vol. 78, no. 6, pp. 1106–1109, Feb. 1997. doi:10.1103/PhysRevLett.78.1106.

[66] T. Kan *et al.*, "Enantiomeric switching of chiral metamaterial for terahertz polarization modulation employing vertically deformable MEMS spirals," *Nat. Commun.*, vol. 6, no. 1, p. 8422, Dec. 2015. doi:10.1038/ncomms9422.

[67] H.-T. Chen *et al.*, "Experimental demonstration of frequency-agile terahertz metamaterials," *Nat. Photonics*, vol. 2, no. 5, pp. 295–298, May 2008. doi:10.1038/nphoton.2008.52.

[68] M. Choi *et al.*, "A terahertz metamaterial with unnaturally high refractive index," *Nature*, vol. 470, no. 7334, pp. 369–373, 2011. doi:10.1038/nature09776.

[69] J. Orenstein and J. S. Dodge, "Terahertz time-domain spectroscopy of transient metallic and superconducting states," *Phys. Rev. B*, vol. 92, no. 13, p. 134507, Oct. 2015. doi:10.1103/PhysRevB.92.134507.

[70] D.-K. Lee *et al.*, "Highly sensitive and selective sugar detection by terahertz nano-antennas," *Sci. Rep.*, vol. 5, no. 1, p. 15459, Dec. 2015. doi:10.1038/srep15459.

[71] M. Lu *et al.*, "Detection and identification of illicit drugs using terahertz imaging," *J. Appl. Phys.*, vol. 100, no. 10, p. 103104, Nov. 2006. doi:10.1063/1.2388041.

[72] H. Dember, "Über eine photoelektronische kraft in kupferoxydul-kristallen," *Z. Phys.*, vol. 32, p. 554, 1931.

[73] V. Apostolopoulos and M. E. Barnes, "THz emitters based on the photo-Dember effect," *J. Phys. D. Appl. Phys.*, vol. 47, no. 37, p. 374002, Sep. 2014. doi:10.1088/0022-3727/47/37/374002.

[74] C. A. Schmuttenmaer, "Exploring Dynamics in the Far-Infrared with Terahertz Spectroscopy," *Chem. Rev.*, vol. 104, no. 4, pp. 1759–1780, Apr. 2004. doi:10.1021/cr020685g.

[75] J. D. Jackson, "Classical Electrodynamics 3rd ed John Wiley & Sons." USA, 1999.

[76] M. Bass, P. A. Franken, J. F. Ward, and G. Weinreich, "Optical Rectification," *Phys. Rev. Lett.*, vol. 9, no. 11, pp. 446–448, Dec. 1962. doi:10.1103/PhysRevLett.9.446.

[77] R. Huber, A. Brodschelm, F. Tauser, and A. Leitenstorfer, "Generation and field-resolved detection of femtosecond electromagnetic pulses tunable up to 41 THz," *Appl. Phys. Lett.*, vol. 76, no. 22, pp. 3191–3193, May 2000. doi:10.1063/1.126625.

[78] P. Y. Han and X.-C. Zhang, "Coherent, broadband midinfrared terahertz beam sensors," *Appl. Phys. Lett.*, vol. 73, no. 21, pp. 3049–3051, Nov. 1998. doi:10.1063/1.122668.

[79] S. Kono, M. Tani, and K. Sakai, "Ultrabroadband photoconductive detection: Comparison with free-space electro-optic sampling," *Appl. Phys. Lett.*, vol. 79, no. 7, pp. 898–900, Aug. 2001. doi:10.1063/1.1394719.

[80] J. Neu and C. A. Schmuttenmaer, "Tutorial: An introduction to terahertz time domain spectroscopy (THz-TDS)," *J. Appl. Phys.*, vol. 124, no. 23, p. 231101, Dec. 2018. doi:10.1063/1.5047659.

[81] M. C. Beard, G. M. Turner, and C. A. Schmuttenmaer, "Transient photoconductivity in GaAs as measured by time-resolved terahertz spectroscopy," *Phys. Rev. B - Condens. Matter Mater. Phys.*, vol. 62, no. 23, pp. 15764–15777, 2000. doi:10.1103/PhysRevB.62.15764.

[82] K. Reimann, R. P. Smith, A. M. Weiner, T. Elsaesser, and M. Woerner, "Direct field-resolved detection of terahertz transients with amplitudes of megavolts per centimeter," *Opt. Lett.*, vol. 28, no. 6, p. 471, Mar. 2003. doi:10.1364/OL.28.000471.

[83] W. Withayachumnankul and D. Abbott, “Metamaterials in the Terahertz Regime,” *IEEE Photonics J.*, vol. 1, no. 2, pp. 99–118, Aug. 2009. doi:10.1109/JPHOT.2009.2026288.

[84] D. R. Smith, “Metamaterials and Negative Refractive Index,” *Science (80-.).*, vol. 305, no. 5685, pp. 788–792, Aug. 2004. doi:10.1126/science.1096796.

[85] Y. Liu and X. Zhang, “Metamaterials: a new frontier of science and technology,” *Chem. Soc. Rev.*, vol. 40, no. 5, p. 2494, 2011. doi:10.1039/c0cs00184h.

[86] J. Pendry, “Metamaterials in the sunshine,” *Nat. Mater.*, vol. 5, no. 8, pp. 599–600, Aug. 2006. doi:10.1038/nmat1697.

[87] D. R. Smith, W. J. Padilla, D. C. Vier, and S. Schultz, “Composite Medium with Simultaneously Negative Permeability and Permittivity,” pp. 1–4, 2000.

[88] Y. Yao *et al.*, “Wide Wavelength Tuning of Optical Antennas on Graphene with Nanosecond Response Time,” *Nano Lett.*, vol. 14, no. 1, pp. 214–219, Jan. 2014. doi:10.1021/nl403751p.

[89] Y. Yao *et al.*, “Broad Electrical Tuning of Graphene-Loaded Plasmonic Antennas,” *Nano Lett.*, vol. 13, no. 3, pp. 1257–1264, Mar. 2013. doi:10.1021/nl3047943.

[90] J. B. Pendry, A. J. Holden, D. J. Robbins, and W. J. Stewart, “Magnetism from conductors and enhanced nonlinear phenomena,” *IEEE Trans. Microw. Theory Tech.*, vol. 47, no. 11, pp. 2075–2084, 1999. doi:10.1109/22.798002.

[91] P. Q. Liu *et al.*, “Highly tunable hybrid metamaterials employing split-ring resonators strongly coupled to graphene surface plasmons,” *Nat. Commun.*, vol. 6, no. 1, p. 8969, Dec. 2015. doi:10.1038/ncomms9969.

[92] H. Chen, W. J. Padilla, J. M. O. Zide, A. C. Gossard, A. J. Taylor, and R. D. Averitt, “Active terahertz metamaterial devices,” *Nature*, vol. 444, no. 7119, pp. 597–600, Nov. 2006. doi:10.1038/nature05343.

[93] J. Niegemann *et al.*, “Absolute extinction cross-section of individual magnetic split-ring resonators,” vol. 2, no. October, pp. 8–11, 2008. doi:10.1038/nphoton.2008.181.

[94] S. Linden, F. B. P. Niesler, J. Förstner, Y. Grynko, T. Meier, and M. Wegener, “Collective Effects in Second-Harmonic Generation from Split-Ring-Resonator Arrays,” *Phys. Rev. Lett.*, vol. 109, no. 1, p. 015502, Jul. 2012. doi:10.1103/PhysRevLett.109.015502.

[95] C. Imhof and R. Zengerle, “Pairs of metallic crosses as a left-handed metamaterial with improved polarization properties,” *Opt. Express*, vol. 14, no. 18, p. 8257, 2006. doi:10.1364/OE.14.008257.

[96] R. Ghaffarivardavagh, J. Nikolajczyk, R. Glynn Holt, S. Anderson, and X. Zhang, “Horn-like space-coiling metamaterials toward simultaneous phase and amplitude modulation,” *Nat. Commun.*, vol. 9, no. 1, p. 1349, Dec. 2018. doi:10.1038/s41467-018-03839-z.

[97] S. J. Kindness *et al.*, “External amplitude and frequency modulation of a terahertz

quantum cascade laser using metamaterial/graphene devices," *Sci. Rep.*, vol. 7, no. 1, p. 7657, Dec. 2017. doi:10.1038/s41598-017-07943-w.

[98] H. Chen, W. J. Padilla, M. J. Cich, A. K. Azad, R. D. Averitt, and A. J. Taylor, "A metamaterial solid-state terahertz phase modulator," vol. 3, no. March, pp. 3–6, 2009. doi:10.1038/NPHOTON.2009.3.

[99] W. Cai, U. K. Chettiar, A. V. Kildishev, and V. M. Shalaev, "Optical cloaking with metamaterials," *Nat. Photonics*, vol. 1, no. 4, pp. 224–227, Apr. 2007. doi:10.1038/nphoton.2007.28.

[100] J. Li and J. B. Pendry, "Hiding under the Carpet: A New Strategy for Cloaking," *Phys. Rev. Lett.*, vol. 101, no. 20, p. 203901, Nov. 2008. doi:10.1103/PhysRevLett.101.203901.

[101] U. Leonhardt and T. Tyc, "Broadband Invisibility by Non-Euclidean Cloaking," *Science (80-.).*, vol. 323, no. 5910, pp. 110–112, Jan. 2009. doi:10.1126/science.1166332.

[102] J. Valentine, J. Li, T. Zentgraf, G. Bartal, and X. Zhang, "An optical cloak made of dielectrics," *Nat. Mater.*, vol. 8, no. 7, pp. 568–571, 2009. doi:10.1038/nmat2461.

[103] V. M. Shalaev, "Optical negative-index metamaterials," *Nat. Photonics*, vol. 1, no. 1, pp. 41–48, Jan. 2007. doi:10.1038/nphoton.2006.49.

[104] N. Fang, "Sub-Diffraction-Limited Optical Imaging with a Silver Superlens," *Science (80-.).*, vol. 308, no. 5721, pp. 534–537, Apr. 2005. doi:10.1126/science.1108759.

[105] T. Taubner, D. Korobkin, Y. Urzhumov, G. Shvets, and R. Hillenbrand, "Near-Field Microscopy Through a SiC Superlens," *Science (80-.).*, vol. 313, no. 5793, pp. 1595–1595, Sep. 2006. doi:10.1126/science.1131025.

[106] L. Ho, M. Pepper, and P. Taday, "Terahertz spectroscopy: Signatures and fingerprints," *Nat. Photonics*, vol. 2, no. 9, pp. 541–543, 2008. doi:10.1038/nphoton.2008.174.

[107] D. F. Plusquellic, K. Siegrist, E. J. Heilweil, and O. Esenturk, "Applications of Terahertz Spectroscopy in Biosystems," *ChemPhysChem*, vol. 8, no. 17, pp. 2412–2431, Dec. 2007. doi:10.1002/cphc.200700332.

[108] D. J. Cook, B. K. Decker, and M. G. Allen, "Quantitative THz Spectroscopy of Explosive Materials," in *Optical Terahertz Science and Technology*, 2005, p. MA6. doi:10.1364/OTST.2005.MA6.

[109] K. Fukunaga and M. Picollo, "Terahertz spectroscopy applied to the analysis of artists' materials," *Appl. Phys. A Mater. Sci. Process.*, vol. 100, no. 3, pp. 591–597, 2010. doi:10.1007/s00339-010-5643-y.

[110] K. Fukunaga, Y. Ogawa, S. Hayashi, and I. Hosako, "Terahertz spectroscopy for art conservation," *IEICE Electron. Express*, vol. 4, no. 8, pp. 258–263, 2007. doi:10.1587/elex.4.258.

[111] P. F. Taday *et al.*, "Applications of terahertz spectroscopy to pharmaceutical sciences," *Philos. Trans. R. Soc. A Math. Phys. Eng. Sci.*, vol. 362, no. 1815, pp. 351–364, 2004. doi:10.1098/rsta.2003.1321.

[112] C. Kulesa, “Terahertz Spectroscopy for Astronomy: From Comets to Cosmology,” *IEEE Trans. Terahertz Sci. Technol.*, vol. 1, no. 1, pp. 232–240, Sep. 2011. doi:10.1109/TTHZ.2011.2159648.

[113] C.E.Shannon, “Communication in the presence of noise,” *Proc. IRE*, vol. 37, no. 1, pp. 10–21, 1949.

[114] J. Federici and L. Moeller, “Review of terahertz and subterahertz wireless communications,” *J. Appl. Phys.*, vol. 107, no. 11, 2010. doi:10.1063/1.3386413.

[115] Q. Itu-r, T. Itu, R. Assembly, R. Bureau, and T. Figure, “RECOMMENDATION ITU-R P . 676-6 Attenuation by atmospheric gases Annex 1 Line-by-line calculation of gaseous attenuation,” pp. 1–23, 2005.

[116] D. J. Richardson, J. M. Fini, and L. E. Nelson, “Space Division Multiplexing in Optical Fibres,” pp. 1–19, 2013. doi:10.1038/nphoton.2013.94.

[117] H.-J. Song, K. Ajito, Y. Muramoto, A. Wakatsuki, T. Nagatsuma, and N. Kukutsu, “Uni-Travelling-Carrier Photodiode Module Generating 300 GHz Power Greater Than 1 mW,” *IEEE Microw. Wirel. Components Lett.*, vol. 22, no. 7, pp. 363–365, Jul. 2012. doi:10.1109/LMWC.2012.2201460.

[118] S. NODA, “Recent Progress and Future Prospect of Photonic Crystals,” *TRENDS Sci.*, vol. 15, no. 9, pp. 78–81, 2010. doi:10.5363/tits.15.9_78.

[119] H. Shams, M. J. Fice, K. Balakier, C. C. Renaud, F. van Dijk, and A. J. Seeds, “Photonic generation for multichannel THz wireless communication,” *Opt. Express*, vol. 22, no. 19, p. 23465, Sep. 2014. doi:10.1364/OE.22.023465.

[120] G. Ducournau *et al.*, “Ultrawide-Bandwidth Single-Channel 0.4-THz Wireless Link Combining Broadband Quasi-Optic Photomixer and Coherent Detection,” *IEEE Trans. Terahertz Sci. Technol.*, vol. 4, no. 3, pp. 328–337, May 2014. doi:10.1109/TTHZ.2014.2309006.

[121] X. Li, J. Yu, J. Zhang, Z. Dong, F. Li, and N. Chi, “A 400G optical wireless integration delivery system.,” *Opt. Express*, vol. 21, no. 16, pp. 18812–9, 2013. doi:10.1364/OE.21.018812.

[122] T. Nagatsuma *et al.*, “Terahertz wireless communications based on photonics technologies,” *Opt. Express*, vol. 21, no. 20, p. 23736, Oct. 2013. doi:10.1364/oe.21.023736.

[123] L. Moeller, J. Federici, and K. Su, “2.5 Gbit/s duobinary signalling with narrow bandwidth 0.625 terahertz source,” *Electron. Lett.*, vol. 47, no. 15, p. 856, 2011. doi:10.1049/el.2011.1451.

[124] C. Jastrow *et al.*, “Wireless digital data transmission at 300 GHz,” *Electron. Lett.*, vol. 46, no. 9, p. 661, 2010. doi:10.1049/el.2010.3509.

[125] I. Kallfass *et al.*, “All active MMIC-based wireless communication at 220 GHz,” *IEEE Trans. Terahertz Sci. Technol.*, vol. 1, no. 2, pp. 477–487, 2011.

doi:10.1109/TTHZ.2011.2160021.

[126] C. Wang *et al.*, “0.34-THz Wireless Link Based on High-Order Modulation for Future Wireless Local Area Network Applications,” *IEEE Trans. Terahertz Sci. Technol.*, vol. 4, no. 1, pp. 75–85, Jan. 2014. doi:10.1109/TTHZ.2013.2293119.

[127] H. Alius and G. Dodel, “Amplitude-, phase-, and frequency modulation of far-infrared radiation by optical excitation of silicon,” *Infrared Phys.*, vol. 32, no. C, pp. 1–11, Jan. 1991. doi:10.1016/0020-0891(91)90090-3.

[128] T. Vogel, G. Dodel, E. Holzhauer, H. Salzmann, and A. Theurer, “High-speed switching of far-infrared radiation by photoionization in a semiconductor,” *Appl. Opt.*, vol. 31, no. 3, p. 329, 1992. doi:10.1364/ao.31.000329.

[129] R. A. Shelby, “Experimental Verification of a Negative Index of Refraction,” *Science (80-.).*, vol. 292, no. 5514, pp. 77–79, Apr. 2001. doi:10.1126/science.1058847.

[130] L. Juárez-Reyes and W. L. Mochán, “Magnetic Response of Metamaterials,” *Phys. Status Solidi Basic Res.*, vol. 255, no. 4, pp. 1351–1354, 2018. doi:10.1002/pssb.201700495.

[131] S. P. Burgos, R. De Waele, A. Polman, and H. A. Atwater, “A single-layer wide-angle negative-index metamaterial at visible frequencies,” *Nat. Mater.*, vol. 9, no. 5, pp. 407–412, 2010. doi:10.1038/nmat2747.

[132] J. B. Pendry, A. J. Holden, W. J. Stewart, and I. Youngs, “Extremely Low Frequency Plasmons in Metallic Mesostructures,” *Phys. Rev. Lett.*, vol. 76, no. 25, pp. 4773–4776, Jun. 1996. doi:10.1103/PhysRevLett.76.4773.

[133] B. B. Hu and M. C. Nuss, “Imaging with terahertz waves,” *Opt. Lett.*, vol. 20, no. 16, p. 1716, Aug. 1995. doi:10.1364/OL.20.001716.

[134] I. N. Dolganova, K. I. Zaytsev, A. A. Metelkina, and S. O. Yurchenko, “The active-passive continuous-wave terahertz imaging system,” *J. Phys. Conf. Ser.*, vol. 735, no. 1, p. 012075, Aug. 2016. doi:10.1088/1742-6596/735/1/012075.

[135] S. Augustin and H.-W. Hubers, “Phase-Sensitive Passive Terahertz Imaging at 5-m Stand-Off Distance,” *IEEE Trans. Terahertz Sci. Technol.*, vol. 4, no. 4, pp. 418–424, Jul. 2014. doi:10.1109/TTHZ.2014.2327388.

[136] Q. Wu and X. C. Zhang, “Free-space electro-optic sampling of terahertz beams,” *Appl. Phys. Lett.*, vol. 67, no. June 1998, p. 3523, 1995. doi:10.1063/1.114909.

[137] Q. Wu and X. -C. Zhang, “Free-space electro-optic sampling of terahertz beams,” *Appl. Phys. Lett.*, vol. 67, no. 24, pp. 3523–3525, Dec. 1995. doi:10.1063/1.114909.

[138] D. M. Mittleman, “Twenty years of terahertz imaging [Invited],” *Opt. Express*, vol. 26, no. 8, p. 9417, Apr. 2018. doi:10.1364/OE.26.009417.

[139] E. Hack, L. Valzania, G. Gäumann, M. Shalaby, C. Hauri, and P. Zolliker, “Comparison of Thermal Detector Arrays for Off-Axis THz Holography and Real-Time THz Imaging,” *Sensors*, vol. 16, no. 2, p. 221, Feb. 2016. doi:10.3390/s16020221.

[140] A. W. M. Lee, Q. Qin, S. Kumar, B. S. Williams, Q. Hu, and J. L. Reno, “Real-time terahertz imaging over a standoff distance (>25 meters),” *Appl. Phys. Lett.*, vol. 89, no. 14, pp. 2–5, 2006. doi:10.1063/1.2360210.

[141] R. I. Stantchev, “Non-invasive near-field THz imaging using a single pixel detector,” *PhD thesis*, no. March, 2017.

[142] W. L. Chan, K. Charan, D. Takhar, K. F. Kelly, R. G. Baraniuk, and D. M. Mittleman, “A single-pixel terahertz imaging system based on compressed sensing,” *Appl. Phys. Lett.*, vol. 93, no. 12, 2008. doi:10.1063/1.2989126.

[143] D. Shrekenhamer, C. M. Watts, and W. J. Padilla, “Terahertz single pixel imaging with an optically controlled dynamic spatial light modulator,” *Opt. Express*, vol. 21, no. 10, p. 12507, May 2013. doi:10.1364/OE.21.012507.

[144] C. M. Watts *et al.*, “Terahertz compressive imaging with metamaterial spatial light modulators,” *Nat. Photonics*, vol. 8, no. 8, pp. 605–609, Aug. 2014. doi:10.1038/nphoton.2014.139.

[145] S. Augustin, S. Frohmann, P. Jung, and H.-W. Hübers, “Mask Responses for Single-Pixel Terahertz Imaging,” *Sci. Rep.*, vol. 8, no. 1, p. 4886, Dec. 2018. doi:10.1038/s41598-018-23313-6.

[146] M. P. Edgar, G. M. Gibson, and M. J. Padgett, “Principles and prospects for single-pixel imaging,” *Nat. Photonics*, vol. 13, no. 1, pp. 13–20, Jan. 2019. doi:10.1038/s41566-018-0300-7.

[147] B. Goldluecke and D. Cremers, “Introducing total curvature for image processing,” in *2011 International Conference on Computer Vision*, 2011, pp. 1267–1274. doi:10.1109/ICCV.2011.6126378.

[148] A. Mathematics, S. Journal, and N. Analysis, “Balanced Implicit Methods for Stiff Stochastic Systems Author (s): G . N . Milstein , E . Platen , H . Schurz Published by : Society for Industrial and Applied Mathematics Stable URL : http://www.jstor.org/stable/2587119 . BALANCED IMPLICIT METHODS FOR ,” vol. 35, no. 3, pp. 1010–1019, 2011.

[149] W. K. Pratt, J. Kane, and H. C. Andrews, “Hadamard transform image coding,” *Proc. IEEE*, vol. 57, no. 1, pp. 58–68, 1969. doi:10.1109/PROC.1969.6869.

[150] Z. Zhang, X. Ma, and J. Zhong, “Single-pixel imaging by means of Fourier spectrum acquisition,” *Nat. Commun.*, vol. 6, no. 1, p. 6225, May 2015. doi:10.1038/ncomms7225.

[151] P. Klarskov, H. Kim, V. L. Colvin, and D. M. Mittleman, “Nanoscale Laser Terahertz Emission Microscopy,” *ACS Photonics*, vol. 4, no. 11, pp. 2676–2680, Nov. 2017. doi:10.1021/acsphotonics.7b00870.

[152] T. Kiwa, M. Tonouchi, M. Yamashita, and K. Kawase, “Laser terahertz-emission microscope for inspecting electrical,” *Opt. Lett.*, vol. 28, no. 21, pp. 2058–2060, 2003.

[153] M. Tonouchi, “Laser Terahertz Emission Microscope,” in *2006 Joint 31st International*

Conference on Infrared Millimeter Waves and 14th International Conference on Teraherz Electronics, 2006, vol. 9, pp. 343–343. doi:10.1109/ICIMW.2006.368551.

[154] R. I. Stantchev *et al.*, "Noninvasive, near-field terahertz imaging of hidden objects using a single-pixel detector," *Sci. Adv.*, vol. 2, no. 6, p. e1600190, Jun. 2016. doi:10.1126/sciadv.1600190.

[155] Y. Ren *et al.*, "Single mode terahertz quantum cascade amplifier," *Appl. Phys. Lett.*, vol. 105, no. 14, 2014. doi:10.1063/1.4897438.

[156] C. Mauro, R. P. Green, A. Tredicucci, F. Beltram, H. E. Beere, and D. A. Ritchie, "Amplification of terahertz radiation in quantum cascade structures," *J. Appl. Phys.*, vol. 102, no. 6, p. 063101, Sep. 2007. doi:10.1063/1.2779265.

[157] T.-Y. Kao, Q. Hu, and J. L. Reno, "Perfectly phase-matched third-order distributed feedback terahertz quantum-cascade lasers," *Opt. Lett.*, vol. 37, no. 11, p. 2070, Jun. 2012. doi:10.1364/OL.37.002070.

[158] J. Xu *et al.*, "Tunable terahertz quantum cascade lasers with an external cavity," *Appl. Phys. Lett.*, vol. 91, no. 12, p. 121104, Sep. 2007. doi:10.1063/1.2786587.

[159] R. Rungsawang *et al.*, "Gain enhancement in a terahertz quantum cascade laser with parylene antireflection coatings," *Appl. Phys. Lett.*, vol. 98, no. 10, p. 3, 2011. doi:101102\r10.1063/1.3562002.

[160] A. J. Gatesman, J. Waldman, M. Ji, C. Musante, and S. Yagvesson, "An anti-reflection coating for silicon optics at terahertz frequencies," *IEEE Microw. Guid. Wave Lett.*, vol. 10, no. 7, pp. 264–266, Jul. 2000. doi:10.1109/75.856983.

[161] E. Xifré Pérez, "Design, fabrication and characterization of porous silicon multilayer optical devices," *TDX (Tesis Dr. en Xarxa)*, Dec. 2007.

[162] Y. Ren *et al.*, "Fast terahertz imaging using a quantum cascade amplifier," *Appl. Phys. Lett.*, vol. 107, no. 1, p. 011107, Jul. 2015. doi:10.1063/1.4926602.

[163] W. Zhang *et al.*, "Noise temperature and beam pattern of an NbN hot electron bolometer mixer at 5.25 THz," *J. Appl. Phys.*, vol. 108, no. 9, p. 093102, Nov. 2010. doi:10.1063/1.3503279.

[164] J. T. Keeley, "Self-Mixing in Terahertz Quantum Cascade Lasers," no. April, p. 262, 2016.

[165] R. Chhantyal-Pun *et al.*, "Gas spectroscopy with integrated frequency monitoring through self-mixing in a terahertz quantum-cascade laser," *Opt. Lett.*, vol. 43, no. 10, pp. 2225–2228, 2018.

[166] J. S. Li, W. Chen, and H. Fischer, "Quantum Cascade Laser Spectrometry Techniques: A New Trend in Atmospheric Chemistry," *Appl. Spectrosc. Rev.*, vol. 48, no. 7, pp. 523–559, Oct. 2013. doi:10.1080/05704928.2012.757232.

[167] M. S. Vitiello *et al.*, "Quantum-limited frequency fluctuations in a terahertz laser," *Nat. Photonics*, vol. 6, no. 8, pp. 525–528, Aug. 2012. doi:10.1038/nphoton.2012.145.

[168] H. M. PICKETT, R. L. POYNTER, E. A. COHEN, M. L. DELITSKY, J. C. PEARSON, and H. S. P. MÜLLER, "SUBMILLIMETER, MILLIMETER, AND MICROWAVE SPECTRAL LINE CATALOG," *J. Quant. Spectrosc. Radiat. Transf.*, vol. 60, no. 5, pp. 883–890, Nov. 1998. doi:10.1016/S0022-4073(98)00091-0.

[169] "HITRAN online." [Online]. Available: https://hitran.org/.

[170] M. Šimečková, D. Jacquemart, L. S. Rothman, R. R. Gamache, and A. Goldman, "Einstein A-coefficients and statistical weights for molecular absorption transitions in the HITRAN database," *J. Quant. Spectrosc. Radiat. Transf.*, vol. 98, no. 1, pp. 130–155, Mar. 2006. doi:10.1016/j.jqsrt.2005.07.003.

[171] "Temperature and pressure dependence of the line width." [Online]. Available: https://hitran.org/docs/definitions-and-units/.

[172] L. Mahler *et al.*, "High-performance operation of single-mode terahertz quantum cascade lasers with metallic gratings," *Appl. Phys. Lett.*, vol. 87, no. 18, p. 181101, Oct. 2005. doi:10.1063/1.2120901.

[173] F. Compagnone, A. Di Carlo, and P. Lugli, "Monte Carlo simulation of electron dynamics in superlattice quantum cascade lasers," *Appl. Phys. Lett.*, vol. 80, no. 6, pp. 920–922, Feb. 2002. doi:10.1063/1.1448664.

[174] L. H. Li *et al.*, "Broadband heterogeneous terahertz frequency quantum cascade laser," *Electron. Lett.*, vol. 54, no. 21, pp. 1229–1231, Oct. 2018. doi:10.1049/el.2018.6062.

[175] G. Scalari, M. I. Amanti, R. Terazzi, C. Walther, M. Beck, and J. Faist, "Broadband THz lasing from a photon-phonon quantum cascade structure emitting from 2.8 to 4.1 THz," in *Optics InfoBase Conference Papers*, 2010, vol. 18, no. 8, p. CTuMM4. doi:10.1364/cleo.2010.ctumm4.

[176] D. Turčinková, G. Scalari, F. Castellano, M. I. Amanti, M. Beck, and J. Faist, "Ultra-broadband heterogeneous quantum cascade laser emitting from 2.2 to 3.2 THz," *Appl. Phys. Lett.*, vol. 99, no. 19, p. 191104, Nov. 2011. doi:10.1063/1.3658874.

[177] W. Terashima and H. Hirayama, "GaN/AlGaN based quantum cascade laser structures emitting at 1.3-2.8 THz," in *Pacific Rim Conference on Lasers and Electro-Optics, CLEO - Technical Digest*, 2013, pp. 1–2. doi:10.1109/CLEOPR.2013.6600216.

[178] J. Kröll, J. Darmo, and K. Unterrainer, "Metallic wave-impedance matching layers for broadband terahertz optical systems," *Opt. Express*, vol. 15, no. 11, p. 6552, 2007. doi:10.1364/OE.15.006552.

[179] A. Thoman, A. Kern, H. Helm, and M. Walther, "Nanostructured gold films as broadband terahertz antireflection coatings," *Phys. Rev. B*, vol. 77, no. 19, p. 195405, May 2008. doi:10.1103/PhysRevB.77.195405.

[180] G. Brooker, *Modern classical optics*, vol. 8. Oxford University Press, 2003.

[181] Y. W. Chen and X.-C. Zhang, "Anti-reflection implementations for terahertz waves," *Front. Optoelectron.*, vol. 7, no. 2, pp. 243–262, 2013. doi:10.1007/s12200-013-0377-z.

[182] S. Barbieri, J. Alton, H. E. Beere, J. Fowler, E. H. Linfield, and D. A. Ritchie, "2.9THz quantum cascade lasers operating up to 70K in continuous wave," *Appl. Phys. Lett.*, vol. 85, no. 10, pp. 1674–1676, Sep. 2004. doi:10.1063/1.1784874.

[183] T. O. Klaassen *et al.*, "How to manipulate the frequency of a terahertz quantum cascade laser," *IRMMW-THz2007 - Conf. Dig. Jt. 32nd Int. Conf. Infrared Millimetre Waves, 15th Int. Conf. Terahertz Electron.*, pp. 955–956, 2007. doi:10.1109/icimw.2007.4516808.

[184] J. R. Freeman, O. P. Marshall, H. E. Beere, and D. A. Ritchie, "Electrically switchable emission in terahertz quantum cascade lasers," *Opt. Express*, vol. 16, no. 24, p. 19830, Nov. 2008. doi:10.1364/OE.16.019830.

[185] L. Lever *et al.*, "Terahertz ambipolar dual-wavelength quantum cascade laser," *Opt. Express*, vol. 17, no. 22, p. 19926, Oct. 2009. doi:10.1364/OE.17.019926.

[186] S. P. Khanna, M. Salih, P. Dean, A. G. Davies, and E. H. Linfield, "Electrically tunable terahertz quantum-cascade laser with a heterogeneous active region," *Appl. Phys. Lett.*, vol. 95, no. 18, p. 181101, Nov. 2009. doi:10.1063/1.3253714.

[187] G. Scalari, M. I. Amanti, C. Walther, R. Terazzi, M. Beck, and J. Faist, "Broadband THz lasing from a photon-phonon quantum cascade structure," *Opt. Express*, vol. 18, no. 8, p. 8043, Apr. 2010. doi:10.1364/OE.18.008043.

[188] T.-Y. Kao, Q. Hu, and J. L. Reno, "Phase-locked arrays of surface-emitting terahertz quantum-cascade lasers," *Appl. Phys. Lett.*, vol. 96, no. 10, p. 101106, Mar. 2010. doi:10.1063/1.3358134.

[189] J. D. Cooper *et al.*, "Surface acoustic wave modulation of quantum cascade lasers," in *2013 International Conference on Advanced Optoelectronics and Lasers (CAOL 2013)*, 2013, pp. 22–24. doi:10.1109/CAOL.2013.6657513.

[190] Q. Qin, B. S. Williams, S. Kumar, J. L. Reno, and Q. Hu, "Tuning a terahertz wire laser," *Nat. Photonics*, vol. 3, no. 12, pp. 732–737, Dec. 2009. doi:10.1038/nphoton.2009.218.

[191] S. Chakraborty, O. P. Marshall, T. G. Folland, Y. J. Kim, A. N. Grigorenko, and K. S. Novoselov, "Applied optics: Gain modulation by graphene plasmons in aperiodic lattice lasers," *Science (80-.).*, vol. 351, no. 6270, pp. 246–248, Jan. 2016. doi:10.1126/science.aad2930.

[192] Q. Y. Lu, N. Bandyopadhyay, S. Slivken, Y. Bai, and M. Razeghi, "Widely tuned room temperature terahertz quantum cascade laser sources based on difference-frequency generation," *Appl. Phys. Lett.*, vol. 101, no. 25, p. 251121, Dec. 2012. doi:10.1063/1.4773189.

[193] K. Vijayraghavan *et al.*, "Broadly tunable terahertz generation in mid-infrared quantum cascade lasers.," *Nat. Commun.*, vol. 4, no. May, p. 2021, 2013. doi:10.1038/ncomms3021.

[194] M. S. Vitiello and A. Tredicucci, "Tunable Emission in THz Quantum Cascade Lasers,"

IEEE Trans. Terahertz Sci. Technol., vol. 1, no. 1, pp. 76–84, Sep. 2011. doi:10.1109/TTHZ.2011.2159543.

[195] A. W. M. Lee, B. S. Williams, S. Kumar, Q. Hu, and J. L. Reno, "Tunable terahertz quantum cascade lasers with external gratings," *Opt. Lett.*, vol. 35, no. 7, p. 910, Apr. 2010. doi:10.1364/OL.35.000910.

[196] D. Rabanus *et al.*, "Phase locking of a 15 Terahertz quantum cascade laser and use as a local oscillator in a heterodyne HEB receiver," *Opt. Express*, vol. 17, no. 3, p. 1159, Feb. 2009. doi:10.1364/OE.17.001159.

[197] R. Eichholz, H. Richter, M. Wienold, L. Schrottke, H. T. Grahn, and H.-W. Hubers, "High-frequency modulation spectroscopy with a THz quantum-cascade laser," in *2013 38th International Conference on Infrared, Millimeter, and Terahertz Waves (IRMMW-THz)*, 2013, vol. 21, no. 26, pp. 1–2. doi:10.1109/IRMMW-THz.2013.6665539.

[198] E. F. Van Dishoeck and A. G. G. M. Tielens, "Space-borne observations of the life cycle of interstellar gas and dust," in *The Century of Space Science*, Springer, 2001, pp. 607–645.

[199] P. Patimisco *et al.*, "A quartz enhanced photo-acoustic gas sensor based on a custom tuning fork and a terahertz quantum cascade laser," *Analyst*, vol. 139, no. 9, pp. 2079–2087, 2014. doi:10.1039/C3AN01219K.

[200] S. Koenig *et al.*, "Wireless sub-THz communication system with high data rate," *Nat. Photonics*, vol. 7, no. 12, pp. 977–981, Dec. 2013. doi:10.1038/nphoton.2013.275.

[201] R. Nelander and A. Wacker, "Temperature dependence of the gain profile for terahertz quantum cascade lasers," *Appl. Phys. Lett.*, vol. 92, no. 8, p. 081102, Feb. 2008. doi:10.1063/1.2884686.

[202] Y. Ren *et al.*, "Frequency and amplitude stabilized terahertz quantum cascade laser as local oscillator," *Appl. Phys. Lett.*, vol. 101, no. 10, p. 101111, Sep. 2012. doi:10.1063/1.4751247.

[203] D. M. Slocum, E. J. Slingerland, R. H. Giles, and T. M. Goyette, "Atmospheric absorption of terahertz radiation and water vapor continuum effects," *J. Quant. Spectrosc. Radiat. Transf.*, vol. 127, pp. 49–63, Sep. 2013. doi:10.1016/j.jqsrt.2013.04.022.

[204] H. Richter *et al.*, "Submegahertz frequency stabilization of a terahertz quantum cascade laser to a molecular absorption line," *Appl. Phys. Lett.*, vol. 96, no. 7, p. 071112, Feb. 2010. doi:10.1063/1.3324703.

[205] D. S. Jessop *et al.*, "Graphene based plasmonic terahertz amplitude modulator operating above 100 MHz," *Appl. Phys. Lett.*, vol. 108, no. 17, p. 171101, Apr. 2016. doi:10.1063/1.4947596.

[206] A. H. Castro Neto, F. Guinea, N. M. R. Peres, K. S. Novoselov, and A. K. Geim, "The electronic properties of graphene," *Rev. Mod. Phys.*, vol. 81, no. 1, pp. 109–162, Jan.

2009. doi:10.1103/RevModPhys.81.109.

[207] R. Degl'Innocenti, S. J. Kindness, H. E. Beere, and D. A. Ritchie, "All-integrated terahertz modulators," *Nanophotonics*, vol. 7, no. 1, pp. 127–144, 2018. doi:10.1515/nanoph-2017-0040.

[208] D. Schurig, J. J. Mock, and D. R. Smith, "Electric-field-coupled resonators for negative permittivity metamaterials," *Appl. Phys. Lett.*, vol. 88, no. 4, p. 041109, Jan. 2006. doi:10.1063/1.2166681.

[209] F. Valmorra *et al.*, "Low-Bias Active Control of Terahertz Waves by Coupling Large-Area CVD Graphene to a Terahertz Metamaterial," *Nano Lett.*, vol. 13, no. 7, pp. 3193–3198, Jul. 2013. doi:10.1021/nl4012547.

[210] R. Degl'Innocenti *et al.*, "Low-Bias Terahertz Amplitude Modulator Based on Split-Ring Resonators and Graphene," *ACS Nano*, vol. 8, no. 3, pp. 2548–2554, Mar. 2014. doi:10.1021/nn406136c.

[211] S. Hofmann, P. Braeuninger-Weimer, and R. S. Weatherup, "CVD-Enabled Graphene Manufacture and Technology," *J. Phys. Chem. Lett.*, vol. 6, no. 14, pp. 2714–2721, Jul. 2015. doi:10.1021/acs.jpclett.5b01052.

[212] K. Kreher, "Fundamentals of Semiconductors – Physics and Materials Properties," *Zeitschrift für Phys. Chemie*, vol. 198, no. Part_1_2, pp. 275–275, Jan. 1997. doi:10.1524/zpch.1997.198.Part_1_2.275.

[213] M. A. Ordal, R. J. Bell, R. W. Alexander, L. A. Newquist, and M. R. Querry, "Optical properties of Al, Fe, Ti, Ta, W, and Mo at submillimeter wavelengths," *Appl. Opt.*, vol. 27, no. 6, p. 1203, Mar. 1988. doi:10.1364/ao.27.001203.

[214] M. A. Ordal, R. J. Bell, R. W. Alexander, L. L. Long, and M. R. Querry, "Optical properties of fourteen metals in the infrared and far infrared: Al, Co, Cu, Au, Fe, Pb, Mo, Ni, Pd, Pt, Ag, Ti, V, and W," *Appl. Opt.*, vol. 24, no. 24, p. 4493, Dec. 1985. doi:10.1364/AO.24.004493.

[215] D. Jessop, "Terahertz Amplitude Modulators Based on Metamaterials and Graphene," PhD thesis, University of Cambridge, 2016.

[216] J. A. Alexander-Webber *et al.*, "Encapsulation of graphene transistors and vertical device integration by interface engineering with atomic layer deposited oxide," *2D Mater.*, vol. 4, no. 1, p. 011008, Nov. 2016. doi:10.1088/2053-1583/4/1/011008.

[217] R. Degl'Innocenti *et al.*, "Fast Room-Temperature Detection of Terahertz Quantum Cascade Lasers with Graphene-Loaded Bow-Tie Plasmonic Antenna Arrays," *ACS Photonics*, vol. 3, no. 10, pp. 1747–1753, Oct. 2016. doi:10.1021/acsphotonics.6b00405.

[218] R. Degl'Innocenti *et al.*, "Bolometric detection of terahertz quantum cascade laser radiation with graphene-plasmonic antenna arrays," *J. Phys. D. Appl. Phys.*, vol. 50, no. 17, p. 174001, May 2017. doi:10.1088/1361-6463/aa64bf.

[219] B. Wei *et al.*, "Amplitude stabilization and active control of a terahertz quantum cascade

laser with a graphene loaded split-ring-resonator array," *Appl. Phys. Lett.*, vol. 112, no. 20, May 2018. doi:10.1063/1.5027687.

[220] Ieee, "IEEE Standard Specification Format Guide and Test Procedure for Single –Axis Interferometric Fiber Optic Gyros," 1998. doi:10.1109/IEEESTD.1998.86153.

[221] L. Novotny and B. Hecht, *Principles of nano-optics*. Cambridge university press, 2012.

[222] S. Mastel, "Enhancing resolution, efficiency, and understanding in IR and THz near-field microscopy," 2018.

[223] P. Alonso-González *et al.*, "Acoustic terahertz graphene plasmons revealed by photocurrent nanoscopy," *Nat. Nanotechnol.*, vol. 12, no. 1, pp. 31–35, 2016. doi:10.1038/nnano.2016.185.

[224] J. Chen *et al.*, "Optical nano-imaging of gate-tunable graphene plasmons," *Nature*, vol. 487, no. 7405, pp. 77–81, Jul. 2012. doi:10.1038/nature11254.

[225] M. Schnell *et al.*, "Real-Space Mapping of the Chiral Near-Field Distributions in Spiral Antennas and Planar Metasurfaces," *Nano Lett.*, vol. 16, no. 1, pp. 663–670, Jan. 2016. doi:10.1021/acs.nanolett.5b04416.

[226] A. Y. Nikitin *et al.*, "Real-space mapping of tailored sheet and edge plasmons in graphene nanoresonators," *Nat. Photonics*, vol. 10, no. 4, pp. 239–243, Apr. 2016. doi:10.1038/nphoton.2016.44.

[227] R. L. Milot *et al.*, "Charge-Carrier Dynamics in 2D Hybrid Metal–Halide Perovskites," *Nano Lett.*, vol. 16, no. 11, pp. 7001–7007, Nov. 2016. doi:10.1021/acs.nanolett.6b03114.

[228] O. V. Yazyev and Y. P. Chen, "Polycrystalline graphene and other two-dimensional materials," *Nat. Nanotechnol.*, vol. 9, no. 10, pp. 755–767, Oct. 2014. doi:10.1038/nnano.2014.166.

[229] A. J. Huber, F. Keilmann, J. Wittborn, J. Aizpurua, and R. Hillenbrand, "Terahertz Near-Field Nanoscopy of Mobile Carriers in Single Semiconductor Nanodevices," *Nano Lett.*, vol. 8, no. 11, pp. 3766–3770, Nov. 2008. doi:10.1021/nl802086x.

[230] E. H. K. Stelzer, "Beyond the diffraction limit?," *Nature*, vol. 417, no. 6891, pp. 806–807, Jun. 2002. doi:10.1038/417806a.

[231] J. W. Dobrucki and U. Kubitscheck, "Fluorescence Microscopy," in *Fluorescence Microscopy*, vol. 2, no. 12, Weinheim, Germany: Wiley-VCH Verlag GmbH & Co. KGaA, 2017, pp. 85–132. doi:10.1002/9783527687732.ch3.

[232] J. B. Pawley, "Fundamental Limits in Confocal Microscopy," in *Handbook Of Biological Confocal Microscopy*, Boston, MA: Springer US, 2006, pp. 20–42. doi:10.1007/978-0-387-45524-2_2.

[233] M. G. L. Gustafsson, D. A. Agard, and J. W. Sedat, "1999_I5M - 3D widefield light microscopy with better than 100 nm axial resolution.pdf," vol. 195, no. March, pp. 10–16, 1999.

[234] J. BEWERSDORF, R. SCHMIDT, and S. W. HELL, “Comparison of I5M and 4Pi-microscopy,” *J. Microsc.*, vol. 222, no. 2, pp. 105–117, May 2006. doi:10.1111/j.1365-2818.2006.01578.x.

[235] “Beyond the diffraction limit,” *Nat. Photonics*, vol. 3, no. 7, pp. 361–361, Jul. 2009. doi:10.1038/nphoton.2009.100.

[236] S. W. Hell, “Toward fluorescence nanoscopy,” *Nat. Biotechnol.*, vol. 21, no. 11, pp. 1347–1355, Nov. 2003. doi:10.1038/nbt895.

[237] S. W. Hell, “Far-Field Optical Nanoscopy,” *Science (80-.).*, vol. 316, no. 5828, pp. 1153–1158, May 2007. doi:10.1126/science.1137395.

[238] S. Kawata, Y. Inouye, and P. Verma, “Plasmonics for near-field nano-imaging and superlensing,” *Nat. Photonics*, vol. 3, no. 7, pp. 388–394, Jul. 2009. doi:10.1038/nphoton.2009.111.

[239] I. I. Smolyaninov, C. C. Davis, J. Elliott, and A. V. Zayats, “Resolution enhancement of a surface immersion microscope near the plasmon resonance,” *Opt. Lett.*, vol. 30, no. 4, p. 382, Feb. 2005. doi:10.1364/OL.30.000382.

[240] E. Betzig and J. K. Trautman, “Near-Field Optics: Microscopy, Spectroscopy, and Surface Modification Beyond the Diffraction Limit,” *Science (80-.).*, vol. 257, no. 5067, pp. 189–195, Jul. 1992. doi:10.1126/science.257.5067.189.

[241] E. A. Ash and G. Nicholls, “Super-resolution aperture scanning microscope,” *Nature*, vol. 237, no. 5357, pp. 510–512, Jun. 1972. doi:10.1038/237510a0.

[242] S. Hunsche, M. Koch, I. Brener, and M. . Nuss, “THz near-field imaging,” *Opt. Commun.*, vol. 150, no. 1–6, pp. 22–26, May 1998. doi:10.1016/S0030-4018(98)00044-3.

[243] O. Mitrofanov *et al.*, “Collection-mode near-field imaging with 0.5-THz pulses,” *IEEE J. Sel. Top. Quantum Electron.*, vol. 7, no. 4, pp. 600–607, 2001. doi:10.1109/2944.974231.

[244] Y. Inouye and S. Kawata, “Near-field scanning optical microscope with a metallic probe tip,” *Opt. Lett.*, vol. 19, no. 3, p. 159, Feb. 1994. doi:10.1364/OL.19.000159.

[245] G. Binnig, H. Rohrer, C. Gerber, and E. Weibel, “Surface Studies by Scanning Tunneling Microscopy,” *Phys. Rev. Lett.*, vol. 49, no. 1, pp. 57–61, Jul. 1982. doi:10.1103/PhysRevLett.49.57.

[246] G. Binnig, C. F. Quate, and C. Gerber, “Atomic Force Microscope,” *Phys. Rev. Lett.*, vol. 56, no. 9, pp. 930–933, Mar. 1986. doi:10.1103/PhysRevLett.56.930.

[247] G. Meyer and N. M. Amer, “Novel optical approach to atomic force microscopy,” *Appl. Phys. Lett.*, vol. 53, no. 12, pp. 1045–1047, Sep. 1988. doi:10.1063/1.100061.

[248] L. Zhou, M. Cai, T. Tong, and H. Wang, “Progress in the Correlative Atomic Force Microscopy and Optical Microscopy,” *Sensors*, vol. 17, no. 4, p. 938, Apr. 2017. doi:10.3390/s17040938.

[249] P. Eaton and P. West, *Atomic force microscopy*. Oxford university press, 2010.

[250] L. Gross, F. Mohn, N. Moll, P. Liljeroth, and G. Meyer, "The Chemical Structure of a Molecule Resolved by Atomic Force Microscopy," *Science (80-.).*, vol. 325, no. 5944, pp. 1110–1114, Aug. 2009. doi:10.1126/science.1176210.

[251] Q. Zhong, D. Inniss, K. Kjoller, and V. B. Elings, "Fractured polymer/silica fiber surface studied by tapping mode atomic force microscopy," *Surf. Sci.*, vol. 290, no. 1–2, pp. L688–L692, Jun. 1993. doi:10.1016/0039-6028(93)90582-5.

[252] R. HillenbRand, B. Knoll, and F. Keilmann, "Pure optical contrast in scattering-type scanning near-field microscopy," *J. Microsc.*, vol. 202, no. 1, pp. 77–83, Apr. 2001. doi:10.1046/j.1365-2818.2001.00794.x.

[253] F. Keilmann and R. Hillenbrand, "Near-field microscopy by elastic light scattering from a tip," *Philos. Trans. R. Soc. London. Ser. A Math. Phys. Eng. Sci.*, vol. 362, no. 1817, pp. 787–805, Apr. 2004. doi:10.1098/rsta.2003.1347.

[254] B. Knoll and F. Keilmann, "Near-field probing of vibrational absorption for chemical microscopy," *Nature*, vol. 399, no. 6732, pp. 134–137, May 1999. doi:10.1038/20154.

[255] L. M. Zhang *et al.*, "Near-field spectroscopy of silicon dioxide thin films," *Phys. Rev. B*, vol. 85, no. 7, p. 075419, Feb. 2012. doi:10.1103/PhysRevB.85.075419.

[256] A. Cvitkovic, N. Ocelic, and R. Hillenbrand, "Analytical model for quantitative prediction of material contrasts in scattering-type near-field optical microscopy," *Opt. Express*, vol. 15, no. 14, p. 8550, 2007. doi:10.1364/oe.15.008550.

[257] M. A. Ordal *et al.*, "Optical properties of the metals Al, Co, Cu, Au, Fe, Pb, Ni, Pd, Pt, Ag, Ti, and W in the infrared and far infrared," *Appl. Opt.*, vol. 22, no. 7, p. 1099, Apr. 1983. doi:10.1364/AO.22.001099.

[258] H. Cheon, H. Yang, S.-H. Lee, Y. A. Kim, and J.-H. Son, "Terahertz molecular resonance of cancer DNA," *Sci. Rep.*, vol. 6, no. 1, p. 37103, Dec. 2016. doi:10.1038/srep37103.

[259] W. L. Chan, J. Deibel, and D. M. Mittleman, "Imaging with terahertz radiation," *Reports Prog. Phys.*, vol. 70, no. 8, pp. 1325–1379, Aug. 2007. doi:10.1088/0034-4885/70/8/R02.

[260] A. A. Govyadinov, S. Mastel, F. Golmar, A. Chuvilin, P. S. Carney, and R. Hillenbrand, "Recovery of Permittivity and Depth from Near-Field Data as a Step toward Infrared Nanotomography," *ACS Nano*, vol. 8, no. 7, pp. 6911–6921, Jul. 2014. doi:10.1021/nn5016314.

[261] E. A. Muller, B. Pollard, and M. B. Raschke, "Infrared Chemical Nano-Imaging: Accessing Structure, Coupling, and Dynamics on Molecular Length Scales," *J. Phys. Chem. Lett.*, vol. 6, no. 7, pp. 1275–1284, Apr. 2015. doi:10.1021/acs.jpclett.5b00108.

[262] H. A. Bechtel, E. A. Muller, R. L. Olmon, M. C. Martin, and M. B. Raschke, "Ultrabroadband infrared nanospectroscopic imaging," *Proc. Natl. Acad. Sci.*, vol. 111,

no. 20, pp. 7191–7196, May 2014. doi:10.1073/pnas.1400502111.

[263] F. Huth, A. Govyadinov, S. Amarie, W. Nuansing, F. Keilmann, and R. Hillenbrand, "Nano-FTIR Absorption Spectroscopy of Molecular Fingerprints at 20 nm Spatial Resolution," *Nano Lett.*, vol. 12, no. 8, pp. 3973–3978, Aug. 2012. doi:10.1021/nl301159v.

[264] S. Dai *et al.*, "Tunable Phonon Polaritons in Atomically Thin van der Waals Crystals of Boron Nitride," *Science (80-.).*, vol. 343, no. 6175, pp. 1125–1129, Mar. 2014. doi:10.1126/science.1246833.

[265] D. N. Basov, M. M. Fogler, and F. J. Garcia de Abajo, "Polaritons in van der Waals materials," *Science (80-.).*, vol. 354, no. 6309, pp. aag1992–aag1992, Oct. 2016. doi:10.1126/science.aag1992.

[266] Z. Fei *et al.*, "Gate-tuning of graphene plasmons revealed by infrared nano-imaging," *Nature*, vol. 487, no. 7405, pp. 82–85, Jul. 2012. doi:10.1038/nature11253.

[267] M. M. Qazilbash *et al.*, "Mott Transition in VO2 Revealed by Infrared Spectroscopy and Nano-Imaging," *Science (80-.).*, vol. 318, no. 5857, pp. 1750–1753, Dec. 2007. doi:10.1126/science.1150124.

[268] A. C. Jones, S. Berweger, J. Wei, D. Cobden, and M. B. Raschke, "Nano-optical Investigations of the Metal−Insulator Phase Behavior of Individual VO 2 Microcrystals," *Nano Lett.*, vol. 10, no. 5, pp. 1574–1581, May 2010. doi:10.1021/nl903765h.

[269] F. Sterl, H. Linnenbank, T. Steinle, F. Mörz, N. Strohfeldt, and H. Giessen, "Nanoscale Hydrogenography on Single Magnesium Nanoparticles," *Nano Lett.*, vol. 18, no. 7, pp. 4293–4302, Jul. 2018. doi:10.1021/acs.nanolett.8b01277.

[270] M. Liu, A. J. Sternbach, and D. N. Basov, "Nanoscale electrodynamics of strongly correlated quantum materials," *Reports Prog. Phys.*, vol. 80, no. 1, p. 014501, Jan. 2017. doi:10.1088/0034-4885/80/1/014501.

[271] H. A. Bethe, "Theory of Diffraction by Small Holes," *Phys. Rev.*, vol. 66, no. 7–8, pp. 163–182, Oct. 1944. doi:10.1103/PhysRev.66.163.

[272] O. Mitrofanov *et al.*, "Near-field terahertz probes with room-temperature nanodetectors for subwavelength resolution imaging," *Sci. Rep.*, vol. 7, no. 1, p. 44240, May 2017. doi:10.1038/srep44240.

[273] H.-T. Chen, R. Kersting, and G. C. Cho, "Terahertz imaging with nanometer resolution," *Appl. Phys. Lett.*, vol. 83, no. 15, pp. 3009–3011, Oct. 2003. doi:10.1063/1.1616668.

[274] P. Dean *et al.*, "Apertureless near-field terahertz imaging using the self-mixing effect in a quantum cascade laser," *Appl. Phys. Lett.*, vol. 108, no. 9, 2016. doi:10.1063/1.4943088.

[275] R. Degl'Innocenti *et al.*, "Terahertz Nanoscopy of Plasmonic Resonances with a Quantum Cascade Laser," *ACS Photonics*, vol. 4, no. 9, pp. 2150–2157, Sep. 2017. doi:10.1021/acsphotonics.7b00687.

[276] B. Wei *et al.*, “Terahertz s-SNOM with > λ/1000 resolution based on self-mixing in quantum cascade lasers,” in *2017 Conference on Lasers and Electro-Optics Europe & European Quantum Electronics Conference (CLEO/Europe-EQEC)*, 2017, vol. Part F82-C, pp. 1–1. doi:10.1109/CLEOE-EQEC.2017.8086433.

[277] K. Moon *et al.*, “Subsurface Nanoimaging by Broadband Terahertz Pulse Near-Field Microscopy,” *Nano Lett.*, vol. 15, no. 1, pp. 549–552, Jan. 2015. doi:10.1021/nl503998v.

[278] R. Degl’Innocenti *et al.*, “Differential Near-Field Scanning Optical Microscopy with THz quantum cascade laser sources,” *Opt. Express*, vol. 17, no. 26, p. 23785, Dec. 2009. doi:10.1364/OE.17.023785.

[279] I. Koga, “Tuning fork made of quartz crystal,” *J. Inst. Electr. Eng. Jpn.*, vol. 48, pp. 100–101, 1928.

[280] E. Momosaki, “A brief review of progress in quartz tuning fork resonators,” in *Proceedings of International Frequency Control Symposium*, 1997, pp. 552–565. doi:10.1109/FREQ.1997.638700.

[281] J.-M. Friedt and É. Carry, “Introduction to the quartz tuning fork,” *Am. J. Phys.*, vol. 75, no. 5, pp. 415–422, May 2007. doi:10.1119/1.2711826.

[282] A. You, M. A. Y. Be, and I. In, “Atomic resolution with an atomic force microscope using piezoresistive detection,” vol. 834, no. October 1992, 1998. doi:10.1063/1.108593.

[283] J. Rychen, T. Ihn, P. Studerus, A. Herrmann, and K. Ensslin, “A low-temperature dynamic mode scanning force microscope operating in high magnetic fields,” *Rev. Sci. Instrum.*, vol. 70, no. 6, pp. 2765–2768, Jun. 1999. doi:10.1063/1.1149842.

[284] K. Karrai and R. D. Grober, “Piezoelectric tip-sample distance control for near field optical microscopes,” *Appl. Phys. Lett.*, vol. 66, no. 14, pp. 1842–1844, Apr. 1995. doi:10.1063/1.113340.

[285] F. J. Giessibl, “Atomic resolution on Si(111)-(7×7) by noncontact atomic force microscopy with a force sensor based on a quartz tuning fork,” *Appl. Phys. Lett.*, vol. 76, no. 11, pp. 1470–1472, Mar. 2000. doi:10.1063/1.126067.

[286] P. Günther, U. C. Fischer, and K. Dransfeld, “Scanning near-field acoustic microscopy,” *Appl. Phys. B Photophysics Laser Chem.*, vol. 48, no. 1, pp. 89–92, Jan. 1989. doi:10.1007/BF00694423.

[287] T. D. Rossing, D. A. Russell, and D. E. Brown, “On the acoustics of tuning forks,” *Am. J. Phys.*, vol. 60, no. 7, pp. 620–626, Jul. 1992. doi:10.1119/1.17116.

[288] J. H. Staudte, “Subminiature Quartz Tuning Fork Resonator,” in *27th Annual Symposium on Frequency Control*, 1973, pp. 50–54. doi:10.1109/FREQ.1973.199941.

[289] J. A. Kusters, C. A. Adams, H. E. Karrer, and R. W. Ward, “Analytical and Experimental Investigations of 32KHz Quartz Tuning Forks,” in *30th Annual Symposium on Frequency Control*, 1976, pp. 175–183. doi:10.1109/FREQ.1976.201311.

[290] H. Itoh and T. Matsumoto, “An analysis of frequency of a quartz crystal tuning fork by

Sezawa's approximation-the effect of clamped position of its base," in *Proceedings of the 1999 Joint Meeting of the European Frequency and Time Forum and the IEEE International Frequency Control Symposium (Cat. No.99CH36313)*, 1999, vol. 1, pp. 494–500. doi:10.1109/FREQ.1999.840814.

[291] H. Itoh and T. Yuasa, "An analysis of frequency of a quartz crystal tuning fork by Sezawa's theory," in *Proceedings of the 1998 IEEE International Frequency Control Symposium (Cat. No.98CH36165)*, 1998, pp. 921–925. doi:10.1109/FREQ.1998.718009.

[292] H. Kawashima and K. Sunaga, "Analysis of frequency characteristics for flexural-mode tuning-fork type quartz crystal resonator, taking into account thickness, rotary inertia and shear force," *Electron. Commun. Japan (Part III Fundam. Electron. Sci.*, vol. 73, no. 9, pp. 49–57, 1990. doi:10.1002/ecjc.4430730906.

[293] X. Xu, J. Wang, Z. Wang, T. Ma, and J. Du, "An analysis of frequency of a quartz crystal tuning fork resonator by modifidy Sezawa's theory," in *2012 Symposium on Piezoelectricity, Acoustic Waves, and Device Applications (SPAWDA)*, 2012, vol. 1, pp. 274–276. doi:10.1109/SPAWDA.2012.6464087.

[294] G. Thornell, H. Rapp, and K. Hjort, "X-cut miniature tuning forks realized by ion track lithography," *IEEE Trans. Ultrason. Ferroelectr. Freq. Control*, vol. 47, no. 1, pp. 8–15, Jan. 2000. doi:10.1109/58.818744.

[295] S. Lee, Y. Moon, J. Yoon, and H. Chung, "Analytical and finite element method design of quartz tuning fork resonators and experimental test of samples manufactured using photolithography 1—significant design parameters affecting static capacitance C0," *Vacuum*, vol. 75, no. 1, pp. 57–69, Jun. 2004. doi:10.1016/j.vacuum.2003.12.156.

[296] K. S. Van Dyke, "The Piezo-Electric Resonator and Its Equivalent Network," *Proc. IRE*, vol. 16, no. 6, pp. 742–764, Jun. 1928. doi:10.1109/JRPROC.1928.221466.

[297] K. S. Van Dyke, "The Electrical Network Equivalent of a Piezo-Electric Resonator," *Phys. Rev.*, vol. 25, no. 6, p. 895, 1925.

[298] Y. Chuang, C. Wang, J. Y. Huang, and C. Pan, "Nonoptical tip–sample distance control for scanning near-field optical microscopy," *Appl. Phys. Lett.*, vol. 69, no. 22, pp. 3312–3314, Nov. 1996. doi:10.1063/1.117290.

[299] F. J. Giessibl, "A direct method to calculate tip-sample forces from frequency shifts in frequency-modulation atomic force microscopy," *Appl. Phys. Lett.*, vol. 78, no. 1, pp. 123–125, 2001. doi:10.1063/1.1335546.

[300] J. W. P. Hsu, M. Lee, and B. S. Deaver, "A nonoptical tip-sample distance control method for near-field scanning optical microscopy using impedance changes in an electromechanical system," *Rev. Sci. Instrum.*, vol. 66, no. 5, pp. 3177–3181, 1995. doi:10.1063/1.1145547.

[301] D. P. Tsai and Y. Y. Lu, "Tapping-mode tuning fork force sensing for near-field scanning optical microscopy," *Appl. Phys. Lett.*, vol. 73, no. 19, pp. 2724–2726, Nov.

1998. doi:10.1063/1.122558.

[302] R. D. Grober *et al.*, “Fundamental limits to force detection using quartz tuning forks,” *Rev. Sci. Instrum.*, vol. 71, no. 7, pp. 2776–2780, Jul. 2000. doi:10.1063/1.1150691.

[303] F. J. Giessibl, “High-speed force sensor for force microscopy and profilometry utilizing a quartz tuning fork,” *Appl. Phys. Lett.*, vol. 73, no. 26, pp. 3956–3958, Dec. 1998. doi:10.1063/1.122948.

[304] H. Edwards, L. Taylor, W. Duncan, and A. J. Melmed, “Fast, high-resolution atomic force microscopy using a quartz tuning fork as actuator and sensor,” *J. Appl. Phys.*, vol. 82, no. 3, pp. 980–984, Aug. 1997. doi:10.1063/1.365936.

[305] L. González, R. Oria, L. Botaya, M. Puig-Vidal, and J. Otero, “Determination of the static spring constant of electrically-driven quartz tuning forks with two freely oscillating prongs,” *Nanotechnology*, vol. 26, no. 5, p. 055501, Feb. 2015. doi:10.1088/0957-4484/26/5/055501.

[306] W. H. J. Rensen, N. F. van Hulst, A. G. T. Ruiter, and P. E. West, “Atomic steps with tuning-fork-based noncontact atomic force microscopy,” *Appl. Phys. Lett.*, vol. 75, no. 11, pp. 1640–1642, Sep. 1999. doi:10.1063/1.124780.

[307] T. R. Albrecht, P. Grütter, D. Horne, and D. Rugar, “Frequency modulation detection using high- Q cantilevers for enhanced force microscope sensitivity,” *J. Appl. Phys.*, vol. 69, no. 2, pp. 668–673, Jan. 1991. doi:10.1063/1.347347.

[308] S. Lee, J. Lee, and H. Chung, “Development of SMD 32.768 kHz tuning fork-type crystals,” *Zeitschrift für Met.*, vol. 94, no. 9, pp. 1027–1033, Sep. 2003. doi:10.3139/146.031027.

[309] M. Gauthier, R. Pérez, T. Arai, M. Tomitori, and M. Tsukada, “Interplay between Nonlinearity, Scan Speed, Damping, and Electronics in Frequency Modulation Atomic-Force Microscopy,” *Phys. Rev. Lett.*, vol. 89, no. 14, p. 146104, Sep. 2002. doi:10.1103/PhysRevLett.89.146104.

[310] Robert Wallis, “Novel THz technologies: waveguiding, imaging, and near-field microscopy,” PhD thesis, University of Cambridge, 2017.

[311] B. Knoll and F. Keilmann, “Enhanced dielectric contrast in scattering-type scanning near-field optical microscopy,” *Opt. Commun.*, vol. 182, no. 4–6, pp. 321–328, Aug. 2000. doi:10.1016/S0030-4018(00)00826-9.

[312] “No Title.” [Online]. Available: https://www.thorlabs.com/newgrouppage9.cfm?objectgroup_id=1129.

[313] “No Title.” [Online]. Available: https://www.newport.com/f/S-2000A-pneumatic-isolators-tie-bar.

[314] “No Title.” [Online]. Available: http://www.herz-f.co.jp/product/docs/TS English 2016.pdf.

[315] Y. L. Lim *et al.*, “Coherent imaging using laser feedback interferometry with pulsed-

mode terahertz quantum cascade lasers," *Opt. Express*, vol. 27, no. 7, p. 10221, Apr. 2019. doi:10.1364/OE.27.010221.

[316] M. Teich, M. Wagner, H. Schneider, and M. Helm, "Semiconductor quantum well excitons in strong, narrowband terahertz fields," *New J. Phys.*, vol. 15, no. 6, p. 065007, Jun. 2013. doi:10.1088/1367-2630/15/6/065007.

[317] G. Keiser and P. Klarskov, "Terahertz Field Confinement in Nonlinear Metamaterials and Near-Field Imaging," *Photonics*, vol. 6, no. 1, p. 22, Feb. 2019. doi:10.3390/photonics6010022.

[318] L. Ju *et al.*, "Graphene plasmonics for tunable terahertz metamaterials," *Nat. Nanotechnol.*, vol. 6, no. 10, pp. 630–634, Oct. 2011. doi:10.1038/nnano.2011.146.

[319] F. H. L. Koppens, M. B. Lundeberg, M. Polini, T. Low, and P. Avouris, "Graphene Plasmonics," in *2D Materials*, no. October, P. Avouris, T. F. Heinz, and T. Low, Eds. Cambridge: Cambridge University Press, 2017, pp. 104–140. doi:10.1017/9781316681619.008.

[320] J. Zhang *et al.*, "Terahertz Nanoimaging of Graphene," *ACS Photonics*, vol. 5, no. 7, pp. 2645–2651, Jul. 2018. doi:10.1021/acsphotonics.8b00190.

[321] E. A. Zibik *et al.*, "Long lifetimes of quantum-dot intersublevel transitions in the terahertz range," *Nat. Mater.*, vol. 8, no. 10, pp. 803–807, Oct. 2009. doi:10.1038/nmat2511.

[322] A. Tredicucci, "Long life in zero dimensions," *Nat. Mater.*, vol. 8, no. 10, pp. 775–776, Oct. 2009. doi:10.1038/nmat2541.

[323] R. Jacob *et al.*, "Intersublevel Spectroscopy on Single InAs-Quantum Dots by Terahertz Near-Field Microscopy," *Nano Lett.*, vol. 12, no. 8, pp. 4336–4340, Aug. 2012. doi:10.1021/nl302078w.

[324] R. Balu, H. Zhang, E. Zukowski, J. Y. Chen, A. G. Markelz, and S. K. Gregurick, "Terahertz spectroscopy of bacteriorhodopsin and rhodopsin: Similarities and differences," *Biophys. J.*, vol. 94, no. 8, pp. 3217–3226, 2008. doi:10.1529/biophysj.107.105163.

[325] P. Dawson, F. de Fornel, and J.-P. Goudonnet, "Imaging of surface plasmon propagation and edge interaction using a photon scanning tunneling microscope," *Phys. Rev. Lett.*, vol. 72, no. 18, pp. 2927–2930, May 1994. doi:10.1103/PhysRevLett.72.2927.

[326] C. Georgi, M. Böhmler, H. Qian, L. Novotny, and A. Hartschuh, "Probing exciton propagation and quenching in carbon nanotubes with near-field optical microscopy," *Phys. status solidi*, vol. 246, no. 11–12, pp. 2683–2688, Dec. 2009. doi:10.1002/pssb.200982306.

[327] R. L. Olmon, P. M. Krenz, A. C. Jones, G. D. Boreman, and M. B. Raschke, "Near-field imaging of optical antenna modes in the mid-infrared," *Opt. Express*, vol. 16, no. 25, p. 20295, Dec. 2008. doi:10.1364/OE.16.020295.

[328] P. Ghenuche, S. Cherukulappurath, T. H. Taminiau, N. F. van Hulst, and R. Quidant, "Spectroscopic Mode Mapping of Resonant Plasmon Nanoantennas," *Phys. Rev. Lett.*, vol. 101, no. 11, p. 116805, Sep. 2008. doi:10.1103/PhysRevLett.101.116805.

[329] E. H. Hwang and S. Das Sarma, "Dielectric function, screening, and plasmons in two-dimensional graphene," *Phys. Rev. B*, vol. 75, no. 20, p. 205418, May 2007. doi:10.1103/PhysRevB.75.205418.

[330] M. Polini, R. Asgari, G. Borghi, Y. Barlas, T. Pereg-Barnea, and A. H. MacDonald, "Plasmons and the spectral function of graphene," *Phys. Rev. B*, vol. 77, no. 8, p. 081411, Feb. 2008. doi:10.1103/PhysRevB.77.081411.

[331] N. Camara *et al.*, "Current status of self-organized epitaxial graphene ribbons on the c face of 6H-SiC substrates," *J. Phys. D. Appl. Phys.*, vol. 43, no. 37, 2010. doi:10.1088/0022-3727/43/37/374011.

[332] Z. Fei *et al.*, "Edge and Surface Plasmons in Graphene Nanoribbons," *Nano Lett.*, vol. 15, no. 12, pp. 8271–8276, Dec. 2015. doi:10.1021/acs.nanolett.5b03834.

[333] K. F. Mak, J. Shan, and T. F. Heinz, "Electronic Structure of Few-Layer Graphene: Experimental Demonstration of Strong Dependence on Stacking Sequence," *Phys. Rev. Lett.*, vol. 104, no. 17, p. 176404, Apr. 2010. doi:10.1103/PhysRevLett.104.176404.

[334] H. Min, "Electronic Properties of Multilayer Graphene," no. 176, 2011, pp. 325–356. doi:10.1007/978-3-642-22984-8_11.

[335] W. Bao *et al.*, "Stacking-dependent band gap and quantum transport in trilayer graphene," *Nat. Phys.*, vol. 7, no. 12, pp. 948–952, Dec. 2011. doi:10.1038/nphys2103.

[336] L. Brown, R. Hovden, P. Huang, M. Wojcik, D. A. Muller, and J. Park, "Twinning and Twisting of Tri- and Bilayer Graphene," *Nano Lett.*, vol. 12, no. 3, pp. 1609–1615, Mar. 2012. doi:10.1021/nl204547v.

[337] M. Yankowitz *et al.*, "Electric field control of soliton motion and stacking in trilayer graphene," *Nat. Mater.*, vol. 13, no. 8, pp. 786–789, Aug. 2014. doi:10.1038/nmat3965.

[338] K. F. Mak, M. Y. Sfeir, J. A. Misewich, and T. F. Heinz, "The evolution of electronic structure in few-layer graphene revealed by optical spectroscopy," *Proc. Natl. Acad. Sci.*, vol. 107, no. 34, pp. 14999–15004, Aug. 2010. doi:10.1073/pnas.1004595107.

[339] Y. Hao *et al.*, "Probing Layer Number and Stacking Order of Few-Layer Graphene by Raman Spectroscopy," *Small*, vol. 6, no. 2, pp. 195–200, Jan. 2010. doi:10.1002/smll.200901173.

[340] A. C. Ferrari *et al.*, "Raman Spectrum of Graphene and Graphene Layers," *Phys. Rev. Lett.*, vol. 97, no. 18, p. 187401, Oct. 2006. doi:10.1103/PhysRevLett.97.187401.

[341] D. Graf *et al.*, "Spatially Resolved Raman Spectroscopy of Single- and Few-Layer Graphene," *Nano Lett.*, vol. 7, no. 2, pp. 238–242, Feb. 2007. doi:10.1021/nl061702a.

[342] D.-S. Kim *et al.*, "Stacking Structures of Few-Layer Graphene Revealed by Phase-Sensitive Infrared Nanoscopy," *ACS Nano*, vol. 9, no. 7, pp. 6765–6773, Jul. 2015.

doi:10.1021/acsnano.5b02813.

[343] E. T. Ritchie, D. J. Hill, T. M. Mastin, P. C. Deguzman, J. F. Cahoon, and J. M. Atkin, "Mapping Free-Carriers in Multijunction Silicon Nanowires Using Infrared Near-Field Optical Microscopy," *Nano Lett.*, vol. 17, no. 11, pp. 6591–6597, Nov. 2017. doi:10.1021/acs.nanolett.7b02340.

[344] O. P. Marshall, V. Apostolopoulos, J. R. Freeman, R. Rungsawang, H. E. Beere, and D. A. Ritchie, "Surface-emitting photonic crystal terahertz quantum cascade lasers," *Appl. Phys. Lett.*, vol. 93, no. 17, p. 171112, Oct. 2008. doi:10.1063/1.3012385.

[345] P. R. Kidambi *et al.*, "Observing graphene grow: Catalyst-graphene interactions during scalable graphene growth on polycrystalline copper," *Nano Lett.*, vol. 13, no. 10, pp. 4769–4778, 2013. doi:10.1021/nl4023572.

[346] A. Black, F. J. Urbanos, M. R. Osorio, R. Miranda, A. L. Vázquez de Parga, and D. Granados, "Encapsulating Chemically Doped Graphene via Atomic Layer Deposition," *ACS Appl. Mater. Interfaces*, vol. 10, no. 9, pp. 8190–8196, Mar. 2018. doi:10.1021/acsami.7b18709.

[347] A. I. Aria *et al.*, "Parameter Space of Atomic Layer Deposition of Ultrathin Oxides on Graphene," *ACS Appl. Mater. Interfaces*, vol. 8, no. 44, pp. 30564–30575, Nov. 2016. doi:10.1021/acsami.6b09596.

[348] M. C. Giordano *et al.*, "Phase-resolved terahertz self-detection near-field microscopy," *Opt. Express*, vol. 26, no. 14, p. 18423, Jul. 2018. doi:10.1364/OE.26.018423.

[349] M. Kenney, J. Grant, Y. D. Shah, I. Escorcia-Carranza, M. Humphreys, and D. R. S. Cumming, "Octave-Spanning Broadband Absorption of Terahertz Light Using Metasurface Fractal-Cross Absorbers," *ACS Photonics*, vol. 4, no. 10, pp. 2604–2612, Oct. 2017. doi:10.1021/acsphotonics.7b00906.

[350] W. P. E. M. op 't Root, G. J. H. Brussaard, P. W. Smorenburg, and O. J. Luiten, "Single-cycle surface plasmon polaritons on a bare metal wire excited by relativistic electrons," *Nat. Commun.*, vol. 7, no. 1, p. 13769, Dec. 2016. doi:10.1038/ncomms13769.

[351] K. Wang and D. M. Mittleman, "Metal wires for terahertz wave guiding," *Nature*, vol. 432, no. 7015, pp. 376–379, Nov. 2004. doi:10.1038/nature03040.

[352] T. Siday, M. Natrella, J. Wu, H. Liu, and O. Mitrofanov, "Resonant terahertz probes for near-field scattering microscopy," *Opt. Express*, vol. 25, no. 22, p. 27874, Oct. 2017. doi:10.1364/OE.25.027874.

[353] S. Mastel *et al.*, "Terahertz Nanofocusing with Cantilevered Terahertz-Resonant Antenna Tips," *Nano Lett.*, vol. 17, no. 11, pp. 6526–6533, Nov. 2017. doi:10.1021/acs.nanolett.7b01924.

[354] H. U. Yang, J. D'Archangel, M. L. Sundheimer, E. Tucker, G. D. Boreman, and M. B. Raschke, "Optical dielectric function of silver," *Phys. Rev. B*, vol. 91, no. 23, p. 235137, Jun. 2015. doi:10.1103/PhysRevB.91.235137.

[355] L. Novotny and S. J. Stranick, “NEAR-FIELD OPTICAL MICROSCOPY AND SPECTROSCOPY WITH POINTED PROBES,” *Annu. Rev. Phys. Chem.*, vol. 57, no. 1, pp. 303–331, May 2006. doi:10.1146/annurev.physchem.56.092503.141236.

[356] F. Huth *et al.*, “Resonant Antenna Probes for Tip-Enhanced Infrared Near-Field Microscopy,” *Nano Lett.*, vol. 13, no. 3, pp. 1065–1072, Mar. 2013. doi:10.1021/nl304289g.

[357] A. Sikora, T. Gotszalk, A. Sankowska, and I. Rangelow, “Application of scanning shear-force microscope for fabrication of nanostructures,” *J. Telecommun. Inf. Technol.*, vol. nr 1, pp. 81–84, 2005.

[358] S. J. Kindness *et al.*, “Active Control of Electromagnetically Induced Transparency in a Terahertz Metamaterial Array with Graphene for Continuous Resonance Frequency Tuning,” *Adv. Opt. Mater.*, Jan. 2018. doi:10.1002/adom.201800570.

[359] S. J. Kindness *et al.*, “Graphene integrated metamaterial device for all electrical polarization control of terahertz quantum cascade lasers,” *ACS Photonics*, 2019.

[360] L. Thiel *et al.*, “Quantitative nanoscale vortex imaging using a cryogenic quantum magnetometer,” *Nat. Nanotechnol.*, vol. 11, no. 8, pp. 677–681, Aug. 2016. doi:10.1038/nnano.2016.63.

[361] A. Lyakh, R. Barron-Jimenez, I. Dunayevskiy, R. Go, and C. K. N. Patel, “External cavity quantum cascade lasers with ultra rapid acousto-optic tuning,” *Appl. Phys. Lett.*, vol. 106, no. 14, p. 141101, Apr. 2015. doi:10.1063/1.4917241.

[362] A. Dunn *et al.*, “High-Speed Modulation of a Terahertz Quantum Cascade Laser Using Coherent Acoustic Phonon Pulses,” in *2019 44th International Conference on Infrared, Millimeter, and Terahertz Waves (IRMMW-THz)*, 2019, vol. 2019-Septe, pp. 1–2. doi:10.1109/IRMMW-THz.2019.8874441.

[363] Q. J. Wang, C. Pflügl, W. F. Andress, D. Ham, F. Capasso, and M. Yamanishi, “Gigahertz surface acoustic wave generation on ZnO thin films deposited by radio frequency magnetron sputtering on III-V semiconductor substrates,” *J. Vac. Sci. Technol. B Microelectron. Nanom. Struct.*, vol. 26, no. 6, pp. 1848–1851, Nov. 2008. doi:10.1116/1.2993176.

[364] B. Meng, M. Yamanishi, C. Pflugl, K. Fujita, F. Capasso, and Q. J. Wang, “Investigation of Tunable Single-Mode Quantum Cascade Lasers Via Surface-Acoustic-Wave Modulation,” *IEEE J. Quantum Electron.*, vol. 49, no. 12, pp. 1053–1061, Dec. 2013. doi:10.1109/JQE.2013.2285935.

[365] F. H. L. Koppens, T. Mueller, P. Avouris, A. C. Ferrari, M. S. Vitiello, and M. Polini, “Photodetectors based on graphene, other two-dimensional materials and hybrid systems,” *Nat. Nanotechnol.*, vol. 9, no. 10, pp. 780–793, Oct. 2014. doi:10.1038/nnano.2014.215.

[366] M. Freitag, T. Low, W. Zhu, H. Yan, F. Xia, and P. Avouris, “Photocurrent in graphene harnessed by tunable intrinsic plasmons,” *Nat. Commun.*, vol. 4, no. 1, p. 1951, Oct.

2013. doi:10.1038/ncomms2951.

[367] T. Mueller, F. Xia, and P. Avouris, “Graphene photodetectors for high-speed optical communications,” *Nat. Photonics*, vol. 4, no. 5, pp. 297–301, May 2010. doi:10.1038/nphoton.2010.40.

[368] N. Youngblood, Y. Anugrah, R. Ma, S. J. Koester, and M. Li, “Multifunctional Graphene Optical Modulator and Photodetector Integrated on Silicon Waveguides,” *Nano Lett.*, vol. 14, no. 5, pp. 2741–2746, May 2014. doi:10.1021/nl500712u.

[369] L. Xiao, “Room-Temperature Terahertz Detection Based on Graphene and Plasmonic Antenna Arrays,” PhD thesis, University of Cambridge, 2017.

[370] T. J. Cui *et al.*, “Coding metamaterials, digital metamaterials and programmable metamaterials,” *Light Sci. Appl.*, vol. 3, no. 10, pp. 1–9, 2014. doi:10.1038/lsa.2014.94.

[371] B. Zeng *et al.*, “Hybrid graphene metasurfaces for high-speed mid-infrared light modulation and single-pixel imaging,” *Light Sci. Appl.*, vol. 7, no. 1, 2018. doi:10.1038/s41377-018-0055-4.

[372] X. Zhao *et al.*, “Voltage-tunable dual-layer terahertz metamaterials,” *Microsystems Nanoeng.*, vol. 2, no. 1, p. 16025, Dec. 2016. doi:10.1038/micronano.2016.25.

[373] J. Zhao, Y. E, K. Williams, X.-C. Zhang, and R. W. Boyd, “Spatial sampling of terahertz fields with sub-wavelength accuracy via probe-beam encoding,” *Light Sci. Appl.*, vol. 8, no. 1, p. 55, Dec. 2019. doi:10.1038/s41377-019-0166-6.

[374] J. Kappa, D. Sokoluk, S. Klingel, C. Shemelya, E. Oesterschulze, and M. Rahm, “Electrically Reconfigurable Micromirror Array for Direct Spatial Light Modulation of Terahertz Waves over a Bandwidth Wider Than 1 THz,” *Sci. Rep.*, vol. 9, no. 1, p. 2597, Dec. 2019. doi:10.1038/s41598-019-39152-y.

Appendix A
THz QCLs in this thesis

Table A.1 Summary of all the THz QCLs in this thesis

No.	Active region design	Central Frequency (THz)	Length (mm)	Width μm	Wafer No.
QCL-A	Reference [182]	2.9	2.2	250	V427
QCL-B	Reference [182]	2.9	3	250	V427
QCL-C	Reference [172]	2.25	2.5	250	V208
QCL-D	Reference [172]	2.25	2	250	V208
QCL-E	Reference [172]	2.35	2	150	V220
QCL-F	Reference [182]	2.85	1.1	250	V557
QCL-G	Reference [182]	2.85	2.5	250	V557
QCL-H	Reference [182]	2.85	2	250	V557

Comments:

1. All the THz QCL in this thesis are fabricated with single-plasmon waveguide.
2. All the active region designs are bound-to-continuum.